

NATIONAL INSTITUTE FOR FUSION SCIENCE

JSPS-NRF-NSFC A3 Foresight Program Seminar Proceedings of Japan-
China-Korea Joint Seminar on Atomic and Molecular Processes in
Plasma Jul. 28 - Aug. 1, 2014, Lanzhou, China

Edited by D. Kato, X. Ding, and C. Dang

(Received - Sep. 29, 2015)

NIFS-PROC-99

Feb. 01, 2016

This report was prepared as a preprint of work performed as a collaboration research of the National Institute for Fusion Science (NIFS) of Japan. The views presented here are solely those of the authors. This document is intended for information only and may be published in a journal after some rearrangement of its contents in the future.

Inquiries about copyright should be addressed to the NIFS Library, National Institute for Fusion Science, 322-6 Oroshi-cho, Toki-shi, Gifu-ken 509-5292 Japan.

E-mail: gakujutsujoho@nifs.ac.jp

<Notice about photocopying>

In order to photocopy and work from this publication, you or your organization must obtain permission from the following organization which has been delegated for copyright for clearance by the copyright owner of this publication.

Except in the USA

Japan Academic Association for Copyright Clearance (JAACC)
6-41 Akasaka 9-chome, Minato-ku, Tokyo 107-0052 Japan
Phone: 81-3-3475-5618 FAX: 81-3-3475-5619 E-mail: jaacc@mtd.biglobe.ne.jp

In the USA

Copyright Clearance Center, Inc.
222 Rosewood Drive, Danvers, MA 01923 USA
Phone: 1-978-750-8400 FAX: 1-978-646-8600

JSPS-NRF-NSFC A3 Foresight Program Seminar
Proceedings of Japan-China-Korea Joint Seminar on
Atomic and Molecular Processes in Plasma

Jul. 28 – Aug. 1, 2014, Lanzhou, China

Edited by

Daiji Kato, Xiaobin Ding, and Chenzhong Dong

Abstract

As one of the activities of JSPS-NRF-NSFC A3 Foresight Program in the field of Plasma Physics “Study on Critical Physics Issues Specific to Steady State Sustainment of High-Performance Plasmas”, Japan-China-Korea Joint Seminar on Atomic and Molecular Processes in Plasma (AMPP2015) was held on July 28 – August 1, 2014, in Lanzhou, China. The total number of the officially registered participants was 50. This seminar is the extension of the last four seminars that were held in 2004 in Lanzhou, in 2007 in Dunhuang, in 2009 in Xi’an, and in 2012 in Lanzhou.

In the nuclear fusion plasma, there are quite a variety of atomic processes such as ionization, excitation, di-electronic recombination, collisional electron transfer, cascade radiation, and cascade Auger decay over the wide range of plasma temperature. The knowledge of those processes is indispensable for the evaluation and improvement of the plasma properties. Because of the diversity of the subjects, it is desirable to investigate them by international collaboration groups. This seminar is held to discuss achievement during the past two years and issues for the future prospect.

Keywords:

atomic and molecular process, plasma spectroscopy, excitation, ionization, recombination, charge transfer, X-ray scattering, EUV, polarization spectroscopy, electron momentum spectroscopy, tokamak, divertor, LHD, molecular processes, atomic structure

Preface

As one of the activities of Post Japan-China Core University Program and JSPS-NSFC-NRF A3 Foresight Program in the field of Plasma Physics “Study on Critical Physics Issues Specific to Steady State Sustainment of High-Performance Plasmas”, Japan-China-Korea Joint Seminar on Atomic and Molecular Processes in Plasma was held on July 28 – August 1, 2014 in Lanzhou, China. This seminar is the extension of the last four seminars that were held on March 6 – 11, 2004 in Lanzhou, China, on October 6 -12, 2007 in Dunhuang, China, on October 26 – 31, 2009 in Xi’an, China, and on July 30 – August 4, 2012 in Lanzhou, China.

Since the last seminar in 2012, researchers from Japan, China and Korea carried out a number of significant studies in atomic and molecular processes in relation to the fusion plasma. The proposal of the present joint seminar has placed its intention not only on the presentations of the collaborative studies, but also on offering an opportunity for the wide range of researchers from the countries to be acquainted with each other, who would have made an extensive exchange of information about the recent progress of the research activities, and also would have made an extensive discussion about the plan of the future collaborations.

In the present seminar, the total number of 23 oral talks was presented by experts from Japan, China and Korea. The total number of the officially registered participants was 50, in which 12 from Japan and 38 from China.

The seminar was in always a friendly and active atmosphere. During the seminar, the participants exchanged their new research results, discussed about the outlook for new research fields. They tried to promote further developments in mutual collaborations between the countries and the experts. Among them, the topics highlighted in the seminar was spectroscopic studies on highly charged ions of heavy elements including tungsten which will be primary heavy impurities in ITER plasmas. The next seminar will be held in 2016 and hosted by Prof. Zhenying Cui in Southwestern Institute of Physics, Chengdu, China.

The present issue of the proceedings has collected 16 papers from the delegates of the seminar. It covers the fundamental properties of atoms and ions, the collisions of electrons, photons and ions with atoms, molecules and ions, the analysis and diagnostics of the confinement fusion plasma especially for the properties of tungsten atoms and ions, atomic processes in high-density laser induced plasmas and, further, topics from wide area of atomic physics. The present issue includes abstracts of all presentations in the seminar, the scientific program, the group photo as well as the list of participants.

On behalf of the organizing committee, we would like to express our sincerest thanks to all the participants who made active contributions not only in the formal presentations but also in the fruitful discussions. We would like to acknowledge everybody who devoted very hard work for preparing the seminar. Finally, we would like to acknowledge the administrative as well as the financial supports from Northwest Normal University, and the National Institute for Fusion Science.

Chenzhong Dong

Local Chairperson,

Northwest Normal University, Lanzhou, China

Daiji Kato

Program Committee,

National Institute for Fusion Science, Toki, Japan

Xiaobin Ding

Seminar Secretary

Northwest Normal University, Lanzhou, China

Contents

Preface

Contents

Photo of Participants

Papers

Intensity ratio among Ne-like FeXVII n=3-2 transitions	1
<u>S. Morita</u> , X. Huang, T. Oishi, I. Murakami, H. Zhang, and M. Goto	
Energy transportation by MeV hot electrons in fast ignition plasma driven with LFEX PW laser	6
<u>H. Nishimura</u> , Z. Zhang, S. Fujioka, Y. Arikawa, M. Nakai, H. Nagatomo, H. Shiraga, S. Kojima, A. Morace, N. Miyanaga, J. Kawanaka, Y. Nakata, T. Jitsuno, H. Azechi, T. Ozaki, H. Chen, J. Park, G. J. Williams, T. Johzaki, and A. Sunahara	
Atomic process modeling based on nearest neighbor approximation	11
<u>T. Nishikawa</u>	
Edge impurity transport study based on carbon emission profile measurement with VUV spectroscopy in the HL-2A tokamak	22
<u>Z.Y. Cui</u> , C.F. Dong, S. Morita, H.Y. Zhou, X.T. Ding, P. Sun, M. Kobayashi, X.W. Cui, Y. Xu, X.L. Huang, Z.B. Shi, J. Cheng, Y.G. Li, B.B. Feng, S.D. Song, L.W. Yan, Q.W. Yang, and X.R. Duan	
Line Spectrum and Ion Temperature of Tungsten Ions at Low Ionization Stages in Large Helical Device Measured Using VUV Spectroscopy in Wavelength Range of 500-2200 Å	26
<u>T. Oishi</u> , S. Morita, X. L. Huang, H. M. Zhang, M. Goto, and the LHD Experiment Group	
Spatial profile measurement and analysis of EUV impurity spectra in HL-2A tokamak	30
<u>C.F. Dong</u> , Z.Y. Cui, H.Y. Zhou, S. Morita, P. Sun, B.Z. Fu, P. Lu, Y. Huang, X.T. Ding, Q.W. Yang, and X.R. Duan	
Electron correlation effects appeared in the lifetimes of sub-valence shell vacancy states in atomic ions	36
<u>F. Koike</u> , N. Suzuki, T. Nagoshi, Y. Yoda, and Y. Azuma	

Electron capture cross section scalings for low-q heavy ions	42
<u>A.M. Imai</u>	
Theoretical study on electron impact excitation and related polarization properties of subsequent radiative emission	48
<u>C.Z. Dong</u> , Z.B. Chen, J. Jiang, Z.W. Wu, and L.Y. Xie	
Development of time-resolved electron momentum spectroscopy: toward real-time imaging of frontier electrons in molecular reactions	61
M. Yamazaki and <u>M. Takahashi</u>	
How do we observe the forbidden lines from He-like ions in charge exchange collisions of H-like ions with neutral gases?	66
<u>H. Tanuma</u> , H. Shimaya, T. Ishida, N. Nakamura, N. Numadate, and K. Okada	
High-resolution X-ray scattering and its applications in atomic and molecular physics	71
<u>L.F. Zhu</u> and X. Kang	
Laser-produced multi-charged heavy ions as efficient soft x-ray sources	77
<u>T. Higashiguchi</u> , Y. Suzuki, M. Kawasaki, H. Ohashi, N. Nakamura, C. Suzuki, H.A. Sakaue, D. Kato, I. Murakami, F. Koike, S. Fujioka, H. Nishimura, A. Sunahara, B.W. Li, P. Dunne, and G. O'Sullivan	
Lost resonance lines in promethiumlike heavy ions	88
<u>N. Nakamura</u> , Y. Kobayashi, D. Kato, H.A. Sakaue, and I. Murakami	
EUV spectrum of highly charged tungsten ions in Electron Beam Ion Trap	94
<u>H.A. Sakaue</u> , D. Kato, I. Murakami, and N. Nakamura	
UV-visible M1 line emission from highly charged tungsten ions in LHD plasmas	100
<u>D. Kato</u> , H.A. Sakaue, I. Murakami, M. Goto, T. Oishi, N. Tamura, C. Suzuki, S. Morita, N. Nakamura, A. Sasaki, F. Koike, X.B. Ding, and C.Z. Dong	
 Agenda	 109
Seminar Program	111
Collection of Abstracts	115
Participants List	156

The 5th China-Japan Joint Seminar on Atomic and Molecular Processes in Plasma

Jul. 29—Aug. 1, 2014, Northwest Normal University, China



Intensity ratio among Ne-like FeXVII n=3-2 transitions

Shigeru MORITA^{1,2}, Xianli HUANG², Tetsutarou OISHI^{1,2}, Izumi MURAKAMI^{1,2},
Hongming ZHANG² and Motoshi GOTO^{1,2}

¹ National Institute for Fusion Science, Toki, Gifu 509-5292, Japan

² Department of Fusion Science, SOKENDAI (The Graduate University for Advanced Studies), Toki, Gifu 509-5292, Japan

Radial profiles of FeXVII 3s-2p and 3d-2p transitions emitted in wavelength range of 15-17Å have been observed in Large Helical Device (LHD). The Chord-integrated radial profiles are converted into radial emissivity profile by means of Abel inversion. The emissivity ratios among FeXVII n=3-2 transitions calculated from the radial emissivity profile are compared with calculation based on a collisional-radiative (CR) model developed for Fe ions. The result reasonably confirms the effect of electron temperature and density on the emissivity ratios. However, the emissivity of 3C ($2p^5 3d \ ^1P_1 \rightarrow 2p^6$) transition is obviously lower than the prediction from the CR model. This discrepancy is consistent with measurements in the solar corona and other laboratory plasmas.

Keywords: Ne-like iron, FeXVII, Intensity ratio, EUV spectroscopy

I. Introduction

Ne-like ion in the ionization balance of iron element is a dominant ionization state existing over a broad electron temperature range in both the cosmic and laboratory plasmas due to its closed L shell atomic configuration. Therefore, the 3s-2p and 3d-2p transitions of Ne-like iron (Fe^{16+}) at wavelength range of 15-17Å, which are prominent for diagnosing high-temperature plasmas, have been extensively studied in both the astrophysical and laboratory plasma studies, including the fusion plasma research [1-7]. A collisional-radiative (CR) model theoretically predicts that the intensities of FeXVII lines at 17.097Å, 17.054Å, and 16.777Å are dependent on not only electron temperature but also electron density. Therefore, the FeXVII lines with transitions of n=3 to n=2 called $L\alpha$ transition are very useful for measurements of electron temperature [8], electron density [5] and ion abundance [1]. In addition to such diagnostics, the $L\alpha$ transitions can be applied to the impurity transport study in fusion plasma research because their intensities are considerably strong [9]. In spite of this importance, however, observed intensities of a few FeXVII lines have not been well interpreted with the C-R modeling. For example, the observed overall intensity of 3s-2p transitions is larger than the theoretically predicted one when it is compared with the intensity of 3d-2p transitions [10]. A significant discrepancy between the observation and calculation exists in the intensity of the 3d-2p transition at 15.015Å [11]. Therefore, further investigation is necessary to explore the underlying physical processes related to the Ne-like FeXVII intensities.

II. Spectra and radial profiles of Ne-like FeXVII n=3-2 transitions

In Large Helical Device (LHD), the Fe n=3-2 $L\alpha$ transition array composed of ionization stages of Ne-like Fe^{16+} to Li-like Fe^{23+} ions have been observed at wavelength interval of 10-20Å. Figure 1 shows typical spectra of Fe $L\alpha$ array in different electron temperatures. Several FeXVII lines have been identified from the spectra as:

$$\begin{aligned} 3C: & 15.015 \text{ \AA} (2p^5 3d \ ^1P_1 \rightarrow 2p^6 \ ^1S_0), \\ 3D: & 15.262 \text{ \AA} (2p^5 3d \ ^3D_1 \rightarrow 2p^6 \ ^1S_0), \\ 3E: & 15.450 \text{ \AA} (2p^5 3d \ ^3P_1 \rightarrow 2p^6 \ ^1S_0), \\ 3F: & 16.777 \text{ \AA} (2p^5 3s \ ^3P_1 \rightarrow 2p^6 \ ^1S_0), \end{aligned}$$

3G: 17.054 \AA ($2p^5 3s \ ^1P_1 \rightarrow 2p^6 \ ^1S_0$) and
M2: 17.097 \AA ($2p^5 3s \ ^3P_2 \rightarrow 2p^6 \ ^1S_0$).

The 3G line is blended into the M2 line due to a limited spectral resolving power. The 3E line is usually weak for the observation. The 3G+M2 and 3C lines show the strongest intensity in the Fe $L\alpha$ transition array. It is very clear that the Ne-like FeXVII is entirely dominant in the Fe $n=3-2$ transition array when the electron temperature is low (see Fig.1 (a)), whereas the Fe $L\alpha$ lines from higher ionization stages, e.g. FeXXI, are gradually strong when the electron temperature increases (see Figs.1 (b) and (c)).

The vertical profiles of FeXVII lines have been measured with a flat-field space-resolved extreme ultraviolet (EUV) spectrometer working in wavelength range of $10-130 \text{ \AA}$ on LHD [12]. The EUV spectrometer consisting of a slit, a holographic grating and a charged coupled device (CCD) detector is installed on a midplane spectrometer port at the backside of a rectangular vacuum extension chamber connected to a midplane LHD port. The observation chords of the spectrometer passing through a horizontal slit for spatial resolution placed between the grating and the entrance slit have a small upper elevation angle to observe a vertical profile at upper half ($Z=0-50 \text{ cm}$) of horizontally elongated plasma cross section. In the present study the vertical profile is observed with a spatial resolution of 3 cm and the data are taken with a temporal resolution of 200 ms . The resolving power ($\equiv \lambda/\Delta\lambda$) at $\lambda=17 \text{ \AA}$ is 400 during the line identification and 80 during the profile measurement. Figure 2 (a) shows the vertical profiles of line intensity integrated along the observation chords against different FeXVII transitions of 3C, 3D, 3F and 3G+M2.

The radial emissivity profiles shown in Fig.2 (b) are derived from the vertical profiles in Fig.2 (a) based on an Abel inversion technique. The magnetic flux surface structure in LHD plasmas is calculated with a variation moments equilibrium code (VMEC) [13]. Then, the integral lengths of emissivity at all magnetic surfaces are evaluated with finite- β value along the observation chords of the spectrometer. Here, it should be pointed out that the magnetic flux surfaces are also assumed outside the last close flux surface (LCFS) by extrapolating the magnetic surface contour. Although the assumption may cause certain uncertainty, it does not strongly affect the emissivity peak inside the LCFS because the emissivity outside the LCFS is usually weak.

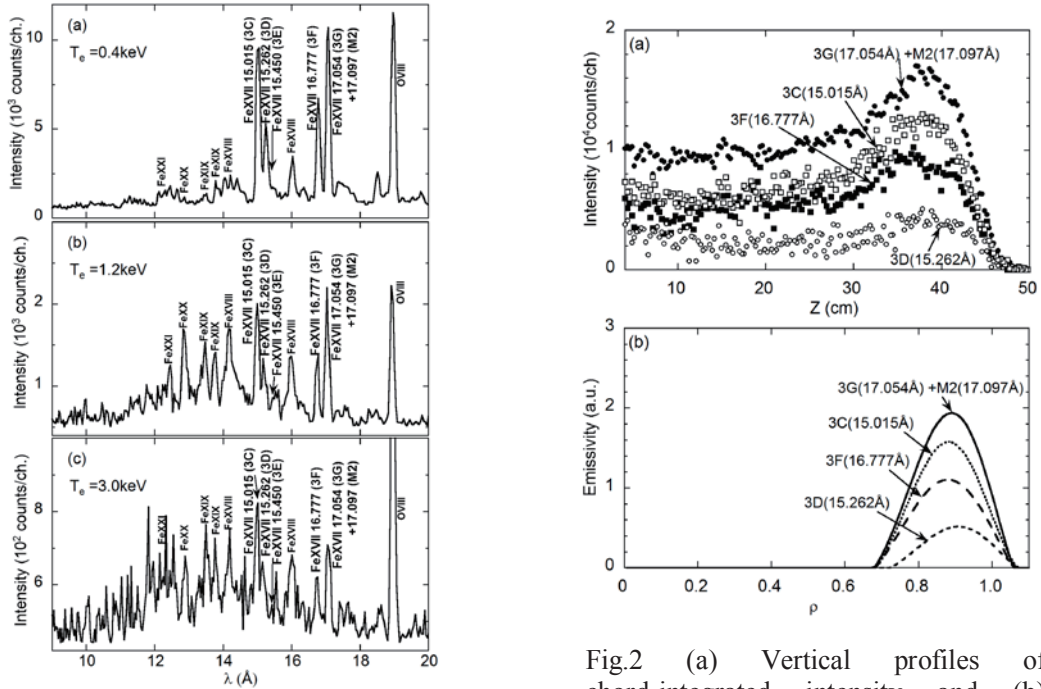


Fig.1 EUV spectra of Fe $n=3-2$ transitions in discharges with different electron temperatures of (a) 0.4 keV , (b) 1.2 keV and (c) 3.0 keV .

Fig.2 (a) Vertical profiles of chord-integrated intensity and (b) emissivity profiles as a function of normalized radius in Ne-like ArVII $n=3-2$ transitions.

III. Collisional-radiative (CR) model for iron

A CR model is developed for Fe ions including the fine-structure levels with the principal quantum number up to $n = 5$ [14, 15]. Assuming a quasi-steady state, the CR model includes all relevant atomic processes necessary for determining the level population. Most of atomic data are calculated with HULLAC code [16]. Although the population density of an excited level contains both the ionizing and recombining plasma components and a recombination component, the ionizing plasma component is the dominant process because the plasma discharge is stable and the recombining process is only dominant in the plasma termination phase.

The intensity coefficients of Fe XVII transitions are calculated with the CR model. The result is shown in Fig.3. The population in the upper levels of 3d-2p transitions (3C, 3D and 3E) is mainly determined by the collisional excitation from the ground level, whereas the upper levels of 3s-2p transitions (3F, 3G and M2) are dominantly populated by the cascade from higher levels [17]. The population redistribution through collision appears in the 3s-2p transitions when the electron density increases above 10^{13} cm^{-3} [5]. As a result, the intensity of 3G and 3F lines increases with density, while the M2 intensity decreases with density because the M2 line is a forbidden transition. The M2 intensity is then more sensitive to the density.

IV. Analysis of emissivity ratio among FeXVII n=3-2 transitions

The emissivity of 3C, 3D and 3F transitions is analyzed by taking the ratio against the 3G+M2 transition. The ratio is evaluated at the peak position of emissivity profiles in electron density range of $n_e = 1-5 \times 10^{13} \text{ cm}^{-3}$. The emissivity ratios analyzed here is shown in Fig.4 as a function of electron temperature, T_e . The result from theoretical calculation with the CR model is also shown in Fig. 4. The temperature and density profiles measured by Thomson scattering diagnostic is used in the analysis.

In the CR model calculation it is predicted that the emissivity ratios of 3D and 3F to 3G+M2 transitions, i.e., $\epsilon_{3D}/\epsilon_{(3G+M2)}$ and $\epsilon_{3F}/\epsilon_{(3G+M2)}$, are not sensitive to the electron temperature. The measurement plotted in Fig.4 also indicates a weak dependence on T_e and show a good agreement with the theoretical prediction. On the other hand, it is also predicted that the emissivity ratio, $\epsilon_{3C}/\epsilon_{(3G+M2)}$, increases with T_e . The ratio is then carefully investigated as plotted in Fig.3. It is found that the measured ratio is smaller than the theoretical calculation by 25-40%. Since the ratios of $\epsilon_{3D}/\epsilon_{(3G+M2)}$ and $\epsilon_{3F}/\epsilon_{(3G+M2)}$ are in good agreement between the measurement and calculation, the discrepancy in the ratio of $\epsilon_{3C}/\epsilon_{(3G+M2)}$ should be attributed to an overestimate of the 3C emissivity.

The discrepancy related to the 3C emissivity has been also studied in laboratory and astrophysical plasmas based on the analysis of the ratio, $R \equiv \epsilon_{3C}/\epsilon_{3D}$. The ratio of R in the present

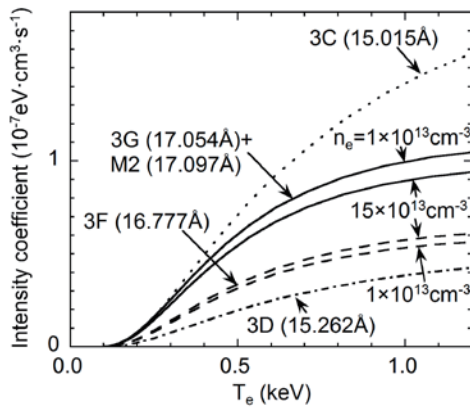


Fig.3 Intensity coefficients of FeXVII n=3-2 transitions as a function of electron temperature calculated with CR model.

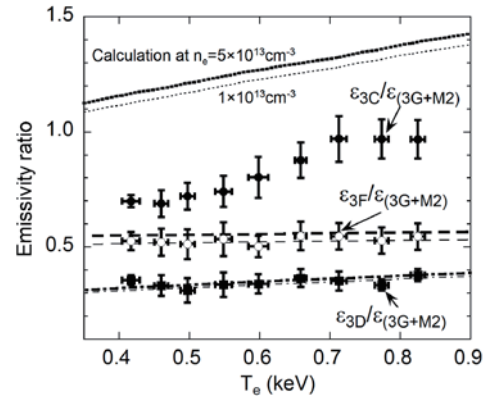


Fig.4 Emissivity ratios of FeXVII transitions as a function of electron temperature (circles and squares: measurement, lines: CR model calculation).

study ranges from 2.0 to 2.9 as T_e increases from 0.4 keV to 0.8 keV. The value is obviously lower than the predicted range of $R=3.6-3.7$. The present result is entirely consistent with the results from the solar corona [18], Princeton Large Torus (PLT) tokamak [6] and electron beam ion traps (EBITs) [3,19]. It also reveals that the discrepancy is not originated in certain effects related to chord-integrated information. Although there is no atomic theory explaining the discrepancy at present, a result from EBIT at Lawrence Livermore National Laboratory (LLNL) suggests that the excitation cross section of the 3C transition in the theoretical calculation is obviously underestimated, while the cross section of the 3D transition is in a good agreement with theory [20]. A recent study on the oscillator strength of 3C/3D suggests that the discrepancy is caused by the accuracy in atomic wave functions [21]. In order to obtain more accurate theoretical ratio, which should be close to the experimental value, further improvement is necessary for theoretical modeling including more complete treatment on spin-orbit interaction.

In addition to the T_e dependence of the ratio, the density effect on the ratio of $\epsilon_{3F}/\epsilon_{(3G+M2)}$ has been also examined. The density effect is studied by analyzing two discharges with distinctly different densities. The result is shown in Fig. 5. The shot numbers of #119551 and #118639 indicate a high-density discharge with flat T_e and centrally peaked n_e profiles and a low-density discharge with centrally peaked T_e and flat n_e profiles, respectively (see Figs.5 (b) and (c)). The emissivity ratio analyzed from the profiles is plotted in Fig.5 (a) with the result from CR model calculation. Due to the data scattering in the vicinity of plasma edge and the uncertainty in the Abel inversion near the plasma center, the emissivity ratio profile is expressed in a limited range of normalized radius from $\rho=0.2$ to 0.8.

The emissivity ratio at high density (#119551) is evidently larger than that at low density (#118639). Since the temperature of two discharge is almost identical in the region of $0.6 < \rho < 0.8$, the difference in the emissivity ratio between two discharges is certainly attributed to the density effect. These different values of measured ratio also show an excellent agreement with the CR model calculation. Furthermore, it is noticed that the ratio of #119551 increases with the density as a function of ρ because the temperature radially keeps constant, while the ratio of #118639 increases with the temperature as a function of ρ .

The space-resolved spectra from discharges similar to shot #119551 have been analyzed to study the density dependence of $\epsilon_{3F}/\epsilon_{(3G+M2)}$. Figure 6 shows the measured ratio as a function of

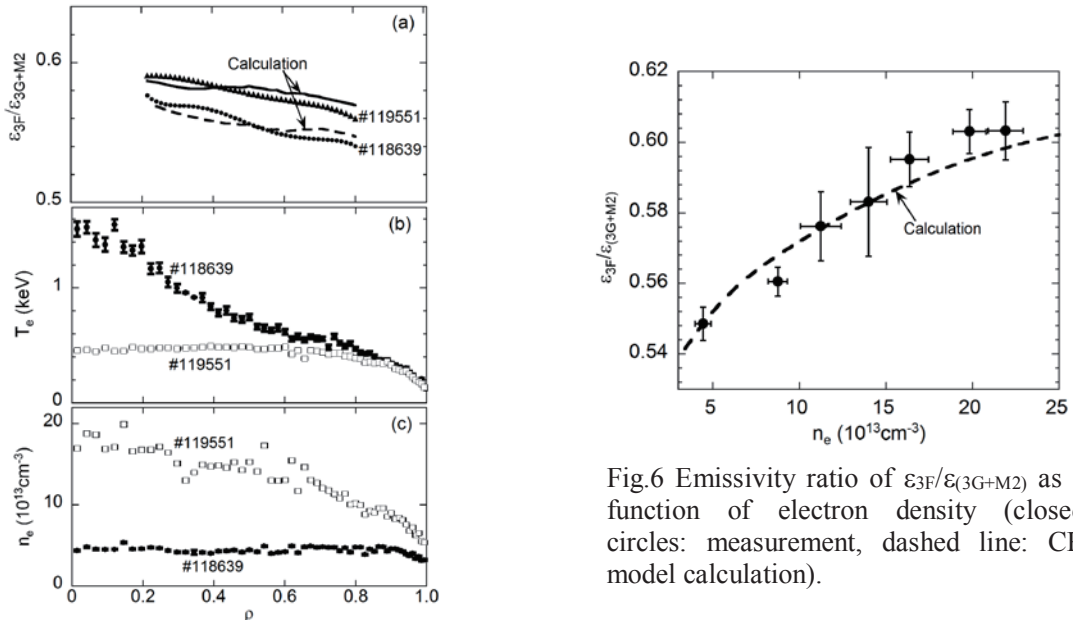


Fig.6 Emissivity ratio of $\epsilon_{3F}/\epsilon_{(3G+M2)}$ as a function of electron density (closed circles: measurement, dashed line: CR model calculation).

Fig.5 (a) Emissivity ratio profiles of $\epsilon_{3F}/\epsilon_{(3G+M2)}$ in two discharges at different densities (triangles and circles: measurement, lines: CR model calculation) (b) electron temperature profiles and (c) electron density profiles.

electron density. The result from CR model calculation is also plotted by dashed line. In the analysis, the electron temperature is fixed at 0.5 keV where the Ne-like iron is usually located. The ratios obtained here agree well with the theoretical calculation in density range of $n_e=4-22\times 10^{13}$ cm⁻³, while the relatively large error bars are due to a low signal-to-noise ratio in the measured signal. As a result, the density effect on the FeXVII emissivity ratio is clearly confirmed through the present study.

V. Summary

Ne-like FeXVII $n=3-2$ $L\alpha$ transitions denoted with labels of 3C, 3D, 3E, 3F, 3G and M2 have been observed with radial intensity profiles from LHD plasmas. Radial emissivity profiles of the FeXVII transitions are calculated from the intensity profiles by means of Abel inversion and the emissivity ratios among the FeXVII transitions are analyzed. A CR model specially developed for Fe ions is applied for analyzing the data. Although the emissivity ratios of $\epsilon_{3D}/\epsilon_{(3G+M2)}$ and $\epsilon_{3F}/\epsilon_{(3G+M2)}$ well agree with the CR model calculations, the emissivity ratio of $\epsilon_{3C}/\epsilon_{(3G+M2)}$ shows a clear discrepancy by 25%-40%. The result indicates that the discrepancy is not caused by the chord-integrated effect in the measured intensity. The density effect on the emissivity ratio of $\epsilon_{3F}/\epsilon_{(3G+M2)}$ is also examined. The result experimentally verifies that the ratio is also sensitive to the electron density as well as to the electron temperature.

Acknowledgements

The authors would like to thank all the members of the LHD team for their cooperation. This work was partially carried out under the LHD project financial support (NIFS13ULPP010) and supported by the JSPS-NRF-NSFC A3 Foresight Program in the field of Plasma Physics (NSFC: No.11261140328, NRF: 2012K2A2A6000443).

References

- [1] K. Waljeski, D. Moses, K.P. Dere, J. Saba, D. Web, and D. Zarro, *Astrophys. J.*, **429**, 909 (1994).
- [2] S.M. Kahn, F.D. Seward, and T. Chlebowski, *Astrophys. J.*, **283**, 286 (1984).
- [3] G. V. Brown *et al.*, *Astrophys. J.*, **502**, 1015 (1998).
- [4] K. J. H. Phillips *et al.*, *Astron. Astrophys.* **324**, 381 (1997).
- [5] M. Klapisch *et al.*, *Phys. Lett. A*, **69**, 34 (1978).
- [6] P. Beiersdorfer, S. von Goeler, M. Bitter, and D.B. Thorn, *Phys. Rev. A*, **64**, 032705 (2001).
- [7] P. Beiersdorfer, M. Bitter, S. von Goeler, and K. W. Hill, *Astrophys. J.*, **610**, 616 (2004).
- [8] J. C. Raymond, and B.W. Smith, *Astrophys. J.*, **306**, 762 (1986).
- [9] P. Beiersdorfer *et al.*, *Rev. Sci. Instrum.*, **60**, 895 (1989).
- [10] U. Feldman, *Comments At. Mol. Phys.*, **31**, 11 (1995).
- [11] J. L. Saba, J. Y. Schmelz, A. K. Bhatia, and K. T. Strong, *Astrophys. J.*, **510**, 1064 (1999).
- [12] X. L. Huang, S. Morita, T. Oishi *et al.*, to be published in *Rev. Sci. Instrum.*
- [13] S. P. Hirshman, *et al.*, *Comput. Phys. Commun.* **43**, 143 (1986).
- [14] N. Yamamoto *et al.*, *Astrophys. J.* **689**, 646 (2008).
- [15] I. Murakami *et al.*, *Plasma and Fusion Research*, **5**, S2021 (2010).
- [16] A. Bar-Shalom, M. Klapisch, and J. Oreg, *J. Quant. Spectrosc. Radiat. Trans.*, **71**, 179 (2001).
- [17] B.W. Smith, J. C. Raymond, J. B. Mann, and R. D. Cowan, *Astrophys. J.*, **298**, 898 (1985).
- [18] A. K. Bhatia and J. L. R. Saba, *Astrophys. J.* **563**, 434 (2001).
- [19] J. M. Laming *et al.*, *Astrophys. J.*, **545**, L161 (2000).
- [20] G. V. Brown, *Can. J. Phys.* **86**, 199 (2008).
- [21] S. Bernitt, *et al.*, *Nature*, **492**, 225 (2012).

Energy transportation by MeV hot electrons in fast ignition plasma driven with LFEX PW laser

H. Nishimura¹⁾, Z. Zhang¹⁾, S. Fujioka¹⁾, Y. Arikawa¹⁾, M. Nakai¹⁾, H. Nagetomo¹⁾, H. Shiraga¹⁾, S. Kojima¹⁾, A. Morace¹⁾, N. Miyanaga¹⁾, J. Kawanaka¹⁾, Y. Nakata¹⁾, T. Jitsuno¹⁾, H. Azechi¹⁾, T. Ozaki²⁾, H. Chen³⁾, J. Park³⁾, G. J. Williams³⁾, T. Johzaki⁴⁾, and A. Sunahara⁵⁾

¹⁾*Institute of Laser Engineering, Osaka University, 2-6 Yamada-oka, Suita, Osaka 565-0871, Japan*

²⁾*National Institute for Fusion Science, LHD, High Temperature Plasma G. 322-6 Oroshi Toki, Gifu 509-5292, Japan*

³⁾*Lawrence Livermore National Laboratory, Livermore, CA 94550, USA*

⁴⁾*The Graduate School of Engineering, Hiroshima University, 1-4-1 Kagamiyama, Higashi Hiroshima 739-8527, Japan*

⁵⁾*Institute for Laser Technology, 2-6 Yamada-oka, Suita, Osaka 565-0871, Japan*

August 31, 2014

Implosion and heating experiments with the scheme of fast ignition (FI) have been performed on Gekko-XII and LFEX laser platform at the Institute of Laser Engineering in Osaka University. A cone-guided CD-shell has been used as a base-line target for the fast ignition realization. The information about energy transfer from LFEX petawatt (PW) laser is quantitatively studied with an absolute $K\alpha$ diagnostics and a fast electron trajectory simulation. The transfer efficiency (η_{TE}) is estimated for a planar interaction as a reference and for several types of guiding-cone. As a general trend, the guiding-cone enhanced the η_{TE} by a factor of 3 comparing with the planar case.

Keywords: Fast ignition, x-ray spectroscopy, Laser transfer efficiency

1 Introduction

Fast ignition is recognized as a promising pathway to efficient thermonuclear fusion in laser-driven inertial confinement fusion. A cone-guided CD-shell has been used as a base-line target for the fast ignition realization at Institute of Laser Engineering in Osaka University [1, 2]. Experiments were taken out with Gekko-XII laser for implosions and LFEX laser for heating. It has long been expected to provide more quantitative information about the hot electron generation and transportation in the cone than those derived only with x-ray imaging and neutron detection. In this research, we propose an absolute $K\alpha$ line spectroscopy dedicated for quantitative measurement of hot electron generation and transportation in high-Z targets. This diagnostic provides local information about the hot electrons propagating through specific materials composing the cone-guided target.

In this study, Sn, Ta and Au were chosen as tracers since they are representative highest-Z materials which are available for the guiding cone, thus better matching with MeV-hot electrons than lower-Z tracers such as Cu.

2 Absolutely $K\alpha$ diagnostics

A Laue spectrometer was developed to cover high energy $K\alpha$ lines from Mo ($K\alpha_1$: 17.48 keV, $K\alpha_2$: 17.37 keV) to Au ($K\alpha_1$: 68.80 keV, $K\alpha_2$: 66.99 keV), as shown in Fig. 1 [3]. The spectrometer consists of a cylindrically curved quartz crystal (10-11) plate and a detector. The quartz plate is bent such that the diffracted x-rays are focused at an intermediate slit [4, 5]. X-ray components propagating in a straightforward manner are shielded from the detector directly with a lead pinhole plate located in front of the crystal and a pair of lead shields located at the intermediate x-ray focus. By varying the distances from the crystal to the source and detector, this spectrometer can cover the energy range of either 10-60 keV or 22-100 keV.

Figure 2 shows a typical image from the Au plasma. The bright spot in the center is the 0th order pinhole image and the line emission was imaged symmetrically on both sides. By plotting the line profile, the $K\alpha_1$, $K\alpha_2$ and $K\beta$ lines from Au were clearly seen.

author's e-mail: nishimu@ile.osaka-u.ac.jp

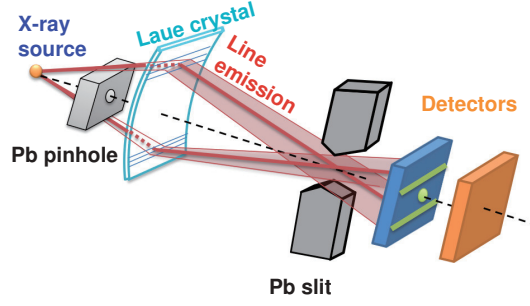


Fig. 1 The Laue spectrometer system.

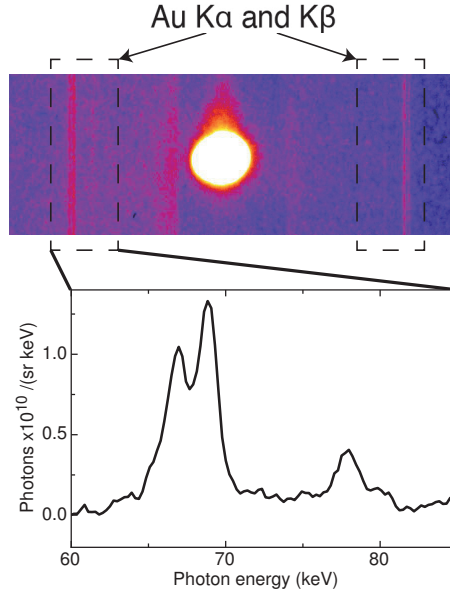


Fig. 2 The image from Au plasma on the Laue spectrometer.

3 Hot electron trajectory

The hot electron trajectory inside the solid target is tracked with a Monte-Carlo simulation. A 3-dimensional code PHITS was applied. The electrons propagation inside the target is treated with the continuous slowing down approximation (CSDA) model, which means that the electrons change their directions of motion due to elastic scattering, and lose their energy between two scattering points continuously. An example is shown in Fig. 3. The black square in the center indicates a 1 mm Ta cube, which is surrounded by low density air with a pressure of 10^{-5} Torr. The hot electron beam was irradiated on the Ta cube from the left side. An initial divergence of 45° and a Gaussian spatial profile were assumed. The energy spectrum was set based on the electron spectrometer (ESM) measurement in experiments. From Fig. 3, it is clearly seen that most of the electrons with energy less than 0.1 MeV were reflected at the front surface. The penetration depth increased along with electron energy; and only part of the electrons with energy higher than 1 MeV can propagate through the Ta cube and escape from the back surface.

4 Laser transfer efficiency

The number of $K\alpha$ photons $N_{K\alpha}$ generated from hot electron with number N_h and temperature T_h can be estimated by the following model [6]:

$$N_{K\alpha} = N_h \frac{n_A \omega_{K\alpha}}{4\pi} \int_0^\infty dE \sigma_{K\alpha}(E) \times \int_0^d dx f_h(E_0, x) \exp\left(-\frac{x}{\lambda_{mfp} \cos(\theta)}\right) \quad (1)$$

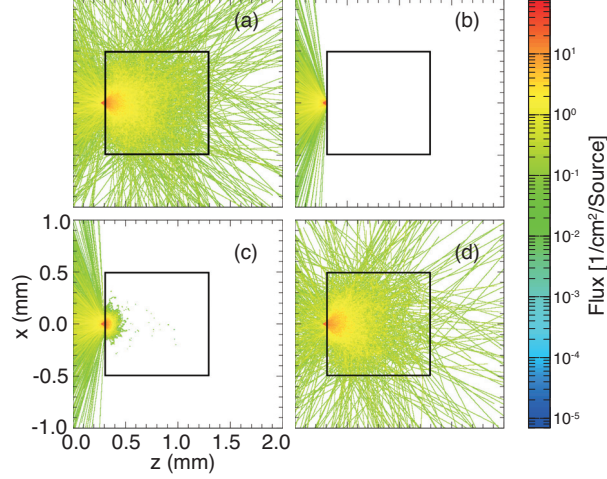


Fig. 3 Electron trajectory in the Ta cube: (a) all electrons, (b) electron with energy less than 0.1 MeV, (c) electron with energy from 0.1 to 1 MeV, (d) electron with energy more than 1 MeV.

where $\sigma_{K\alpha}$, $\omega_{K\alpha}$, and n_A are, respectively, the cross section for K-shell ionization, the $K\alpha$ fluorescence yield, and the atomic number density. The term $\exp(-\frac{x}{\lambda_{mfp} \cos(\theta)})$ describes the reabsorption of $K\alpha$ photons during the propagation through the target material, where θ is the angle between the spectrometer and the target normal. $f_h(E_0, x)$ describes the energy spectrum for the hot electron propagating inside the Ta cube with a depth x , where the information was achieved with the Monte-Carlo simulations. At $x = 0$, the hot electron energy spectrum has an one or two temperature exponential distribution as:

$$f_h(E_0) = N_{h1} \times \exp(-\frac{E}{T_{h1}}) + N_{h2} \times \exp(-\frac{E}{T_{h2}}) \quad (2)$$

where N_{h1} and N_{h2} represent the number of hot electron with temperature T_{h1} and T_{h2} . Considering the absolute $K\alpha$ photon number $N_{K\alpha}(exp)$ measured by the Laue spectrometer, the transfer efficiency η_{TE} can be estimated by comparing the experimental measurement with simulation results as:

$$\eta_{K\alpha} = \frac{\frac{N_{K\alpha}(exp)}{N_{K\alpha}(sim)} \times \int_0^\infty f_h(E_0)(sim)dE}{E_{laser}} \quad (3)$$

The transfer efficiency from LFEX laser to target has been estimated in the cases of planar and cone-guided geometries. In the case of planar target, an Au plate was placed at the target chamber center and LFEX laser with maximum energy of 1.8 kJ was focused on the front surface with an incident angle of 10° . The $K\alpha$ from Au was recorded by the Laue spectrometer and an ESM was located from the back surface for the hot electron temperature. The η_{TE} as a function of laser intensity is shown in Fig. 4. As a general trend, the η_{TE} is increased by increasing the laser intensity.

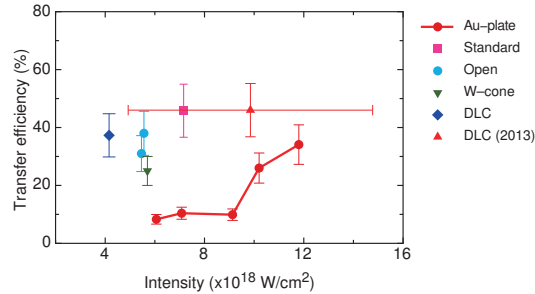


Fig. 4 The η_{TE} as a function of laser intensity for the planar and cone-guided targets. DLC(2013) is the DLC cone attached with a double-layer target.

The cone-guided configuration is shown in Fig. 5. A cone is attached with a CH hemi-shell, which was irradiated by three beams of Gekko-XII laser [2]. A dense plasma surrounding the tip of the cone was produced to mimic the condition of the fast ignition Au cone+CD shell target. The Ta cube was attached as the $K\alpha$ tracer after the CH hemi-shell. Four types of cone were used, as shown in Fig. 5 (b)-(e): (b) is the standard Au cone with $7 \mu\text{m}$ thickness; (c) is the Au open-cone

without the tip; (d) is the W-cone with double Au layers; and (e) is the diamond like carbon (DLC) cone. The estimated η_{TE} was shown in Fig. 4.

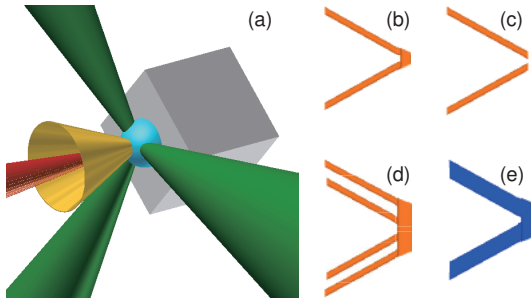


Fig. 5 (a). The configuration of a cone+CH hemi shell+Ta cube target; (b). Standard Au cone; (c). Open Au cone; (d). W-cone; (d). DLC cone.

5 Double-layer target

In order to achieve more information about the low energy hot electrons rather than that derived only from ESM, a double-layer target has been designed and tested experimentally. The basic idea is to add a second $K\alpha$ tracer layer in front of the Ta. Tentatively, a $200\ \mu\text{m}$ Sn was chosen: firstly, the $K\alpha$ lines from Sn can be clearly separated from Ta in the Laue spectrometer; secondly, the electrical resistivity of Sn is very similar to Ta, which can suppress the hot electron current change between the intermediate surface. The ratio of Sn to Ta $K\alpha$ photon numbers was simulated as a function of the effective hot electron temperature as shown in Fig. 6. This ratio is very sensitive for low temperature hot electrons. One of this double-layer target was experimentally tested with DLC cone. The ratio of Sn to Ta $K\alpha$ photon number was measured with Laue spectrometer as 4.6. From Fig. 6, the effective hot electron temperature is 5.3 MeV. Considering the quantitative yield of Sn and Ta $K\alpha$ photons, the η_{TE} was estimated to be about 46%, as plotted in Fig. 4.

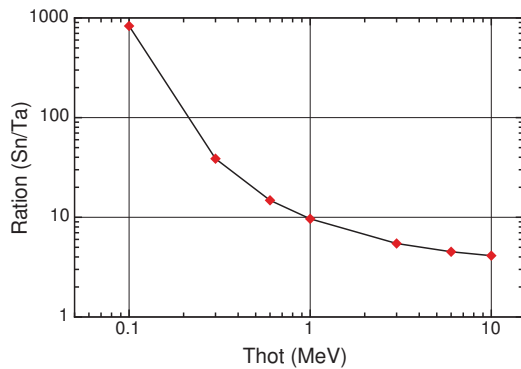


Fig. 6 The ratio of Sn to Ta $K\alpha$ photon numbers as a function of effective hot electron temperature.

6 Conclusion

$K\alpha$ line spectroscopy, particularly for hard x-ray region, has been proposed for quantitative measurement of cone-guided fast ignition experiment. The Sn, Ta and Au $K\alpha$ lines were observed and the energy transfer efficiency was provided. Compared with the planar geometry, the LFEX laser transfer efficiency is significantly enhanced with a guiding cone. Besides ESM, a double-layer target was designed to achieve more information about the low energy hot electrons. The $K\alpha$ photon numbers from the two tracer materials were used to estimate the effective hot electron temperature. In the near future, the thickness and materials of the double-layer target will be further optimized.

Acknowledgments

The authors would like to thank the Gekko-XII and LFEX laser operation crew, the target fabrication group, the plasma diagnostics group, and the computer operation staffs for their great contribution to this work. The work by LLNL staffs were performed under the auspices of the U.S. DOE by LLNL under Contract DE-AC52-07NA27344.

- [1] R. Kodama et. al., *Nature* **412** 798 (2001).
- [2] H. Shiraga, S. Fujioka, M. Nakai et. al., *Plasma Phys. Contr. Fusion* **53** 124029 (2011).
- [3] Z. Zhang, H. Nishimura, T. Namimoto et. al., *Rev. Sci. Instrum.* **83** 053502 (2012).
- [4] Y. Cauchois, *J. de Phys. et le Radium*, **3** 320-336 (1932).
- [5] J. F. Seely, L. T. Hudson, G. E. Holland, and A. Henins, *Appl. Opt.* **47** 2767-2778 (2008).
- [6] D. Salzmann, C. Reich, I. Uschmann, E. Förster, and P. Gibbon, *Phys. Rev. E* **65** 036402 (2002).

Atomic process modeling based on nearest neighbor approximation

NISHIKAWA Takeshi

Graduate School of Natural Science and Technology, Okayama University,

3-1-1 Tsushima-naka, Okayama 700-8530, Japan

e-mail: nishikawa.takeshi@okayama-u.ac.jp

Abstract

An atomic modeling based on the nearest neighbor approximation (NNA) to solve atomic process in plasmas was considered. In the atomic modeling, it includes the plasma effect to the electron state densities of the atom or ion as the potential due to the nearest neighbor atom or ion. Using the modeling, I was able to compute the ionization degrees of hydrogen plasmas without any *ad hoc* assumption adopted in the atomic modeling based on the plasma microfield. In order to apply the NNA to the plasmas of near and above solid density, three adequate treatments were required to obtain physically acceptable results. The first one was the Coulomb interaction between pairs of ions. The second one was the modification of the Saha equation. The third one was the adequate treatment of the neutral atom's contribution to the potential distribution as the nearest neighbor particle.

Keywords: bound state, free state, statistical weight, state density, Saha equation, nearest neighbor approximation, ionization degree

1. Introduction

Calculating the Ionization degrees is one of the basic problems in the analysis of the atomic process in plasmas. When a plasma can be assumed to be in the local thermodynamic equilibrium, we usually use the Saha equation to solve the atomic process in the plasma:

$$\begin{aligned} \frac{N_{Z+1}N_e}{N_Z} &= \frac{U_{Z+1}}{U_Z} \exp\left(-\frac{I_p}{k_B T_e}\right) \frac{8\pi\sqrt{2m_e^3}}{h^3} \int_0^\infty \sqrt{E} \exp\left(-\frac{E}{k_B T_e}\right) dE \\ &= \frac{U_{Z+1}}{U_Z} \exp\left(-\frac{I_p}{k_B T_e}\right) 2 \left(\frac{2\pi m_e k_B T_e}{h^2}\right)^{3/2}. \end{aligned} \quad (1)$$

where N_{Z+1} , N_Z , U_{Z+1} , U_Z , N_e , I_p , k_B , T_e , m_e , h , and E denote the number densities of $(Z + 1)$ -charged ions, and Z -charged ions; the statistical weights of the $(Z + 1)$ -charged ions and Z -charged ions; the number density of the electrons and the ionization potential from the Z -charged to the $(Z + 1)$ -charged states, the Boltzmann constant, the electron

temperature, the mass of the electron, the Planck constant and the electron energy level, respectively. The Saha equation gives a relation between a bound state and free state. For the free state, we know that the state density is proportional to the square root of the electron's energy. Usually we see, in the Saha equation, the factor as integrated one with the Boltzmann factor. This equation is just for the ground state. Thus, there are equations for many excited states. In principle, the number of bound states of hydrogen atom is infinite if the atom is set in an infinite volume. Consequently, if we want to solve the atomic process to obtain ionization degrees by the Saha equation, we have to determine a finite set of the bound states from considering the plasma effect. But to determine the set of the bound states is sometimes difficult. This is one of the famous problems considered for a long time. Now, in the most of the atomic modeling, the set of the bound states is determined by the plasma microfield[1,2].

But for the free state, only few models consider the effect of the plasma to evaluate the state density[2,3]. If we use the atomic model based on the nearest neighbor approximation, we can also evaluate the plasma effect upon the free states. In this paper, I will show the plasma effect on the free state densities in detail. Moreover, its applicability to the higher densities near and above the solid density is also discussed.

2. State Density

I begin with a basic property of the electron state density. The quantum statics says that the electron state density per unit volume is given by the equation:

$$8\pi p^2/h^3 dp, \quad (2)$$

expressed by momentum p . If the relation between the energy E and the momentum of the electron is given by the relation:

$$E = \frac{p^2}{2m_e}, \quad (3)$$

Eq. (2) is translated to be as a function of the electron's energy:

$$f(E) dE = \frac{8\sqrt{2}\pi m_e^{3/2}}{h^3} \sqrt{E} dE. \quad (4)$$

This square root dependency on the electron's energy in the state density has already seen in Eq. (1).

I have already refer the word 'state density' many times in this paper. Here, I annotate the exact definition of the word 'state density' in the modeling of the electron state. Using the quantum mechanics, even the free electron has discrete energy levels under the certain

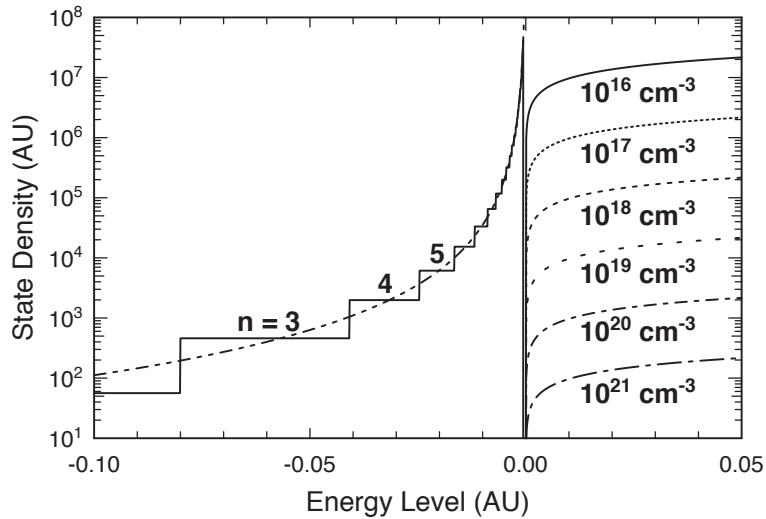


Figure 1: Electron state densities of hydrogen atom as a function of the electron energy level. For the bound electron of which energy is below zero, the number of state are shown as the reduced state density described in the text up to $n = 30$. For the free electron of which energy is above zero, the state densities of the various ion number densities of the plasma ranging from $N_i = 10^{16} \text{ cm}^{-3}$ to 10^{21} cm^{-3} are shown.

boundary conditions in the plasma. I assumed that various ions have various radii of ion sphere in the plasma. The ion sphere is an effective volume where an ion can occupy in the plasma. If the number of state of the free electron is averaged over the various ion's contribution due to the various radii of the ion sphere, the number of state for the free electron can be continuously expressed as a function of its energy. What I refer to as the state density is the continuous number of electron's state as a function of energy throughout this paper.

Figure 1 shows the state density of the free and bound electrons. The state densities of the free electrons are shown above the energy equal to zero. The state densities of the bound electrons are shown as the reduced bound state densities up to $n = 30$ below the energy equal to zero. The reduced bound state densities will be discussed later in this paper. The energy equal to zero is defined as the value at infinity. Equation (4) represents the state density per unit volume. If the volume per an atom becomes smaller, the state density of the free electron per an atom becomes also smaller. We can see that the state density becomes 10 times smaller if the number density of the plasma becomes 10 times larger as shown in Fig. 1. Here, I emphasize that these state densities for free electrons are just for the free electrons in free space. Basically in plasmas, there are ions, and therefore, there are potential contributions owing to the other ions, i.e., the free electron in a plasma does not exist in free space.

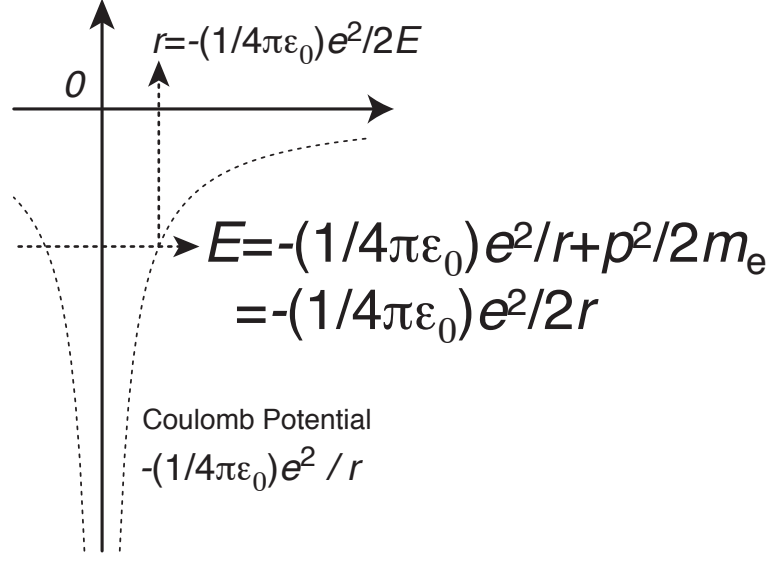


Figure 2: Potential profile of hydrogen atom and its energy level are shown with its classical radius.

By the quantum mechanics, the energy levels below zero is obtained as discrete, i.e., the bound states. But using the way to calculate the state density of the free state described above, we can also calculate the electron's state density below the energy equal to zero in the Coulomb potential if we introduce a difference from the situation of free electrons. For free electrons, the relation between the energy level and momentum is Eq. (3). But in the Coulomb potential, the additional term due to the potential is included to sustain the orbit at r in the Coulomb potential from the classical point of view,

$$E = \frac{p^2}{2m_e} - \frac{1}{4\pi\epsilon_0} \frac{e^2}{r} \quad (5)$$

where e and ϵ_0 are the elementary charge and the permittivity of the vacuum, respectively. For the electron of energy E , the available volume in the Coulomb potential is the ion sphere of radius $-(1/4\pi\epsilon_0)e^2/2E$ (Fig. 2), the resulting state density of the bound electron can be calculated by the integration,

$$\int_0^{-(1/4\pi\epsilon_0)e^2/2E} dr f'(E) dE 4\pi r^2 = \frac{2\sqrt{2}\pi^3 m_e^{3/2} e^6}{h(-E)^{5/2}} dE \quad (6)$$

In the Coulomb potential, the state density is proportional to energy to the power of minus five halves.

What is the meaning of the Eq. (6)? In the quantum mechanics, the bound state is obtained as discrete levels. But if the levels are located between the middles of nearby levels

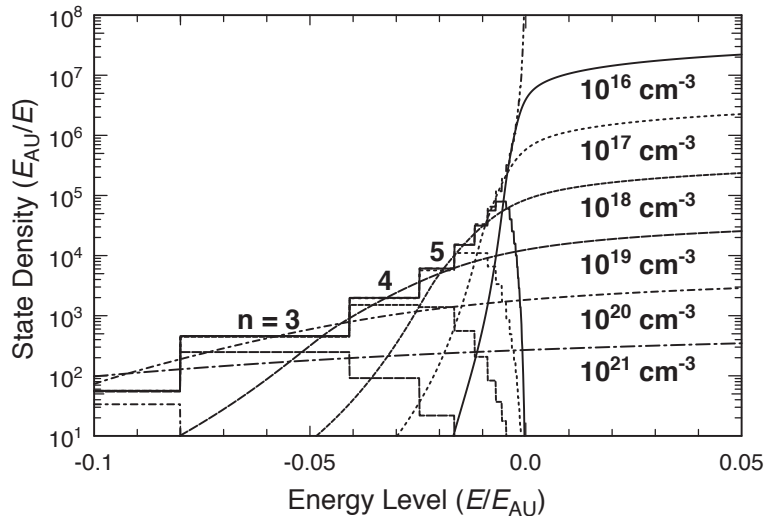


Figure 3: State density obtained by the atomic model based on the plasma microfield with modification in potential assuming the mirror symmetry with respect to saddle point for various ion number densities ranging from $N_i = 10^{16} \text{ cm}^{-3}$ to 10^{21} cm^{-3} for hydrogen plasmas.

continuously, the state densities of bound electron can be expressed like the equation:

$$f(E) = \frac{2n^2}{E_{n+1/2} - E_{n-1/2}} \quad (7)$$

This state density has stepwise shape and is referred as the reduced bound state density in this paper. The stepwise state density converges into the Eq. (6).

Although the energy levels of the bound states are broadened by various perturbations in real plasmas, the broadening widths are much narrower than those of the separation. If we draw the number of states of the bound electron as they are, it is difficult to examine the adequacy of the state density. But if we draw the bound state densities as Eq. (7), we can easily compare the values of the state densities in a finite volume from the continuity of the state density even when the state changes from bound to free.

In the last this seminar[4], I had presented the atomic model based on the plasma microfield. Using the microfield-based atomic model, I had successfully been able to calculate the state densities of bound and free electrons shown in Fig. 3. For the case of $N_i = 10^{16} \text{ cm}^{-3}$, the bound state of up to $n = 8$ exists, and the higher excited states disappear due to the plasma microfield. Alternatively, the free state covers the vacant state density due to the plasma microfield. In the microfield-based atomic model, the potential distribution has the saddle point formed by the Coulomb potential and uniform electric field and I assumed that the states are free if the electron's energy is above the saddle

point. But the simple calculation of the state densities were not physically acceptable. Therefore, I had to assume that the strong electric field does not exist uniformly within the ion sphere. When the saddle point is inside the ion sphere, I had to assume that the potential distribution forms mirror symmetry with respect to the saddle point.

From this knowledge, I tried to develop a new atomic model in which the nearest neighbor ion is explicitly considered.

3. Nearest Neighbor Approximation(NNA)

I consider the simplest case of pure hydrogen plasmas without Coulomb correlations to demonstrate the new atomic process model. The evaluation of the potential distribution, including the nearest-neighbor-ion perturbations, involves the nearest-neighbor probability distribution at a distance R (in spherical coordinates). If the ions are evenly distributed in space, the probability of finding a perturbing ion in a small volume δV is given by $N_p \delta V$, where N_p is the number density of the perturbing ion. If there are no ions inside the ion sphere of radius R , and only one ion is found on the surface, the probability of finding the nearest-neighbor ion at R is given by:

$$P(R) dR = (1 - N_p \delta V)^{4\pi R^3/3\delta V} 4\pi R^2 N_p dR = 4\pi R^2 N_p \exp\left(-\frac{4}{3}\pi R^3 N_p\right) dR. \quad (8)$$

N_p is essentially equal to the ion number density N_i . For the special case of a fully ionized plasma (as used below to compute the state densities of the bound and free electrons), N_p is equal to the total number density of the ions and neutral atoms, N_0 .

To calculate the bound-electron state density, the two hydrogen ions are placed next to each other and the potential distribution at a nearby location \mathbf{r} is given by the superposition of their respective Coulomb potential:

$$\phi = \frac{1}{4\pi\epsilon_0} \frac{Z_a e}{\mathbf{r}} + \frac{1}{4\pi\epsilon_0} \frac{Z_p e}{R - \mathbf{r}} \quad (9)$$

The origin ($\mathbf{r} = 0$) is at the ion considered, which carries a nuclear charge Z_a . This potential distribution has a saddle point. The hydrogen ion has classical bound states with energies $-m_e e^4 Z_a^2 / 8\epsilon_0^2 h^2 n^2$, which are assumed to be unaltered, even in potential distributions other than the Coulomb potential. Here, n denotes the principal quantum number of the state. An electronic state is assumed to represent a free electron for energies above this saddle point, and a bound state for energies below it. A bound state therefore disappears when its energy coincides with the saddle-point potential energy. Thus, the threshold radius for which the bound state n exists is given by $r_{th} = 8\epsilon_0 h^2 n^2 / \pi m_e e^2 Z_a$, where I used $Z_p = Z_a$. Because the bound state exists when the nearest-neighbor ion is

farther than the threshold radius r_{th} , the probability that the bound state of the hydrogen ion with principal quantum number n exists is given by

$$w_n = \int_{r_{\text{th}}}^{\infty} P(R) dR \quad (10)$$

To accommodate the potential effect in evaluating the free-state density, we rewrite the relation between the energy and momentum p of the electron at (r, θ) in spherical coordinates as

$$\frac{p^2}{2m_e} = E + \frac{1}{4\pi\epsilon_0} \left(\frac{Z_a e^2}{r} + \frac{Z_p e^2}{\sqrt{R^2 - 2rR \cos \theta + r^2}} \right) \quad (11)$$

instead of its conventional form, $p^2/2m_e = E$. The first term inside the brackets on the right-hand side of Eq. (11) is the Coulomb potential of the ion used to compute the state density of the free electron, and the second term inside the brackets is the Coulomb potential of the nearest neighboring ion. The free-state density $f(E)$, as a function of the electron energy, is calculated by

$$\begin{aligned} f(E) &= \frac{8\pi\sqrt{2m_e^3}}{h^3} \int_0^{\infty} P(R) \\ &\quad \frac{V_e(E)}{V_i} \iint_D \sqrt{E + \frac{Z_a e^2}{4\pi\epsilon_0} \left(\frac{1}{r} + \frac{1}{\sqrt{R^2 - 2rR \cos \theta + r^2}} \right)} 2\pi r^2 \sin \theta dr d\theta dR, \\ D &= \left\{ (r, \theta) : r \leq R_i, E \geq -\frac{Z_a e^2}{4\pi\epsilon_0} \left(\frac{1}{r} + \frac{1}{\sqrt{R^2 - 2rR \cos \theta + r^2}} \right), E \geq E_{\text{th}} \right\} \quad (12) \end{aligned}$$

where $Z_p = Z_a$. The double integral covers the ion sphere of radius R_i defined by $4\pi R_i^3 N_i/3 = 1$. Regions where the potential energy is greater than E are excluded from the integration because the value inside the square root in Eq. (12) is negative, which forbids the existence of electrons from the classical viewpoint. Moreover, as we assume the free-electron states for energies above the saddle point, the double integration is performed for E values greater than $E_{\text{th}} = -Z_a e^2/\pi\epsilon_0 R$. Basically, the free-state density is defined per unit volume of the ion sphere $V_i = 1/N_i = 1/N_e$, where N_e denoted the number density of electrons. (In the normal Saha equation, this factor is found in the left-hand side of the Eq. (1) as N_e .) In the present model, the available volume for an electron with energy E , determined by $V_e(E) = \iint_D 2\pi r^2 \sin \theta dr d\theta$, may become smaller than that of the ion sphere V_i . In this case, the state density becomes sparse in the energy space due to the limitation of the available volume of an electron. Therefore, the additional factor $V_e(E)/V_i$ is required in the equation. Using this factor, we can calculate the bound-state density in the pure Coulomb potential converging to the classical bound-state density discussed in Sec. 2. Figure 4 shows the energy dependence of the state densities of the bound

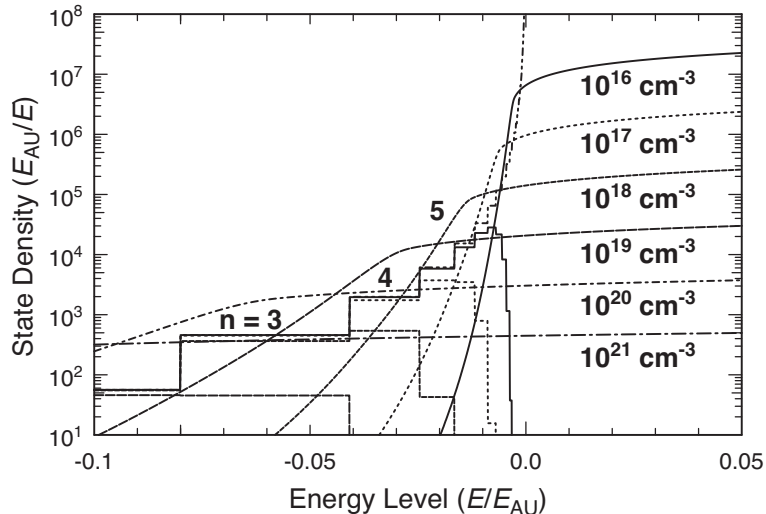


Figure 4: State densities by the nearest neighbor approximation for various ion number densities ranging from $N_i = 10^{16} \text{ cm}^{-3}$ to 10^{21} cm^{-3} for hydrogen plasmas.

and free electrons of the hydrogen plasmas obtained using the above potential modeling. The results are plotted for the same six cases as those in Fig. 3, with N_0 ranging from 10^{16} cm^{-3} to 10^{21} cm^{-3} . In evaluating the probability of finding the first-nearest neighbor ion at a given location, the plasmas were assumed to be fully ionized, i.e., $N_p = N_0$. By using the atomic model based on the nearest-neighbor approximation, physically appropriate free-state densities can be calculated without requiring any *ad-hoc* assumptions, such as a mirror symmetry in the potential distribution with the saddle point that was introduced in the microfield-based model[2].

The models based on the plasma microfield and on the nearest-neighbor approximation give similar global results. In the latter case, the total state density for bound and free electrons continuously changes as a function of the electron energy. The maximum principal quantum numbers of the bound state for $N_p = 10^{16}$ and 10^{17} cm^{-3} , which can be compared to the experimental results[5], are the same. However, the resulting reduction in the bound-state densities occurs slightly more rapidly using the atomic model based on the nearest-neighbor approximation.

On the other hand, the two models yield substantially different free-state densities. More specifically, the free-state densities evaluated within the nearest-neighbor approximation are significantly greater than the densities of the bound states that disappear at the corresponding energy, whereas the free-state densities are almost the same as the densities of the bound states that disappear when the atomic model based on the plasma

microfield is used.

4. Near and Above Solid Density

I was successfully able to obtain the electron state densities by the atomic modeling based on the nearest neighbor approximation. But the assumption that ions are evenly spread in space is realized in relatively low densities and high temperatures. In order to apply the NNA for the practical purpose, solving the plasmas of near and above solid density is necessary. Many improvements will be likely required to apply the NNA to the high density and low temperature plasmas. My preliminary study showed that three key physical modelings on the electron state densities in a plasma are at least necessary.

The first one was the effect of the Coulomb interaction between pairs of ions into the distribution of the nearest neighbor ion. In order to introduce the Coulomb interactions, I rewrite the nearest neighbor ion's distribution to be

$$P_i(R) = C_i \times 4\pi R^2 N_p \exp\left(-\frac{4}{3}\pi R^3 N_p - \frac{1}{4\pi\epsilon_0} \frac{Z_a^2 e^2}{R k_B T_i}\right) \quad (13)$$

where T_i is the temperature of the ion. The second term inside the exponential is due to the Coulomb interaction which is described by the ratio of the Coulomb potential to the electron temperature. But the integration of $P_i(R)$ from zero to infinity does not become unity, so the constant factor to fulfill the integrated values equal to unity is necessary. In Eq. (13), C_i is introduced to satisfy

$$\int_0^\infty P_i(R) dR = 1 \quad (14)$$

The second one is the modification of the Saha equation. Identically, the integration of counting the number of free electrons is from the minus infinity when we use the NNA. In the original Saha equation, Eq. (1), the integration is from the bottom of the ionization potential where the Boltzmann factor becomes unity. When the energy level is below the ionization potential, the Boltzmann factor becomes larger than unity. Thus the number of electrons unphysically becomes larger than the state densities. To avoid this difficulty, I separate the integral into two parts. One is that from minus infinity to the ground state, in which the Boltzmann factor is omitted, therefore, all states for the energy levels are fully occupied by the electrons.

$$\frac{N_{Z+1} N_e}{N_Z} = \frac{U_{Z+1}}{U_Z} \exp\left(-\frac{I_p}{k_B T_e}\right) \frac{8\pi\sqrt{2m_e^3}}{h^3} \left(\int_{-\infty}^{-I_p} f(E) dE + \int_{-I_p}^{\infty} f(E) \exp\left(-\frac{E}{k_B T_e}\right) dE \right) \quad (15)$$

The other is that from the ground state to infinity. For this case, the normal Saha equation is used. This treatment is just *ad hoc*, so more sophisticated way is expected.

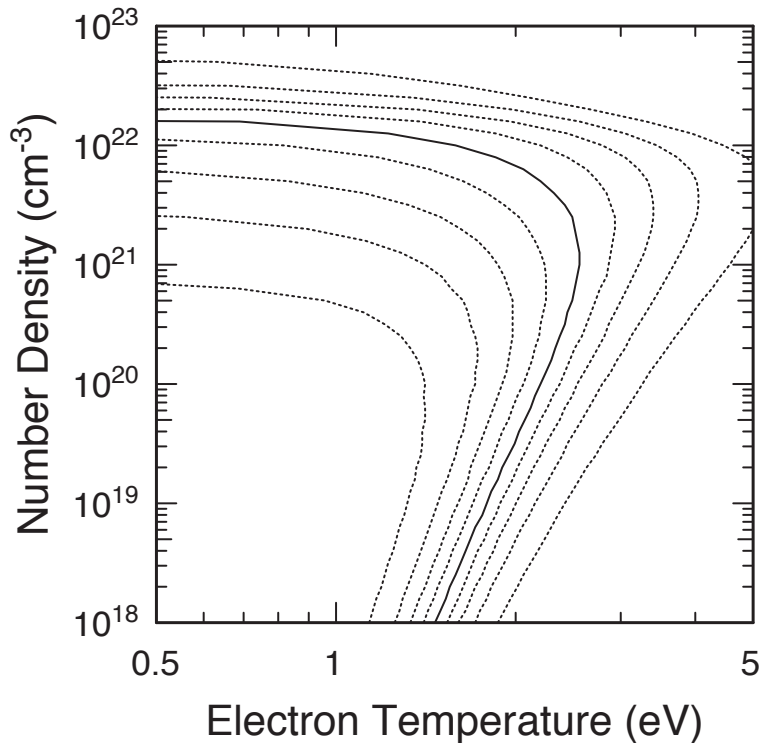


Figure 5: Contours of the ionization degrees of hydrogen plasmas obtained by the atomic model based on the nearest neighbor approximation. The pressure ionization can be observed near and above solid densities at low temperatures.

The third element was the treatment of the neutral atom's contribution to the nearest neighbor ion's distribution, and therefore, the neutral atom's contribution to the potential distribution. The contribution by the atom's located within the threshold radius and outside the threshold radius were separately considered. If the atom's location is within the threshold radius, there are no bound states and therefore, the Coulomb interactions are treated as ions, so that the potential profile can be assume to be those from two Coulomb potentials. But if the atom's location is outside the threshold radius, no Coulomb interaction is expected between an atom and an ion, so that the potential profile is without nearest neighbor atom's contribution at the position R where the nearest neighbor ion is located. Therefore, if $R > R_{\text{th},n=1}$, I used the distribution of the nearest neighbor particles:

$$P_n(R) dR = C_n \times 4\pi R^2 N_n \exp\left(-\frac{4}{3}\pi R^3 N_n - \frac{Z^2 e^2}{4\pi\epsilon_0 r_{\text{th},n=1} k_B T_i}\right) dr \quad (16)$$

in stead of Eq. (13). C_n is the constant to fulfill the integrated values equal to unity.

Improving the neutral atom's contribution, I was able to calculate the ionization degrees

as a function of number densities of plasmas. Figure 5 shows the resulting ionization degrees shown as the contours for various temperatures and number densities of particles of hydrogen plasmas. By the improved treatment of the neutral atoms, pressure ionization was observed from about 10 times lower densities than the results by the previously explained NNA model.

This trail to apply the NNA to the dense plasmas is just preliminary. I'm afraid there are many physical treatments I have to improve. But the presented modification is, at least, necessary to apply the NNA to the dense plasmas.

5. Conclusions

I have developed an atomic model based on the nearest neighbor approximation and showed some results on hydrogen plasmas.

Without the Coulomb interactions, the obtained results of the free state densities do not conflict with the experimental data. We conventionally believed that when the bound states disappear, the same amount of the free states appears, but in reality, appeared free state is basically larger than those disappeared bound states.

In order to apply the NNA to the dense plasmas, the Coulomb interaction between pairs of ions, the modification of the Saha equation, and the adequate treatment of the neutral atom are necessary. As a result, the pressure ionization was observed, but the pressure ionization occurs not abruptly, but begins moderately from about 1/10 lower density.

Acknowledgement

This work was partly supported by the JSPS - NRF - NSFC A3 Foresight Program in the field of Plasma Physics (NSFC: No.11261140328, NRF : No. 2012K2A2A6000443).

References

- [1] T. Nishikawa, *Astrophysical J.* **532**, 670 (2000).
- [2] T. Nishikawa, *Plasma and Fusion Science* 7, 1401142 (2012).
- [3] I. Shimamura and T. Fujimoto, *Phys. Rev. A* **42**, 2346 (1990).
- [4] *Proceedings of Japan-China Joint Seminar on Atomic and Molecular Processes in Plasma*, ed. Fumihiro Koike, Chenzhong Dong, and Xiaobin Ding, NIFS Proc. 91. (2013).
- [5] W. L. Wiese, D. E. Kelleher, and D. R. Paquette, *Phys. Rev. A* **6**, 1132 (1972).

Edge impurity transport study based on carbon emission profile measurement with VUV spectroscopy in the HL-2A tokamak

Z. Y. Cui¹⁾, C. F. Dong¹⁾, S. Morita²⁾, H. Y. Zhou¹⁾, X. T. Ding¹⁾, P. Sun¹⁾, M. Kobayashi²⁾, X. W. Cui¹⁾, Y. Xu¹⁾, X. L. Huang¹⁾, Z. B. Shi¹⁾, J. Cheng¹⁾, Y. G. Li¹⁾, B. B. Feng¹⁾, S. D. Song¹⁾, L. W. Yan¹⁾, Q. W. Yang¹⁾ and X.R. Duan¹⁾

¹⁾*Southwestern Institute of Physics, P. O. Box 432, Chengdu 610041, China*

²⁾*National Institute for Fusion Science, Toki 509-5292, Gifu, Japan*

E-mail contact of main author: cuizy@swip.ac.cn

Abstract

A one meter normal-incidence vacuum ultraviolet (VUV) spectrometer has been utilized for measuring impurity line emissions in the wavelength range of 300-3200 Å. The radial profile of carbon emissions of CV (2271 Å: 1s2s ³S-1s2p ³P) and CIV (1548 Å: 1s²2s ²S-1s²2p ²P) with an excellent spatial resolution of 2 mm is observed by the spectrometer equipped with a back-illuminated charge-coupled device (CCD) with size of 6.6×26.6 mm² (255×1024 pixels). Based on the analysis of carbon emissions, the diffusion coefficient and convective velocity of carbon ions are determined for the electron cyclotron resonance heating (ECRH) discharges of HL-2A. The ratio of CV to CIV is also used to characterize the edge impurity transport. The experimental observation and analysis using the impurity transport code indicate that the convective velocity of C⁴⁺ ions is changed to outward direction during ECRH phase, while the inward velocity is usually observed in Ohmic phase. The result is also compared with neon injection discharges.

Keywords: VUV spectroscopy, impurity emission, transport coefficients

1, Introduction

Impurity study is one of important issues in the fusion research, since light and heavy impurities bring fuel dilution and huge radiation loss in magnetically confined plasmas, respectively. In ITER the reduction of impurity concentration, in particular, in the plasma core is then strictly required, while a strong radiative cooling in the plasma edge is contrastively desired for the divertor heat load mitigation. Therefore, the impurity transport study is of great importance not only in the plasma core but also in the plasma edge. Spectroscopy in vacuum ultraviolet (VUV) and extreme ultraviolet (EUV) regions is commonly used for impurity diagnostic of magnetically confined fusion plasmas [1-3].

In general, the impurity transport coefficient has been examined using a tracer impurity injected with laser blow-off (LBO) technique and pellet injection. However, the data analysis based on these methods is limited only in the plasma core. It becomes difficult due to a lack of sufficient signal intensity in the outer region of plasmas ($\rho > 0.8$). On the other hand, when the absolute intensity profile of carbon emissions is measured, the edge impurity transport coefficient can be examined even if intrinsic impurities are adopted for the analysis. Based on this method, the edge impurity transport has been studied in the HL-2A discharges with ECRH heating.

2, Intensity calibration of VUV spectrometer

In the HL-2A tokamak, a 1 meter normal-incidence VUV spectrometer with Rowland mounting has been developed for measuring impurity line emissions in the wavelength range of 300-3200 Å. The spectrometer has been equipped with a back-illuminated charge-coupled device (CCD) with size of 6.6×26.6 mm² (255×1024 pixels) [4]. An excellent spatial resolution of 2 mm is achieved when a space-resolved slit of 50 μm in width is set between the entrance slit and the grating. A schematic view of the space-resolved VUV spectrometer is shown in Fig. 1. A lower half of the HL-2A plasma with averaged minor radius of 40 cm can be observed when the spectrometer is placed at about 6.3 m away from the plasma center.

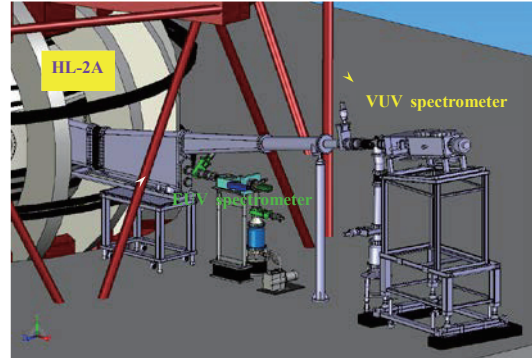


FIG.1. Schematic view of space-resolved VUV spectrometer system in the HL-2A tokamak. Vertical region over 400 mm can be observed at the plasma core.

In order to determine the transport coefficient of impurities with the space-resolved VUV spectrometer the intensity calibration of the system is necessary. For the purpose bremsstrahlung continuum in the VUV wavelength range emitted from the HL-2A plasmas is utilized for *in situ* absolute intensity calibration [5]. The absolute intensity of VUV bremsstrahlung continuum is calculated along the line of sight of the spectrometer by taking into account plasma parameters. The density dependence of measured VUV bremsstrahlung continuum is checked at several wavelength positions to verify the validity of the present method. Thus, the intensity calibration factor is obtained against the wavelength by comparing measured data with the calculated bremsstrahlung intensities.

3, Determination of impurity transport coefficients

There are several resonance transitions of carbon in the VUV wavelength range right for the edge impurity transport study. Reflecting the temperature profile of HL-2A plasmas, CIV (64 eV) and CV (392 eV) are usually located around last closed flux surface (LCFS) and deeply inside the LCFS, respectively. Since the CIV intensity can express the carbon influx entering the main plasma and the CV intensity reflects the transport in the core plasma through the LCFS, the ratio of CV to CIV can be applied to the edge impurity transport study near the LCFS. The chord-integrated vertical profile of CV and CIV from Ohmic and ECRH discharges is shown in Fig. 2. The intensity of CV and CIV are clearly enhanced when the ECRH is turned on. However, the ratio of CV/CIV is largely decreased by a factor of three compared with the ratio in the ohmic heating phase (it is not shown here). The result can be interpreted by the enhanced carbon influx at the LCFS. The carbon ions transferred to the plasma core does not increase, at least not proportional to the edge carbon

influx. Since the electron density and temperature profiles are changed during the ECRH phase, the simulation for the radial profile of CV and the ratio of CV to CIV has been done with a 1D impurity transport code STRAHL [6]. The effect of plasma parameter profiles measured with several diagnostics is included. The CIV is used as the source term of carbon in the simulation.

In the present study the diffusion coefficient $D(r)$ and convective velocity $V(r)$ profiles in the STRAHL code are assumed as a spatially constant value

and a linear function of $V(r) = V(a) \times r/40$, respectively. The simulation result is shown in Fig. 3 (a) and (b) for the Ohmic plasma and the ECRH plasma, respectively. The good agreement is obtained between the modeling and experiment for the Ohmic plasma with transport coefficients of $D = 0.6 \text{ m}^2/\text{s}$ and $V(a) = -1 \text{ m/s}$. These values are consistent with the previous experimental result attained by the laser blow-off method in HL-2A [7]. The transport coefficients obtained for the Ohmic plasma is applied to the analysis of ECRH plasma, as shown by dashed-dotted line. Although the source Q is set to fit the CIV intensity measured in the ECRH plasma, the resultant CV intensity (dashed-dotted line) is too much large compared to the measured CV (closed squares) in Fig. 3(b). It means the measured CV profile cannot be reproduced even if the temperature and density profiles are considered in the simulation. A good agreement is obtained when the convective velocity is increased to $V(a) = 7 \text{ m/s}$, as shown with solid line in Fig. 3(b). It can also make a good agreement for the density dependence of CV/CIV. Therefore, the result strongly suggests that the convective velocity of C^{4+} changes to outward direction during the ECRH phase, while it is inward direction in the Ohmic phase [8].

The impurity transport coefficient has also been examined using tracer impurity injection technique for the HL-2A ECRH plasma. Neon is injected during the ECRH phase with supersonic molecular beam injection (SMBI). The convection and diffusion of neon ions are analyzed by using a soft x-ray camera and bolometer array with good temporal and spatial resolutions. The transport coefficient obtained with good data fitting is $D(\rho = 0.9) = 1 \text{ m}^2/\text{s}$ and $V(\rho = 0.8) = 8 \text{ m/s}$, where ρ is the normalized poloidal flux coordinate. The convective velocity of neon also indicates the outward direction [9]. We can conclude the impurity transport coefficient obtained from intrinsic impurity emission is in good agreement with that obtained from tracer impurity method.

4, Summary

Edge impurity transport in ECRH discharges have been studied in HL-2A tokamak based on the profile measurement of intrinsic carbon line emissions of CIV

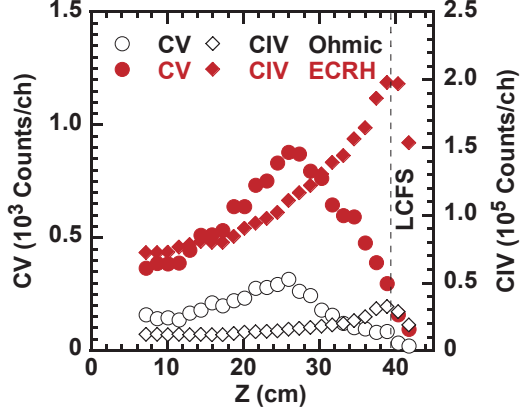


FIG. 2. Vertical profiles of CV (circles) and CIV (diamonds) in Ohmic (open symbols) and ECRH (full symbols) plasma phase.

and CV. The ratio of CV/CIV and its absolute intensity enable us to examine the impurity transport coefficient in the plasma edge. The transport coefficient is analyzed with 1-D impurity transport code. The radial profile of carbon emissions observed with the space-resolved VUV spectrometer, of which the spectral intensity is absolutely calibrated, is a key experimental data to determine the transport coefficient and convective velocity. As a result, we found from the analysis that the impurity transport in the plasma edge largely changes when ECRH is turned on and the change in the edge transport originates in the convective channel. The present result obtained with intrinsic impurity ions, i.e. change in the direction from inward velocity at Ohmic phase to outward velocity at ECRH phase, is reasonably confirmed from experiments with extrinsically injected neon as a tracer impurity.

Acknowledgements

The authors would like to acknowledge Dr. Motoshi Goto from NIFS for his effort on data acquisition system. The authors are also thankful to the HL-2A team for their technical supports. This work is partially supported by the National Natural Science Foundation of China under Grant (No. 11375057 and No. 11175061), National Magnetic Confinement Fusion Science Program (No. 2014GB108003) and the JSPS-NRF-NSFC A3 Foresight Program in the field of Plasma Physics (NSFC: No. 11261140328, NRF: No. 2012K2A2A6000443).

References

- [1] S. Morita and M. Goto, *Rev. Sci. Instrum.* **74** (2003) 2375.
- [2] M. B. Chowdhuri et al., *Rev. Sci. Instrum.* **78** (2007) 023501.
- [3] Z.Y. Cui et al., *Rev. Sci. Instrum.* **85** (2014).
- [4] Z.Y. Cui, et al., *Rev. Sci. Instrum.* **81** (2010) 043503.
- [5] C. F. Dong, S. Morita, M. Goto and E. H. Wang, *Rev. Sci. Instrum.* **82** (2011) 113102.
- [6] R. Dux, IPP Garching Technical Report No 10/30, 2006.
- [7] W. Chen, Z.Y. Cui et al., *Chin. Phys.* **16** (2007) 3451.
- [8] Z.Y. Cui, S. Morita, H.Y. Zhou et al., *Nucl. Fusion* **53** (2013) 093017.
- [9] X.W. Cui, Z.Y. Cui, B.B. Feng et al., *Chin. Phys. B* **22** (2013) 125201.

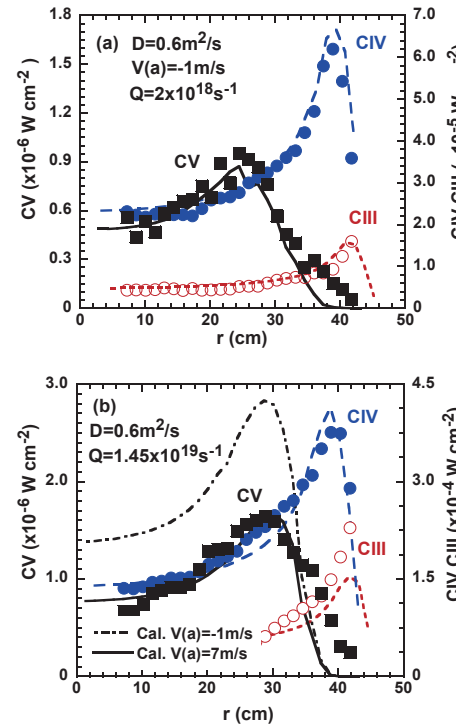


FIG. 3. Comparison between measured profiles (symbols) and modeling profiles (lines) obtained by 1D transport code STRAHL for (a) Ohmic discharge with $D = 0.6 \text{ m}^2/\text{s}$, $V(a) = -1 \text{ m/s}$, and (b) ECRH case with $V(a) = -1 \text{ m/s}$ (dashed lines) and $V(a) = 7 \text{ m/s}$ (solid lines).

Line Spectrum and Ion Temperature of Tungsten Ions at Low Ionization Stages in Large Helical Device Measured Using VUV Spectroscopy in Wavelength Range of 500-2200 Å

T. Oishi^{1,2}, S. Morita^{1,2}, X. L. Huang², H. M. Zhang², M. Goto^{1,2} and the LHD Experiment Group

¹ National Institute for Fusion Science, 322-6, Oroshi-cho, Toki, 509-5292, Japan

² Department of Fusion Science, SOKENDAI (Graduate University for Advanced Studies), 322-6, Oroshi-cho, Toki, 509-5292, Japan

Abstract

Vacuum ultraviolet (VUV) spectra of emissions released from tungsten ions at lower ionization stages were measured in the Large Helical Device (LHD) in the wavelength range of 500 to 2200 Å using a 3 m normal incidence spectrometer. Tungsten ions were distributed in the LHD plasma by injecting a pellet consisting of a small piece of tungsten metal and polyethylene tube. Many lines having different wavelengths from intrinsic impurity ions were observed just after the tungsten pellet injection. Doppler broadening of a tungsten candidate line was successfully measured and the ion temperature was obtained.

Keywords

Vacuum ultraviolet, plasma spectroscopy, magnetically confined fusion, impurity transport, tungsten

I. INTRODUCTION

Tungsten is regarded as a leading candidate material for the plasma facing components in ITER and future fusion reactors. Thus, behavior of tungsten in toroidal plasmas has attracted attention¹⁻³. Considering tungsten impurity transport in ITER, the following three transport processes need to be evaluated: (1) release of neutral tungsten atoms from the divertor plates; (2) transport of tungsten ions at lower ionization stages in the edge plasmas; and (3) accumulation of tungsten ions at higher ionization stages in the core plasmas. Therefore, diagnostics for tungsten impurity ions in magnetically-confined high-temperature plasmas have been intensively conducted, such as visible spectroscopy for neutral tungsten atoms in the wavelength range around 4000 Å and extreme ultraviolet spectroscopy for highly-ionized tungsten ions in the wavelength range around 60 Å⁴. However, tungsten ions at lower ionization stages have not been measured except for several cases of vacuum ultraviolet (VUV) spectroscopy in basic plasma experiments even though it is necessary for accurate evaluation of tungsten influx and comprehensive understanding of the tungsten impurity transport in high temperature plasmas^{5,6}. In the present study, VUV spectra of emissions released from tungsten ions are measured using a 3 m normal incidence spectrometer in the Large Helical Device (LHD) in the wavelength range of 500 to 2200 Å. Identification of lines which are useful for diagnostics of tungsten ions at low ionization stages in ITER is attempted for the study of transport phenomena of tungsten ions in the edge plasmas.

II. EXPERIMENTAL SETUP

In this study, tungsten ions are distributed in the LHD plasma by injecting a polyethylene pellet containing a small piece of tungsten metal. Figure 1 is a schematic drawing of VUV spectroscopy in impurity pellet injection experiments. LHD has the major/minor radii of 3.6/0.64 m in the standard configuration with maximum plasma volume of 30 m³ and toroidal magnetic field of 3 T. The coil system consists of a set of two continuous superconducting helical coils with poloidal pitch number of 2 and toroidal pitch number of 10 and three pairs of superconducting poloidal coils. Figure 1(a) illustrates the top view of the instruments together with the optical axis of the VUV spectrometer and the incident orbit of the impurity pellet. The enlarged view of the vertical view angle of the VUV spectroscopy and the pellet orbit on the horizontally-elongated cross section of the magnetic field in LHD are also illustrated in Fig. 1(b). The tungsten impurity pellet consists of a small piece of tungsten wire covered by a polyethylene tube. The length and diameter of tungsten wire is 0.6 mm and 0.15 mm, respectively. The polyethylene tube has a dimension of 0.6 mm in length, 0.6 mm in outer diameter, and 0.3 mm in inner diameter⁷. The pellet is accelerated by pressurized He gas of 10-20 atm. The

pellet injection orbit is located on the midplane of the plasma having a 12° angle from the normal to the toroidal magnetic axis⁸. The 3m normal incidence VUV spectrometer (McPherson model 2253) is installed on an outboard midplane diagnostic port which is the same as the impurity pellet injector^{9,10}. The working wavelength range of the spectrometer is of 300 to 3200 Å. A mirror unit which consists of a convex mirror and a flat mirror is mounted in front of the entrance slit of the spectrometer, which expands the view angle so that the elliptical plasma of LHD can be fully observed at the horizontally-elongated plasma cross section. A back-illuminated CCD detector (Andor model DO435-BN: 1024×1024 pixels) is placed at the position of the exit slit of the spectrometer. CCD was operated in the “Full-binning” mode in which all 1024 vertical pixels are replaced by a single channel. Then, the spatial resolution is entirely eliminated. A slit for spatial resolution mounted between the entrance slit and the grating was fully opened to increase S/N ratio. Each spectrum can be taken with a time interval of 50 ms. The width of the entrance slit is set to 50 μm and the instrumental function is 0.194 Å in the full width of half maximum. A high wavelength dispersion of 0.037 Å/pixel enables measurements of the Doppler broadening of the impurity lines to obtain the ion temperature. The wavelength interval which can be measured in a single discharge is about 37 Å. Therefore, we conducted measurements by scanning the wavelength shot by shot between the wavelength range of 500-2200 Å in this study¹¹.

III. LINE SPECTRA AND ION TEMPERATURE MEASUREMENT

Figure 2 shows VUV spectra measured in the time frame just after the tungsten pellet injection in hydrogen discharge in LHD. The plasma was initiated by the electron cyclotron heating, and three neutral hydrogen beams based on negative ion sources with total port-through power of 8 MW were injected. Central electron density and temperature just before the pellet injection was $2 \times 10^{13} \text{ cm}^{-3}$ and 3 keV, respectively. In Fig. 2, well-known intrinsic impurity lines used for absolute wavelength calibration are indicated by solid arrows¹².

Except for those intrinsic impurity lines, several bright lines have been successfully observed, such as 605.93 Å in Fig. 2(a), 639.66 Å in Fig. 2(b), 677.72 Å in Fig. 2(c), and 1168.15 Å in Fig. 2(d). These lines have wavelengths almost identical to WVI lines with the wavelengths of 605.926 Å, 639.683 Å, 677.722 Å (5d-6p), and 1168.151 Å (6s-6p)¹². The second order emission of 605.93 Å, 639.66 Å and 677.72 Å lines were also observed as shown in Figs. 2(e-g). In this experiment, those lines appeared at the time frame just after pellet injection and almost all of them disappeared immediately. Therefore, they are considered to be tungsten emission from the pellet ablation process. Those newly found tungsten candidate lines will be useful for spectroscopic study because they have a relatively large intensity and are isolated from other intrinsic impurity lines. On the other hand, a few tungsten candidate lines including 677.72 Å line existed for a finite time after the pellet injection. This means that tungsten ions are distributed in plasmas. The temporal evolution of the line emission was investigated, as shown in Fig. 3. In this discharge, the heating scenario was the same as stated above. When the pellet is injected, the electron temperature drops and the electron density increases rapidly. Figure 3(b) shows the temporal evolution of line emission intensity evaluated by the area of the spectral peak and the ion temperature, T_i , obtained from the Doppler

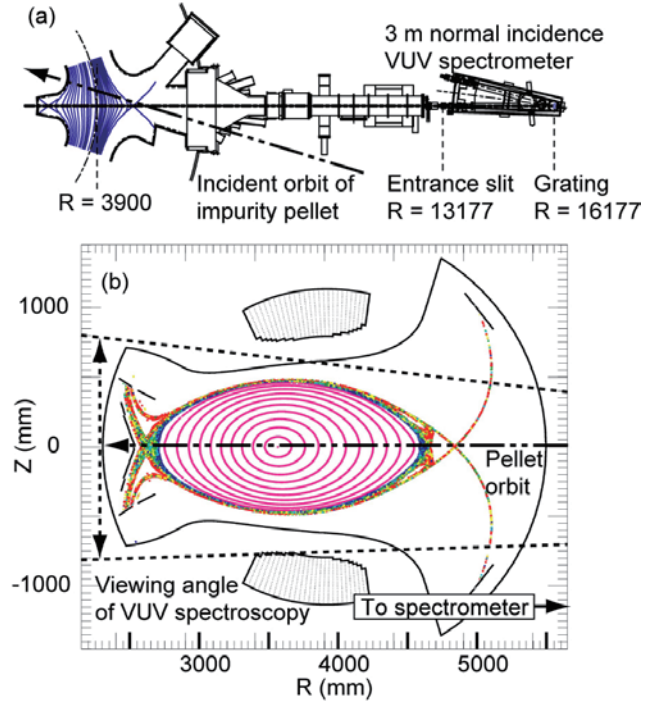


FIG. 1. Schematic drawing of VUV spectroscopy in impurity pellet injection experiments. (a) Top view of the instruments together with the optical axis of the VUV spectrometer and the incident orbit of the impurity pellet. (b) Vertical viewing angle and the pellet orbit on the poloidal cross section of the magnetic field in LHD.

broadening of the spectrum when the atom mass is assumed to be that of tungsten. The line intensity indicated by opened circles increased once at the timing of the pellet injection and turned to decrease down to 4.3s, and finally disappeared. During the period 4.0-4.3s in which the line existed, T_i increased from 400 eV to 700 eV. However, some arguments remain for the reasonability of these values of T_i if this line is assumed to be WVI. During the high density period after the pellet injection, a condition of $T_e = T_i$ is achieved because of the high collisionality. Therefore, impurity ions in a certain charge state cannot exist in a region in which T_i is much higher than the ionization potential, E_i , for the charge state. However, T_i obtained from the Doppler broadening of W 677.72 Å line ranging from 400 eV to 700 eV is much larger than E_i (W⁵⁺) of 64.8 eV. At present, the reason for this contradiction has not yet been clarified. Several reasons may be considered, such as emission from an unidentified line of tungsten ion at higher ionization stages or other broadening mechanisms of the spectra, which should be investigated in future studies. Figures 3 (c) and (d) show line intensities and ion temperatures evaluated from CIII 690.52 Å (1s²2s2p-1s²2s3s) and OIII 703.85 Å (2s²2p²-2s2p³) lines, respectively, measured in the same wavelength range to W 677.72 Å line. Signals were averaged over every 250 ms because of low intensities. The values of T_i for these lines were likely to be measured correctly because they ranged around their ionization potentials, E_i (CIII) of 47.9 eV and E_i (OIII) of 54.9 eV. Figure 4 shows enlarged wavelength spectra of W 677.72 Å line in several time frames after the pellet injection. We can find that broadening of the spectra was measured under adequate wavelength resolution and signal-to-noise ratio. These results indicate validity of the measurement and analysis methods applied in this study to obtain temperatures of impurity ions. In addition to strong lines discussed above, we found many tungsten candidate lines in this study. Their wavelengths will be summarized and compared to references, calculations, and basic experiments for accurate line identification. We also intend to propose the useful tungsten line for the spectroscopic study in ITER edge plasmas based on the progress of this study.

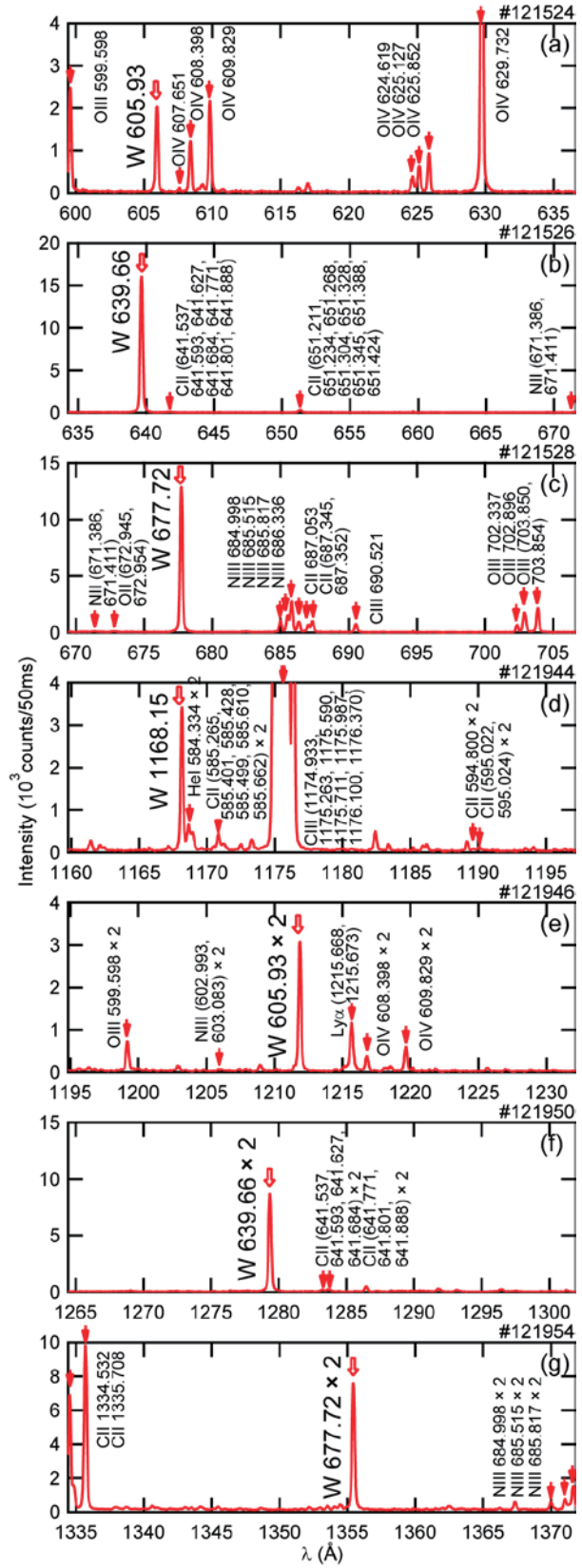


FIG. 2. VUV spectra including tungsten candidate lines.

IV. SUMMARY

A VUV spectroscopy using a 3 m normal incidence spectrometer was applied to measure VUV lines from tungsten ions at lower ionization stages in the wavelength range of 500-2000 Å. Many lines having different wavelengths from intrinsic impurity ions were observed just after the tungsten pellet injection. 605.93 Å, 639.66 Å, 677.72 Å, and 1168.15 Å were clearly identified as tungsten candidate lines, which have the possibility to be useful lines for spectroscopic study in the ITER edge plasmas. While the Doppler broadening of 677.72 Å line was successfully measured, identification of the charge state based upon a comparison between obtained T_i and the ionization potential requires further discussion.

ACKNOWLEDGMENTS

The authors thank all the members of the LHD team for their cooperation with the LHD operation. This work is partially conducted under the LHD project financial support (NIFS13ULPP010). This work was also supported by Grant-in-Aid for Young Scientists (B) 26800282 and partially supported by the JSPS-NRF-NSFC A3 Foresight Program in the field of Plasma Physics (NSFC: No.11261140328, NRF: No.2012K2A2A6000443).

REFERENCES

- ¹ITER Physics Basis Editors *et al.*, Nucl. Fusion **39**, 2137 (1999).
- ²R. Neu *et al.*, Nucl. Fusion **45**, 209 (2005).
- ³J. Roth *et al.*, *Plasma Phys. Control. Fusion* **50**, 103001 (2008).
- ⁴S. Morita *et al.*, AIP Conf. Proc. **1545**, 143 (2013); *Proceedings of ICAMDATA-2012*, Gaithersburg, 30 September–4 October 2012.
- ⁵R. Radtke *et al.*, *Atomic and Plasma-Material Interaction Data for Fusion* (IAEA, 2007), Vol. 13, p. 45.
- ⁶J. Clementson *et al.*, J. Phys. B: At. Mol. Opt. Phys. **43**, 144009 (2010).
- ⁷X. L. Huang *et al.*, “Coaxial Pellets for Metallic Impurity Injection on the Large Helical Device”, Rev. Sci. Instrum. (submitted)
- ⁸H. Nozato *et al.*, Rev. Sci. Instrum. **74**, 2032 (2003).
- ⁹T. Oishi *et al.*, Plasma Fusion Res. **8**, 2402093 (2013).
- ¹⁰T. Oishi *et al.*, J. Korean Phys. Soc. **64**, 840 (2014).
- ¹¹T. Oishi *et al.*, Rev. Sci. Instrum. **85**, 11E415 (2014)
- ¹²A. Kramida *et al.*, *NIST Atomic Spectra Database*, Version 5.1 (National Institute of Standards and Technology, Gaithersburg, MD, 2013), see <http://physics.nist.gov/asd>.

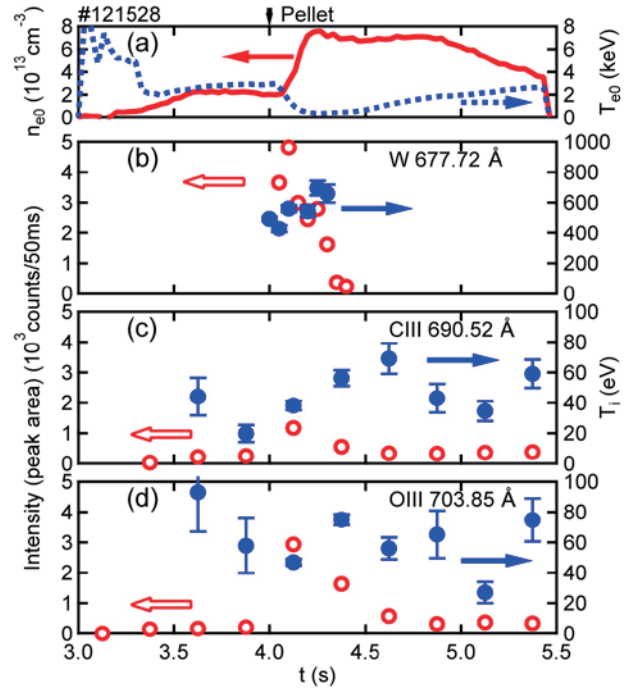


FIG. 3. (a) Temporal evolutions of central electron density and temperature in a hydrogen discharge with tungsten pellet injection. Line intensities and ion temperatures were evaluated from (b) tungsten candidate line located at 677.72 Å, (c) CIII 690.52 Å and (d) OIII 703.85 Å.

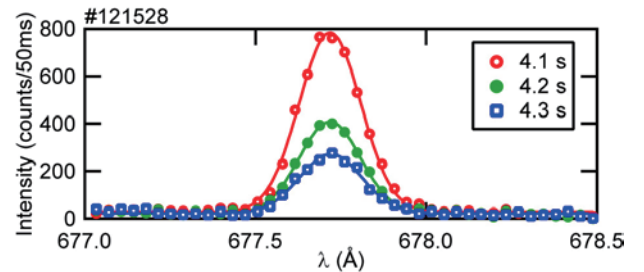


FIG. 4. Enlarged wavelength spectra of W 677.72 Å line in several time frames after the pellet injection.

Spatial profile measurement and analysis of EUV impurity spectra in HL-2A tokamak

Chunfeng Dong¹, Zhengying Cui¹, Hangyu Zhou¹, Shigeru Morita², Ping Sun¹, Bingzhong Fu¹, Ping Lu¹, Yuan Huang¹, Xuanton Ding¹, Qingwei Yang¹ and Xuru Duan¹

¹*Southwestern Institute of Physics, P. O. Box 432, Chengdu 610041, China*

²*National Institute for Fusion Science, Toki 509-5292, Japan*

Abstract:

A space-resolved EUV spectrometer working in wavelength range of 20-500Å has been successfully developed in HL-2A tokamak to study impurity transport and monitor impurity behavior. The EUV spectrometer consists of an entrance slit, a space-resolved slit, a varied-line-spacing holographic grating and a CCD detector. An excellent spectral resolution of 0.22Å at 200Å could be achieved when the entrance slit of 30µm is adopted. The spectrometer is placed at a distance of ~7500 mm from the plasma center, therefore, a half size of HL-2A plasma (a=400 mm) can be observed. Calculated wavelength based on grating working theory cannot be applied to EUV spectra identification. Result shows there is a small discrepancy between experimentally observed and theoretically calculated reciprocal linear dispersions. The spectra are compared with simulation results obtained by the CHIANTI code, which is based on the collisional-radiative models with a large number of accurate atomic data. A good agreement between the experimental and calculated results is obtained. The EUV spectra are excellently identified and result shows that the spectra are dominated by carbon, oxygen and nitrogen.

Key words: EUV spectrometer, spectra measurement, spectra identification, spectra simulation

1. Introduction

The study on impurity behavior is one of the most essentially important subjects in the magnetic-confined fusion plasma field. Peaked density profile is one of the necessary conditions for the plasma fusion, meanwhile it will result in high-Z impurity accumulation at plasma core, which will enhance the radiation power loss, leading to plasma disruption and discharge termination finally. Plasma disruption has to be avoided during plasma operation, since it has serious damage to the wall and plasma facing component. Light impurity, for instance, carbon and oxygen, can dilute the fuel ion density, enhance the bremsstrahlung continuum radiation, making fusion reaction difficult. On the other hand, high Z metal tungsten has been designated as the only material for ITER divertor plate [1]. Study on tungsten transport in plasma and the effect of tungsten to plasma performance is one of the essential subjects, however, the atomic structure of tungsten is not well known, therefore the identification of tungsten spectra becomes very difficult. The heat load onto ITER divertor plates is another critical issue and the radiative diveror is proposed for the heat load mitigation [2]. Radiative divertor plasma (detached plasma) is generally obtained by injection of gaseous impurities, for instance, neon and argon, into divertor in tokamaks. All the situation mentioned above will introduce impurity into plasma.

Spectroscopy is one of the important and effective diagnostics for the impurity study, and has been utilized in fusion devices worldwide. These spectrometers, however, focus on the impurity emissions in VUV and visible ranges. For instance, the space-resolved VUV

spectrometer working in wavelength range of 400-1600Å is installed in CHS [3]; a similar system is installed in ASDEX-U tokamak to observe the wavelength range of 400-1600Å [4]; a space-resolved VUV spectrometer based on CCD camera is developed in HL-2A in wavelength range of 300-3200Å [5]; and a visible spectrometer working in wavelength range of 4500-6000Å is installed in LHD for the profile measurement [6].

The plasma temperature is significantly increased recently based on the advanced heating technique, and the impurity line emission shifts towards the short wavelength range. Particularly for the high-Z material tungsten, the spectra are mainly measured below 100Å in the high temperature plasma from previous study [7-9]. On the other hand, study on impurity transport at plasma core is important for impurity control. Tracing the time evolution of impurity line emission has been used as a conventional method for impurity transport study. Recently, Dong and Morita proposed a new method for the impurity transport study based on impurity profile measurement [10,11]. Therefore, an EUV spectrometer with spatial resolution is desired for HL-2A tokamka.

2. Space-resolved EUV spectrometer

EUV spectrometer consists of an entrance slit, a spatial-resolution slit, a varied-line-spacing holographic grating and a CCD detector. Three entrance slits can be used and widths are 30, 100 and 200µm. When the 30µm is used, the spectral resolution is 0.22Å at 200Å. The wavelength range of EUV spectrometer is 20-500Å. A varied-line-spacing holographic grating with 1200 grooves/mm is equipped to this spectrometer in addition with a Andor CCD detector. The detective area of CCD camera is 26.6×6.6mm² with 1024×255 pixels. The angle of incidence of this spectrometer is 87°. The distance between the entrance slit and grating center is 237mm and the distance from grating center to focal plane is 235mm.

The vertical profile measurement is realized based on the principle of pin-hole imaging. A space-resolved slit is attached to the entrance slit, creating a pin-hole. The widths of entrance slit and space-resolve slit are 100µm and 0.5mm, therefore, a size of pin-hole of 5×10⁻⁸m² is obtained. The spectrometer is placed above the equatorial plane and the distance from plasma center to entrance slit is ~7500 mm, therefore, the EUV emission from the lower half (~400 mm) of HL-2A plasma can be observed. Two CCD operation modes are utilized for the measurement, i.e., full vertical binning mode and sub-image mode. Full vertical binning mode is adopted for

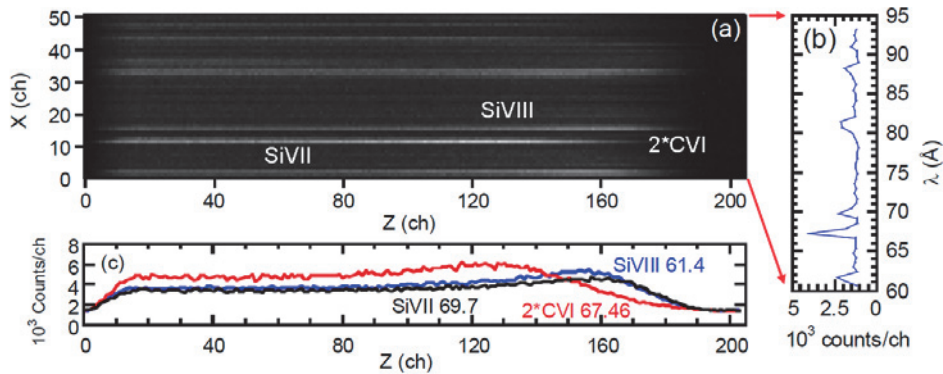


Fig. 1 (a) Two-dimensional image of vertical profile measurement, (b) wavelength distribution at Z=120ch, (c) vertical profiles of SiVII(69.7Å), SiVIII(61.4Å) and

wavelength distribution measurement with time resolution of 6ms, and sub-image mode is adopted for profile measurement with time resolution of 200ms. The detailed information on CCD operation can refer [12]. Here, 5 pixels binning on both directions is adopted for the profile measurement in HL-2A, then the number of practical working channel at both directions becomes 204×51chs. Fig. 1(a) shows the two-dimensional CCD image from profile measurement, in which Z direction denotes the vertical position of the impurity emission and X direction denotes the wavelength distribution. Fig. 1(b) shows the spectra wavelength distribution at Z=120ch, and (c) shows the vertical profiles of SiVII(69.7Å), SiVIII(61.4Å) and CVI(67.46Å=2×33.73Å). In Fig. 1(c), Z=0ch denotes plasma core area and Z=204ch denotes the plasma edge. The intensities of the three emissions decreasing towards plasma core shown in Fig. 1(c) is not real signal, and this is because the vacuum pipe does not match this measurement, therefore the light from plasma core is hid. SiVII, SiVIII and CVI shown in Fig. 1(c) have the similar distribution pattern, in which the profile tends to be flat towards plasma core and forms a slight peak at plasma edge, however, the peak location is dramatically different. As seen from Fig. 1(c), the peak location of CVI is innermost, and peak location of SiVII is outermost, and SiVIII is located between CVI and SiVII. The change in peak location is consistent with the change in ionization energy of the three ions.

3. Identification on EUV spectra

The wavelength detected by EUV spectrometer can be expressed by equation (1), where m is

$$m\lambda = \sigma_0(\sin\alpha + \sin\beta) \quad (1)$$

diffraction order, σ_0 is the nominal groove spacing, α is angle of incidence, and β is angle of diffraction. The wavelength corresponding to each CCD pixel can be calculated and the spectra then can be identified based on the calculated wavelength. Fig. 2 shows the EUV spectra distribution as a function of calculated wavelength, which has been calibrated based on line

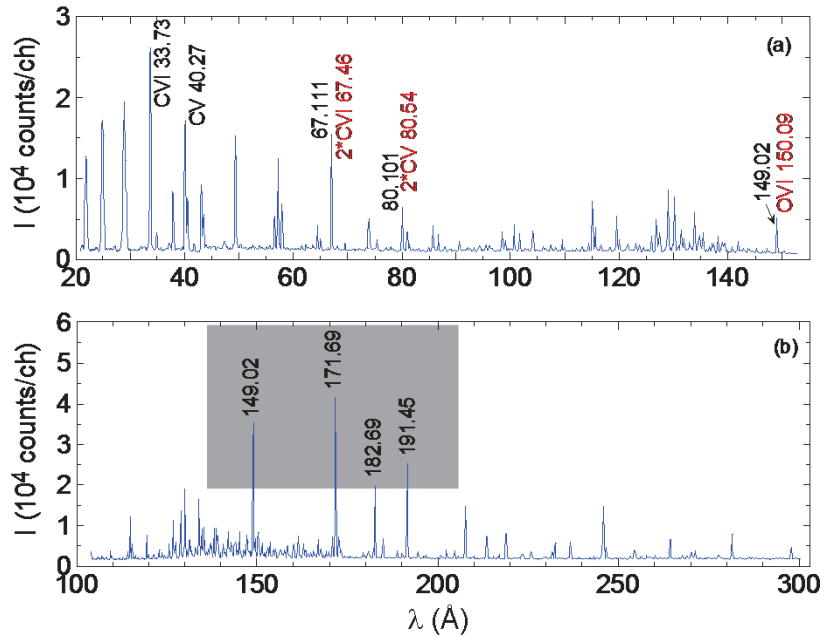


Fig. 2 EUV spectra distribution from typical HL-2A plasma as a function of wavelength calculated from Equation (1).

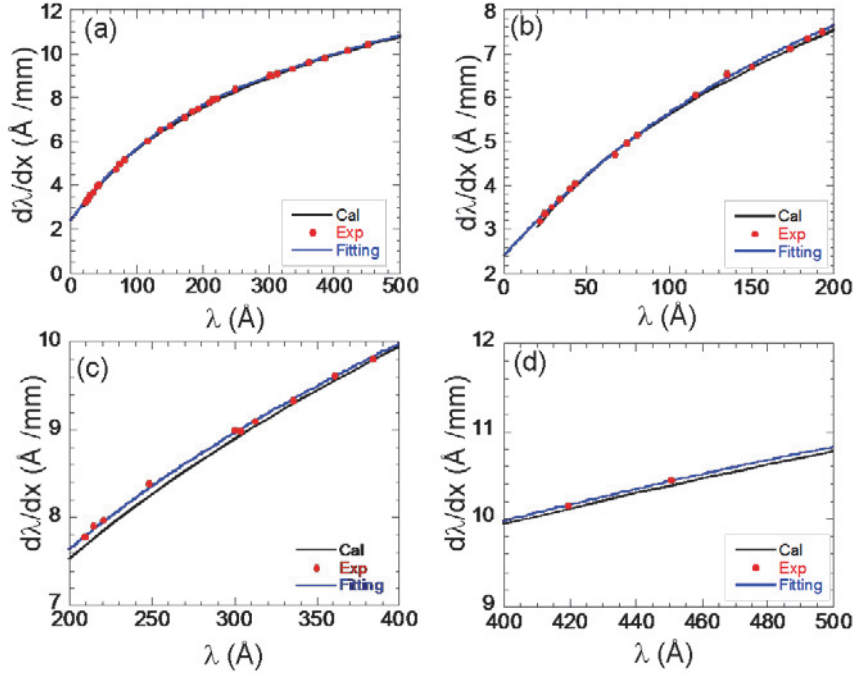


Fig 3. Calculated (black solid line) and experimental (red circular point) reciprocal linear dispersion as a function of wavelength in wavelength range of (a) 20-500Å, (b) 20-200Å, (c) 200-400Å and (d) 400-500Å. Here, blue line is the fitting curve of experimental value.

emission of CVI (33.73Å). It is found that the wavelength of the second order of CVI should be 67.46Å, whereas it is 67.11Å from calculation as shown in Fig. 2(a). Discrepancy of 0.35Å is observed. The wavelength of the second order of CV (40.27Å) should be 80.54Å, whereas it is 80.101Å from calculation as shown in Fig. 2(a). Discrepancy of 0.44Å is observed. A line emission at wavelength of 149.02 shown in Fig. 2(a) is observed, however, it is verified to be OVI (150.09Å) finally. The discrepancy between experiment and calculation is 1Å. And the discrepancy is increasing with wavelength, make the spectra identification difficult. Particularly, the four line emissions with shadow in Fig. 2(b), which have been confirmed to be oxygen line radiations, can not be correctly identified according to the calculated wavelength. Therefore, the correction of wavelength has to be done in order to identify the observed spectra precisely. The reciprocal linear dispersion shown in Fig. 3 is calculated to understand the difference between the calculated wavelength and experimental result. Here, black line is calculated result, red point is experimental result and blue line is fitting curve of experimental result. It seems that the experimental result agrees with the calculation very well in Fig. 3(a), however, a slight discrepancy can be seen when the scale is enlarged as shown in Fig. 3(b), (c) and (d). On the other hand, after analysis it is found that the slight discrepancy does not give a serious impact to our measurement.

The EUV spectra obtained from typical HL-2A tokamak at wavelength range of 20-490Å is completely identified based on the corrected wavelength distribution, as shown in Fig. 4(a) and (b). It can be seen that the spectra are dominated by carbon, oxygen and nitrogen. Carbon is originated from the graphite wall, and oxygen and nitrogen is from air. Meanwhile, the content of metal impurity is quite low.

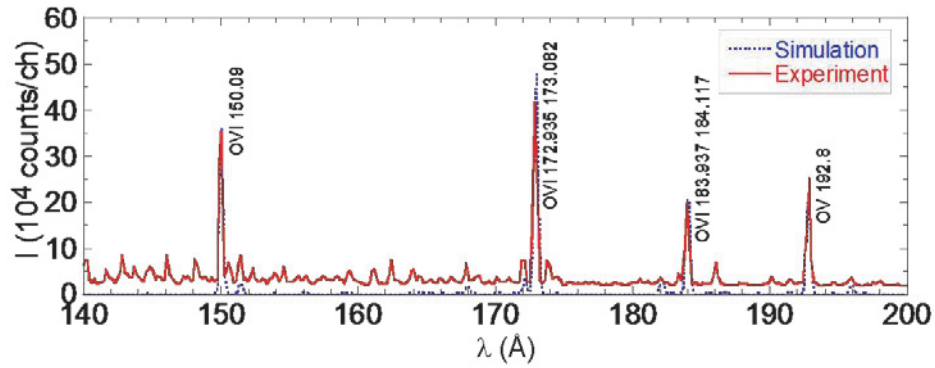


Fig. 5 Comparison of the EUV spectra obtained from experiment (blue dash line) and calculation (red solid line) based on CHIANTI code.

4. Summary

The excellent EUV spectra distribution has been measured based on the EUV spectrometer, and the spectral resolution of 0.22\AA at 200\AA is achieved when the entrance slit of $30\mu\text{m}$ is adopted. Identification of EUV spectra found that the calculated wavelength based on grating working theory can not explain the observed spectra. Analysis on the reciprocal linear dispersion shows that there is a small discrepancy between experimentally observed and theoretically calculated results. Most of EUV line emissions from typical HL-2A plasmas are identified and the spectra are dominated by carbon, oxygen and nitrogen. Comparison of experimental spectra and simulated spectra shows a good agreement, validating the wavelength correction and spectra identification.

Acknowledgement

We are grateful to CHIANTI code for the free open access. This work was partly supported by the JSPS-NRF-NSFC A3 Foresight Program in the field of Plasma Physics (NSFC: No.11261140328, NRF: No.2012K2A2A6000443).

Reference

- [1] ITER Physics Basis Editors, Nucl. Fusion **39**, 2391 (1999).
- [2] ITER Physics Basis Editors, Nucl. Fusion **39**, 2137 (1999).
- [3] S. Morita, et al., Fusion Eng. Des. **34-35**, 211 (1997).
- [4] A. R. Field, et al., Rev. Sci. Instrum. **66**, 5433 (1995).
- [5] Z. Y. Cui, et al., Plasma Sci. Tech. **10**, 298 (2008).
- [6] H. Y. Zhou, et al., Rev. Sci. Instrum. **79**, 10F536 (2008).
- [7] R. Isler et al., Phys. Lett. A **63**, 295 (1977).
- [8] Hinnov et al., Phys. Lett. A **66**, 109 (1978).
- [9] K. Asmussen, et al., Nucl. Fusion **38**, 967 (1998).
- [10] C. F. Dong, et al., Jns. J. Appl. Phys. **51**, 010205 (2012).
- [11] S. Morita, et al., Nucl. Fusion **53**, 093017 (2013).
- [12] C. F. Dong, et al., Rev. Sci. Instrum. **81**, 033107 (2010).
- [13] P. Mazzotta, et al. Astron. Astrophys. Suppl. **81**, 403 (1998).
- [14] K. P. Dere, et al., A&AS **125**, 149 (1997).
- [15] K. P. Dere, et al., A&A **498**, 915 (2009).

Electron correlation effects appeared in the lifetimes of sub-valence shell vacancy states in atomic ions

F. Koike, N. Suzuki, T. Nagoshi, Y. Yoda, Y. Azuma

*Faculty of Science and Engineering, Sophia University, 7-1 Kioi-cho, Chiyoda-ku,
Tokyo, 102-8554 Japan*

e-mail: koikef@sophia.ac.jp

Abstract

The effect of lifetime elongation of neon and argon sub-valence shell vacancy states are discussed in relation to the mixing of adjacent singly excited ionic state configuration. The lifetime of neon 2s-hole state is calculated theoretically to be 0.126 ns, which is in good agreement with experimental data 0.132 ns. The lifetime of argon 3s-hole state is calculated to be 4.67 ns, which is in satisfactorily good agreement with the experimental data 4.62 ns. Transitions are significantly weaker than those under the absence of configuration interaction. The superposition of the transition amplitudes from sub-valence hole and singly excited configurations strongly suppress the transition rates.

Keywords: lifetime, rare gas ion, electron correlation, fluorescence, MCDF

1 Introduction

Sub-valence shell vacancy states of rare gas atoms such as $\text{Ne}^+ 2s2p^6$ or $\text{Ar}^+ 3s3p^6$ decay into the ground states exclusively through the optical-dipole transitions. It is worthy to investigate the role of electron correlations in atomic ions under such simple circumstances; we have an opportunity to understand the correlated electron motions, which appears beyond the mean field models in the electronic state description of atoms or atomic ions, without being bothered by various other minor effects.

Recently, Azuma and his company have developed a time-resolved fluorescence spectroscopy technique and measured the time-dependent fluorescence yield curve. By fitting the exponentially decaying functions to the experimental data, they determined the lifetimes of the hole states of Ne^+ and Ar^+ ions. The experimentally determined lifetimes are found to be significantly longer than the radiative lifetimes that can be expected by single electron $ns - np$ transitions, where n is the principal quantum number of the atomic orbitals; $n = 2$ for Ne^+ and $n = 3$ for Ar^+ . In most of the atoms with moderate atomic number, there are energy differences between sub-shell atomic orbitals due to the deviation of the effective potentials from Coulombic nature; the screening of the nuclear charge by core electrons provides us with the modification of the Coulombic nuclear attraction potential. In the case of Ar^+ ions, for example, the energy difference between 3s-orbitals

and $3p$ -orbitals is not very different from the energy difference between $3p$ -orbitals and $3d$ -orbitals. Thus the $3s$ sub-shell single-hole configuration $3s3p^6$ may have strong interaction with the $3p$ sub-shell single-electron excited configuration $3s^23p^43d$ when both configurations belong to the same symmetry. The actual system are to be represented by the linear combination of $3s3p^6$ and $3s^23p^43d$ configurations; the $3s$ sub-shell hole is, in reality, partially filled by electron. The electric dipole transitions to fill the hole with electrons inevitably suffer modification by this configuration mixing. In spite of the simple appearance of the problems, theoretical calculations have not yet been tackled with sufficient accuracy owing to the presence of such serious electron correlations.

In the present paper, we theoretically investigate the role of the configuration mixing to the effect of lifetime elongation in Ne^+ and Ar^+ sub-valence vacancy states. Because the experimental work will be illustrated elsewhere in one of the future publications, we, here, concentrate ourselves to the theoretical calculations and discussions.

2 Lifetime calculation for $\text{Ne}^+ 2s2p^6$ and $\text{Ar}^+ 3s3p^6$

We consider the following radiative decay processes.

$$\text{Ne}^+ 2s2p^6 \ ^2S_{\frac{1}{2}} \rightarrow \text{Ne}^+ 2s^22p^5 \ ^2P_{\frac{1}{2},\frac{3}{2}} + \hbar\omega \quad (1)$$

for Ne^+ , and

$$\text{Ar}^+ 3s3p^6 \ ^2S_{\frac{1}{2}} \rightarrow \text{Ar}^+ 3s^23p^5 \ ^2P_{\frac{1}{2},\frac{3}{2}} + \hbar\omega \quad (2)$$

for Ar^+ , which take place after the sub-valence shell photoionization by the incidence of synchrotron radiation light. These sub-valence hole states are energetically below the ionization threshold; their decay into lower lying states undergo exclusively through the radiative processes. The lifetime of these sub-valence hole states can be evaluated solely in terms of radiative transition rates. As pointed out in the previous section, we should take into account the interaction with the valence-shell singly excited configurations in the calculation of sub-valence hole atomic states. We employ the General purpose Relativistic Atomic Structure Program 92 (GRASP92) [1] for the electronic structure of the atomic ions, and the Relativistic Atomic Transition and Ionization Properties (RATIP) code [2,3] for transition wavelengths and strengths. The advantage of these programs is that we can treat the two electron non-local potentials as they are [4]; we can properly evaluate the electron correlations through configuration interactions in a sophisticated way.

We, first, consider the radiative decay of $\text{Ne}^+ 2s2p^6$. As found in Fig.1, there are levels of single electron excited states $2s^22p^43s$ and $2s^22p^43d$ slightly above the level of sub-valence shell hole state $\text{Ne}^+ 2s2p^6$. Because these levels may belong to the same symmetry, which

is the ${}^2S_{1/2}$ symmetry in this case, they may interact through configuration interaction. The single electron orbitals themselves will suffer considerable modification due to the configuration interaction; to account for these modifications, we can carry out the optimization for the relevant orbitals by means of Multi-configuration Dirac-Fock procedure. To obtain a set of orbitals we employ a so called active space method [5] [6]; starting from

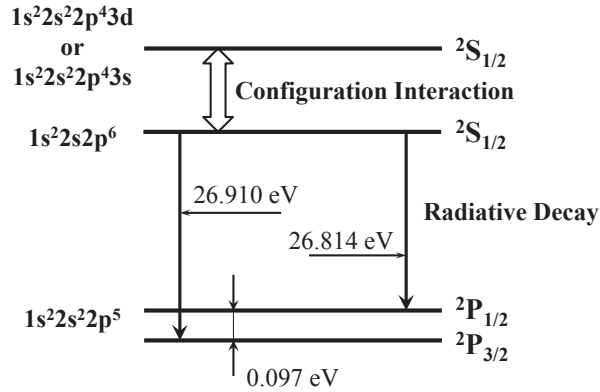


Figure 1: (color on line) Energy level diagram of Ne⁺ states. There are levels of single electron excited states $2s^2 2p^4 3s$ and $2s^2 2p^4 3d$ slightly above the level of sub-valence shell hole state Ne⁺ $2s 2p^6$. Because these levels may belong to the same symmetry, which is the ${}^2S_{1/2}$ symmetry in this case, they may interact through configuration interaction.

the minimal orbital set, we increase the number of orbitals stepwise to those with the principal quantum number $n = 6$. In the first step, we included $1s$, $2s$, and $2p$ orbitals. In the second step, we considered the inclusion of $3s$ and $3d$ to investigate the role of the valence-shell singly excited configurations $2s^2 2p^4 3s$ and $2s^2 2p^4 3d$; in this step $3s$ and $3d$ orbitals are treated as the spectroscopic orbitals instead of the correlation orbitals to properly evaluate the correlations between the configurations $2s 2p^6$ and $2s^2 2p^4 3s$ or $3d$. In virtue of the active space method for obtaining the accurate state energies and other physical quantities [5], it is not indispensable to treat the $3s$ and $3d$ orbitals as spectroscopic orbitals if we can include enough large number of basis orbitals. The advantage of the present treatment is that we can substantially accelerate the convergence of active space method procedure. In the third and further steps, we included the orbitals with $n = 3$ to 6 in steps and considered the single and double virtual excitations from the reference configuration state functions (CSF's): $2s 2p^6$, $2s^2 2p^4 3s$, and $2s^2 2p^4 3d$. In every step, we fix the lower lying orbitals and leave only the newly included orbitals flexible in

the MCDF optimization procedure. The ground state $\text{Ne}^+ 2s^2 2p^5 \ ^2P_{\frac{1}{2},\frac{3}{2}}$ is simultaneously optimized using the same orbital set for stability of further calculations on dynamical processes, although RATIP [2,3] allows the use of non-orthogonal basis orbitals.

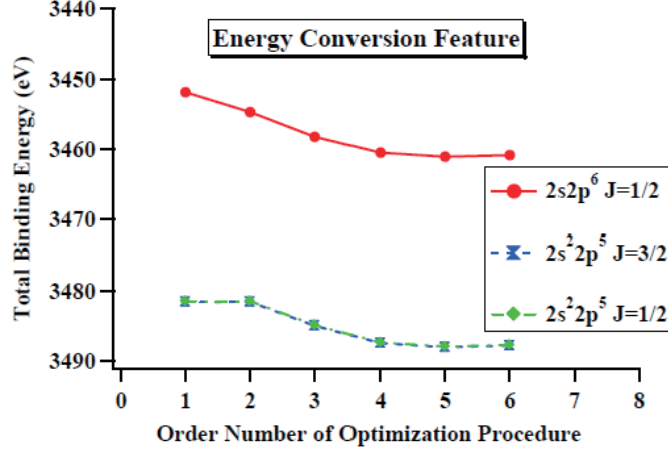


Figure 2: (color on line) Total binding energies of sub-valence shell hole state $\text{Ne}^+ 2s2p^6$ and the fine structure levels of the ground state $\text{Ne}^+ 2s^2 2p^5 \ ^2P_{\frac{1}{2},\frac{3}{2}}$ plotted against the MCDF optimization steps. Effective convergence of the total energies is attained at step 4.

In Fig.2 we show the convergence feature of total electronic energies of both sub-valence hole and ground states in Ne^+ . We can see in the figure that the convergence is effectively obtained at step 4. At this step, we have obtained the percent fraction of the configurations in the sub-valence hole state in the following way; they are $2s2p^6 \ ^2S_{\frac{1}{2}}$: 90.96%, $2s^2 2p^4 3d \ ^2S_{\frac{1}{2}}$: 4.76%, $2s^2 2p^4 3s \ ^2S_{\frac{1}{2}}$: 1.77%, $2s2p^4 3p^2 \ ^2S_{\frac{1}{2}}$: 0.70%, $2s2p^4 3d^2 \ ^2S_{\frac{1}{2}}$: 0.41%, and *others* : 1.40%. We find that about 6.5% of the $2s^2 2p^4 3s$ or $3d$ mixing has been realized due to the configuration interaction. In Fig.3, we find that the calculated lifetimes in velocity form are 0.075ns for minimal base calculation at step 1 while the corresponding value at step 6 is 0.126ns. This shows that the 6.5% of the $2s^2 2p^4 3s$ or $3d$ contribution could cause almost 60% of the lifetime elongation. On the other hand, the experimentally determined lifetime by Sophia University group is found to be 0.137ns, which agrees well to the present MCDF calculations with configuration interaction.

We, next, consider the lifetime of $\text{Ar}^+ 3s3p^6$ sub-valence hole state. In this system, we can expect the intra-shell correlation contribution from the configuration $3s^2 3p^4 3d$. We have performed the similar series of calculations as we have done for Ne^+ . We have observed about 33% contribution of $3s^2 3p^4 3d$ configuration at the convergence. The life-

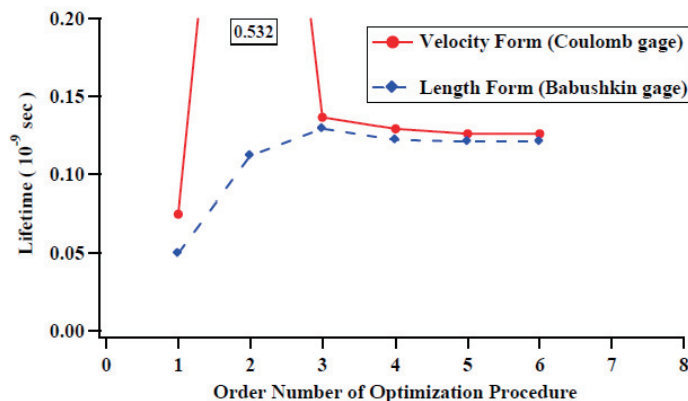


Figure 3: (color on line) Convergence feature of radiative lifetime of sub-valence shell hole state $\text{Ne}^+ 2s2p^6$ plotted against the MCDF optimization steps. The lifetime elongation due to the incorporation of $3s$ and $3d$ orbitals can be observed by comparing the minimal base calculation in step 1 and the calculation in other steps.

times of the $\text{Ar}^+ 3s3p^6$ state are found to be 0.113ns for minimal base calculation, i.e., the calculation without considering the configuration interaction, and 4.67ns at convergence with configuration interaction by means of the MCDF procedure. We can say that the configuration interaction effects may induce drastic elongation of the lifetime against the dipole radiative transitions. The experimentally determined value by Sophia University group is 4.62ns, which is in good agreement with the present theory. We can also compare the present results with a previous experimental value 4.684 ± 0.019 ns by Lauer et al [7] and a theoretical value 5.507ns by Berrington et al [8].

3 Discussion

In Ne^+ and Ar^+ , the energy levels that are labeled as the sub-valence shell hole states are of the states of which holes are partially filled by electrons. Due to the configuration interaction, the atomic state function (ASF) of the states which are labeled as the sub-valence hole state is, in reality, the linear combination of the sub-valence hole and valence excited state configurations. Because the idea of holes or electrons in atoms is solely of the mean field model, the integral number of electron occupations can be expected exclusively within the framework of this model. In other words, it is natural that we have fractional occupation numbers if we take into account the effects of electron correlations. And, therefore, the way to specify the electronic states in terms of the list of occupation

numbers, such as $1s^22s^22p^63s3p^6$, should be limited to the cases in which the mean field model works well if we want to label the states in a strict sense. Our electron holes in Ne^+ and Ar^+ are partially filled by electrons, and the optical transitions are significantly modified accordingly. In Ne^+ , we find 60% of lifetime elongation, and in Ar^+ , we find one order of magnitude lifetime elongation due to the contribution of ss or sd type configurations. In the case of Ne^+ , the major contribution to the electron correlation is of the inter-shell configuration such as $2s^22p^43s$ or $2s^22p^43d$ whereas in the case of Ar^+ , the major contribution is from the intra-shell configurations such as $3s^23p^43d$. We can point out that this difference of the types of contributing configurations is the source of the difference of the magnitude of lifetime elongations between Ne^+ and Ar^+ .

Acknowledgement

This work was partly supported by the JSPS-NRF-NSFC A3 Foresight Program in the field of Plasma Physics.

References

- [1] F. A. Parpia, C. F. Fischer, and I. P. Grant, *Commpt. Phys. Commun.*, **94**, 249 (1996).
- [2] S. Fritzsche, *J. Elec. Spec. Rel. Phenom.*, **114–116**, 1155 (2001).
- [3] S. Fritzsche, *Comput. Phys. Commun.* **183**, 1525 (2012).
- [4] F. Koike and S. Fritzsche, *J. Phys. Conf. Ser.*, **58** 157 (2007).
- [5] C. F. Fischer, T. Brage and PJoensson *Computational Atomic Structure: An MCHF Approach (Bristol: Institute of Physics Publishing)* (1997).
- [6] X. B. Ding, F. Koike, et al, *J. Phys. B: At. Mol. Opt. Phys.*, **44**, 145004 (2011).
- [7] S Lauer, H Liebel, F Vollweiler, H Schmoranzler, B M Lagutin, Ph V Demekhin, I D Petrov and V L Sukhorukov, *J. Phys. B: At. Mol. Opt. Phys.*, **32** 2015 (1999).
- [8] K A Berrington and J C Pelan and J A Waldock, *J. Phys. B: At. Mol. Opt. Phys.*, **34** L149 (2001).

Electron capture cross section scalings for low- q heavy ions

Alex M Imai^{*,1}

^{*} Department of Nuclear Engineering, Kyoto University, Nishikyo, Kyoto 615-8540, Japan

Abstract

Single electron capture cross sections for low initial charge state (low- q) ions of Be, B, C, Fe, Ni, and W colliding with gaseous targets of He, Ne, Ar, Kr, H₂, D₂, CH₄, C₂H₆, C₃H₈, CO, CO₂, and N₂ were derived experimentally in low energy region. An attempt was made to draw scaling behavior of these cross sections on target species and scalings on ΔIP , the first ionization potential of the target atoms and molecules subtracted by that of the projectile ions after electron capture, were found to reproduce the measured cross sections generally within a magnitude and with higher precision for specific initial charge state and target species.

Keywords: charge transfer, electron capture, cross section, scaling formula, heavy ion, tungsten

Introduction

The need and importance for accurate atomic and molecular data have always been recognized. Both static properties of atoms and molecules, such as electric energy levels and emitting photon energies for highly charged heavy ions, and dynamic properties of atoms and molecules including elastic and inelastic collision processes for energetic atoms/molecules and their ions are essential to use in fusion science. Since it is never possible to experimentally derive every collision cross section for all possible combinations of projectile and target particles from the lowest to highest collision energy, nor to develop an all-round theory to predict all the collision cross sections, the contents of dynamic atomic and molecular data are less comprehensive than those of static data. Attempts to make empirical or semi-empirical scaling formulae have been made for decades and evaluation and compilation efforts for atomic and molecular collision data have also been made. [1]

The general energy dependence of elastic and inelastic collision cross sections for ionic projectile and atomic target is illustrated in Fig. 1, taking an example of the simplest collision system, proton on atomic hydrogen. Elastic collision cross sections decrease rather monotonously as the collision energy increases. Cross sections for target excitation and ionization processes, the collision systems of which are always endothermic, show so-called threshold behavior, steeply increase at some threshold-energy, show maxima or plateaus, and finally decrease as the collision energy grows. The decrease of the excitation cross sections in the high energy limit follows $\log E/E$ or $1/E$ rules for optically allowed and forbidden transitions, respectively, and that of the ionization cross sections follow $\log E/E$ rule, where E denotes the collision energy. Electron capture cross sections are known to show either the threshold behavior or saturation behavior of monotonous decrease from a finite value at the low-energy limit, depending on the collision process is endothermic or exothermic. In the examples in Fig.1, total electron capture process is mostly consisted of resonant electron capture from the target ground (1s) state to the projectile ground (1s) state and its cross section shows the saturation behavior, whereas electron capture into projectile excited states (2s, 2p) shows the threshold behavior. Many attempts have been made to extract general tendencies among reliable cross sections for available experimental and theoretical cross sections and to formulate these tendencies into empirical or semi-empirical formula to predict unknown cross sections. Ones of the well-known formulae are for single electron capture cross section scalings for collisions between ions in charge state q and molecular hydrogen target in high-energy region, using the scaled cross section σ/q^n and the scaled collision energy E/q^m , where σ denotes the cross section in cm² and n and m are constants. Schlachter *et al.* [2], Sanders *et al.* [3], and Cornelius [4] determined empirical scaling formula specifying their own n and m values as are shown in Fig. 2. Another well-known example of semi-empirical formula, which are based on theoretically derived formula with fitting parameters adjusted to reliable experimental cross sections, is for single electron capture cross section scaling by Knudsen [5] for collisions between ions in charge state q , greater than or equal to

4, and atomic targets of H, He, Ar, Kr, using the scaled cross section σ/q and the scaled collision energy $E/q^{4/7}$. (Fig. 3)

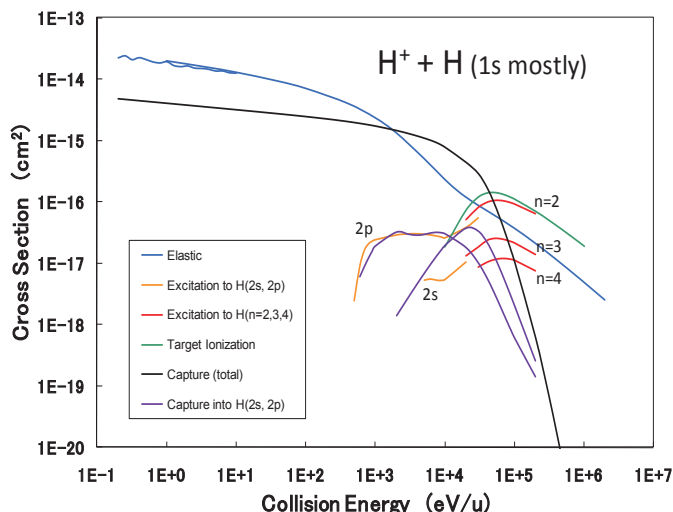


Fig. 1 General energy dependence of elastic and inelastic collision cross sections for ion-atom collisions.

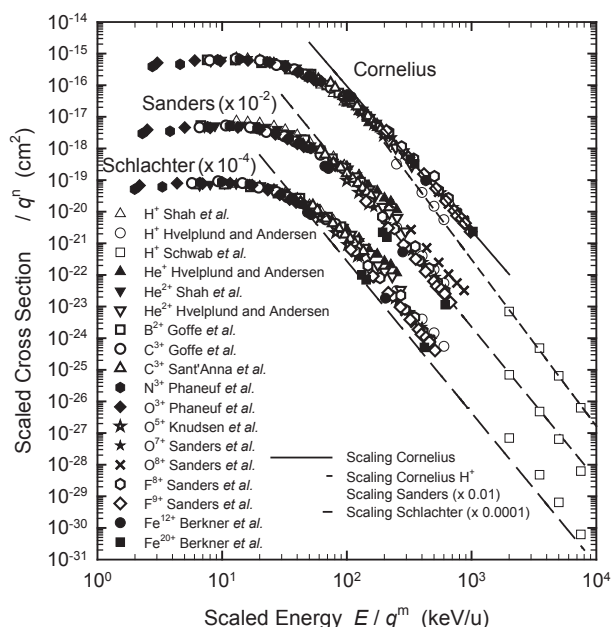


Fig. 2 Single electron capture cross section scalings for $A^{q+} + H_2$ collisions by Schlachter *et al.* [2], Sanders *et al.* [3], and Cornelius [4].

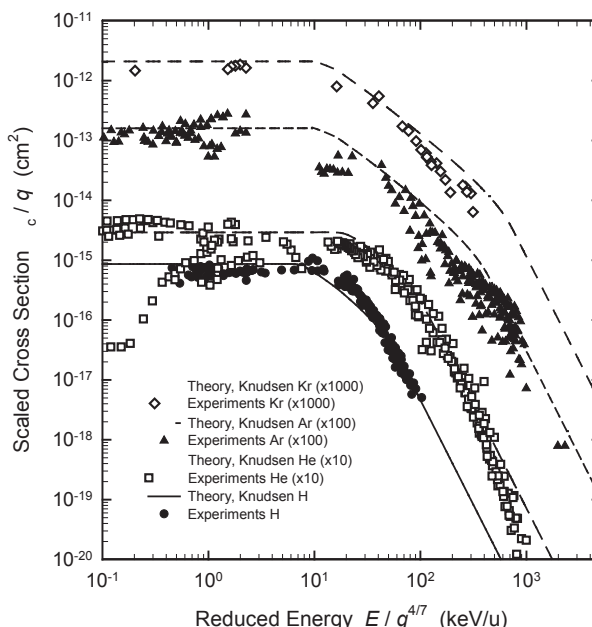


Fig. 3 Single electron capture cross section scalings by Knudsen *et al.* for A^{q+} projectile ions from H, He, Ar, and Kr targets. [5]

As for scaling rules in low-energy collision region, single, double, triple, and four-fold electron capture cross section scalings predicting the low-energy limit cross sections for exothermic collision processes by Mueller and Salzborn [6] are important. These scalings made use of the first ionization potential (IP) of the target and the initial charge state q of the projectile ion, and q had to be limited to high values to make the collision processes exothermic. Similar scalings for single electron capture cross sections for high- q collisions were introduced by Kusakabe *et al.* [7] and Yamada *et al.* [8] as illustrated in Fig. 4, but no such scaling behavior has been reported yet for electron capture cross sections for low- q collision systems in the low energy range. We started with measuring single electron capture cross sections for low- q ($q = 1, 2$) ions of Be, B, C, Fe, Ni, and W atoms from atomic and molecular targets of He, Ne, Ar, Kr, H_2 , D_2 , CH_4 , C_2H_6 , C_3H_8 , CO, CO_2 , N_2 and have determined scaling formula in these cross sections, using ΔIP , *i.e.*, the first ionization potential of the target atoms/molecules subtracted by that of the projectile ions after electron capture, which corresponds to the energy defect of the collision process in case all the involved projectile and target particles before and after the collision are in the ground states.

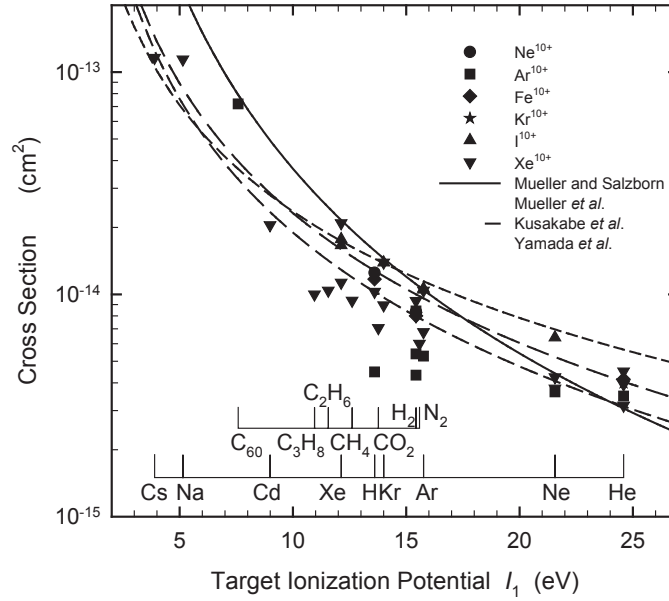


Fig. 4 Single electron capture cross section scalings at low-energy limit for A^{q+} ions by Mueller and Salzborn [6], Kusakabe *et al.* [7], and Yamada *et al.* [8].

Experiments

The experiments were performed at the Van de Graaff Accelerator Facility of the Quantum Science and Engineering Center, Kyoto University. As has been given elsewhere [9–13], the incident ions were obtained by an ion-impact ion source, in which a pump beam of 1.7 MeV O^+ ions impacted a CO_2 gas jet for C ion production and that of 0.9 MeV CO_2^+ ions impacted metallic wires of 1.0 mm diameter for producing other ions of Be, B, C, Fe, Ni, and W. An accelerating voltage between 4 and 20 kV was applied to the exit capillary of the gas jet or to the metallic wires. Mass and charge analysis was made to the extracted beam using a combination of Wien filter ($E \times B$ filter) and neutral particle rejector. A pure projectile beam of desired charge state and energy was introduced into a target gas cell filled with He, Ne, Ar, Kr, H_2 , D_2 , CH_4 , C_2H_6 , C_3H_8 , CO, CO_2 , and N_2 targets, gas pressure inside the target gas cell was monitored by a high-sensitivity Pirani gauge calibrated with a capacitance manometer. Single and double electron capture cross sections were derived by the growth method under the single collision condition with target gas pressure of 10^{-2} to 10^{-1} Pa, while the base pressure of the vacuum chamber was kept below 5×10^{-6} Pa. Total systematic uncertainties were estimated to be 9% to 20%. Measured single and double electron capture cross sections have been published in [9] for C projectile ions, in [10,11] for Be, B, Fe, and Ni projectile ions, and in [12,13] for W projectile ions.

Electron capture cross section scalings

It is well known that single electron capture cross sections at the low-energy limit can be scaled using the first ionization potential (IP) of the target when the collision is exothermic. Mueller and Salzborn derived the $IP^{-2.76}$ power law dependence [6], whereas Kusakabe *et al.* [7] and Yamada *et al.* [8] reported $IP^{-2.0}$ and $IP^{-1.59}$ power laws, respectively. The measured single electron capture cross sections are plotted as a function of the first IP of the rare gas targets in Fig. 5 and that of the molecular gas targets in Fig. 6, after selecting appropriate collision energies to achieve similar projectile velocities and a larger number of data points. The solid and dashed lines in the Figs. 5 and 6 denote power law dependence on the IP of the target for each projectile ion with initial charge state $q = 1$ and 2, respectively. The power dependence terms were $IP^{-5.0}$, $IP^{-5.2}$, $IP^{-9.0}$, $IP^{-7.6}$, and $IP^{-4.3}$ for W^+ , Ni^+ , Fe^+ , B^+ , and Be^+ ions, respectively, and $IP^{-3.8}$, $IP^{-9.2}$, $IP^{-2.2}$, and $IP^{-8.3}$ for W^{2+} , Ni^{2+} , B^{2+} , and Be^{2+} ions, respectively, for the rare gas targets in Fig. 5, whereas they were $IP^{-11.6}$, $IP^{-8.7}$, $IP^{-7.9}$, and $IP^{-6.4}$ for W^+ , Ni^+ , Fe^+ , and C^+ ions, respectively, and $IP^{-8.3}$, $IP^{-5.5}$, $IP^{-0.7}$, and $IP^{-2.9}$ for W^{2+} , Ni^{2+} , C^{2+} , and Be^{2+} ions, respectively, for the molecular gas targets in Fig. 6. The power law dependence seemed to offer little possibility in scaling these cross sections on IP, since only the single electron capture cross sections σ_{21} for B^{2+} ions on the rare gas targets and for Be^{2+} and C^{2+} ions on the molecular gas targets were seen to follow similar IP power law dependence discussed above, and all

the other cross sections (both σ_{10} and σ_{21}) showed steeper and divergent power law dependence on IP. It is quite understandable, however, because only the collision processes for B^{2+} projectile ions are always exothermic and collision processes for all the singly charged projectile ions are always endothermic for all the rare gas targets in Fig. 5. As for the molecular gas targets in Fig. 6, the collision processes for most of the singly charged projectile ions are always endothermic, the only exception being Fe^+ on C_3H_8 , and all the collision processes for the doubly charged projectile ions are always exothermic. As a result, only cross sections σ_{21} for B^{2+} ions on the rare gas targets and for Be^{2+} and C^{2+} ions on the molecular gas targets followed the IP power law dependence derived for exothermic collision processes, and cross sections for endothermic collision processes showed those steeper decrease on IP dependence.

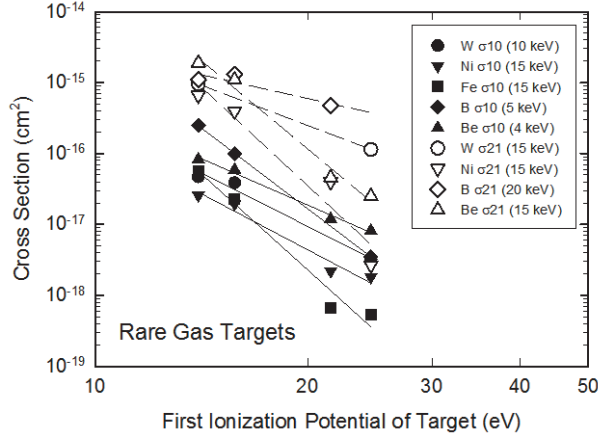


Fig. 5 Single electron capture cross sections for Be, B, Fe, Ni, and W projectile ions on atomic gas targets of He, Ne, Ar, and Kr. [13]

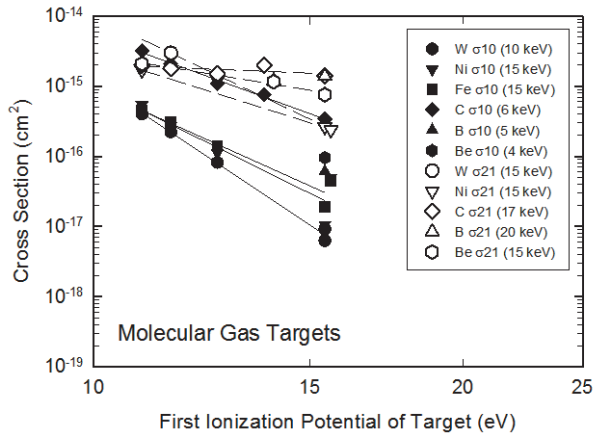


Fig. 6 Single electron capture cross sections for Be, B, C, Fe, Ni, and W projectile ions on molecular gas targets of H_2 , D_2 , CH_4 , C_2H_6 , C_3H_8 , CO , and CO_2 . [13]

A more uniform tendency appeared when the measured single electron capture cross sections for singly and doubly charged projectile ions were plotted as a function of ΔIP , *i.e.*, the first IP of the target atoms/molecules subtracted by that of the projectile ions after electron capture, as illustrated in Figs. 7 and 8 for atomic and molecular targets, respectively. For atomic targets in Fig. 7, the cross sections decreased rather gradually up to ΔIP around -2 eV and turned to decrease steeply by three orders of magnitude between -3 and $+16$ eV as ΔIP increased. For molecular targets in Fig. 8, the same tendency was found, where the cross sections for singly and doubly charged projectile ions were aligned separately in the endo- and exothermic regions, respectively. This picture suggests a possibility of scaling electron capture cross sections for not only exothermic but also endothermic collision processes for slow low- q projectile ions using ΔIP . Since the horizontal axis expanded into the negative values, the IP power law dependence used in the existing scaling rules for high- q ions [1–3] could not be applied, and fits to exponential functions have been attempted to formulate the behavior respectively for exo- and endothermic regions as

$$\sigma_{\text{exo}} (\text{cm}^2) = 7.45 \times 10^{-16} \times 10^{-0.029 \Delta IP (\text{eV})},$$

$$\sigma_{\text{endo}} (\text{cm}^2) = 7.13 \times 10^{-16} \times 10^{-0.17 \Delta IP (\text{eV})},$$

which reproduced the measured cross sections within -0.57 to 0.62 order of magnitude for exothermic processes and within -1.36 to 0.64 order of magnitude for endothermic processes. Other fitting attempts have been made, both individually and collectively, for the singly and doubly charged projectile ions, and for the atomic and molecular targets, in either or both ΔIP regions, where the collision processes became exo- or endothermic, as summarized in Table 1. These scaling rules are drawn in Figs. 7 and 8 with thin solid and dashed lines for either atomic or molecular targets for $q = 1$ and 2, with thick solid and dashed lines for both atomic and molecular targets for $q = 1$ and 2. It can be seen that all the attempted scaling rules reproduced the measured cross sections almost within an order of magnitude, and the more specific the scaling is, *i.e.*, for limited initial charge state and target species, the smaller the deviation becomes.

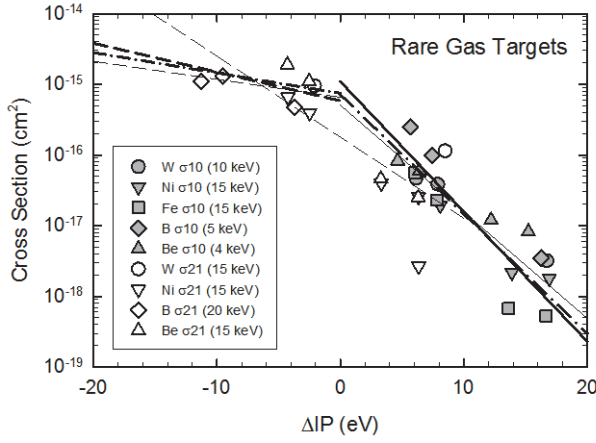


Fig. 7 Single electron capture cross sections from Fig. 5, plotted as a function of ΔIP . [13]

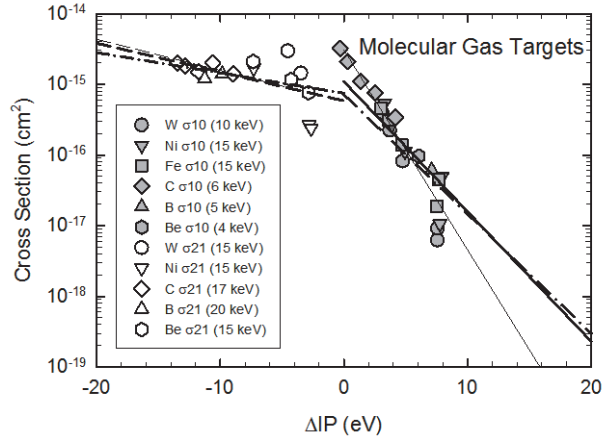


Fig. 8 Single electron capture cross sections from Fig. 6, plotted as a function of ΔIP . [13]

Cross section	Target	Cross section scaling (cm ²)	Deviation range (order of mag.)	ΔIP region of interest
σ_{10}	A	$5.06 \times 10^{-16} \times 10^{-0.15 \Delta IP}$	-0.82 ~ 0.55	+ (endothermic)
σ_{21}	A	$1.78 \times 10^{-16} \times 10^{-0.11 \Delta IP}$	-1.10 ~ 0.78	\pm (exo- and endothermic)
σ_{21}	A	$6.53 \times 10^{-16} \times 10^{-0.025 \Delta IP}$	-0.28 ~ 0.35	- (exothermic)
σ_{10}	M	$3.07 \times 10^{-15} \times 10^{-0.28 \Delta IP}$	-0.55 ~ 0.45	+ (endothermic)
σ_{21}	M	$5.67 \times 10^{-16} \times 10^{-0.044 \Delta IP}$	-0.49 ~ 0.52	- (exothermic)
σ_{10}	A+M	$1.09 \times 10^{-15} \times 10^{-0.18 \Delta IP}$	-0.85 ~ 0.67	+ (endothermic)
σ_{21}	A+M	$5.82 \times 10^{-16} \times 10^{-0.041 \Delta IP}$	-0.50 ~ 0.52	- (exothermic)
$\sigma_{10} + \sigma_{21}$	A+M	$7.13 \times 10^{-16} \times 10^{-0.17 \Delta IP}$	-1.36 ~ 0.64	+ (endothermic)
$\sigma_{10} + \sigma_{21}$	A+M	$7.45 \times 10^{-16} \times 10^{-0.029 \Delta IP}$	-0.57 ~ 0.62	- (exothermic)

Table. 1 Single electron capture cross section scalings for singly and doubly charged projectile ions on atomic and molecular gas targets in low energy. [13]

Acknowledgement

The author is grateful to his colleagues Akio Itoh, Yoichi Haruyama, and Manabu Saito as well as students in Kyoto University for their help in performing the experiments. This work was partly supported by the JSPS-NRF-NSFC A3 Foresight Program in the field of Plasma Physics (NSFC: No. 11261140328, NRF: No. 2012K2A2A6000443).

References

- [1] M. Imai, 2012 in *Atomic Processes in Basic and Applied Physics*, eds. V. Shevelko and H. Tawara, Springer Series on Atomic, Optical, and Plasma Physics, Vol. 68, Springer-Verlag, New York, 455.
- [2] A.S. Schlachter, J.W. Stearns, W.G. Graham, K.H. Berkner, R.V. Pyle, J.A. Tanis, 1983 *Phys. Rev. A* 27, 3372.
- [3] J.M. Sanders, T.N. Tipping, J. Hall, J.L. Sinpaugh, D.H. Lee, P. Richard, 1991 *Nucl. Instr. Meth. B* 56/57, 104.
- [4] K.R. Cornelius, 2006 *Phys. Rev. A* 73, 032710.
- [5] H. Knudsen, H.K. Haugen, P. Hvelplund, 1981 *Phys. Rev. A* 23, 597.
- [6] A. Mueller, E. Salzborn, 1977 *Phys. Lett. A* 62, 391.
- [7] T. Kusakabe *et al.*, 1986 *J. Phys. B* 19, 2165.
- [8] I. Yamada *et al.*, 1999 in *Abstracts of Contributed Papers, 21st Int. Conf. Physics of Electronic and Atomic Collisions, Sendai, Japan, July 22-27, 1999*, eds. Y. Itikawa *et al.*, Vol. II, 553.
- [9] A. Itoh *et al.*, 1995 *J. Phys. Soc. Jpn.* 64, 3255.
- [10] M. Imai *et al.*, 2006 *J. Plasma Fusion Res. Ser.* 7, 323.
- [11] M.V. Khoma *et al.*, 2008 *Chem. Phys.* 352, 142.

[12] I.Yu. Tolstikhina *et al.*, 2012 *J. Phys. B* 45, 145201.

[13] M. Imai, Y. Iriki, A. Itoh, 2013 *Fusion Sci. Tech.* 63, 392.

¹ E-mail: imai@nucleng.kyoto-u.ac.jp

Theoretical study on electron impact excitation and related polarization properties of subsequent radiative emission

Chen-Zhong Dong, Zhan-Bin Chen, Jun Jiang, Zhong-Wen Wu, and Lu-You Xie

Key Laboratory of Atomic and Molecular Physics Functional Material of Gansu Province, College of Physics and Electronic Engineering, Northwest Normal University, Lanzhou 730070, China

E-mail: dongcz@nwnu.edu.cn

Abstract. The polarization of x-ray line emission from highly charged ions undergoing collisions with an electron beam has been a topic of continuous fundamental interest for decades. The understanding of the processes is important not only to diagnose the electron distribution anisotropy in high temperature plasmas, but also to provide the information on both the incident electrons and the excitation dynamics. Recently, on the basis of the well-known GRASP92/2K and RATIP packages, a new fully relativistic distorted wave program, named REIE06 has been developed by our group. In this composition, some selected applications of the program are shown. A special attention has been paid on influences of the higher order effects to the polarization properties of the subsequent photoemission following electron impact excitation process. We hope these works will be helpful for further understanding the contributions from the higher order effects and getting more accurate polarization data.

PACS numbers: 34.80.Dp, 34.80.Lx

1. Introduction

Electron-impact excitation (EIE) processes occur frequently in various laboratory and astrophysical plasmas, which is one of the most important fields of atomic physics. From the analysis of the polarization and angular distribution of decay products following the collision processes, valuable information can be obtained for both the dynamical process and the magnetic sublevels population of the excited states. These polarization data have become indispensable tools for the diagnosis of plasma state and the analysis of complex spectra formation mechanism. When compared to the conventional observable cross sections or rate coefficients, such polarization studies were found to be much more effective to the details of the various effects and interactions and, in fact, helped provide new insight into the electron-electron and electron-photon interactions in the presence of strong Coulomb fields. Recently, an important diagnostic tool has been successfully developed and applied to describe both the angular and energy distributions of non-thermal electrons existing in astrophysical and laboratory plasmas, particularly in the solar corona plasmas [1-3], tokamak plasmas [4] and laser-produced plasmas [5-9].

During the last few years, the degree of linear polarization of x-ray emission from highly charged ions colliding with an electron beam has been extensively investigated. With respect to experiments, several important polarization measurements were reported for H-like and He-like few-electron ions [10-20]. With respect to theory, Reed et al. [21] have investigated the relativistic effects on the degree of linear polarization of x-ray emission following the EIE for highly charge H-like and He-like ions. Fontes et al. [22] have studied the contribution of the Breit interaction on the collision strength and the degree of linear polarization of the radiation emission following the electron impact excitation of He-like ions. Sharma et al. [23] have studied the degree of linear polarization of the $ns_{1/2}$ - $np_{1/2}$ and $ns_{1/2}$ - $np_{3/2}$ resonance transitions for the singly charged Mg^+ ($n=3$), Ca^+ ($n=4$), Zn^+ ($n=4$), Cd^+ ($n=5$), and Ba^+ ($n=6$) ions with the use of a fully relativistic distorted-wave method. Amaro et al. [24] have analyzed the angular correlation and the degree of linear polarization for the radiation emitted in two-photon decay of H-like ions. There are also many other theoretical studies for the degree of linear polarization [25–39]. However, most of these works have paid attention to the decay from individual magnetic sublevels to the ground state; there is a lack of studies on various transitions among the different excited states. In addition, to our knowledge, the accuracy of available polarization data is often suspect, different calculations using similar methods/codes sometimes differ so much due to the presence of the higher order effects.

Recently, based on the multi-configuration Dirac-Fock (MCDF) method and the corresponding packages GRASP92/2K [40] and RATIP [41], a new fully relativistic distorted wave program, named REIE06 [37,42] has been developed by our group. By using the program, a series of electron-impact excitation processes have been studied systematically. A special attention has been paid on the influences of the higher order effects [43-51] to the polarization properties of the subsequent photoemission. As

examples, the effects of intermediate resonance states in an isolated resonance approximation, the effects of Breit interactions, the effects of E1-M2 interference, the effects of plasma screening and so on were briefly reviewed in this report.

2. Influence of resonance electron-impact excitation on the linear polarization of Ne-like Ba⁴⁶⁺ ions

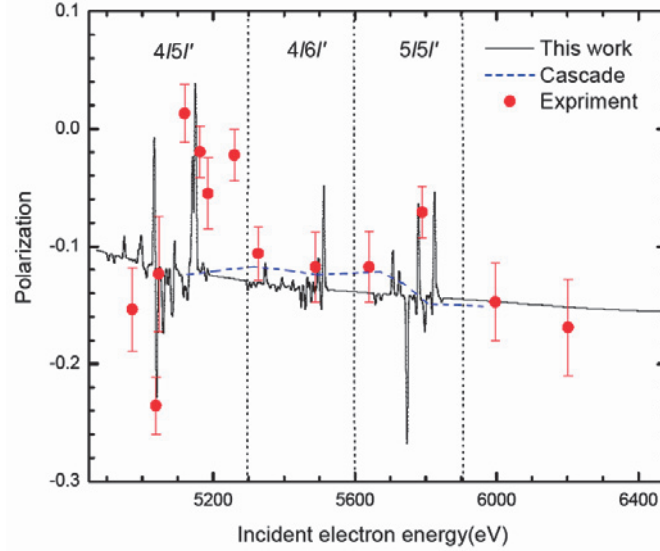


Figure.1 Linear polarization degree of neonlike Ba⁴⁶⁺ M2 line ($2p^{-1}_{3/2}3s_{1/2}2 \rightarrow 2p^6$ ($J = 0$)) as a function of the incident electron energy. Solid line represents the present work; dashed lines represent Takács *et al.* [12]'s calculations which considered the cascade scheme. The experimental data [12] are given as solid circles.

The resonant excitation processes are very important in the polarization properties for some special EIE processes. In Fig. 1, the calculated linear polarization of M2 line are compared with the experimental measurements of Takács *et al.* [12]. The present results were shifted to left 130eV for considering the space charge effects in the experiment. It can be seen that if only the direct impact excitation were considered in the calculations, the negative polarization degree increases from 10% to 13% smoothly with increasing of electron energy, which agree with the experiment of Takács *et al.* [12] very well. The averaged polarization degree of .12 10% also agrees with the assumption of -510% by Beiersdorfer *et al.* [43] at the considered energy range. The resonance excitations result in the sharp change of polarization degree, especially for the energy ranging from 5 keV to 5.3 keV, where the contribution of the double excited states 4/5I' is dominant. At the energy near 5 keV, the negative polarization degree were largely enhanced to -22%, and at the energy near 5.1 keV the polarization effects were decreases strongly, which agree with the experiments excellently. However, at the energy near 5.25 keV, there is a strongly decreases of polarization in the experiment, but could not be reproduced by the theory. For the energy from 5.3 keV to 5.6 keV, where the 4/6I' resonance series is dominant, the

change of polarization is relatively small because of relatively small resonance excitation contributions. However, when the energy is larger than 5.6 keV, the effects of the 5151 resonance excitation on the polarization are very obviously. There are two peaks with the obvious decreasing polarization for the energy close to 5.8 keV, and one of them was measured by Takács *et al.* [12] For the energy near 5.75 keV, the polarization were increased to -26%, which were not measured by experiment because of the limited energy points. Comparing with Takács *et al.* [12]'s calculations with cascade scheme. It is found that the cascade effects may play a relatively small role.

2. Influence of quantum interference on the polarization and angular distribution of highly charged H-like and He-like ions

X-ray lines emitted by highly charged ions arise not only from optically allowed electric dipole transitions but also from forbidden magnetic and higher-order electric transitions. This concerns in most cases mixtures of dipole and quadrupole[48,49]. It has been pointed out recently that even if one of the multipoles contributes about 1% to the total transition probability, the angular distribution of radiation can be significantly affected by the interference between multipoles[50].

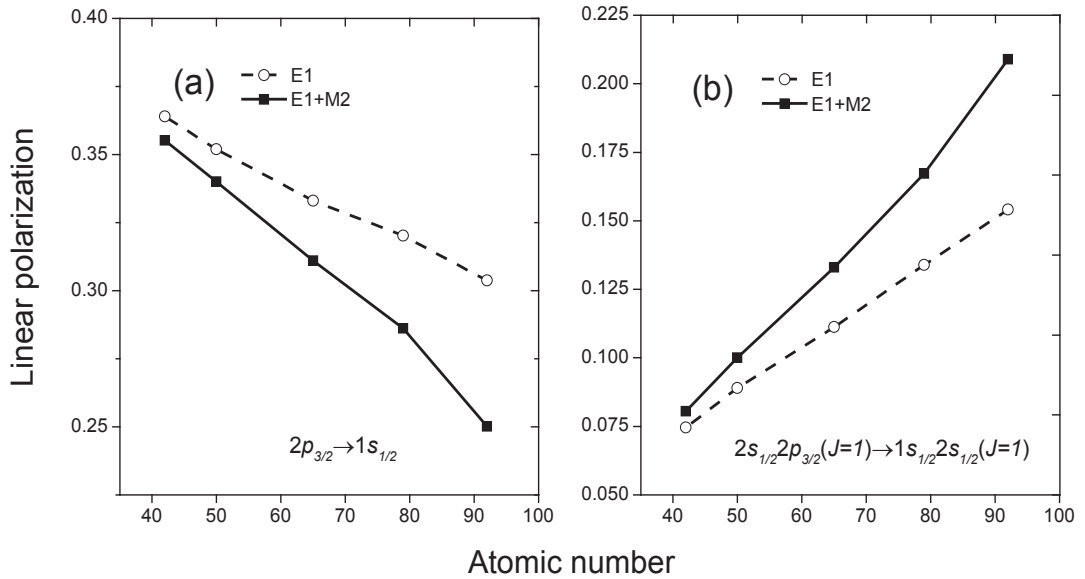


Figure 2. The degree of linear polarization of the transition line $2p_{3/2} \rightarrow 1s_{1/2}$ for H-like (left) and the transition line $2s_{1/2}2p_{3/2}(J=1) \rightarrow 1s_{1/2}2s_{1/2}(J=1)$ for He-like (right) molybdenum, gold, and uranium ions as functions of the incident electron energy in threshold units. E1 + M2 represents values with inclusion of E1-M2 interference, E1 represents inclusion of only the electric-dipole approximation.

In Fig.2, the polarization with and without the E1-M2 interference effects at 1.2 times of the threshold energy for H-like of $2p_{3/2} \rightarrow 1s_{1/2}$ transition line and at 3 times of the threshold energy for He-like $2s_{1/2}2p_{3/2}(J=1) \rightarrow 1s_{1/2}2s_{1/2}(J=1)$ transition line are

displayed versus the atomic number. From the figure, we can clearly found that the E1-M2 interference effects make the degree of linear polarization decrease for H-like ions, while increase for He-like ions. Furthermore, we can also found that the degree of linear polarization with only electric-dipole approximation change relatively slow with a little rate, while with the E1-M2 interference effects become rapidly with increasing of the atomic number for both H-like and He-like ions. It appears, thus, the differences between the degrees of linear polarization with and without the E1-M2 interference effects at the given energies become more evident with increasing of the atomic number.

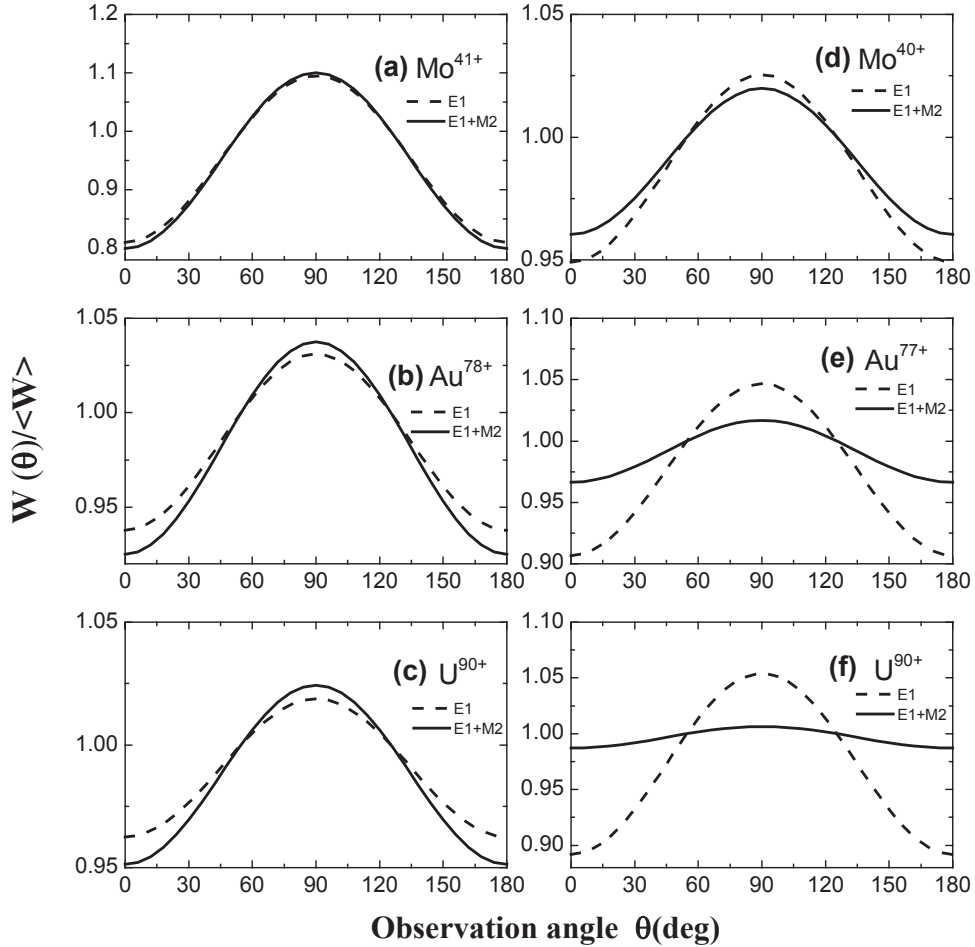


Figure 3. $W(\theta)/\langle W \rangle$ ratio the transition line $2p_{3/2} \rightarrow 1s_{1/2}$ for H-like (left) and the transition line $2s_{1/2}2p_{3/2}(J=1) \rightarrow 1s_{1/2}2s_{1/2}(J=1)$ for He-like (right) molybdenum, gold, and uranium ions as functions of the observation angle θ relative to the electron beam. E1 + M2 represents values with inclusion of E1-M2 interference, E1 represents inclusion of only the electric-dipole approximation.

To examine the influence of E1-M2 interference on the angular distribution of photoemission, we calculated the $W(\theta)/\langle W \rangle$ ratio versus angle θ both with and without the E1-M2 interference effects for $2p_{3/2} \rightarrow 1s_{1/2}$ transition line of H-like of Mo^{41+} , Au^{78+} and U^{91+} ions at 1.2 times of the threshold energy and the

$2s_{1/2}2p_{3/2}(J=1) \rightarrow 1s_{1/2}2s_{1/2}(J=1)$ transition line of He-like Mo^{40+} , Au^{77+} and U^{90+} ions at 3 times of the threshold. The results are presented in Fig.3. For the $2p_{3/2} \rightarrow 1s_{1/2}$ line of H-like ions, as can be seen from Fig.3(a)-(c), the E1-M2 interference effects can lead to a slightly increase in the anisotropy of the intensity angular distribution, contrary to the polarization. These characters mean a dominant photon emission perpendicular to the electron beam including the E1-M2 interference has been enhanced. The contributions of the E1-M2 interference effects to the angular distribution of radiation $W(\theta)/W$ ratio at $\theta = 90^\circ$ is 0.4%, 0.6% and 0.9% for the H-like Mo^{41+} , Au^{78+} and U^{91+} ions, respectively. However, for He-like ions, as can be seen from Fig.3(d)-(f), the E1-M2 interference effects lead to a reduction in the anisotropy of the angular distribution of radiation. And a dominant photon emission perpendicular to the electron beam, while including the E1-M2 interference clearly favors a collinear emission along the electrons beam, contrary to the H-like ions. The contributions of the E1-M2 interference effects to the angular distribution of radiation at $\theta = 90^\circ$ is about 1.2%, 3% and 5% for the He-like Mo^{40+} , Au^{77+} and U^{90+} ions, respectively. Finally, we noted that the differences between the $W(\theta)/W$ ratio with and without the E1-M2 interference effects become more evident with increasing of the atomic number for both H-like and He-like ions.

4. Influence of Breit interaction on the linear polarization of highly charged Be-like ions

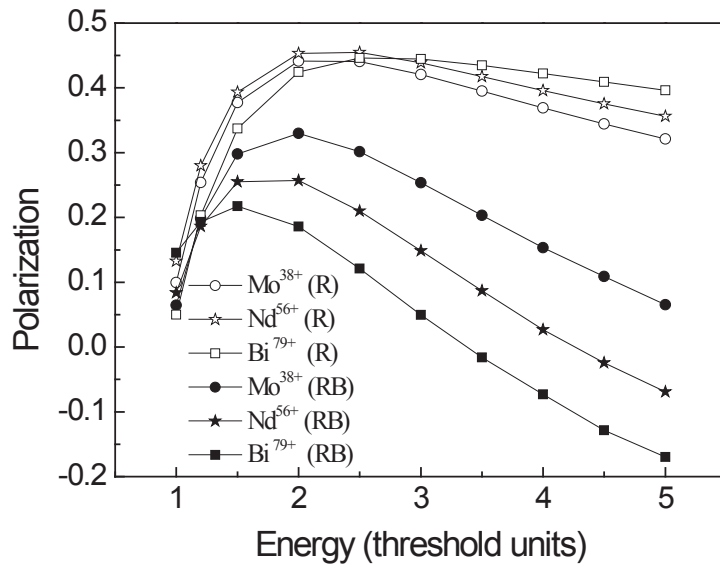


Figure 4. The degree of linear polarization of transition line $1s2s^22p_{1/2}(J=1) \rightarrow 1s^22s^2(J=0)$ for the Be-like Mo^{38+} , Nd^{56+} , and Bi^{79+} ions as functions of incident electron energy in threshold units. R represents the value with inclusion of only the Coulomb interaction, and RB represents the one with the Breit interaction included.

The effects of Breit interactions on the electron collision processes are very

important, and have been studied for many years. In Fig.4, we show the degree of linear polarization as functions of incident electron energy for the beryllium-like Mo^{38+} , Nd^{56+} , and Bi^{79+} ions. Both the degrees of linear polarization with and without the Breit interaction included increase sharply with increasing of incident electron energy before starting to decrease at higher energy region. And when the incident electron energies are greater than about 2 times of the threshold energies, the degree of linear polarization without the Breit interaction included decreases very slowly, however, the degree of linear polarization with the Breit interaction included decreases rapidly. This same pattern of an increase in the degree of linear polarization after the threshold energy followed by a steady decrease was apparent in the intermediate coupling calculations for helium-like Fe ion reported by Inal *et al.* [26] and in the distorted-wave calculations for several other helium-like ions reported by Reed *et al.* [28]. It is found that the Breit interaction makes the degree of linear polarization decrease at given incident electron energies, and the contribution of the Breit interaction on the degree of linear polarization is more and more important with increasing of incident electron energy. For example, the Breit interaction even causes a change of the sign of the linear polarization for the beryllium-like Nd^{56+} , and Bi^{79+} ions at about 4.5 and 3.5 times of the threshold energy, respectively. The reason is that, the cross sections for excitations to the sublevels $m_f=0$ and $m_f=\pm 1$ with the Breit interaction included cross each other at about 4.5 and 3.5 times of the threshold energy for the beryllium-like Nd^{56+} , and Bi^{79+} ions, respectively. It is also found that the contribution of the Breit interaction on the degree of linear polarization is more and more important with increasing of atomic number at given incident electron energies.

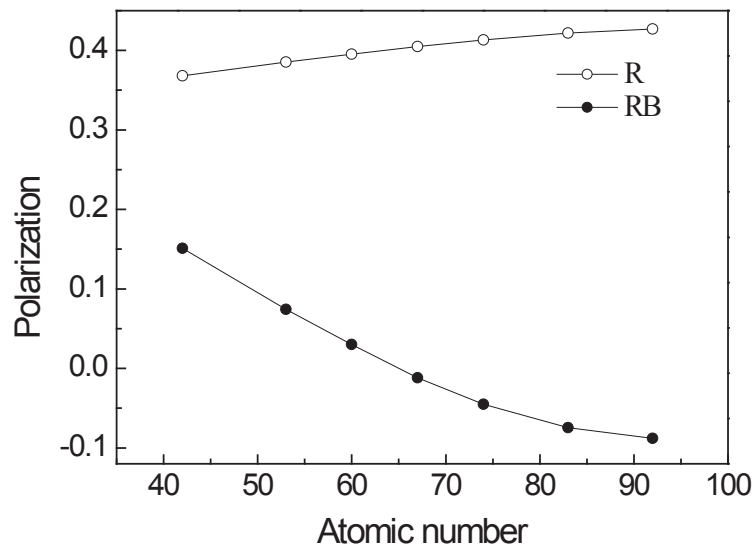


Figure 5. The degree of linear polarization of transition line $1s2s^22p_{1/2}(J=1) \rightarrow 1s^22s^2(J=0)$ for the Be-like Mo^{38+} , Nd^{56+} , and Bi^{79+} ions as functions of atomic number. R represents the value with inclusion of only the Coulomb interaction, and RB represents the one with the Breit interaction included.

In order to illuminate the dependence of the degree of linear polarization on atomic number at given incident electron energy more clearly, the degrees of linear polarization with and without the Breit interaction included as functions of atomic number at four times of the threshold energy are displayed in Fig.5. It is found that the Breit interaction makes the degree of linear polarization decrease for all of the beryllium-like ions. It is also found that the degree of linear polarization with only the Coulomb interaction included increases very slowly as atomic number increases, and the degree of linear polarization with inclusion of the Coulomb plus Breit interaction decreases rapidly with increase of atomic number. So the differences between the degrees of linear polarization with and without the Breit interaction included at the given energies become more evident with increasing of atomic number. However, for the degree of linear polarization of the same lines but formed by the dielectronic recombination process [39], the situations are very different, the Breit interaction makes the degree of linear polarization increase, furthermore, the degree of linear polarization with the Breit interaction included increases with increasing of atomic number.

5. Influence of Breit interaction on the cross section and circular polarization of highly charged Be-like ions

As is well-known, the excitation of ions by a polarized electron beam will leads to an orientation of the excited level in general; i.e., the magnetic sublevels M_J and $-M_J$ are differently populated[27,30]. The radiation subsequently emitted in the decay of these oriented levels is circularly polarized.

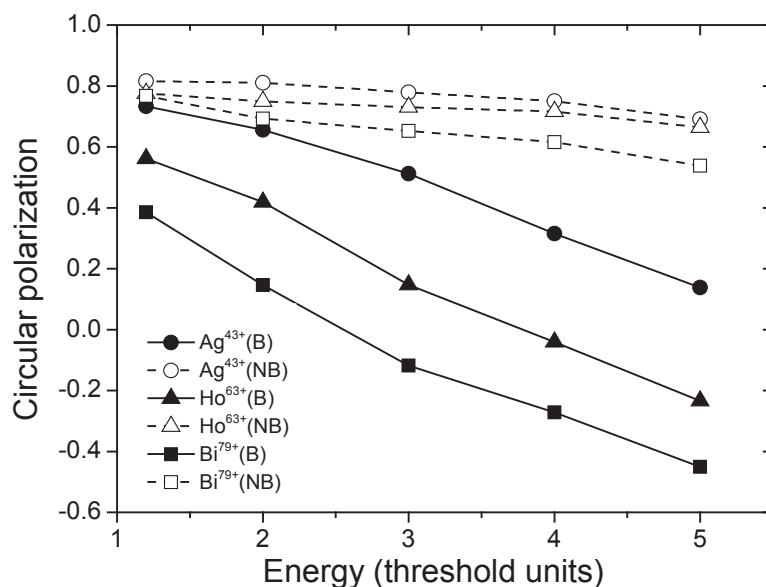


FIG. 6. The degree of circular polarization of the transition line $1s2s^22p_{3/2}(J=2)-1s^22s^2(J=0)$ for Be-like Ag^{43+} , Ho^{63+} , and Bi^{79+} ions as functions of incident polarized electron energy in threshold units. NB represents the values with inclusion of only the Coulomb interaction, and B represents the ones with the Breit interaction included.

Fig. 6 shows the circular polarization of $1s2s^22p_{3/2}(J=2)-1s^22s^2(J=0)$ line of Be-like Ag^{43+} , Ho^{63+} , and Bi^{79+} ions as functions of incident polarized electron energy. In the case of including only the Coulomb interaction, the degree of circular polarization has a very large value and decreases very slowly with the increasing incident energy. When the Breit interaction is taken into account, the circular polarization decreases rapidly for each ion with increasing energy. The Breit interaction decreases circular polarization from 0.79 to 0.22, 0.78 to 0.21, and 0.65 to 0.43 at 5 times the threshold energy for Be-like Ag^{43+} , Ho^{63+} , and Bi^{79+} ions, respectively. Moreover, the Breit interaction causes a change of the sign of the circular polarization for the Be-like Ho^{63+} and Bi^{79+} ions at about 4 and 2.2 times the threshold energy, respectively.

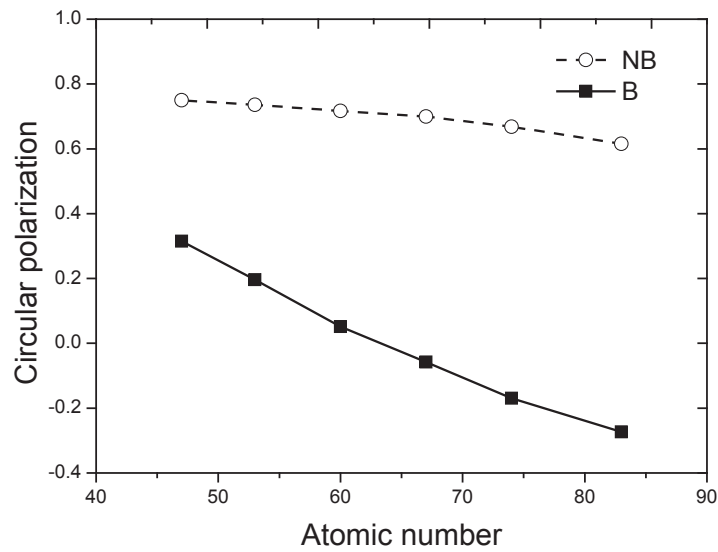


Figure 7. The degree of circular polarization of the transition line $1s2s^22p_{3/2}(J=2) \rightarrow 1s^22s^2(J=0)$ for the Be-like Ag^{43+} , Ho^{63+} , and Bi^{79+} ions as functions of atomic number at incident energy is four times of threshold energy. NB represents the values with inclusion of only the Coulomb interaction, and B represents the ones with the Breit interaction included.

In Fig.7, we display the degrees of circular polarization with and without the Breit interaction included as functions of atomic number at four times of the threshold energy. It is obvious that the Breit interaction makes the degree of circular polarization decrease for all of the Be-like ions. And the degree of circular polarization with only the Coulomb interaction included decreases very slowly as atomic number increases, while with inclusion of the Coulomb plus Breit interaction decreases rapidly with increase of atomic number.

6. Influence of Debye plasma on the polarization of He-like Fe^{24+} ions

The study of spectral properties and atomic collision processes of high charged ions embedded in hot, dense plasma environments has become an active and interested topic in recently years[44-47]. Treating the effect of plasma environment in atoms and ions atomic processes along with an accurate treatment of electron-electron correlation and relativistic effects are nontrivial.

Table.I The polarization of the $1s2p\ ^{1,3}P_1 - 1s^2\ ^1S_0$ emission lines, (X, threshold unit), λ is the Debye length (a_0).

ϵ_i	1P_1					3P_1				
	$\lambda=2$	$\lambda=5$	$\lambda=10$	$\lambda=50$	$\lambda=\infty$	$\lambda=2$	$\lambda=5$	$\lambda=10$	$\lambda=50$	$\lambda=\infty$
6.8keV	0.590	0.595	0.592	0.596	0.596	-0.269	-0.224	-0.205	-0.191	-0.188
8.0keV	0.593	0.597	0.601	0.602	0.603	-0.090	-0.054	-0.046	-0.038	-0.036
1.5X	0.579	0.578	0.582	0.583	0.581	0.085	0.108	0.115	0.120	0.122
2X	0.529	0.533	0.534	0.538	0.534	0.205	0.218	0.222	0.225	0.226
3X	0.427	0.434	0.438	0.440	0.441	0.248	0.256	0.259	0.261	0.261
4X	0.345	0.359	0.362	0.367	0.368	0.230	0.240	0.243	0.245	0.246

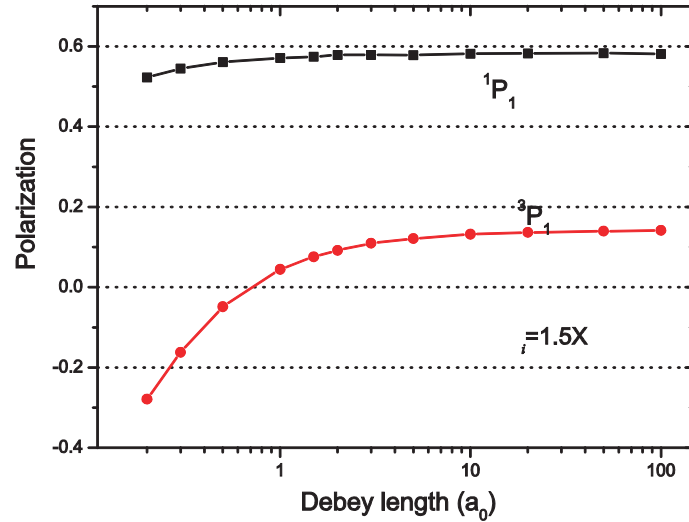


Figure 8. The linear polarization of the $1s2p\ ^{1,3}P_1 - 1s^2\ ^1S_0$ emission lines as a function of debye length. The incident electron energy is 1.5 time threshold.

Table I gives the linear polarizations of the $1s2p\ ^{1,3}P_1 \rightarrow 1s^2\ ^1S_0$ lines in the presence of plasma screening for several impact energies. From this table, it can be found that, with increasing of incident energy, the polarization of the 1P_1 resonance line for the unscreened case ($\lambda=\infty$) decrease from 0.60 to 0.358, and the effects of plasma screening on the polarization are quite small. However, the polarization of the 3P_1 line

for the unscreened case vary from the negative to positive with the increasing of incident energy, nevertheless, the influence of plasma screening are significant especially at the low impact energy, but for the high impact energy, the influence becomes small. As an example, Fig. 8, in relationship to Fig.6, shows the Debye length dependence of the linear polarization of the $1s2p\ ^1P_1$ and 3P_1 to the $1s^2\ ^1S_0$ at the incident energy is 1.5 times the excitation threshold. We found that for the 3P_1 line the polarization degree decreases from 14% to -28% with the decreasing of the debye length. However, for the 1P_1 line, changes of the polarization degree are very small, and when $\lambda > 2 a_0$, the polarization are almost invariant. The reason is that the change trend of the cross sections excite to the $M = 0$ and $M = 1$ sublevels for 3P_1 and 1P_1 state are different.

7. Conclusions

In summary, a new program, REIE06 for electron impact excitation have been developed in the frame of distorted wave approximation. By combining this program with the widely used GRASP92/2K and RATIP packages, atomic/ionic structures and collision dynamic process can be treated uniformly to include the effects of relativistic, electron correlation and Breit interaction. As the application, some higher order effects to the polarization properties of the subsequent photoemission such as, the resonant EIE process of Ne-like ions, the Briet interactions on the EIE process of Be-like ions, the E1-M2 interference effects, the plasma screening effects have been studied in details. Good agreements between available experiments and other calculations were found. We hope these works will be helpful for further understanding the contributions from the higher order effects and getting more accurate polarization data.

Acknowledgments

This work has been supported by the National Natural Science Foundation of China (Grant No.11274254, U1332206, 11147018).

References

- [1] J. Dubau, M. K. Inal, and A. M. Urnov, *Physica Scripta* **T65**, 179 (1996)
- [2] E. Haug, *Sol. Phys.* **61**, 129 (1979)
- [3] E. Haug, *Sol. Phys.* **71**, 77 (1981)
- [4] A. S. Shlyaptseva, S. B. Hansen, V. L. Kantsyrev, B. S. Bauer, D. A. Fedin, N. Ouart, S. A. Kazantsev, A. G. Petrashen, and U. I. Safronova, *Rev. Sci. Instrum.* **72**, 1241 (2001)
- [5] J. C. Kieffer, J. P. Matte, H. Pépin, M. Chaker, Y. Beaudoin, T. W. Johnston, C. Y. Chien, S. Coe, G. Mourou, and J. Dubau, *Phys. Rev. Lett.* **68**, 480 (1992)
- [6] J. C. Kieffer, J. P. Matte, M. Chaker, Y. Beaudoin, C. Y. Chien, S. Coe, G. Mourou, J. Dubau, and M. K. Inal, *Phys. Rev. E* **48**, 4648 (1993)

- [7] P. Hakel, R. C. Mancini, J.-C. Gauthier, E. Mínguez, J. Dubau, and M. Cornille, *Phys. Rev. E* **69**, 056405 (2004)
- [8] Y. Inubushi, T. Kai, T. Nakamura, S. Fujioka, H. Nishimura, and K. Mima, *Phys. Rev. E* **75**, 026401 (2007)
- [9] P. Hakel, R. C. Mancini, J. Abdallah, M. E. Sherrill, and H. L. Zhang, *J. Phys. B* **42**, 085701 (2009).
- [10] J. R. Henderson, P. Beiersdorfer, C. L. Bennett, S. Chantrenne, D. A. Knapp, R. E. Marrs, M. B. Schneider, K. L. Wong, G. A. Doschek, J. F. Seely, C. M. Brown, R. E. LaVilla, J. Dubau, and M. A. Levine, *Phys. Rev. Lett.* **65**, 705 (1990)
- [11] P. Beiersdorfer, D. A. Vogel, K. J. Reed, V. Decaux, J. H. Scofield, K. Widmann, G. Hölzer, E. Förster, O. Wehrhan, D. W. Savin, and L. Schweikhard, *Phys. Rev. A* **53**, 3974 (1996).
- [12] E. Takács, E. S. Meyer, J. D. Gillaspay, J. R. Roberts, C. T. Chantler, L. T. Hudson, R. D. Deslattes, C. M. Brown, J. M. Laming, J. Dubau, and M. K. Inal, *Phys. Rev. A* **54**, 1342 (1996).
- [13] A. S. Shlyaptseva, R. C. Mancini, P. Neill, and P. Beiersdorfer, *Rev. Sci. Instrum.* **68**, 1095 (1997)
- [14] P. Beiersdorfer, J. C. López-Urrutia, V. Decaux, K. Widmann, and P. Neill, *Rev. Sci. Instrum.* **68**, 1073 (1997)
- [15] P. Beiersdorfer, G. Brown, S. Utter, P. Neill, K. J. Reed, A. J. Smith, and R. S. Thoe, *Phys. Rev. A* **60**, 4156 (1999).
- [16] F. Walden, H.-J. Kunze, A. Petoyan, A. Urnov, and J. Dubau, *Phys. Rev. E* **59**, 3562 (1999)
- [17] N. Nakamura, D. Kato, N. Miura, T. Nakahara, and S. Ohtani, *Phys. Rev. A* **63**, 024501 (2001).
- [18] D. L. Robbins, A. Ya. Faenov, T. A. Pikuz, H. Chen, P. Beiersdorfer, M. J. May, J. Dunn, K. J. Reed, and A. J. Smith, *Phys. Rev. A* **70**, 022715 (2004).
- [19] D. L. Robbins, P. Beiersdorfer, A. Ya. Faenov, T. A. Pikuz, D. B. Thorn, H. Chen, K. J. Reed, A. J. Smith, K. R. Boyce, G. V. Brown, R. L. Kelley, C. A. Kilbourne, and F. S. Porter, *Phys. Rev. A* **74**, 022713 (2006).
- [20] Y. M. Liu, S. Singha, T. E. Witt, Y. T. Cheng, and R. J. Gordon, *Appl. Phys. Lett.* **93**, 161502 (2008)
- [21] K. J. Reed and M. H. Chen, *Phys. Rev. A* **48**, 3644 (1993)
- [22] C. J. Fontes, H. L. Zhang, and D. H. Sampson, *Phys. Rev. A* **59**, 295 (1999)
- [23] L. Sharma, A. Surzhykov, R. Srivastava, and S. Fritzsche, *Phys. Rev. A* **83**, 062701 (2011)
- [24] P. Amaro, F. Fratini, S. Fritzsche, P. Indelicato, J. P. Santos, and A. Surzhykov *Phys. Rev. A* **86**, 042509 (2012)
- [25] Y. Itikawa, R. Srivastava, and K. Sakimoto, *Phys. Rev. A* **44**, 7195 (1991)
- [26] M. K. Inal and J. Dubau, *J. Phys. B* **20**, 4221 (1987).
- [27] M. K. Inal, H. L. Zhang, and D. H. Sampson, *Phys. Rev. A* **46**, 2449 (1992).
- [28] M. K. Inal and J. Dubau, *Phys. Rev. A* **47**, 4794 (1993).
- [29] M. K. Inal, D. H. Sampson, H. L. Zhang, and J. Dubau, *Physica Scripta* **55**, 170 (1997).
- [30] M. K. Inal, H. L. Zhang, D. H. Sampson, and C. J. Fontes, *Phys. Rev. A* **65**, 032727 (2002).
- [31] M. K. Inal, A. Surzhykov, and S. Fritzsche, *Phys. Rev. A* **72**, 042720 (2005).
- [32] T. Kai, R. Srivastava, and S. Nakazaki, *Phys. Rev. A* **70**, 062705 (2004)
- [33] T. Kai, S. Nakazaki, and K. A. Berrington, *Nucl. Instrum. Methods Phys. Res. B* **235**, 249 (2005)

- [34] T. Kai, S. Nakazaki, T. Kawamura, H. Nishimura, and K. Mima, Phys. Rev. A **75**, 012703 (2007)
- [35] T. Kai, S. Nakazaki, T. Kawamura, H. Nishimura, and K. Mima, Phys. Rev. A **75**, 062710 (2007)
- [36] Z. Q. Wu, Y. M. Li, B. Duan, J. Yan, and H. Zhang, Chin. Phys. Lett. **24**, 1560 (2007)
- [37] J. Jiang, C. Z. Dong, L. Y. Xie, and J. G. Wang, Phys. Rev. A **78**, 022709 (2008).
- [38] M. H. Chen and J. H. Scofield, Phys. Rev. A **52**, 2057 (1995)
- [39] S. Fritzsche, A. Surzhykov, and T. Stöhlker, Phys. Rev. Lett. **103**, 113001 (2009)
- [40] F. A. Parpia, C. F. Fischer, and I. P. Grant, Comput. Phys. Commun. **94**, 249 (1996)
- [41] S. Fritzsche, H. Aksela, C. Z. Dong, S. **Heiniäsmäki**, and J. E. Sienkiewicz, Nucl. Instrum. Methods Phys. Res. B **205**, 93 (2003)
- [42] J. Jiang, C. Z. Dong, L. Y. Xie, J. G. Wang, J. Yan, and S. Fritzsche, Chin. Phys. Lett. **24**, 691 (2007)
- [43] P. Beiersdorfer, A. L. Osterheld, M. H. Chen, J. R. Henderson, D. A. Knapp, M. A. Levine, R. E. Marrs, K. J. Reed, M. B. Schneider, and D. A. Vogel, Phys. Rev. Lett. **65**, 1995 (1990)
- [44] J. Jiang, C. Z. Dong, L. Y. Xie, Chin. Phys. Lett. **31**, 023401 (2014)
- [45] M. S. Pindzola, S. D. Loch, J. Colgan and C. J. Fontes, Phys. Rev. A **77**, 062707 (2008)
- [46] Z. Q. Wu, G. X. Han, J. Yan, and J. Q. Pang, J. Phys. B **35**, 2305 (2002)
- [47] L. Liu, J. G. Wang, and R. K. Janev, Phys. Rev. A **77**, 042712 (2008)
- [48] L. Liu, J. G. Wang, and R. K. Janev, Phys. Rev. A **77**, 032709 (2008)
- [49] Z. B. Chen, C. Z. Dong L. Y. Xie, and J. Jiang, Phys. Rev. A **90** 012703 (2014)
- [50] R. Bensaid, M. K. Inal, and J. Dubau, J. Phys. B **39**, 4131 (2006)
- [51] A. Surzhykov, S. Fritzsche, A. Gumberidze, and T. Stöhlker, Phys. Rev. Lett. **88**, 153001 (2002)

Development of time-resolved electron momentum spectroscopy: toward real-time imaging of frontier electrons in molecular reactions

M. Yamazaki and M. Takahashi*

*Institute of Multidisciplinary Research for Advanced Materials, Tohoku University,
Sendai 980-8577, Japan*

*Corresponding author: masahiko@tagen.tohoku.ac.jp (M. Takahashi)

ABSTRACT

This report will introduce a new experimental technique to readers, which we would like to propose towards advances in the field of molecular reaction dynamics. It is time-resolved electron momentum spectroscopy and aims to take in momentum space snapshots of the rapid change of molecular orbitals, which is the driving force behind any structural changes occurring in transient molecules. Following a description of the working principle of the technique, some preliminary result will be presented in order to illustrate the current performance of the apparatus.

Keywords: (e,2e) electron momentum spectroscopy; pump-probe technique;
molecular reaction; frontier electron dynamics

1 Introduction

Through the last four decades of studies of binary (e,2e) spectroscopy or electron momentum spectroscopy (EMS), it has been demonstrated that the ionization reaction near the Bethe ridge is a sensitive probe for electronic structure and electron correlation in matter [1, 2]. This method involves coincident detection of the two outgoing electrons produced by electron impact ionization of a target atom or molecule. The ion recoil momentum \mathbf{q} and the electron binding energy E_{bind} can be determined by coincident detection of the two outgoing electrons with the help of the laws of conservation of linear momentum and energy:

$$\mathbf{q} = \mathbf{p}_0 - \mathbf{p}_1 - \mathbf{p}_2 \quad (1)$$

and

$$E_{\text{bind}} = E_0 - E_1 - E_2. \quad (2)$$

Here the \mathbf{p}_j 's and E_j 's ($j = 0, 1, 2$) are momenta and kinetic energies of the incident and two outgoing electrons, respectively. Under the high-energy Bethe ridge conditions [1-2], the collision kinematics can be described by the so-called electron Compton scattering [3],

analogous to X-ray Compton scattering, that most nearly corresponds to collision of two free electrons with the residual ion acting as a spectator. Then the momentum of the target electron before ionization \mathbf{p} is equal in magnitude but opposite in sign to the ion recoil momentum \mathbf{q} .

$$\mathbf{p} = -\mathbf{q} = \mathbf{p}_1 + \mathbf{p}_2 - \mathbf{p}_0 \quad (3)$$

Fig. 1 shows the symmetric noncoplanar geometry that has widely been used for EMS experiments. In this kinematic scheme, two outgoing electrons having the equal energy ($E_1 = E_2$) and the equal scattering angle ($\theta_1 = \theta_2 = 45^\circ$) with respect to the incident electron momentum vector are detected in coincidence. Then magnitude of the ion recoil momentum q or that of the target electron momentum p is expressed by

$$p = q = \sqrt{(p_0 - \sqrt{2}p_1)^2 + (\sqrt{2}p_1 \sin(\Delta\phi/2))^2} \quad (4)$$

where $\Delta\phi (= \phi_2 - \phi_1 + \pi)$ is the out-of-plane azimuthal angle difference between the two outgoing electrons. In this way, EMS cross section can be measured as a function of binding energy and target electron momentum. In other words, EMS enables one to look at electron orbitals in momentum space, providing unique and versatile information about electronic structure of matter.

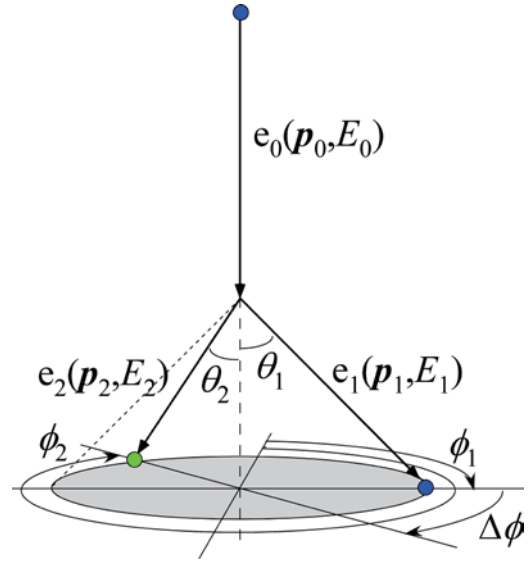


Fig. 1. Symmetric noncoplanar geometry for the binary (e,2e) reaction.

In spite of the remarkable feature, however, application of EMS has long been limited only to stable target atoms and molecules in their ground states. The reason for this may be due to an experimental difficulty that (e,2e) cross sections under the high-energy Bethe ridge conditions employed is extremely small compared to those at small momentum transfers or in the forward scattering directions of the electron projectile. Thus, in order to make EMS applicable to short-lived transient species, we have first developed a traditional, but extremely highly sensitive EMS spectrometer [4]. Based on this technical achievement, we have subsequently developed a time-resolved EMS (TR-EMS) apparatus [5] that employs an ultrashort-pulsed incident electron beam with a temporal width being in the order of a picosecond. This apparatus can be expected to be applied widely. One of the possible applications would be to take in momentum space snapshots of the rapid change of molecular orbitals, which is the driving force behind any chemical reactions. In the present paper, details and the working principle of the apparatus are given. Then, a preliminary result obtained by using the apparatus is presented in order to illustrate the current performance of the apparatus.

2 Time-resolved electron momentum spectroscopy apparatus

Details of the TR-EMS apparatus have been described elsewhere [5], so a brief account of

it is given here (Fig. 2). The 800 nm output from a 5-kHz femtosecond laser is split into a pump path and an electron-generation path. 90% of the output is used to yield the pump laser pulse with an optical parametric amplifier, which is used to initiate chemical reaction of molecules in the target gas beam produced through either of a single tube gas nozzle and a multi-capillary beam source, after the 5-kHz repetition rate being halved by an optical chopper. On the other hand, 10% of the output is frequency tripled in a third-harmonic generator to produce electron pulses via the photoelectric effect. The photocathode is made of a silver film of forty-nm thickness, which is negatively biased to accelerate the electron pulses. The electron pulses are then used to induce EMS scattering. The time delay between the arrival of the pump laser pulse and the probe electron pulse is controlled with a computer-driven translation stage. The resulting EMS events are recorded by an EMS spectrometer for which an exceptionally large spherical analyzer (mean radius of 220 mm) is employed. Here, the two outgoing electrons in the symmetric noncoplanar geometry are dispersed by the spherical analyzer and detected by a large-area position sensitive detector. It should be noted that this apparatus produces two kinds of EMS datasets. One is data that are measured with pump laser and the other is reference data that are measured without pump laser. TR-EMS results can be obtained as difference spectra between these two datasets with an appropriate weight factor for the reference data.

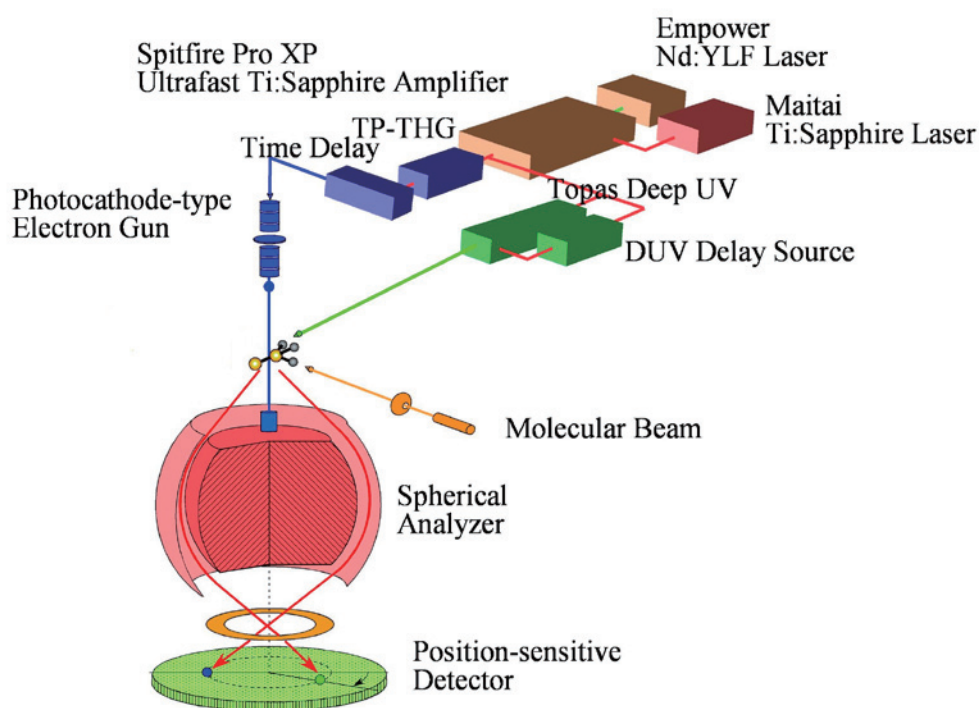


Fig. 2. Schematic of a time-resolved electron momentum spectroscopy apparatus.

3 Sample result

A show-case experiment has been conducted by using the TR-EMS apparatus but without pump laser. Here, the target molecule of choice is the deuterated acetone molecule in its ground state. The incident electron energy was about twelve hundreds electron volt and its beam intensity was 50 pA. Diameter of the target gas beam was 2 mm. The energy resolution in binding energy spectra was 5 eV, which was almost the same as the energy spread in the incident electron beam due to space charge effects. The experimental results were obtained through accumulation of data for 14 days runtime. Fig. 3 shows a $\Delta\phi$ -angle integrated binding energy spectrum of the deuterated acetone molecule thus obtained without pump laser. Note that ionization bands from the valence molecular orbitals are significantly overlapped to the adjacent bands due to the poor energy resolution of 5 eV employed. Nevertheless, it is possible to check the quality of the experimental data by making a comparison with theory.

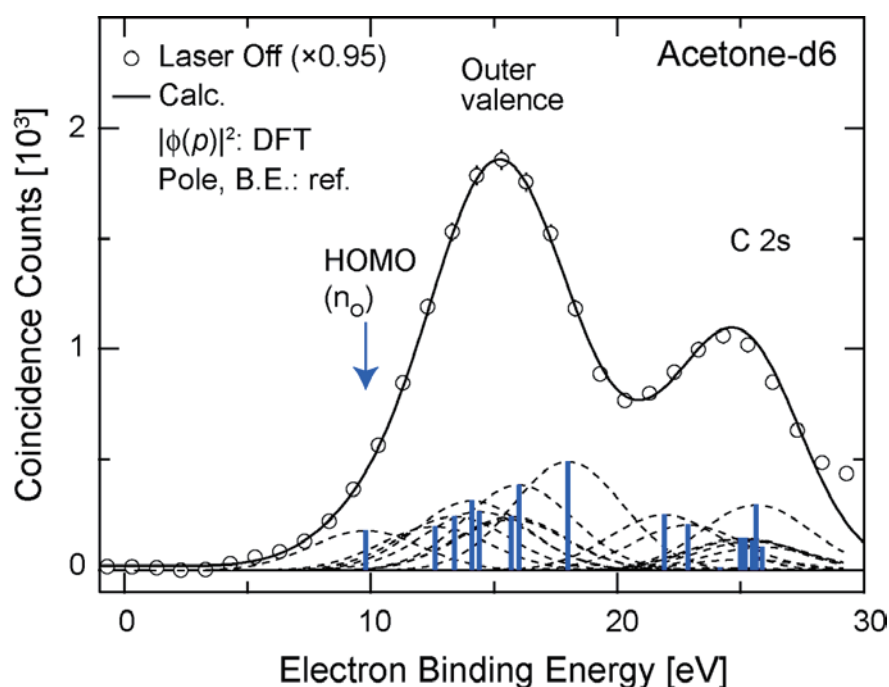


Fig. 3. $\Delta\phi$ -angle integrated binding energy spectrum for the deuterated acetone molecule, obtained by using an ultrashort-pulsed incident electron beam.

The scattering theory most used in EMS is the plane wave impulse approximation (PWIA). Within the PWIA, EMS cross section for a gaseous molecule is proportional to the product of two physical quantities. One is a quantity called pole strength or spectroscopic factor, which represents a probability for finding one-hole electron configuration in the final ion state. The other quantity is the spherically-averaged electron momentum density distribution of the ionized orbital. Here, the spherically averaging is due to the random orientation of gaseous targets. According to the PWIA, an associated binding energy spectrum can be created by calculating the integrated value of the spherically-averaged electron momentum distribution over the covered momentum range for each bound molecular orbital with their own binding energies, and by summing up those after being convoluted with the instrumental energy

resolution of 5 eV. The resulting theoretical spectrum is also presented in Fig. 3. Here, the relevant wave functions for molecular orbitals were obtained with density functional theory at the equilibrium molecular geometry and the experimental pole strength distribution in the literature [6] was employed.

It can be seen from Fig. 3 that there is a good agreement between experiment and theory. This observation confirms that successful EMS measurements by using an ultrashort pulsed incident electron beam have been achieved, opening the door for detailed future studies of the change of molecular orbitals that are the driving force behind any molecular reactions. In fact, a preliminary but the first TR-EMS result has successfully been obtained recently, for the photo-induced three body dissociation process of acetone at 195 nm [7].

Acknowledgements

One of the authors MT gratefully thanks the organizing committee for giving him the opportunity to be involved in the exciting seminar, the 5th China-Japan-Korea Joint Seminar on Atomic and Molecular Processes in Plasma (Jul. 28 – Aug. 1, 2014, Lanzhou, China). This work was partially supported by Grant-in-Aids for Scientific Research (S) (No. 20225001) and for Young Scientists (B) (No. 21750005) from the Ministry of Education, Culture, Sports, Science and Technology, as well as by the JSPS - NRF - NSFC A3 Foresight Program in the field of Plasma Physics (NSFC: No.11261140328, NRF : No.2012K2A2A6000443).

References

- [1] E. Weigold and I.E. McCarthy, *Electron Momentum Spectroscopy* (Kluwer Academic /Plenum Publishers, New York, 1999).
- [2] M. Takahashi, Bull. Chem. Soc. Jpn. **82**, 751 (2009).
- [3] R.A. Bonham and H.F. Wellenstein, in: B. Williams (Ed.), *Compton Scattering* (McGraw-Hill, New York, 1977).
- [4] M. Yamazaki, H. Satoh, M. Ueda, D. B. Jones, Y. Asano, N. Watanabe, A. Czasch, O. Jagutzki, and M. Takahashi, Meas. Sci. Technol. **22**, 075602 (2011).
- [5] M. Yamazaki, Y. Kasai, K. Oishi, H. Nakazawa, and M. Takahashi, Rev. Sci. Instrum. **84**, 063105 (2013).
- [6] Y. Zheng, J. J. Neville, C. E. Brion, Y. Wang, and E. R. Davidson, Chem. Phys. **188**, 109 (1994).
- [7] M. Yamazaki, Y. Kasai, K. Oishi, H. Nakazawa, and M. Takahashi, 2013 XXVIII ICPEAC Abstracts of Contributed Papers.

How do we observe the forbidden lines from He-like ions in charge exchange collisions of H-like ions with neutral gases?

Hajime TANUMA, Hirofumi SHIMAYA, Takuya ISHIDA,

Nobuyuki NAKAMURA*, Naoki NUMADATE†, and Kunihiro OKADA†

*Department of Physics, Tokyo Metropolitan University, 1-1 Minami-Ohsawa, Hachioji,
Tokyo 192-0397, Japan*

**Institute for Laser Science, The University of Electro-Communications,
1-5-1 Chofugaoka, Chofu, Tokyo 182-0021, Japan*

*†Department of Physics, Sophia University, 7-1 Kioicho, Chiyoda, Tokyo 102-8554, Japan
e-mail: tanuma-hajime@tmu.ac.jp*

Abstract

We have observed the emission spectra in collisions of O^{7+} with He gas in the soft x-ray region with a window-less solid state detector. The emission corresponds to the $1s^2 \leftarrow 1snp$ ($n \geq 2$) transition of the O^{6+} ions produced by a single-electron capture. Emissions from the collision center are all resonance line from the singlet states with very short lifetimes. However, the triplet states might be produced in charge exchange collisions. To observe the forbidden transition from the triplet states to the singlet ground state, we have developed a Kingdon trap.

Keywords: solar wind charge exchange, multiply charged ions, soft x-ray emission, forbidden transition, atomic orbital close coupling method, Kingdon ion trap

1. Introduction

Generally speaking, in charge exchange collisions of multiply charged ions with neutral target gases, single electron captures are dominant reaction processes. Therefore, both singlet and triplet states of helium-like ions might be produced in the collisions of hydrogen-like ions. The resonance lines, $1s^2 \ ^1S_0 \leftarrow 1snp \ ^1P_1$ ($n \geq 2$), have very short lifetimes about ps, and these can be observed easily. On the other hand, the transitions between $1s^2 \ ^1S_0$ and $1s2s \ ^3S_1$ are optically forbidden with very long lifetimes, and the inter-combination lines between $1s^2 \ ^1S_0$ and $1s2p \ ^3P_J$ ($J = 1, 2$) have also longer lifetimes than typical electric dipole allowed transitions. For example, the lifetimes of $1s^2 \ ^1S_0$, $1s2p \ ^3P_1^o$, $1s2p \ ^3P_2^o$ states of O^{6+} ions are about 1 ms, 2 ns, and 3 μ s, respectively [1]. Therefore, it is very difficult to observe the emission with long lifetimes and measure the emission cross sections of the these transitions in the ordinary ion beam collision experiments.

The soft x-ray emissions by the solar wind charge exchange, which have been observed by the x-ray observatory satellites, might consist of the resonance lines, inter-combination lines, and forbidden lines, even though the separation of these lines has not been performed

yet, because the energy resolution of the spectrometers in the satellites is not enough for this purpose [2, 3]. Therefore, the observation of the forbidden lines in the laboratory must be carried out to measure the emission cross sections for the quantitative analysis of the observed spectra by the satellites.

We had observed the soft x-ray emission spectra in collisions of some multiply charged ions, N^{6+} , O^{7+} , O^{8+} , with He [4, 5]. In those works, the observed spectra correspond to only the resonance lines, namely $1s^2\ ^1S_0 \leftarrow 1snp\ ^1P_1^\circ$ ($n \geq 2$) for helium-like ions and $1s\ ^2S_{1/2} \leftarrow np\ ^2P_{1/2}$ ($n \geq 2$) for hydrogen-like ions, with very short lifetimes of less than 1 ps, because the emission from the collision center had been observed in our experimental setup. Therefore, in order to observe the forbidden transitions of helium-like ions produced in collisions of hydrogen-like ions with neutral gases, we have developed a Kingdon ion trap.

2. Experiment for Resonance Lines

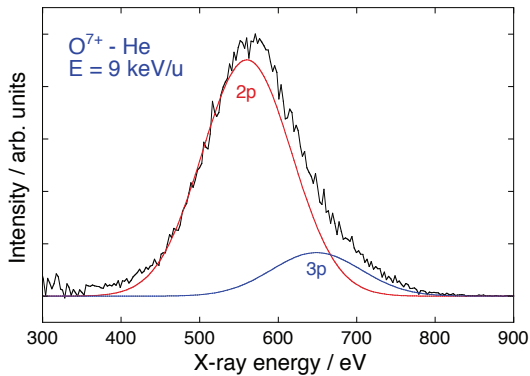


Figure 1: The soft x-ray emission spectrum measured with the Si(Li) detector in collisions of O^{7+} ions with He gas at a collision energy of 140 keV.

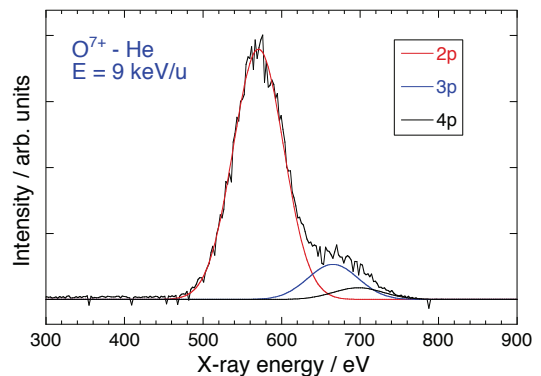


Figure 2: The soft x-ray emission spectrum measured with the SDD detector in collisions of O^{7+} ions with He gas at a collision energy of 140 keV.

Multiply charged ions were produced in a 14.25 GHz ECR (electron cyclotron resonance) ion source. The plasma chamber in the ion source were kept on the high voltage about 5–20 kV from the ground potential. Therefore, the extracted ions had kinetic energies of 5–20 keV/charge. The single species of the ions selected by an analyzing magnet were fed into a collision chamber. In this collision chamber, we had a collision cell which can be applied by high-voltage to reduce the ion beam velocity. Then we can achieve the solar wind velocity for ions, i.e. 200–900 km/s, which corresponds to 0.2–4.2 keV/u. When the target gas was filled in the cell with a low pressure about 2×10^{-3} Pa to

keep the single collision conditions, the soft x-ray emissions of the resonance transitions had been observed by window-less solid state detectors, namely, Si(Li) detector (Oxford, model 6834) and silicon drift detector (PGT, SDD100145WL) [4, 5].

The soft x-ray spectra measured in collisions of O^{7+} with He at collision energy of 140 keV with the Si(Li) and SDD detectors are shown in Figures 1 and 2. The energy resolution of the Si(Li) detector is 120 eV. However, the energy resolution of the SDD is about 70 eV and much better than than of the Si(LI) detector. As can be seen in these figures, the improvement of the energy resolution is very effective, and the contribution of the $1s^2 \leftarrow 1s4p$ transition is clearly observed in only the SDD spectrum.

According to the classical over the barrier model, the dominant electron chapter level is $n = 4$ in collisions of O^{7+} with He [6, 7]. In general, Two-Center Atomic Orbital Close Coupling (TC-AOCC) calculation gives very reliable cross sections of charge exchange collisions at higher energies than 1 keV/u. In the case of the collision between O^{7+} and He, the results of the TC-AOCC calculation was shown in Figure 3 [8].

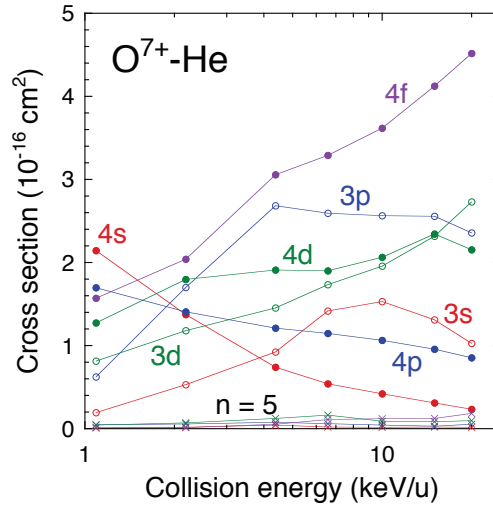


Figure 3: The state-selective one-electron capture cross sections in collisions of O^{7+} with He calculated by the TC-AOCC method.

The mostly capture levels are $n = 3$ and 4 as shown in Figure 3, however, the dominant emission line corresponds to the $1s^2 \leftarrow 1s2p$ transition. This finding is explained with the consideration of the cascade processes from the upper exacted states to the lower ones. However, the observed emissions are only resonance lines of $1s^2 \leftarrow 1snp$ ($n = 2 - 5$) which

are very short lifetimes about ps.

3. Development of a Kingdon Trap

In order to observe the emission with long lifetime, we have developed a Kingdon ion trap. As can be seen in Figure 4, this trap is an electrostatic ion trap which has a very simple structure with a cylinder electrode, central wire, and two end caps [9]. The performance of this trap had been tested with the injection of multiply charged ions by using of a compact ECR ion source (NANOGUN 10 GHz, Panthechnik) in Sophia University [10]. A number of stored ions in the trap might be proportional to a number of ions which ejected from the trap passing through a mesh and detected with a multiple channel plate. From a decay curve of the trapped ions as a function of the storage time, we observed the decay time of 42 ms when we used Ar^{7+} ions and the background pressure was about 4.4×10^{-7} Pa. As we mentioned before, the lifetime of the metastable helium-like O ion is about 1 ms. Therefore, it is obvious that this trap has enough storage time to observe the forbidden transition of O^{6+} ($1s2s\ ^3S_1$).

Now we have just started the experiment for the observation of the forbidden transition from O^{6+} produced in collisions of O^{7+} with H_2 and He. We will show the experimental results in the next Japan-China-Korea Joint Seminar on Atomic and Molecular Processes in Plasma.

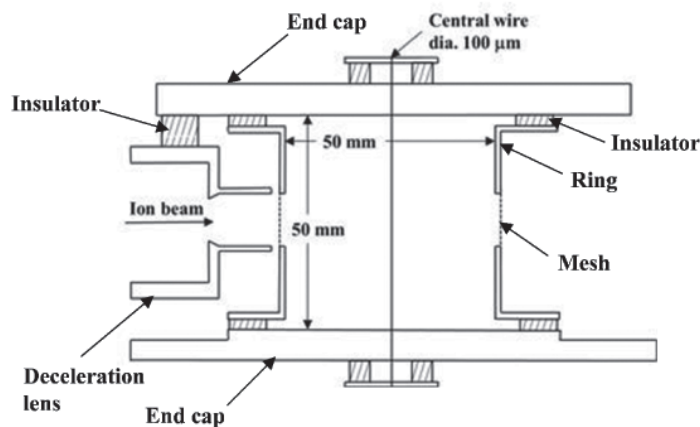


Figure 4: A schematic drawing of the Kingdon ion trap developed in this work.

Acknowledgement

The TC-AOCC calculations have been carried out by Ling Liu and Jianguo Wang

in Institute of Applied Physics and Computational Mathematics, Beijing. We would like to thank them for the collaboration with us. This work was supported in part by Grants-in-Aid for Scientific Research from the Japanese Society for Promotion of Science (No. 21246017, and 23244083), and the JSPS - NRF - NSFC A3 Foresight Program in the field of Plasma Physics (NSFC: No. 11261140328, NRF : No. 2012K2A2A6000443).

References

- [1] I.M. Savukov, W. R. Johnson, and U.I. Safronova, 2003, *At. Data Nucl. Data Tables* **85**, 83.
- [2] C.M. Lisse *et al.*, 2001, *Science* **292**, 1343.
- [3] R. Fujimoto, K. Mitsuda *et al.*, 2007, *Publ. Astron. Soc. Jpn.* **59**, S133.
- [4] T. Kanda *et al.*, 2011, *Phys. Scr.* **T144**, 014025.
- [5] H. Shimaya, T. Ishida, S. Ishikawa *et al.*, 2013, *Phys. Scr.* **T156**, 014002.
- [6] H. Ryufuku, K. Sasaki, and T. Watanabe, 1980, *Phys. Rev. A* **21**,745.
- [7] A. Niehaus, 1986, *J. Phys. B* **19**, 2925.
- [8] L. Liu and J-G. Wang *private communication*.
- [9] K.H. Kingdon, 1923, *Phys. Rev.* **21**, 408.
- [10] N. Numadate, H. Okada, N. Nakamura, and H. Tanuma, *submitted to Rev. Sci. Instrum.*

High-resolution X-ray scattering and its applications in atomic and molecular physics

Lin-Fan Zhu^{1,2,*} Xu Kang^{1,2}

¹ *Hefei National Laboratory for Physical Sciences at Microscale and Department of Modern Physics,
University of Science and Technology of China,
Hefei, Anhui 230026, People's Republic of China*

² *Synergetic Innovation Center of Quantum Information and Quantum Physics,
University of Science and Technology of China,
Hefei, Anhui 230026, People's Republic of China*

With the help of high photon flux synchrotron radiation light source, high resolution x-ray scattering technique is applied in atomic and molecular physics. Several branches of x-ray scattering, which are classified by the final state of the atom or molecule, are summarized in this review. Good agreement between results of x-ray scattering and theoretical calculation are observed, indicating the x-ray is an outstanding probe for the atomic and molecular physics. The existing differences between calculation and traditional electron scattering are clarified.

Keywords: X-ray scattering, Synchrotron radiation, electronic structure, atom and molecule

The studies of excitation processes including determination of both energy levels and dynamic parameters sustain for more than a hundred years and still attract enough attentions nowadays. This is due to that the energy levels and dynamic parameters are not only the basic issue of atomic and molecular physics but also the fundamental physical quantities that are useful almost everywhere. Furthermore, the excitation dynamic parameters of atoms and molecules are of significant importance, since they are closely related to the characterization of scattering process and can test the theoretical mode and calculation method rigorously.

Traditionally, the dynamic parameters of atoms or molecules were determined by the electron energy loss spectroscopy (EELS), such as the low-energy or high-energy EELS methods. The electron scattering experiments with low impact energy not only aim at the practical applications but also form the test ground for the underlying quantum collision theory [1, 2], while the high-energy EELS is a better choice to obtain the structure of atoms and molecules [3]. Although the high energy EELS gain great success in determining the optical oscillator strength (OOS) [4], the strong interaction between the incident electron and target leads to the invalidity of the first Born approximation (FBA) to obtain the generalized oscillator strength (GOS) [5–7], and that will strengthen the complexity of the theoretical calculations.

Besides electron, the x-ray photon can also be a good probe to measure the excitation dynamic parameters. The photon impact has proven to be a powerful tool to investigate excitation dynamic parameters of gaseous atoms and molecules until lately [7–9], although it has been widely used in condensed matter physics. The very first IXS experiment should retrospect to Compton scattering studied by Compton and Debye separately in 1923. It was pointed out by DuMond that the Compton scattering can reveal the electronic density distribution in momentum space [10], and subsequently Nozieres and Pines predicted that the valence shell excitation by IXS can give valuable information about the correlated motion of electrons in a many-particle system [11].

The great challenge of IXS experiment to investigate atoms and molecules in gas phase is the extremely low cross-section whose typical magnitude is the square of classical electron radius ($\sim 10^{-25}\text{cm}^2$), as well as the low density of gases if compared with condensed matters. The common way that the recent investigators [7–9] used to overcome these two difficulties is keeping the target gas in a sealed container to a relatively high pressure ($\sim\text{MPa}$) and choosing an appropriate synchrotron radiation beamline that can offer

* lfzhu@ustc.edu.cn.

high photon flux (more than 10^{11} photons per second).

The classification of x-ray scattering techniques can be presented in several levels. In the energy level there are two kinds named as the elastic x-ray scattering (EXS) and the inelastic x-ray scattering (IXS). Here the “elastic” and “inelastic” represent the state of the scattered photon. If the photon does not loss energy after the collision, it is elastic, and if does, it is inelastic. When considering the process, the inelastic x-ray scattering can be classified into resonant and non-resonant X-ray scattering. If the incident photon energy matches the excitation energy of an atom or a molecule (commonly it is an inner shell excitation), the corresponding scattering is the resonant X-ray scattering (RIXS), which can be treated as a two-step processes, i.e., a photoabsorption process followed by a photoemission process. If the incident photon energy does not match the excitation energy of an atom or a molecule (generally the incident photon energy is much larger than the excitation energy), the corresponding scattering is the non-resonant X-ray scattering (NIXS), which is a one-step processes. Further on, the inelastic x-ray scattering can be classified into valence shell IXS (IXS for short), x-ray Raman scattering (XRS) and Compton scattering according to the final state of the sample, i.e. the valence shell excitation, the inner shell excitation and the ionization respectively.

Those different branches of the x-ray scattering differ from another according to the Hamiltonian describing the interaction of the electromagnetic field of the photon with the nonrelativistic electron system. This Hamiltonian, containing the radiation field, the electrons and the interaction terms, can be presented as [12]:

$$H = \sum_j \frac{1}{2m} [\mathbf{p}_j - (e/c)\mathbf{A}(\mathbf{r}_j)]^2 + \sum_{jj'} V(r_{jj'}) - \frac{e\hbar}{2mc} \sum_j \boldsymbol{\sigma}_j \cdot \nabla \times \mathbf{A}(\mathbf{r}_j) - \frac{e\hbar}{4m^2c^2} \sum_j \boldsymbol{\sigma}_j \cdot \mathbf{E}(\mathbf{r}_j) \times [\mathbf{p}_j - (e/c)\mathbf{A}(\mathbf{r}_j)] + \sum_{\mathbf{K}\lambda} \hbar\omega_{\mathbf{K}} [c^+(\mathbf{K}\lambda)c(\mathbf{K}\lambda) + 1/2] \quad (1)$$

$$= \left\{ \sum_j \frac{1}{2m} \mathbf{p}_j^2 + \sum_{jj'} V(r_{jj'}) + \frac{e\hbar}{4m^2c^2} \sum_j \boldsymbol{\sigma}_j \cdot (\nabla\phi \times \mathbf{p}_j) \right\} + \left\{ \frac{e^2}{2mc^2} \sum_j \mathbf{A}^2(\mathbf{r}_j) - \frac{e^2\hbar}{4m^2c^4} \sum_j \boldsymbol{\sigma}_j \cdot [\dot{\mathbf{A}}(\mathbf{r}_j) \times \mathbf{A}(\mathbf{r}_j)] \right\} - \left\{ \frac{e}{mc} \sum_j \mathbf{A}(\mathbf{r}_j) \cdot \mathbf{p}_j + \frac{e\hbar}{2mc} \sum_j \boldsymbol{\sigma}_j \cdot \nabla \times \mathbf{A}(\mathbf{r}_j) \right\} + \left\{ \sum_{\mathbf{K}\lambda} \hbar\omega_{\mathbf{K}} [c^+(\mathbf{K}\lambda)c(\mathbf{K}\lambda) + 1/2] \right\}. \quad (2)$$

\mathbf{p} is the momentum operator and $\mathbf{A}(\mathbf{r})$ the operator of the vector potential of the electromagnetic wave at the position \mathbf{r} of the electron. $\boldsymbol{\sigma}$ is the spin vector operator whose components are the well-known Pauli matrices, and $\mathbf{E}(\mathbf{r})$ is the operator of the electric field at the electron position \mathbf{r} . The summation j, j' is over all electrons of the scattering system, and the summation $\mathbf{K}\lambda$ over all modes of the photon field. The formula (2) can be derived from formula (1) via the gauge equation:

$$\mathbf{E} = -\nabla\phi - \frac{1}{c}\dot{\mathbf{A}}, \quad (3)$$

where ϕ is the Coulomb potential.

There are four parts in formula (2) with braces. The first part describes the electron system including the \mathbf{A} free part of the spin-orbit term and the ordinary spin-orbit coupling term for electrons, and the last part stands for the radiation field. The second part, which is quadratic in \mathbf{A} , delivers contributions to the scattering amplitude in a first-order perturbation treatment. Specifically, the first \mathbf{A}^2 term gives the Thomson charge scattering amplitude, which is the only interaction term in the EXS, IXS and XRS process for gaseous atoms or molecules, and the second term gives spin originated magnetic scattering amplitude, which can be seen for magnetic materials. The third part is linear in \mathbf{A} and contribute to the scattering amplitude only in a second-order perturbation treatment [12]. It interpret the RIXS process, which will not be discussed in detail in this review.

The EXS is the simplest process in x-ray scattering, without changing of the sample's state and photon's energy. However the momentum of the photon can be changed after the collision, which makes it possible

to obtain the electron density distribution for the sample by analyze the scattering intensities at different scattering angles. The relation between the differential cross section and the electronic structure of an atom or molecule is [12, 13]:

$$\zeta(\mathbf{q}) = \frac{1}{r_0^2} \frac{1}{|\boldsymbol{\epsilon}_i \cdot \boldsymbol{\epsilon}_f^*|^2} \left(\frac{d\sigma}{d\Omega} \right)_\gamma \quad (4)$$

$$= \left| \langle \Psi_0 | \sum_{j=1}^N \exp(i\mathbf{q} \cdot \mathbf{r}_j) | \Psi_0 \rangle \right|^2. \quad (5)$$

Here $\zeta(\mathbf{q}, \omega_n)$ presents the electronic structure of an atom or molecule as is presented in formula (5), and is called the squared form factor (SFF). \mathbf{q} is the momentum transfer, varying with the scattering angle. The SFFs of molecular hydrogen verse squared momentum transfer is shown in Fig. 1 [14].

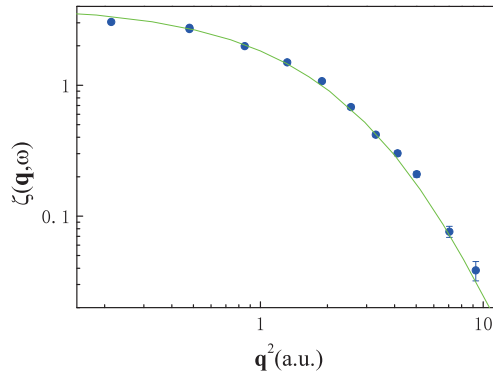


FIG. 1: (Color online) (Color online) Elastic squared form factor $\zeta(\mathbf{q}, \omega)$ of molecular hydrogen. Solid blue circle: elastic x-ray scattering results. Green solid line: the theoretical results of Bentley et al. [15] using the Davidson-Jones (DJ) wave function.

In fact, the photon is a very special probe for detecting the electronic structure of ground state compared with any other charged particles. For collision between charged particle and an atom or molecule, such as electron scattering with molecular hydrogen, the interaction between the colliding electron and the molecule can be presented in the potential term as:

$$V = - \sum_{j=1}^2 \frac{1}{|\mathbf{r} - \mathbf{r}_j|} + \frac{1}{|\mathbf{r} - \mathbf{R}_a|} + \frac{1}{|\mathbf{r} - \mathbf{R}_b|}, \quad (6)$$

where \mathbf{R}_a and \mathbf{R}_b are the position vectors of the nuclei, and \mathbf{r} is the position operator of the incident electron. The last two terms in formula (6) describe the interaction between the incident electron and the nuclei, giving additional two parts to the pure electron-electron scattering in differential cross section [14]:

$$\begin{aligned} \left(\frac{d\sigma}{d\Omega} \right)_e &= 4q^{-4} \left| \langle \Psi_0 | \exp(i\mathbf{q} \cdot \mathbf{R}_a) + \exp(i\mathbf{q} \cdot \mathbf{R}_b) - \sum_{j=1}^2 \exp(i\mathbf{q} \cdot \mathbf{r}_j) | \Psi_0 \rangle \right|^2 \\ &= \frac{1}{\pi} q^{-4} \int \int \sin \theta d\theta d\varphi \left| \int \Psi_0^*(\mathbf{R}) \times [2 \cos(\mathbf{q} \cdot \mathbf{R}/2) - \varepsilon_0(\mathbf{q}; \mathbf{R}, \theta, \varphi)] \Psi_0(\mathbf{R}) d\mathbf{R} \right|^2. \end{aligned} \quad (7)$$

$\varepsilon_0(\mathbf{q}; \mathbf{R}, \theta, \varphi)$ and $\cos(\mathbf{q} \cdot \mathbf{R}/2)$ stand for the electron-electron scattering term and the pure nuclei scattering term. The interference term arising from the electron-electron and electron-nuclei scattering prevent one from extracting the electronic structure information by the experimental elastic differential cross sections by high-energy electron scattering.

The valence shell IXS shares the same theoretical presentation with the EXS. The SFF of the IXS can be written as [12, 13]:

$$\zeta(\mathbf{q}, \omega_n) = \frac{1}{r_0^2} \frac{\omega_i}{\omega_f} \frac{1}{|\boldsymbol{\epsilon}_i \cdot \boldsymbol{\epsilon}_f^*|^2} \left(\frac{d\sigma}{d\Omega} \right)_\gamma \quad (8)$$

$$= \left| \langle \Psi_n | \sum_{j=1}^N \exp(i\mathbf{q} \cdot \mathbf{r}_j) | \Psi_0 \rangle \right|^2 \quad (9)$$

$$= \int d\mathbf{p} \Psi_n^*(\mathbf{p}) \Psi_0(\mathbf{p} + \mathbf{q}), \quad (10)$$

in which ω_i and ω_f are the energies of the incident and scattered photons. Obviously the factor ω_i/ω_f is eliminated in the EXS. The SFFs of some excitations for argon is presented in Fig. 2 [6]. Good agreement is observed between the IXS and theoretical calculation. Unlike the EXS, the maximum of SFFs of IXS will never lie in extremely small momentum transfer because of the orthogonality of the wave functions of different electronic states in momentum space (see formula (10)).

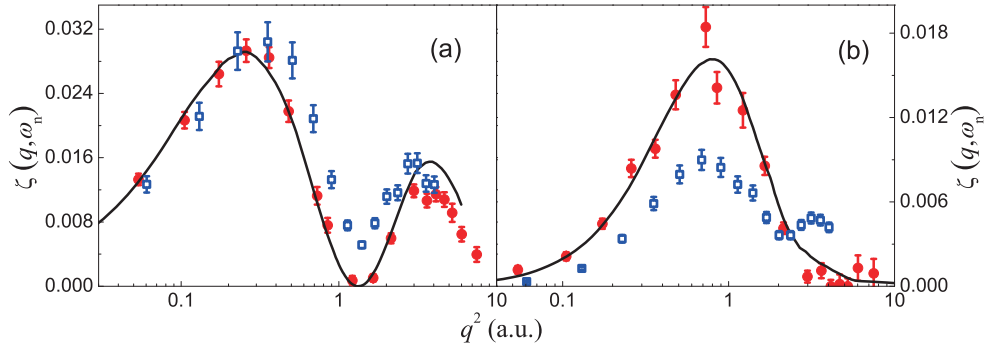


FIG. 2: (Color online) (a) The squared form factors $\zeta(\mathbf{q}, \omega_n)$ for the electric dipolar excitations to $3p^5 4s'[1/2]_1$, and (b) the electric monopolar excitations to $3p^5 4p'[1/2]_0$. Solid red circle: the present IXS results; hollow blue square: the 2500 eV EELS results by Zhu *et al.* [16]; solid black line: RPAE calculations by Amusia *et al.* [17].

Similar with the EXS, the results of high-energy EELS is available for comparison. It can be seen from Fig. 3 that they match with the SFFs neither of the IXS nor of the calculation. The SFFs of the EELS can not reach 0 at the minimum for dipole allowed excitation to $3p^5 4s'[1/2]_1$, and is much smaller around the first maximum for monopolar excitation to $3p^5 4p'[1/2]_0$. Moreover, a second maximum is observed for the monopolar excitation only by the electron scattering. However, situation is a little different in valence shell excitation from the elastic scattering. That is for valence shell excitation the high-energy electron scattering is free from the nuclear term because of the orthogonality of the electronic wavefunctions of the ground state and excited state. These deviations shown in Fig. 2 indicate the failure of the first Born approximation and come from higher order Born terms. The main part is the intramolecular scattering described by the second order Born term.

In Compton scattering, obtaining the projection of electronic momentum density along z direction is the goal of the experiment. By utilizing the impulse approximation, the differential cross section can be presented as:

$$\frac{d\sigma}{d\Omega d\omega} = r_0^2 |\boldsymbol{\epsilon}_i \cdot \boldsymbol{\epsilon}_f^*|^2 \frac{\omega_i}{\omega_f} \frac{1}{k} J(p_z), \quad (11)$$

where $J(p_z)$ is the so-called Compton profile and describes the electron momentum distribution of ground state in z direction. k is the modulus of the photon momentum transfer and $p_z = \frac{k}{2} - \frac{\omega_i - \omega_f}{k}$.

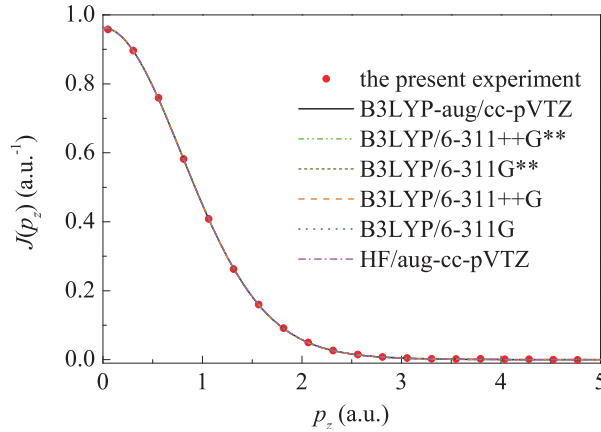


FIG. 3: (Color online) The Compton profile for molecular hydrogen. The calculations are convolved with the experimental resolution.

Fig. 3 shows the Compton profile of molecular hydrogen, and the experimental result matches the theoretical calculations excellently. The main progress of the Compton profile measurements is the dramatic improvement of the accuracy, i.e., a typical experimental uncertainty of 0.1% is achieved at $p_z = 0$ [18, 19].

In this review, the elastic x-ray scattering, valence shell inelastic x-ray scattering and Compton scattering are summarized. These different kinds of measurements can reflect the structures of atoms or molecules in different aspects. Compared with the electron, the x-ray is a more electronic “clean” probe for the atomic and molecular physics. As the sub-field of application of the IXS is just being open, more investigations on a various of atoms and molecules are likely to be seen.

Acknowledgments

The measurements of the EXS and the IXS were carried out on the Taiwan beamline of Spring-8, approved by the National Synchrotron Radiation Research Center, Taiwan, Republic of China (No. 2010-3-073-4 and 2012-2-013-1) and the Japan Synchrotron Radiation Research Institute (Proposal No. 2011B4256 and 2012A4256), and the measurement of the Compton scattering was carried out on the 15U1 beamline of the Shanghai Synchrotron Radiation Facility (SSRF), approved by the SSRF, Shanghai, P. R. China (No. 11sr0210, 12sr0009 and 13SRBL15U15487). These works are supported by the National Natural Science Foundation of China (Grant No. U1332204, 11274291 and 11104309), National Basic Research Program of China (Grant No. 2010CB923301). This work was partly supported by the JSPS-NRF-NSFC A3 Foresight Program in the field of Plasma Physics (NSFC: No. 11261140328, NRF: No.2012K2A26000443).

-
- [1] I. Bray, D. V. Fursa, A. S. Kadyrov, A. T. Stelbovics, A. S. Kheifets, and A. M. Mukhamedzhanov, *Phys. Rep.* **520**, 135 (2012).
 - [2] M. J. Brunger and S. J. Buckman, *Phys. Rep.* **357**, 215 (2002).
 - [3] M. Inokuti, *Rev. Mod. Phys.* **43**, 297 (1971).
 - [4] A. P. Hitchcock and K. T. Leung, *J. Electron Spectrosc. Relat. Phenom.* **123**, 103 (2002).
 - [5] L. F. Zhu, W. Q. Xu, K. Yang, Z. Jiang, X. Kang, B. P. Xie, D. L. Feng, N. Hiraoka, and K. D. Tsuei, *Phys. Rev. A* **85**, 030501(R) (2012).
 - [6] X. Kang, K. Yang, Y. W. Liu, W. Q. X. N. Hiraoka, K. D. Tsuei, P. F. Zhang, and L. F. Zhu, *Phys. Rev. A* **86**, 022509 (2012).

- [7] J. A. Bradley, G. T. Seidler, G. Cooper, M. Vos, A. P. Hitchcock, A. P. Sorini, C. Schlimmer, and K. P. Nagle, *Phys. Rev. Lett.* **105**, 053202 (2010).
- [8] B. P. Xie, L. F. Zhu, K. Yang, B. Zhou, N. Hiraoka, Y. Q. Cai, Y. Yao, C. Q. Wu, E. L. Wang, and D. L. Feng, *Phys. Rev. A* **82**, 032501 (2010).
- [9] L. F. Zhu, L. S. Wang, B. P. Xie, K. Yang, N. Hiraoka, Y. Q. Cai, and D. L. Feng, *J. Phys. B: At. Mol. Opt. Phys.* **44**, 025203 (2011).
- [10] J. M. W. DuMond, *Phys. Rev.* **33**, 643 (1929).
- [11] P. Nozieres and D. Pines, *Phys. Rev.* **113**, 1254 (1959).
- [12] W. Schülke, *Electron Dynamics by Inelastic X-Ray Scattering* (Oxford Science Publications, Oxford, 2007).
- [13] P. Eisenberger and P. M. Platzman, *Phys. Rev. A* **2**, 415 (1970).
- [14] Y. W. Liu, X. X. Mei, X. Kang, K. Yang, W. Q. Xu, Y. G. Peng, N. Hiraoka, K. D. Tsuei, P. F. Zhang, and L. F. Zhu, *Phys. Rev. A* **89**, 014502 (2014).
- [15] J. J. Bentley and R. F. Stewart, *J. Comput. Phys.* **11**, 127 (1973).
- [16] L. F. Zhu, H. D. Cheng, Z. S. Yuan, X. J. Liu, J. M. Sun, and K. Z. Xu, *Phys. Rev. A* **73**, 042703 (2006).
- [17] Z. Chen, A. Z. Msezane, and M. Y. Amusia, *Phys. Rev. A* **60**, 5115 (1999).
- [18] K. Kobayashi, M. Itou, T. Hosoya, N. Tsuji, Y. Sakurai, and H. Sakurai, *J. Phys. B: At. Mol. Opt. Phys.* **44**, 115102 (2011).
- [19] H. Sakurai, H. Ota, N. Tsuji, M. Itou, and Y. Sakurai, *J. Phys. B: At. Mol. Opt. Phys.* **44**, 065001 (2011).

Laser-produced multi-charged heavy ions as efficient soft x-ray sources

Takeshi Higashiguchi¹, Yuhei Suzuki¹, Masato Kawasaki¹, Hayato Ohashi², Nobuyuki Nakamura³, Chihiro Suzuki⁴, Hiroyuki A. Sakaue⁴, Daiji Kato⁴, Izumi Murakami⁴, Fumihiro Koike⁵, Shinsuke Fujioka⁶, Hiroaki Nishimura⁶, Atsushi Sunahara⁷, Bowen Li⁸, Pdraig Dunne⁹, and Gerry O'Sullivan⁹

¹Department of Advanced Interdisciplinary Sciences and Center for Optical Research and Education (CORE), Utsunomiya University, Utsunomiya, Tochigi 321-8585, Japan

²Graduate School of Science and Engineering for Research, University of Toyama, Toyama, Toyama 930-8555, Japan

³Institute for Laser Science, The University of Electro-Communications, Chofugaoka 1-5-1, Chofu, Tokyo 182-8585, Japan

⁴National Institute for Fusion Science, Toki, Gifu 509-5292, Japan

⁵Faculty of Science and Technology, Sophia University, Chiyoda, Tokyo 102-8554, Japan

⁶Institute of Laser Engineering, Osaka University, 2-6 Yamada-oka, Suita, Osaka 565-0871, Japan

⁷Institute for Laser Technology, 2-6 Yamada-oka, Suita, Osaka 565-0871, Japan

⁸School of Nuclear Science and Technology, Lanzhou University, Lanzhou, 730000, China

⁹School of Physics, University College Dublin, Belfield, Dublin 4, Ireland

We demonstrate EUV and soft x-ray sources in the 2 to 7 nm spectral region related to the beyond EUV (BEUV) question at 6.x nm and a water window source based on laser-produced high-Z plasmas. Resonance emission from multiply charged ions merges to produce intense unresolved transition arrays (UTAs), extending below the carbon K edge (4.37 nm). An outline of a microscope design for single-shot live cell imaging is proposed based on a high-Z plasma UTA source, coupled to x-ray optics. We will discuss the progress and Z-scaling of UTA emission spectra to achieve lab-scale table-top, efficient, high-brightness high-Z plasma EUV-soft x-ray sources for in vivo bio-imaging applications.

Keywords: high-Z, unresolved transition array (UTA), EUV, soft x-ray, water window

I. Introduction

In the past decade, the development of plasma light sources has progressed rapidly, especially for lithography in the extreme ultraviolet (EUV) region predicated on the development of multilayer mirrors (MLMs) with good reflectivity at specific wavelengths. A xenon (Xe) plasma was the candidate first proposed for 11-nm EUV lithography, but development was not pursued because of the high toxicity of the beryllium/molybdenum MLMs used at this wavelength [1]. While Xe

plasmas were also initially studied for 13.5-nm lithography with molybdenum/silicon MLMs because of the low debris associated with gaseous fuels, the conversion efficiency was low. A tin laser-produced plasma (LPP) provides the optimum source for 13.5-nm EUV lithography from the point of view of conversion efficiency [2]. Source development at a wavelength of 6.x-nm is regarded as the next step in EUV lithography, so-called Beyond EUV (BEUV), for more highly integrated electronic devices. Gadolinium (Gd) plasmas are the main focus of significant efforts as candidates for a BEUV light source [3]. The 13.5-nm and 6.x-nm light sources exploit the advantage that $4p^6 4d^N - 4p^6 4d^{N-1} 4f + 4p^5 4d^{N+1}$ ($n = 4 - n = 4$, $\Delta n = 0$) unresolved transition arrays (UTAs) in several charge states appear at almost same wavelength [4] in spectra from LPPs of these elements, while transitions of type $4d^{10} 4f^M - 4d^9 4f^{M+1}$ also make contributions to the 6.x nm region. In this regard, it follows that $n = 4 - n = 4$ UTAs from LPPs of other elements could provide light sources at other wavelengths for other applications such as x-ray microscopy in the water window of 2.3–4.4 nm [5] and the carbon window of 4.4–5.0nm [6]. This wavelength range also has attracted attention for x-ray absorption fine structure (XAFS) measurements due to carbon absorption in biomolecules. While a laboratory scale krypton-LPP source is already used as a broad-band excitation source for XAFS experiments [7], its emission has complicated structure. The simpler structure of a LPP source emitting $n = 4 - n = 4$ UTAs is more appropriate for XAFS measurements. Systematic calculations for UTA positions were performed for elements with atomic number $Z = 49-92$ that enabled the peak wavelength of the $4d-4f$ and $4p-4d$ component transitions of the $n = 4 - n = 4$ UTAs to be estimated [8]. There is, however, a discrepancy between experimental and calculated results for high- Z elements due to the complexity of configuration interaction effects [4,9] and the tendency for the $4p-4d$ contribution to the actual emission to be overestimated in calculations based solely on line strength distributions. Previous studies were performed with previous-generation ns-lasers that produce optically thicker plasmas than with a ps-laser [10]. It is known that optically thick plasmas can strongly self-absorb resonance line emission [11]. Optically thin plasmas thus provide more efficient light sources. Therefore, systematic LPP studies with up-to-date intense ps-lasers are needed to determine available light source wavelengths for future applications.

In this paper, we report the efficient water window source by strong UTA band emission in laser-produced high- Z plasmas. Our proposed procedure for producing the water window emission is expected to be efficient and scalable in output yield. We have initiated a number of experiments to explore how this emission may be optimized in practice.

II. Characteristics of the Gd plasmas for BEUV source applications

We characterize extreme ultraviolet (EUV) emission from mid-infrared (mid-IR) laser-produced plasmas (LPPs) of the rare-earth element Gd. The energy conversion efficiency (CE) and the spectral purity in the mid-IR LPPs at $\lambda_L = 10.6 \mu\text{m}$ were higher than for solid-state LPPs at $\lambda_L = 1.06 \mu\text{m}$, because the plasma produced is optically thin due to the lower critical density,

resulting in a CE of 0.7%. The peak wavelength remained fixed at 6.76 nm for all laser intensities studied. Plasma parameters at a mid-IR laser intensity of 1.3×10^{11} W/cm² was also evaluated by use of the hydrodynamic simulation code to produce the EUV emission at 6.76 nm.

Figure 1(a) shows time-integrated EUV emission spectra from the Nd:YAG LPPs at different laser intensities ranging from 9.7×10^{11} to 6.6×10^{12} W/cm². The peak wavelength shifts from 6.7 to 6.8 nm, and is mainly due to $n = 4 - n = 4$ ($\Delta n = 0$) transitions in ions with an open $4f$ or $4d$ outermost subshell. The sharp peak at 6.65 nm and the dip structure below 6.59 nm first appear at a laser intensity of 2.4×10^{11} W/cm². Emission at wavelengths less than 6 nm, increases with increasing laser intensity and according to numerical evaluation, lines in the $\lambda = 2.5\text{--}6$ nm ($h\nu = 207\text{--}496$ eV) spectral region originate from Gd ionic charge states between Gd¹⁹⁺ and Gd²⁷⁺, and arise from $n = 4 - n = 5$ ($\Delta n = 1$) transitions.

In the case of CO₂ LPPs, on the other hand, the main spectral features near 6.7 nm are narrower than for Nd:YAG laser irradiation, as shown in Fig. 1(b). The CO₂ laser intensity was varied from 5.5×10^{10} to 1.2×10^{11} W/cm². The spectral structure is dramatically different to that from the Nd:YAG LPPs. The peak wavelength of 6.76 nm remains constant with increasing laser intensity. Moreover the intensity of the peak at 6.76 nm increases more rapidly with laser intensity than emission in the ranges $\lambda = 3\text{--}6.6$ nm and $\lambda = 6.8\text{--}12$ nm. Under the optically thin plasma conditions imposed by the CO₂ LPP, this peak, which is mainly due to the $4d^{10} \ ^1S_0\text{--}4d^9 4f^1 \ P_1$ transition of Pd-like Gd¹⁸⁺ overlapped with $^2F\text{--}^2D$ lines of Ag-like Gd¹⁷⁺, known to lie near 6.76 nm shows that these ions are indeed present in the plasma. Somewhat similar structure has been also observed in a discharge-produced plasma, which like the CO₂ LPP has low density and is optically thin. It is noted that the peak wavelength of 6.76 nm was constant with high spectral and energy conversion efficiencies in optically thin mid-IR CO₂ laser-produced Gd plasmas. The maximum CE was observed to be 0.7% [3].

In order to infer the laser parameters which maximize 6.x-nm Gd-LPP emission, direct comparison between emission from a Gd-LPP and that of Gd ions from well-defined charge states is necessary, as the charge state dependence of emission at 6.x nm is defined by the electron temperature. We present a study of the charge-state-defined emission spectra to explain the laser power density dependence of the Gd-LPP spectra and to evaluate the charge states contributing to the 6.x-nm emission.

The profile of the intense emission at 6.x nm becomes broader and its peak wavelength shifts to longer wavelength with increasing laser power density, as shown in Fig. 2(a). However the range of wavelengths involved is quite small and the peak lies between 6.7 and 6.8 nm over this entire range of power densities. The emission from each of these peak wavelengths within a 0.6% bandwidth (BW) becomes more intense with increasing laser flux. This behavior causes difficulty in fixing the precise wavelength of 6.x nm and optimization of the spectral efficiency while simultaneously maximizing the CE. The spectral efficiency denotes the ratio of the in-band energy at

6.70 nm within a 0.6% BW to that in the spectral range from 3 nm to 12 nm. An increase in laser power density raises the electron temperature which, in turn, implies an increase of both the highest charge state and the abundance of higher charge states. This change in the ion population must cause the observed shift of the peak wavelength for Gd-LPPs. Up to now, there was no direct experimental evidence that changes in emitting ion populations were responsible for this shift.

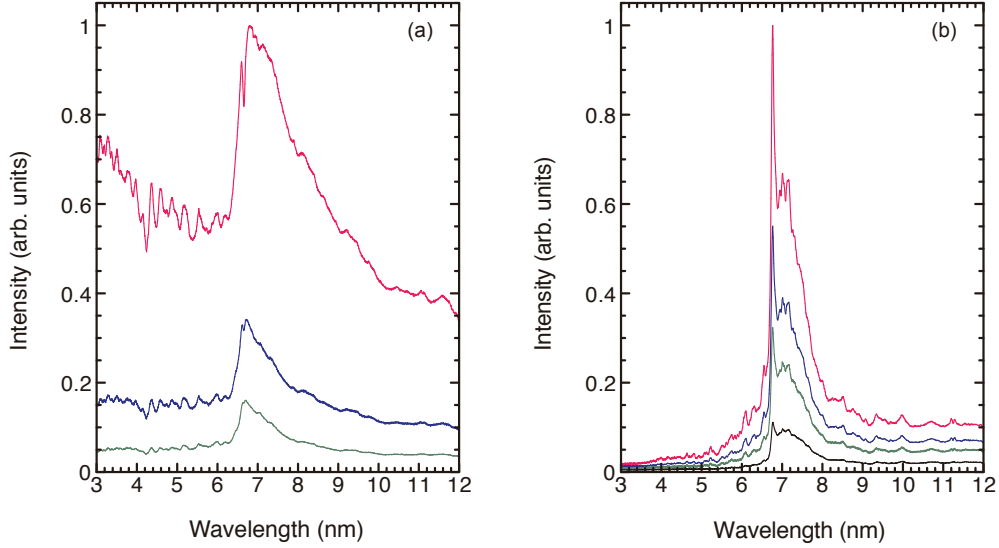


Fig. 1. (a) Time-integrated EUV emission spectra from the Nd:YAG LPPs at different laser intensities of 9.7×10^{11} , 2.2×10^{12} , and 6.6×10^{12} W/cm², respectively. The peak wavelength shifts from 6.7 to 6.8 nm with increasing the laser intensity. (b) Time-integrated EUV emission spectra from the CO₂ LPPs at different laser intensities of 5.5×10^{10} , 8×10^{10} , 9.8×10^{10} , and 1.3×10^{11} W/cm², respectively. The peak wavelength of 6.76 nm remains constant with increasing the laser intensity.

To verify the above explanation, charge-defined emission spectra were measured with the EBITs for different highest charge states. EUV emission spectra from EBIT experiments are shown in Fig. 2(b) and calculated gA values of $4d-4f$ transitions for corresponding highest charge states are shown in Fig. 2(c) to compare the charge state dependence of the emission near $6.x$ nm. The gA values are the transition probabilities from excited states multiplied by their statistical weights and thus are proportional to the emission intensities of the transitions. Note that the EBIT spectra include a subset of all possible radiative transitions that are predominantly resonant transitions to the ground state. For Pd-like Gd¹⁸⁺, only one strong line is predicted corresponding to the $4d^{10} \ ^1S_0-4d^9 4f^1 P_1$ at 6.7636 nm and this is clearly seen in the spectrum. In the absence of CI, according to the unresolved transition array (UTA) model, the position of the intensity-weighted peak of the $4d^N-4d^{N-1}4f$ array depends directly on the occupancy of the $4d$ subshell, N , and the Slater-Condon $F^k(4d,4f)$ and

$G^k(4d,4f)$ parameters. In the present case, the values of F^k and G^k change little with ionization stage and, therefore, the position of the array moves to lower energy with decreasing N . The presence of CI causes this shift to be reduced but nevertheless the overall trend is to move to longer wavelength with increasing ionization stage. The dominant emissions around 7 nm in the EBIT spectra indeed move to longer wavelengths with an increase of the highest charge state. The EBIT can thus generate charge defined-emission spectra, which are essential both for analysis of plasma emission spectra and the benchmarking of theoretical calculations [12].

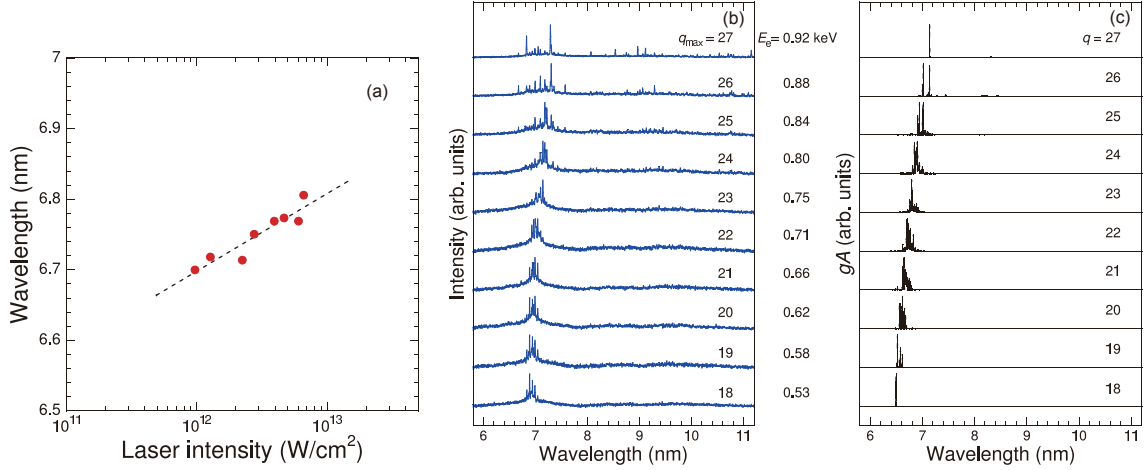


Fig. 2. (a) The wavelength of emission peaks near $6.x$ nm as a function of the Nd:YAG laser power density. The dotted line is a fitted curve. (b) EUV emission spectra of Gd ions with electron beam energies (E_e) of 0.43–0.92 keV. In the case of $E_e = 0.43$ keV, the compact EBIT with lower resolution was employed while the Tokyo-EBIT was used in other cases. (c) Calculated gA values for $4d-4f$ transitions of the corresponding highest charge states (q_{\max}) from Fig. 2(b). The ground configuration of Gd^{18+} is $[\text{Kr}]4d^{10}$.

III. Quasi-Moseley's law for UTA emission

In this section, we show that the strong resonance UTAs of Nd:YAG LPPs for elements with $Z = 50-83$ obey a quasi-Moseley's law. A 150-ps Nd:YAG laser with a maximum energy of 250 mJ at $\lambda_L = 1.064 \mu\text{m}$ and an 8-ns Nd:YAG laser giving 400 mJ at $\lambda_L = 1.064 \mu\text{m}$ were employed to provide the desired variation of laser intensity. The laser beam was incident normally onto planar high- Z metal targets *in vacuo*. The expected focal spot size, produced by an anti-reflection coated plano-convex BK7 lens with a focal length of 10 cm, had a full width at half-maximum (FWHM) of approximately $50 \mu\text{m}$. The laser was operated in single shot mode and the target surface was translated to provide a fresh surface after each laser shot. A flat-field grazing incidence spectrometer (GIS) with an unequally ruled 2400 grooves/mm grating was placed at 45° with respect to the axis of the incident laser. Time-integrated spectra were recorded by a Peltier-cooled back-illuminated

charge-coupled device (CCD) camera and were corrected by its quantum efficiency. The typical resolution was better than 0.005 nm (FWHM). The Large Helical Device (LHD) is one of the largest devices for magnetically confined fusion research and is described in detail elsewhere.¹⁶ The LHD plasmas were produced by the injection of a small amount of target elements into the background hydrogen plasma. The plasma density is about 10^{13} cm^{-3} , much lower than that in a LPP, and guarantees an optically thin condition. Emission spectra were recorded by a 2-m grazing incidence Schwob-Fraenkel spectrometer with a 600 grooves/mm grating. The exposure time of the detector was set at 0.2 s and the spectral resolution is about 0.01 nm (FWHM).

Figures 3(a)–3(k) show LPP emission spectra from high-Z metal targets. The main UTA peak at 8.17 nm in the case of Nd clearly shifts to shorter wavelength with increasing atomic number, 3.95 nm in the case of Bi. This movement indicates the availability of a wide wavelength range for a LPP light source. While the main UTA peaks correspond to $4p^6 4d^N - 4p^6 4d^{N-1} 4f$ transitions, the $4p^6 4d^N - 4p^5 4d^{N+1}$ UTAs were also observed around them, at 4 nm for the Pt-LPP, in the case of ps-LPPs. The difference in the broad emission features at shorter wavelengths is caused by the different charge state distribution in LPPs for ps and ns excitation and will be discussed later. Optically thinner LHD plasma spectra are shown in Figs. 3(l)–3(q). It should be noted that the electron temperatures of LHD plasma were relatively low, $\leq 1 \text{ keV}$, but higher than in ps-LPPs. As a result, we have not observed significant emission of the type $4f^N - 4f^{N-1} 5l$ from stages with open $4f$ valence subshells in LHD spectra. Comparing LPP and LHD spectra, the UTA widths in LHD spectra are relatively narrower than in LPPs especially for lighter elements. This arises as a result of a number of factors: the increased contributions from ions with an outermost $4d^{10} 4f^N$ configuration from transitions of the type $4d^{10} 4f^N - 4d^9 4f^{N+1}$ in LPP spectra and the differences in opacity that reduce the intensity of the strongest lines and the increased contribution from satellite emission. In addition, earlier research demonstrated that if the majority of radiation originates from open $4f$ subshell ions, whose complexity inhibits the emission of strong isolated lines, then no strong isolated lines are expected to appear throughout the EUV emission, which is clearly seen for the LPP spectra in Fig. 3. Moreover, self-absorption effects are clearly observed in the case of ns-LPP for Nd due to optical thickness. Although the $n = 4 - n = 4$ UTA transition peak was observed at 8.05 nm in the LHD spectrum, the strongest $4d - 4f$ transitions essentially disappear in the ns-LPP owing to self-absorption. Because of their large transition probabilities, resonant lines that are strong in emission also strongly absorb in underdense ($n_e < n_c$, where n_c is the critical electron density) or optically thick plasma conditions. An optically thinner plasma reduces the self-absorption effects and increases the spectral efficiency of $n = 4 - n = 4$ UTA emissions.

Figure 4 shows the atomic number dependence of the observed peak wavelength of $n = 4 - n = 4$ UTAs. The solid line is an approximated curve for ps-LPPs with a power-law scaling of the peak wavelength given by $\lambda = aR_*^{-1}(Z - s)^b$ in nm where $a = 21.86 \pm 12.09$, $b = 1.52 \pm 0.12$, $s = 23.23 \pm 2.87$ is the screening constant while Slater's rule gives $s = 36 - 39.15$ for $4d$ electrons [13], and R_* is

the Rydberg constant. This empirical law is surprisingly similar to Moseley's law where $a = 4/3$, $b = 2$ and $s = 1$ were used to give the transition wavelength of the $K\alpha$ -line of characteristic x-rays. It is noted that the Moseley's law derived from the Bohr model gives $\lambda = 0$ for $\Delta n = 0$ transitions in terms of the energy difference. It can however be fitted as a quasi-Moseley's law because there are energy differences between $\Delta n = 0$ levels due to different angular momentum quantum numbers.

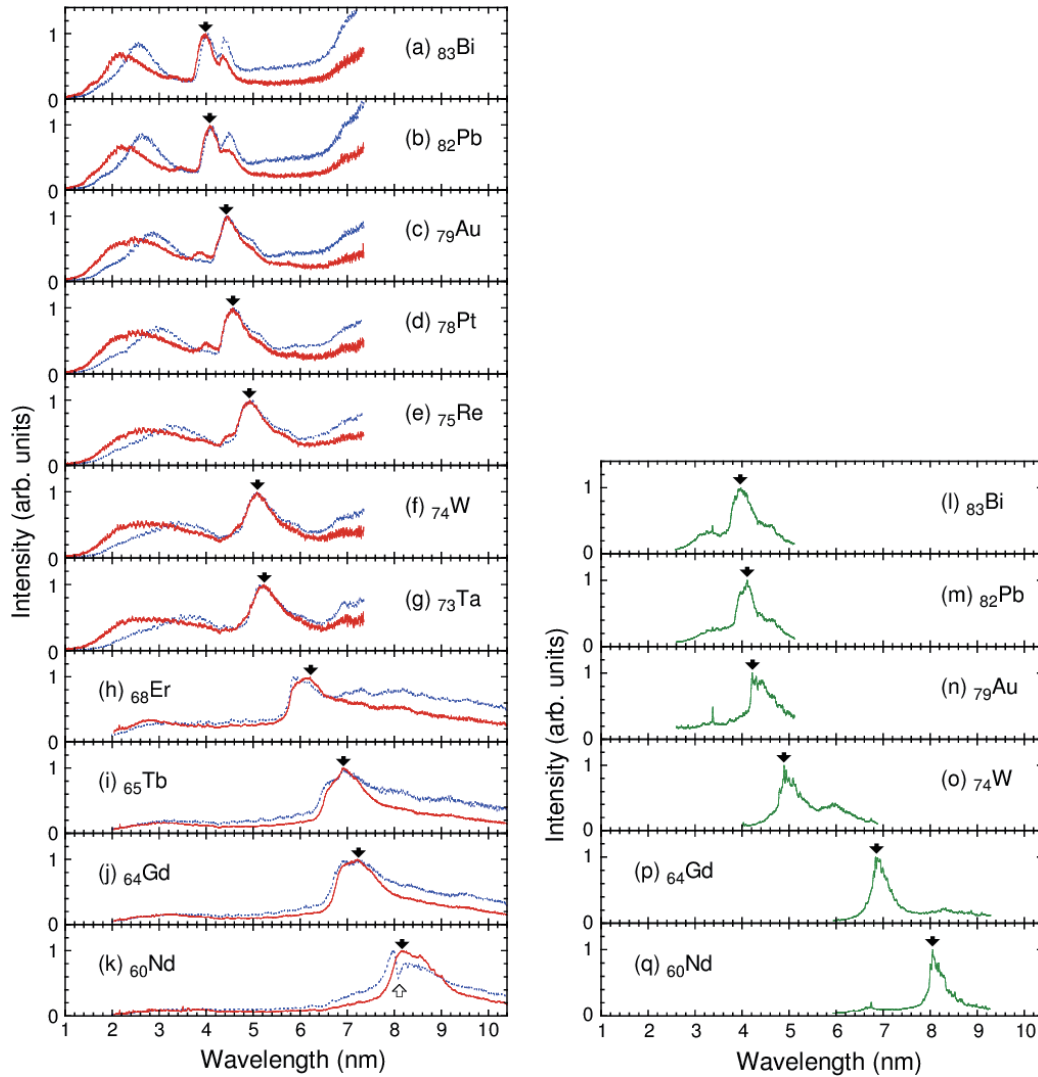


Fig. 3. Time-integrated EUV emission spectra of the Nd:YAG LPPs for (a) ^{83}Bi , (b) ^{82}Pb , (c) ^{79}Au , (d) ^{78}Pt , (e) ^{75}Re , (f) ^{74}W , (g) ^{73}Ta , (h) ^{68}Er , (i) ^{65}Tb , (j) ^{64}Gd and (k) ^{60}Nd targets with 150-ps laser (red, solid line) and 8-ns laser (blue, dotted line), respectively. Typical laser power densities were $2.5 \times 10^{14} \text{ W/cm}^2$ for ps-laser illumination and $5.6 \times 10^{12} \text{ W/cm}^2$ for ns-laser irradiation. The measured LHD spectra (green, solid) for (l) Bi, (m) Pb, (n) Au, (o) W, (p) Gd and (q) Nd targets, respectively. An emission line at 3.4 nm is from impurity carbon ions. Intensities were normalized at each maximum of the $n = 4 - n = 4$ UTAs. Solid arrows indicate peak position of $n = 4 - n = 4$ UTAs of ps-LPP and LHD spectra. An open arrow indicates structure due to self-absorption.

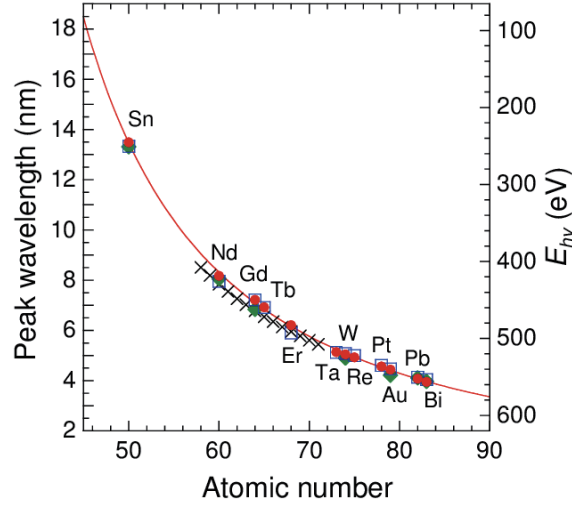


Fig. 4. Atomic number dependence of the peak wavelength of $n = 4-n = 4$ UTAs in ps-LPP (red, circles), ns-LPP (blue, squares) and LHD (green, diamonds) spectra. Calculated peak wavelengths with GRASP [14] are also shown (black, crosses). Sn spectra are not shown in Fig. 3. The solid line is an approximated curve for $n = 4-n = 4$ UTAs in ps-LPPs with a power-law scaling.

We propose here a pathway to produce feasible laboratory-scale high-Z LPP sources for a wide range of applications. For efficient UTA emission, plasmas of higher-Z elements need high electron temperatures to produce higher charge state ions contributing to the $4p^6 4d^N - 4p^6 4d^{N-1} 4f$ UTAs. The electron temperature, T_e , rises with increasing laser intensity as $T_e \propto (I_L \lambda_L^2)^{0.4}$, where I_L and λ_L are the laser intensity and wavelength, respectively [3,15]. On the other hand, an optically thin plasma has a low electron density, n_e , which decreases with increasing λ_L as $n_e \propto \lambda_L^{-2}$. In terms of these features, use of a longer laser wavelength is necessary to generate the brightest LPP, such as a CO₂ laser operating at 10.6 μm due to the low critical density of $1 \times 10^{19} \text{ cm}^{-3}$ attainable with a pulse duration sufficiently short to give a laser intensity of the order of 10^{13} W/cm^2 but sufficiently long to permit excitation to the appropriate ionization stages, i.e. $\sim 1 \text{ ns}$ [16]. Moreover, we can also obtain longer wavelengths, $> 10.6 \mu\text{m}$, with a Raman conversion system.

IV. Water window soft x-ray source by high-Z plasmas

Figures 5(a)–5(c) show time-integrated spectra from Au, Pb, and Bi plasmas at a laser intensity of $1 \times 10^{14} \text{ W/cm}^2$ with a 150-ps pulse duration. Time-integrated EUV spectra between 1 and 6 nm from each element display strong broadband emission near 4 nm, which is mainly due to $n = 4-n = 4$ transitions from ions with an open $4f$ or $4d$ outermost subshell, together with broadband emission around 2–4 nm due to $n = 4-n = 5$ transitions from multi-charged state ions with an outermost $4f$ subshell. The latter merge to form a structured feature from which the contributing ion stages may be readily inferred. The intensity of the $n = 4-n = 4$ UTA emission is higher than that of the $n = 4-n = 5$ emission. The atomic number spectral dependence is summarized in Fig. 5(d). The predicted photon energy of each

experimental peak wavelength was shifted to higher photon energy with increasing atomic number. Neither the emission spectra nor the plasma electron temperatures, however, have been optimized, as shown below. The emission intensity of the $n = 4 - n = 5$ transitions, however, was compared with that of the $n = 4 - n = 4$ UTAs.

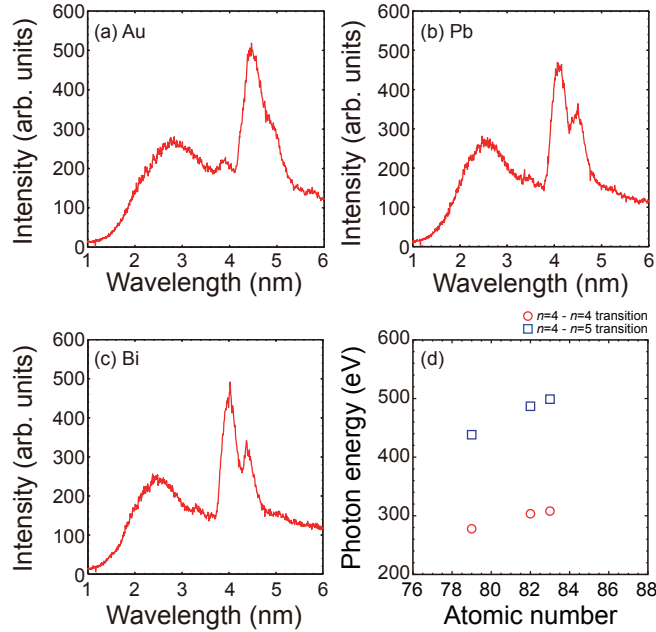


Fig. 5. Time-integrated spectra from the picosecond-laser-produced high- Z plasmas by use of Au (a), Pb (b), and Bi (c), and the atomic number dependence on the photon energies of peak emission of the $n = 4 - n = 4$ transition (circles) and the $n = 4 - n = 5$ transition (rectangles) [17].

We compare the results of calculation for some experimental temperatures with the experimental spectrum, as shown in Fig. 6(a). Four regions corresponding to emission peaks are identified. Note that this spectrum is integrated both spatially and temporally over the duration of the laser pulse. The emission in region “1” results primarily from $4f-5g$ transitions in ions with an open $4f$ subshell, i.e., stages lower than Bi^{35+} . The emission in regions “2” and “3” comes from $4p-4d$ and $4d-4f$ transitions in ions with an open $4d$ subshell ($\text{Bi}^{36+} - \text{Bi}^{45+}$), and calculations show that the higher energy feature results from the more highly ionized species ($> \text{Bi}^{42+}$). The emission in region “4” is again associated mainly with $4d-4f$ emission from lower stages with an open $4f$ outermost subshell. Thus the bulk of the emission, especially from regions “1” and “4”, is associated with the recombining phase of the expanding plasma plume. In this figure we show for comparison spectra calculated for steady state electron temperatures of 180 and 700 eV, while the higher temperatures are required to generate the emission in region “2”, the calculations verify that both the longer and shorter wavelength features are consistent with much lower plasma temperatures.

In Fig. 6(b) calculated spectra at different electron temperatures higher than 900 eV are presented. Our calculations show that high- Z plasmas, at an electron temperature lower than 700 eV, as shown in Fig.

3(a), radiate strongly near 3.9 nm. However, in the case of higher electron temperatures, from 800 to 1500 eV, the strongest emission is expected at around 3.2 nm, suitable for coupling to Sc/Cr MLMs. Thus for an optimized source, we should produce a plasma at a higher electron temperature plasma of around 1 keV. The intensity of the Bi plasma emission in our experiment was compared with 2.48-nm nitrogen line emission from a Si₃N₄ planar target, in the same experimental setup, and was observed to be 1.2 times higher within a bandwidth of 0.008 nm (FWHM) even though the plasma electron temperature was much lower than the optimum value [3].

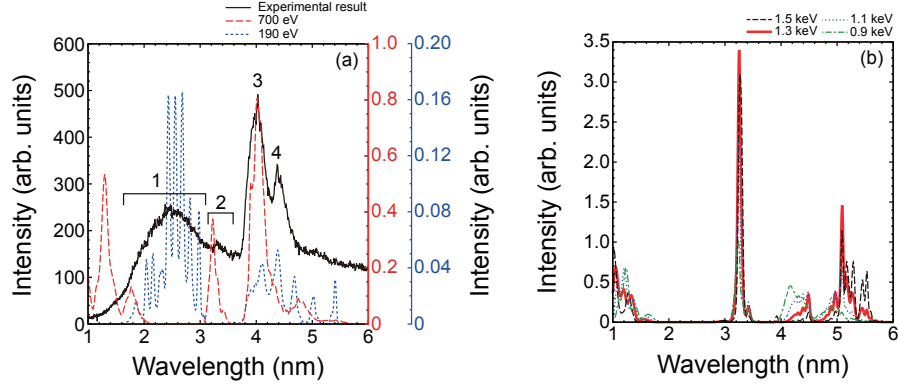


Fig. 6. Spectral behaviors of the Bi plasmas in the laser intensity dependence on the observed emission spectra (a), the peak wavelength of the $n = 4-n = 4$ transition (circles) and the $n = 4-n = 5$ transition (rectangles) (b).

V. Summary

We have reported on EUV and soft x-ray sources in the 2 to 7 nm spectral region related to the beyond EUV (BEUV) question at 6.x nm and a water window source based on laser-produced high-Z plasmas., which was high-efficiency for a beyond EUV source at 6.76 nm, because the peak at this wavelength was constant with high spectral and energy conversion efficiencies in optically thin mid-IR CO₂ laser-produced Gd plasmas. The maximum CE was observed to be 0.7%. The EBIT spectra proved experimentally that the mean wavelength for $n = 4-n = 4$ transitions of different charge states of Gd ions shifts to longer wavelength with increasing the ionic charge. Combined with the EBIT spectra, the FAC calculations explained the overall structures in the Gd-LPP spectrum. we have demonstrated the atomic number scaling of $n = 4-n = 4$ UTA wavelengths for optically thin ps-laser-produced high-Z plasmas and obtained a quasi-Moseley's law, $\lambda = aR_{\infty}^{-1}(Z - s)^{-b}$ in nm where $a = 21.86 \pm 12.09$, $b = 1.52 \pm 0.12$, $s = 23.23 \pm 2.87$ in nm for $Z = 50-83$, that enables prediction of suitable elements as LPP sources for future applications. We have also proposed high-efficiency Bi plasmas and have proposed methods to increase it still further. Resonance emission from multiply charged ions merges to produce intense UTA, extending to wavelengths below the carbon K edge. The overall spectral behavior is well described by simulations. The experimental results also provide an outline for the design concept for single-shot cell imaging with a novel microscope optical system. The method presented here opens the way for applications in

next-generation biological science.

Acknowledgements

The authors are grateful to Gigaphoton, Inc. for providing a laser system. A part of this work was performed under the auspices of MEXT (Ministry of Education, Culture, Sports, Science and Technology, Japan), and “Project for Bio-Imaging and Sensing at Utsunomiya University” from MEXT. One of the authors (T.H.) also acknowledges support from The Canon Foundation, Research Grant (Basic Research) on TEPCO Memorial Foundation, and Gigaphoton Inc., while B.L. was supported by the Fundamental Research Funds for the Central Universities and G.O’S. wishes to acknowledge support from the Japanese Society for the Promotion of Science (JSPS). The UCD group was supported by Science Foundation Ireland International Co-operation Strategic Award No. 13/ISCA/2846. This work was performed with the support and under the auspices of the NIFS Collaboration Research program (Nos. NIFS12KLPH025 and NIFS13KLPH020).

References

- [1] C. Wagner and N. Harned, *Nat. Photonics* **4**, 24 (2010).
- [2] H. Mizoguchi *et al.*, *Proc. SPIE* **8679**, 86790A (2013).
- [3] T. Higashiguchi *et al.*, *Opt. Exp.* **21**, 31837 (2013).
- [4] H. Ohashi *et al.*, *J. Phys. B* **43**, 065204 (2010).
- [5] P. A. C. Takman *et al.*, *J. Microsc.* **226**, 175 (2007).
- [6] I. A. Artyukov *et al.*, *Micron*. **41**, 722 (2010).
- [7] C. Peth *et al.*, *J. Phys. D* **41**, 105202 (2008).
- [8] T. Higashiguchi *et al.*, *SPIE Newsroom*, 2011.
- [9] D. Kilbane, *J. Phys. B: At. Mol. Opt. Phys.* **44**, 165006 (2011).
- [10] C. O’Gorman *et al.*, *Appl. Phys. Lett.* **100**, 141108 (2012).
- [11] C. S. Harte *et al.*, *J. Phys. B* **45**, 205002 (2012).
- [12] H. Ohashi *et al.*, *J. Appl. Phys.* **115**, 033302 (2014).
- [13] J. C. Slater, *Phys. Rev.* **36**, 57 (1930).
- [14] P. Jönsson *et al.*, *Comp. Phys. Comm.* **177**, 597 (2007).
- [15] D. Colombant and G. F. Tonon, *J. Appl. Phys.* **44**, 3524 (1973).
- [16] Y. Ueno *et al.*, *Appl. Phys. Lett.* **90**, 191503 (2007).
- [17] T. Higashiguchi *et al.*, *Appl. Phys. Lett.* **100**, 014103 (2012).

Lost resonance lines in promethiumlike heavy ions

NAKAMURA Nobuyuki¹, KOBAYASHI Yusuke¹,

KATO Daiji^{2,3}, SAKAUE Hiroyuki A.², and MURAKAMI Izumi^{2,3}

1) *Institute for Laser Science, The University of Electro-Communications,
Chofu, Tokyo 182-8585, Japan*

2) *National Institute for Fusion Science, Toki, Gifu 509-5292, Japan*

3) *Department of Fusion Science, SOKENDAI (The Graduate University for Advanced Studies)*

e-mail: n_nakamu@ils.uec.ac.jp

Abstract

Identifying the $ns - np$ resonance lines in alkali-metal-like ions is an important issue in fusion plasma science in the view of spectroscopic diagnostics and radiation power loss. Whereas for $n = 2, 3$ and 4 these resonances are prominent and well studied, so far no one could clearly identify the resonance lines for $n = 5$ in the promethiumlike sequence. We have now experimentally clarified the reason for the “lost resonance lines. In the present study, highly-charged bismuth ions have been studied using a compact electron beam ion trap (EBIT). Extreme ultraviolet emission from the bismuth ions produced and trapped in the EBIT is observed with a grazing-incidence flat-field spectrometer. The energy dependent spectra are compared with a collisional-radiative model calculation, and we show that the $5s - 5p$ resonance lines are very weak in plasma with a wide range of electron density due to the presence of a long-lived metastable state.

Keywords: promethiumlike heavy ions, electron beam ion trap, extreme ultraviolet (EUV) spectra

1. Introduction

The $ns - np$ resonance lines in alkali-metal-like ions with a closed $(n - 1)$ shell are important for fusion plasmas; their prominence can cause serious radiation loss while also being useful for spectroscopic diagnostics. Thus, the hydrogenlike, lithiumlike ($n = 2$), sodiumlike ($n = 3$), and copperlike ($n = 4$) sequences have been extensively studied both experimentally and theoretically. Their $ns - np$ resonance lines have been identified and their wavelengths have been compiled for a wide range of atomic number (Z) [1, 2, 3, 4, 5]. For $n = 5$ (i.e., the promethiumlike sequence), Curtis and Ellis [6] predicted in 1980 that the alkali-metal-like $4f^{14}5s$ configuration can be achieved for elements with $Z > 73$ and that experimentalists would observe the prominent $5s - 5p$ resonance doublet lines for

promethiumlike heavy ions. Following their prediction, many experimental and theoretical efforts were devoted to identifying the predicted resonance lines.

The first attempt to find the resonance lines was by beam-foil spectroscopy with gold ($Z = 79$) [7, 8] in the 1980s. Träbert and Heckmann [8] identified the $5s - 5p$ doublet lines in their beam-foil spectra of gold, but the spectra contained complex features because many lines exist near the identified lines, making the identification tentative. In 1994, Fournier *et al.* [9] identified the brightest line in their spectra of uranium ($Z = 92$) obtained with a high-temperature low-density tokamak plasma as the $5s - 5p_{3/2}$ resonance line, while their collisional-radiative (CR) model calculations showed that lines due to the transitions to the metastable $4f^{13}5s^2$ state could be brighter than the resonance lines. This inconsistency and the complex spectra containing many lines from a broad charge-state distribution made the identification tentative.

In the 2000s, another attempt to find the resonance lines, this time using an electron beam ion trap (EBIT) in Berlin [10], was made for tungsten ($Z = 74$) [11]. An EBIT can produce and trap highly charged ions that interact with a monoenergetic electron beam, making it possible to obtain simple spectra based on narrow charge-state distributions. Thus, an EBIT is a powerful tool to observe and identify previously unreported lines [12]. In fact, the tungsten spectra obtained with the Berlin EBIT revealed simple spectra containing a few prominent lines [11, 13]. However, in spite of intensive ongoing theoretical efforts [14, 15, 16, 17], the observed spectra are still not well understood. As a result, the identification made from the Berlin EBIT spectra was also tentative. Thus, in the three decades since the prediction by Curtis and Ellis, there has yet to be a definite identification of the resonance lines.

In this paper, we report the clear identification of promethiumlike bismuth ($Z = 83$) observed by using the compact EBIT at The University of Electro-Communications in Tokyo. We also show that the $5s - 5p$ resonance lines are negligibly weak in plasma over a wide range of electron densities, even though the ground state configuration is $4f^{14}5s$ as predicted.

2. Experiment

For the present study, a compact EBIT called CoBIT [18] was used to produce highly charged bismuth ions. Spectra from the trapped bismuth ions were observed with a grazing-incidence flat-field spectrometer [19] through an observation slit in the drift tube. Figure 1 shows the schematic drawing of the spectrometer and CoBIT. The spectrometer consists of a laminar-type diffraction grating with 1200 grooves per mm (Hitachi 001-

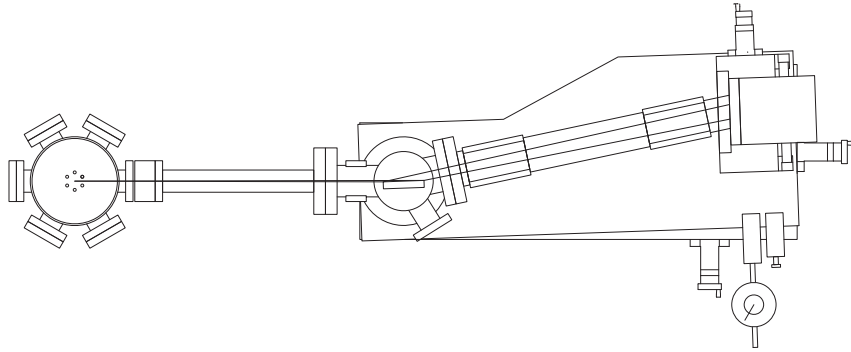


Figure 1: CoBIT and spectrometer.

0660) and a Peltier-cooled back-illuminated CCD (Roper PIXIS-XO: 400B). The spectral resolution of this arrangement was typically 0.03 nm, which was mainly limited by the electron-beam width. The wavelength was calibrated by using well-known transitions in Fe XIV and Fe XV [20] measured separately from the bismuth spectra by injecting an $\text{Fe}(\text{C}_5\text{H}_5)_2$ vapor into CoBIT. The uncertainty in the wavelength calibration was estimated to be 0.01 nm.

3. Results and discussion

The spectra for electron energies of 500, 580, and 640 eV are shown in Fig. 2 (a). It is noted that no sensitivity correction was applied, which means that the intensities at different wavelengths cannot be compared. The lines indicated by the arrows in the spectrum at 580 eV are not observed in the spectrum at 500 eV; thus, these lines can be assigned to transitions in samariumlike Bi^{21+} because the ionization energy of europiumlike Bi^{20+} (532 eV [?] or 548 eV [21]) is greater than 500 eV. Similarly, the lines indicated by the arrows in the spectrum at 640 eV can be assigned to transitions in promethiumlike Bi^{22+} because they are not observed in the spectrum at 580 eV, which is below the ionization energy of samariumlike Bi^{21+} (608 eV ¹ or 621 eV [21]).

Spectra for promethiumlike Bi^{22+} and samariumlike Bi^{21+} calculated with the CR model are shown in Figs. 2 (b) and (c), respectively. An electron density of 10^{10} cm^{-3} , which is typical for CoBIT [22], was assumed for the model calculation. The results in Fig. 2 indicate that the experimental results agree overall with those calculated by the CR model, although there is a slight shift in wavelength between the two. According to the present calculation, the ground state of promethiumlike Bi^{22+} is $4f^{14}5s$, as predicted by Curtis

1

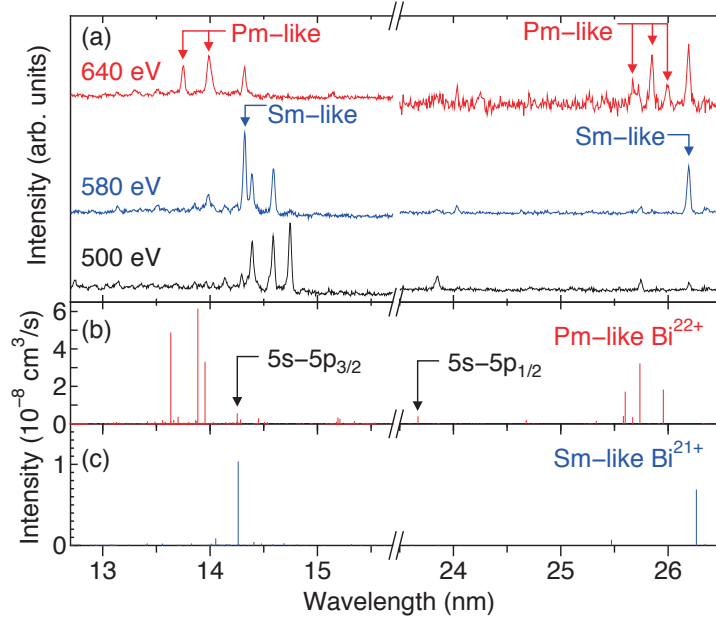


Figure 2: (Color online) (a) Experimental spectra of highly charged bismuth ions observed at electron energies of 500, 580, and 640 eV. (b) Spectrum of promethiumlike bismuth calculated with CR model for an electron energy of 640 eV. (c) Spectrum of samariumlike bismuth calculated with CR model for an electron energy of 580 eV. The vertical axes in panels (b) and (c) correspond to the photon emissivity coefficient, which is defined as nA/n_e , where n is the fractional population of the upper level, A is the Einstein A coefficient, and n_e is the electron density. An electron density of 10^{10} cm⁻³ is assumed for both (b) and (c).

and Ellis [6]. However, the prominent lines in the CR-model spectrum of promethiumlike Bi²²⁺ are not the $5s - 5p$ resonance lines (indicated by arrows in Fig. 2 (b)), but the $4f^{13}5s^2 - 4f^{13}5s5p$ transitions. This seemingly peculiar phenomenon is explained below.

The excitation rate from the ground state $4f^{14}5s$ level is largest to the $4f^{14}5p$ levels, which means that the $5s - 5p$ resonance lines should be prominent if the population of the ground state is dominant. However, because the metastable $[4f^{13}5s^2]_{7/2}$ state has a long lifetime (estimated by the present calculation to be ~ 40 s), its population can dominate that of the ground state mainly through indirect excitation. Actually, in the present calculation, the equilibrium population of the metastable $[4f^{13}5s^2]_{7/2}$ state is estimated to be an order of magnitude larger than that of the ground state. As a result, the $[4f^{13}5s^2]_{7/2} - 4f^{13}5s5p$ transitions dominate the $5s - 5p$ resonance lines in the spectrum of the promethiumlike ion.

Because the EBIT technique provides simple spectra with a narrow charge-state dis-

tribution compared with beam-foil and plasma spectroscopies, these identifications for promethiumlike and samariumlike heavy ions are definite rather than tentative. Hutton *et al.* [11] also observed promethiumlike tungsten using an EBIT and a spectrometer with spectral resolution comparable to that of our present spectrometer, but they gave no clear identification. The complexity for tungsten is likely due to the fact that the ground state of promethiumlike tungsten is not $4f^{14}5s$ but $4f^{13}5s^2$; furthermore, the metastable $4f^{12}5s^25p$ states are near the ground state [14, 16]. Note that, although Curtis and Ellis [6] predicted through non-relativistic calculation that the transition of the ground state configuration from $4f^{13}5s^2$ to $4f^{14}5s$ occurs between $Z = 73$ and 74, their relativistic calculation [23] and several subsequent theoretical studies [14, 24, 25] indicate that the transition should occur near $Z = 78$.

4. Summary and outlook

In summary, by using a compact electron beam ion trap, we observe $5s - 5p$ transitions in promethiumlike and samariumlike bismuth. Comparing the experimental results with calculations based on a collisional-radiative model allow us to definitely identify several lines for promethiumlike heavy ions. We show that, because of the large population of the $4f^{13}5s^2$ metastable state, the alkali-metal-like $5s - 5p$ resonance lines in promethiumlike ions are negligible in plasmas over a wide range of electron densities, even though the ground state configuration is alkali-metal-like $4f^{14}5s$.

Acknowledgement

This work was performed with the support and under the auspices of the NIFS Collaboration Research program (NIFS09KOAJ003) and JSPS KAKENHI Grant Number 23246165, and partly supported by the JSPS - NRF - NSFC A3 Foresight Program in the field of Plasma Physics (NSFC: No.11261140328, NRF : No. 2012K2A2A6000443).

References

- [1] E. Hinnov, Phys. Rev. A **14**, 1533 (1976).
- [2] J. Reader and N. Acquista, Phys. Rev. Lett. **39**, 184 (1977).
- [3] W. R. Johnson, S. A. Blundell, and J. Sapirstein, Phys. Rev. A **37**, 2764 (1988).
- [4] W. R. Johnson, S. A. Blundell, and J. Sapirstein, Phys. Rev. A **38**, 2699 (1988).
- [5] W. R. Johnson, S. A. Blundell, and J. Sapirstein, Phys. Rev. A **42**, 1087 (1990).
- [6] L. J. Curtis and D. G. Ellis, Phys. Rev. Lett. **45**, 2099 (1980).

- [7] B. M. Johnson *et al.*, Nucl. Instrum. Methods **202**, 53 (1982).
- [8] E. Träbert and P. H. Heckmann, Z. Phys. D **1**, 381 (1986).
- [9] K. B. Fournier *et al.*, Phys. Rev. A **50**, 3727 (1994).
- [10] C. Biedermann *et al.*, Phys. Scr. **T73**, 360 (1997).
- [11] R. Hutton *et al.*, Nucl. Instrum. Methods B **205**, 114 (2003).
- [12] A. Komatsu *et al.*, Plasma Fusion Res. **7**, 1201158 (2012).
- [13] S. Wu and R. Hutton, Can. J. Phys. **86**, 125 (2008).
- [14] M. J. Wilkas, Y. Ishikawa, and E. Träbert, Phys. Rev. A **77**, 042510 (2008).
- [15] E. Träbert, M. J. Wilkas, and Y. Ishikawa, J. Phys.: Conf. Ser. **163**, 012017 (2009).
- [16] V. Jonauskas *et al.*, J. Quant. Spectrosc. and Radiat. Transfer **127**, 64 (2013).
- [17] U. I. Safronova *et al.*, Phys. Rev. A **88**, 032512 (2013).
- [18] N. Nakamura *et al.*, Rev. Sci. Instrum. **79**, 063104 (2008).
- [19] H. Ohashi *et al.*, Review of Scientific Instruments **82**, 083103 (2011).
- [20] A. Kramida *et al.*, NIST Atomic Spectra Database (version 5.0).
- [21] T. A. Carlson *et al.*, At. Data **2**, 63 (1970).
- [22] N. Nakamura, *et al.*, The Astrophysical Journal **739**, 17 (2011).
- [23] D. G. Ellis and L. J. Curtis, Nucl. Instrum. Methods **202**, 339 (1982).
- [24] C. E. Theodosiou and V. Raftopoulos, Phys. Rev. A **28**, 1186 (1983).
- [25] V. Kaufman *et al.*, Phys. Scr. **42**, 705 (1990).

EUV spectrum of highly charged tungsten ions in Electron Beam Ion Trap

H.A. Sakaue, D. Kato, I. Murakami

National Institute for Fusion Science, Toki, 509-5292 Japan

N. Nakamura

Inst. Laser Science, Univ. Electro-Communications, Tokyo 182-8585, Japan

Abstract

We present spectra of highly charged tungsten ions in the extreme ultra-violet (EUV) by using electron beam ion traps. The electron energy dependence of spectra was investigated for electron energy from 540 to 1370 eV. Previously unreported lines were presented in the EUV range, and comparing the wavelengths with theoretical calculations identified them.

Keywords: Electron beam ion traps, tungsten, highly charged ion, EUV spectra

1.Introduction

Tungsten will be used as material for the divertor plates in ITER because of higher sputtering threshold energy for light ion bombardment, the highest melting point among all the elements, and less tritium retention compared with carbon based materials. However, since extremely high particle- and heat-fluxes of the intermittent edge plasma transport (*e.g.* edge-localized-mode) in ITER would cause serious damages to such components, tungsten is considered to be one of the most abundant impurities in the ITER plasma. Emission lines of highly charged tungsten ions thus play an important role in the spectroscopic diagnostics of the ITER plasma, and consequently the spectroscopic data of tungsten ions have been studied at several facilities [1-3]. An electron beam ion trap is a useful device for the systematic spectroscopic studies of highly charged tungsten ions [4-7]. We have constructed a compact electron beam ion trap, called CoBIT [8-10], for spectroscopic studies of moderate charge state ions.

On the other hand, an electron beam ion trap is a useful device for the systematic spectroscopic studies of highly charged tungsten ions. We have constructed a compact electron beam ion trap, called CoBIT [4-6], and observed extreme ultraviolet (EUV) spectra of highly charged tungsten ions.

2. Experimental apparatus

For the spectroscopic studies of such moderate charge state ions, we have developed a new compact EBIT [7]. The electron energy range of the present EBIT is 100 - 2500 eV, which is suitable for this purpose. A schematic drawing of the present EBIT and EUV spectrometer are shown in Fig. 1. The electron energy and current are 100-2500 eV and <30 mA, respectively. Those parameters, which are rather low compared to those of ordinary EBITs, enabled us to downsize the device. We adopted a high critical temperature super-conducting coil for the compression of the electron beam to reduce the running cost. The electron gun, drift tubes (DT), electron collector and extractor are fixed in the liquid nitrogen tank with the ceramic insulator Shapal M-soft. Because this insulator has a high thermal conductivity (90 W/m K), the electron collector can be cooled only by the thermal conduction from the liquid nitrogen tank without any water-cooling channels. This also helped to downsizing the device. The CoBIT has six ports currently used for an EUV spectrometer, a visible spectrometer, gas injector and pinhole camera. Tungsten was injected from gas injector, as a vapor of tungsten carbonyl ($W(CO)_6$). The various charge state ions in the trap of the CoBIT can be selectively produced with narrow charge state distribution by adjusting the electron beam energy and tungsten atom vapor density. The EUV spectrometer is of a slit-less type especially designed for the present CoBIT. The two kinds of laminar-type replica diffraction gratings are used to focus the radiation on the surface of a back illuminated CCD, and the measurement wavelength ranges are 1-6 nm and 5-20 nm, respectively.

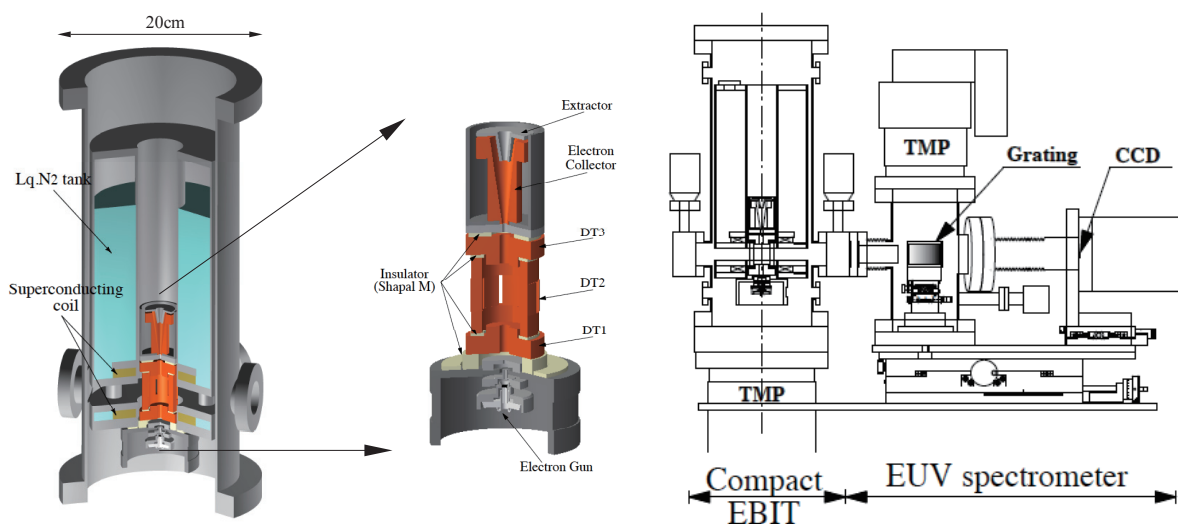


Figure 1. A schematic drawing of the present EBIT and EUV spectrometer.

3. Results and discussion

We present extreme ultraviolet (EUV) spectra of highly charged tungsten ions ($W\ XX \sim W\ XXXIV$) in the wavelength range of 15-45 Å obtained with a compact electron beam ion trap. The electron energy

dependence of spectra is investigated for electron energies from 540 to 1370 eV. Several tens of previously unreported lines are presented, and comparing the wavelength with theoretical calculations identifies some of them. Figure 2(a) shows the EUV spectra at electron energies (E_e) between 540 and 1370 eV. Corrections for spectrometer response and detector efficiencies were applied to the spectra using catalog data. As seen in the figure, the overall EUV spectra show significant dependence on the electron energy. As the electron energy increases, the wavelength of strong emission lines shifts to shorter wavelength region. The charge state of ions responsible for these lines can be identified from the appearance energy in a similar way to the previous study [8]. In fig. 2(b), the charge state dependence of calculated wavelengths is shown. The solid line, dashed line, dotted line and dashed two-dot line are calculated average wavelengths corresponding to the 6g-4f, 5f-4d, 5g-4f and 5p-4d transition manifolds, respectively. The wavelength was obtained by averaging the wavelengths of all transitions in the each manifold weighted by their line strengths which were calculated by an originally developed collisional-radiative model (CR-model) [9]. The atomic data used in the model were calculated by using the HULLAC code [10] in so-called configuration mode. In the configuration mode, fine-structure energy levels were not calculated, and a configuration averaged energy of a given configuration and a total angular momentum J was concerned. Thus, the multiplet term and configuration interaction were not considered in this calculation. From the comparison, some observed lines have been identified as the 6g-4f, 5f-4d, 5p-4d and 5g-4f transitions of W^{20-35+} .

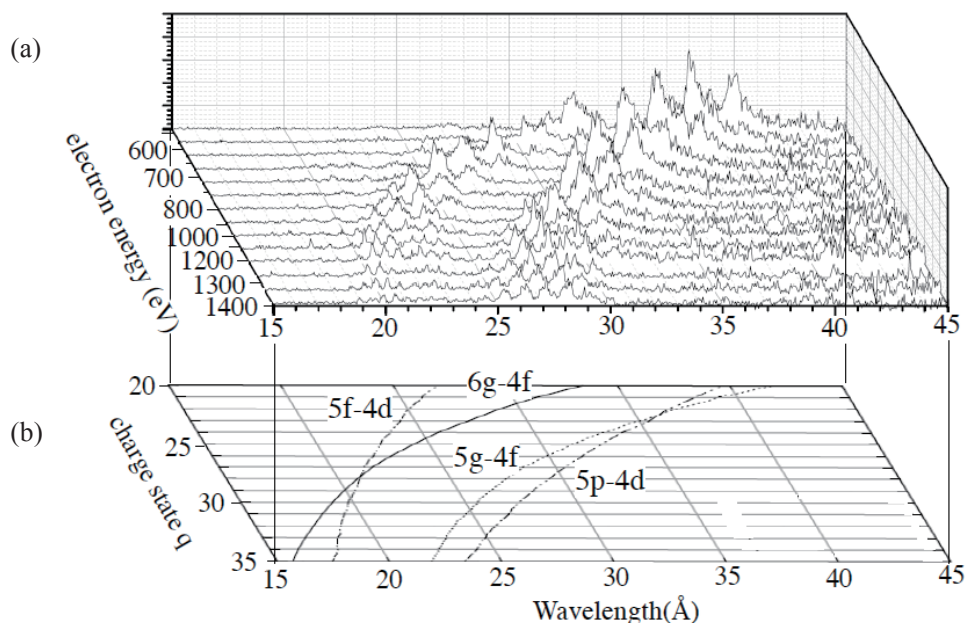


Figure 2 (a): Typical EUV spectra of highly charged tungsten ions obtained at electron energy E_e from 540 to 1370 eV in CoBIT. (b): The charge dependence of calculated wavelength.

Figure 3 shows the typical EUV spectra of highly charged tungsten ions. The observation wavelength ranges are from 15 to 45 and 40 to 60 Å, respectively. To identify the observed lines, we have calculated the spectra using a collisional-radiative (CR) model [9]. From the comparison, the observed lines have been identified as the 5f-4d, 5p-4d, and 4f-4d transitions of W^{27-30+} as indicated in the figure.

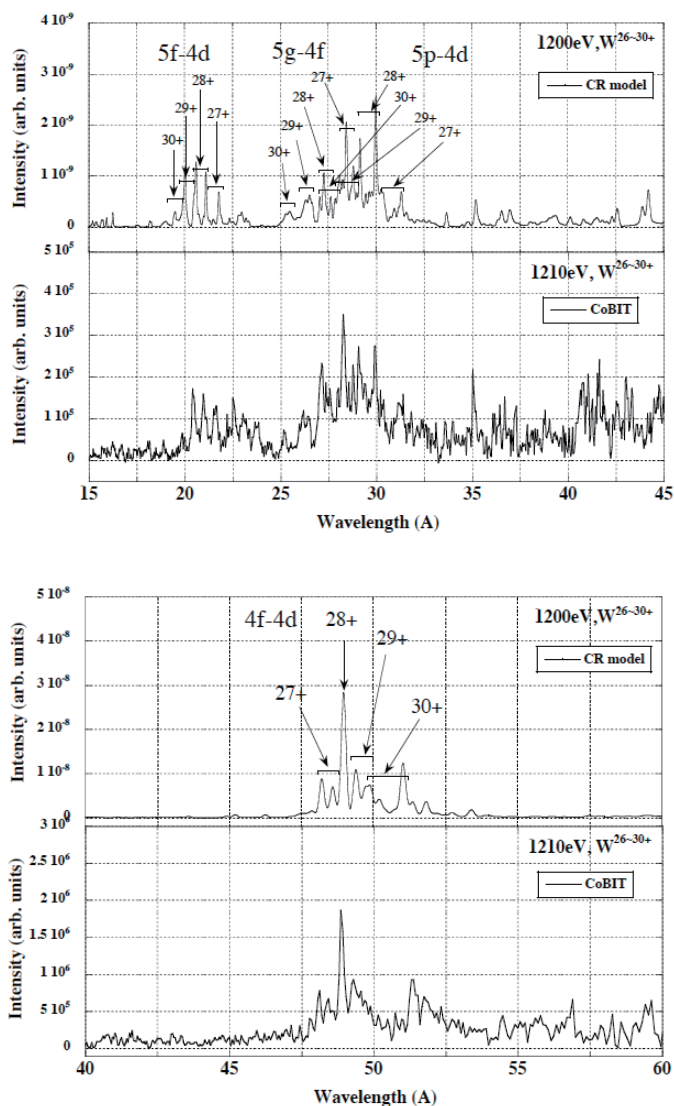


Fig. 3. EUV spectra of highly charged tungsten ions. The upper panels are calculated CR-model spectra and the lower panels are experimental spectra.

We observed an unidentified emission lines which are expected from theoretical calculations from W^{26+} around 100 Å at CoBIT. As electron energy of CoBIT is increased across the ionization energy ($I_p(25+)=786.3\text{eV}$) of W^{25+} , new emission lines were appeared in the spectrum. These emission lines are identified as emission lines from W^{26+} . In Figure 4 (a) and (b), EUV spectra of CoBIT are shown. As subtracting the spectrum of electron energy $E_e=770\text{eV}$ from the spectrum of electron energy $E_e=800\text{eV}$,

emission lines only from W^{26+} appears. Because the electron energy is increased to 800eV beyond the ionization energy of W^{25+} ($I_p=786.3\text{eV}$), W^{26+} ions were generated in the trap. Then, new emission lines from W^{26+} appear in the spectrum. In Figure 5, we show the spectrum of W^{26+} obtained by subtracting spectrum of $E_e=770\text{eV}$ from spectrum of $E_e=800\text{eV}$. Strong peak was observed at 102\AA and other emission lines were also observed at both ends of this strong peak. These lines are emission lines of W^{26+} $4f5s \rightarrow 4f^2$ by electron excitation. In future, we will promote detailed studies for the spectroscopic diagnostics of plasma, such as electron energy dependence and electron density dependence of these.

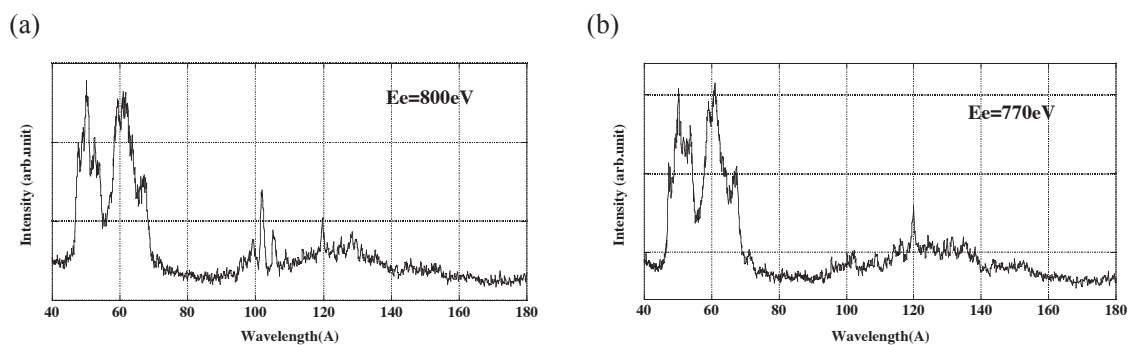


Fig. 4. EUV spectra of CoBIT. Electron energy of spectra (a) and (b) are 800eV and 770eV, respectively.

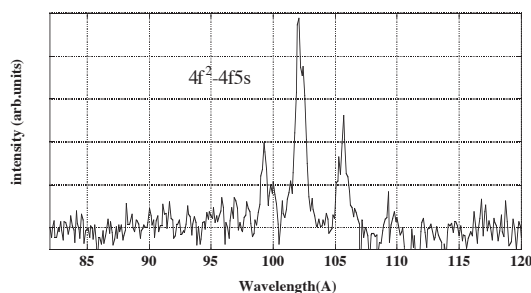


Fig. 5. Subtracted W^{26+} EUV spectrum of CoBIT.

4.Summary

We presented the measurements of the EUV spectra of highly charged tungsten ions in the wavelength from 15 to 180 \AA . From the electron energy dependence of experimental spectra, the emission lines of $6g-4f$, $5g-4f$, $5f-4d$, $5p-4d$, $4f-4d$ and $5s-4f$ transitions were identified. We have constructed an original CR model for W^{19+} - W^{34+} ions and these calculated spectra agree with experimental spectra of CoBIT.

Acknowledgement

This work is performed with the support and under the auspices of the NIFS Collaboration Research program (NIFS13KLPF032) and JSPS-NRF-NSFC A3 Foresight Program in the field of Plasma Physics

(NSFC: No.11261140328, NRF: 2012K2A2A6000443).

References

- [1] T. Pütterich, R. Neu, C. Biedermann, R. Radtke and ASDEX Upgrade Team, *J. Phys. B* **38** 3071 (2005)
- [2] M.B. Chowdhuri, S. Morita, M. Goto, H. Nishimura, K. Nagai and S. Fujioka, *Plasma and Fusion Research Vol.2*, S1060 (2007)
- [3] J. C.J. Clementson, P. Beiersdorfer, E.W. Magee, H.S.McLean and R.D. Wood, *J. Phys. B* **43** 144009 (2010)
- [4] Nakamura, N. *et al.*: *Rev. Sci. Instrum.* **79** (2008) 063104
- [5] Sakaue, H. A. *et al.*: *J. Phys.: Conf. Ser.* **163** (2009) 012020
- [6] Sakaue, H. A. *et al.*: *AIP Conf. Proc.* (2012) 143891
- [7] N. Nakamura *et al.*, 2008 *Rev. Sci. Instrum.* **79**, 063104.
- [8] Sakaue, H. A. *et al.*: *AIP Conf. Proc.* (2012) 143891
- [9] Sakaue, H. A. *et al.*: *J. Appl. Phys.* **109** (2011) 073304
- [10] Bar-Shalom, A *et al.*: *J Quant. Spect. Rad. Transf.* **71** (2001) 179

UV-visible M1 line emission from highly charged tungsten ions in LHD plasmas

D. Kato, H.A. Sakaue, I. Murakami, M. Goto, T. Oishi, N. Tamura, C. Suzuki, S. Morita

National Institute for Fusion Science, Toki, 509-5292 Japan

N. Nakamura

Inst. Laser Science, Univ. Electro-Communications, Tokyo 182-8585, Japan

A. Sasaki

Japan Atomic Energy Agency, Kyoto 619-0215, Japan

F. Koike

Faculty of Sci. and Tech., Sophia University, Tokyo 102-8554, Japan

X.-B. Ding, C.-Z. Dong

*College of Phys. and Electronic Eng., Northwest Normal University, Lanzhou,
730070, China*

Abstract

UV-visible magnetic-dipole (M1) line emission of highly charged tungsten ions in magnetically confined high-density high-temperature plasmas is investigated. Emission lines due to the M1 transitions in the ground-term fine structure of W^{26+} and W^{27+} ions have been identified in UV-visible spectra measured at Large Helical Device (LHD), and its intensity distribution on a poloidal cross section was measured. The measured intensity distribution of W^{27+} was compared with the ion distributions calculated using available data of the ionization and recombination rate coefficients at electron temperatures measured by Thomson scattering.

Keywords: magnetic-dipole transition, tungsten, highly charged ion, LHD, UV-visible spectra, plasma diagnostics, ionization, recombination

1. Introduction

One of important issues concerning steady state sustainment of magnetically confined plasmas (MCPs) is distribution of impurity ions in the MCPs and radiation powers by the ions. Since tungsten divertors will be used in ITER, the primary element of heavy impurity ions would be tungsten. Tungsten cannot be fully ionized even in core plasmas of ITER. Line radiations by bound electrons of the tungsten ions following electron impact excitations decrease temperatures of the core plasmas. Thus, it is required to keep tungsten concentration in the core plasmas as small as possible; some theoretical simulations predict that the concentration should be limited below 5×10^{-5}

[1].

Emission lines of the tungsten ions are useful for identifying the ion distribution as well as plasma diagnostics. Electron temperatures in the core plasma of the Large Helical Device (LHD) is a few keV or lower using neutral beam injection (NBI) heating. We can, therefore, investigate tungsten line emissions of relatively low charge states (the charge states of 30+ or lower, open 4f and 5f sub-shells) with the LHD, which are anticipated in peripheral regions of ITER. A novel idea of this work is to use magnetic-dipole (M1) lines in UV-visible ranges to measure the tungsten ion distributions as well as plasma diagnostics. Inherently narrow natural width of the forbidden lines is a suitable feature for identifying a specific charge state of ions in emission spectra.

Recently, Komatsu [2, 3] and Watanabe [4] found visible M1 lines of Cd-like W^{26+} by means of electron-beam-ion-traps (EBITs). The lines has been identified as the ground-term fine-structure transitions of $4f^2 \ ^3H_5 - \ ^3H_4$, $\ ^3H_6 - \ ^3H_5$, and $\ ^3F_3 - \ ^3F_2$ [3, 5]. The ground-term M1 transition, $4f \ ^2F_{5/2} - \ ^2F_{7/2}$, of Ag-like W^{27+} has been identified by measurements using an EBIT at Fudan University [6].

2. Magnetic-dipole (M1) transition of highly charged ions

M1 transition is the primary forbidden transition. Relativistic effects enhance strongly the transition rate. A formal expression of the transition operator associated with the M1 component of a photon wavefunction whose wave number is k and polarization $p = \pm 1$ is,

$$H_{\text{int}}^{M1} = -i3\sqrt{3/2}j_1(kr)\sum_{m,q}\begin{pmatrix} 1 & 1 & 1 \\ m & q & -p \end{pmatrix}C_m^{(1)}\alpha_q^{(1)},$$

where j_1 is the spherical Bessel function of the 1st order, the matrix the Clebsch-Gordan coefficient, $C_m^{(1)}$ the renormalized spherical harmonics of the 1st order, and $\alpha_q^{(1)}$ the Dirac matrices in the spherical tensor representation. The transition rate (Einstein's A coefficient) from the upper level (γJ) to the lower level ($\gamma' J'$) is written as,

$$\begin{aligned} A_{M1}(\gamma J \rightarrow \gamma' J') &= \frac{4\alpha\Delta E}{(2J+1)}\sum_{M,M'}\left|\langle \gamma JM | H_{\text{int}}^{M1} | \gamma' J' M' \rangle\right|^2, \\ &= 4\alpha\Delta E \left| \int (P_\gamma Q_\gamma + Q_\gamma P_\gamma) j_1(kr) dr \right|^2 \rightarrow \alpha^5 (\Delta E)^3 \left| \int P_\gamma P_{\gamma'} j_0(kr) dr \right|^2 \end{aligned}$$

where α is the fine-structure constant, ΔE the energy difference between the upper and the lower levels, P and Q are the large and the small components of the relativistic wavefunctions of the orbital electrons, respectively. The last equation is a non-relativistic expression of the rate, which is obtained by the Pauli approximation. The M1 rate within a fine-structure of an electronic term of single electronic configuration scales as Z^{12} , where Z is atomic number, because the fine-structure splitting increases as Z^4 . The transition rate between different n levels scales as Z^{10} approximately, because the energy difference increases as Z^2 and the orbital radius shrinks as Z^{-1} . Thus, the M1 transition rate rapidly increases as Z increases and becomes significantly large for high Z highly charged ions. The M1 lines can be observed in emission spectra of high-temperature

plasmas where the highly charged ions exist.

The ground-term M1 transition of high Z ions falls into a visible range. The visible M1 transitions have been found in dilute plasmas in space, e.g. the solar corona, nebulae, supernova remnants. In the EBITs also, electron densities are relatively low, i.e. $\sim 10^{16} \text{ m}^{-3}$. In such the dilute plasmas, electrons in the upper levels of the transition can decay emitting M1 photons before being depopulated by subsequent collisions in the plasmas (corona phase). However, such the visible M1 transitions have not been explored in high density MCPs, where the core electron densities attain to an order of 10^{19} m^{-3} or higher.

Thus, collisional-radiative model (CR-model) calculations were performed to investigate the visible M1 line emission for W^{26+} ions in high-density thermal plasmas. In the present work, atomic data (energy levels, transition probabilities, electron collision cross sections) were calculated with HULALC code [7], an integrated code for calculating atomic structure, collision cross sections and radiative processes. Fully relativistic wavefunctions are used for calculations of the transition rates and the collision cross sections. The cross sections are calculated in the distorted wave approximation. Atomic structure calculations are implemented by using a parametric potential method, which are generally less accurate comparing with *ab-initio* methods, e.g. multi-configuration Dirac-Fock (MCDF) method.

The ground state of W^{26+} has two $4f$ electrons in the valence shell with the fully occupied $4d$ sub-valence shell, i.e. $4d^{10}4f^2$. Electronic configurations of excited levels included in the present model are $4d^{10}4fnl$ ($n=5-6$, $l=0-5$) and $4d^94f^3$. Electron collision rate coefficients at a given electron temperature are obtained with the cross sections assuming the Maxwellian velocity distribution of electrons. Fig. 1 shows calculated emissivities of lines from W^{26+} ions excited by electron collisions from the ground state at an electron temperature of 800 eV and a density of 10^{19} m^{-3} . Energy level diagram (fine-structure) of the ground state of W^{26+} also is shown in the figure. Five lines (indicated

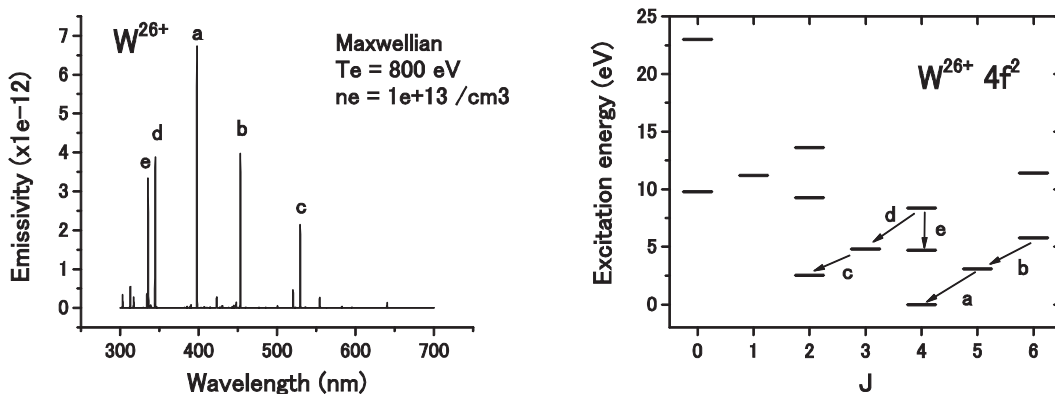


Fig. 1 CR-model calculation of line emissivity of W^{26+} ions and energy level diagram of the $4f^2$ ground state.

as a-e in the figure) have large emissivities in this wavelength range. The lines a, b and c are assigned to the M1 transitions of ${}^3\text{H}_5\text{-}{}^3\text{H}_4$ (389.4 nm), ${}^3\text{H}_6\text{-}{}^3\text{H}_5$ (464.7 nm), and ${}^3\text{F}_3\text{-}{}^3\text{F}_2$ (501.9 nm), respectively, which have already been identified by previous EBIT measurements [3]. Recently, the first line was observed in the LHD spectra also [8]. However, present calculations of the wavelengths for these lines are 402 nm, 457 nm, and 536 nm, respectively. Agreements are very poor due to a less accurate approximation (the parametric potential method) to atomic structure calculations adopted in HULLAC code. More elaborate calculations can in principle improve the predictions; for the line a, 388.4 nm has theoretically been obtained by implementing a large scale MCDF calculation using grasp2K code [5].

Electron density dependence of the line intensities is depicted in Fig. 2 for the lines a-e. The intensities are defined as fractional populations of the upper levels multiplied by Einstein's A coefficients of the radiative transitions. The emissivities in Fig. 1 are the intensities divided by the electron density. At low densities, indicated as *corona phase*, the intensities increase linearly along with the density as the direct excitation rate to the upper levels by electron collision. The intensities are larger than the collisional excitation rate indicating radiative cascades from higher levels have a significant contribution to populations of the upper levels. At high densities, indicated as *saturation phase*, the intensities saturate along with the density, indicating the ladder-like excitation-ionization mechanism dominates the population kinetics of the upper levels. In this phase, electron collision excitation and de-excitation rates dominate over radiative decay rates of excited states. The line intensity ratios in the *saturation phase* are in accord with ratios of their gA values, where g is the statistical weight of the level. It is noted that the ratios change the values in an intermediate density

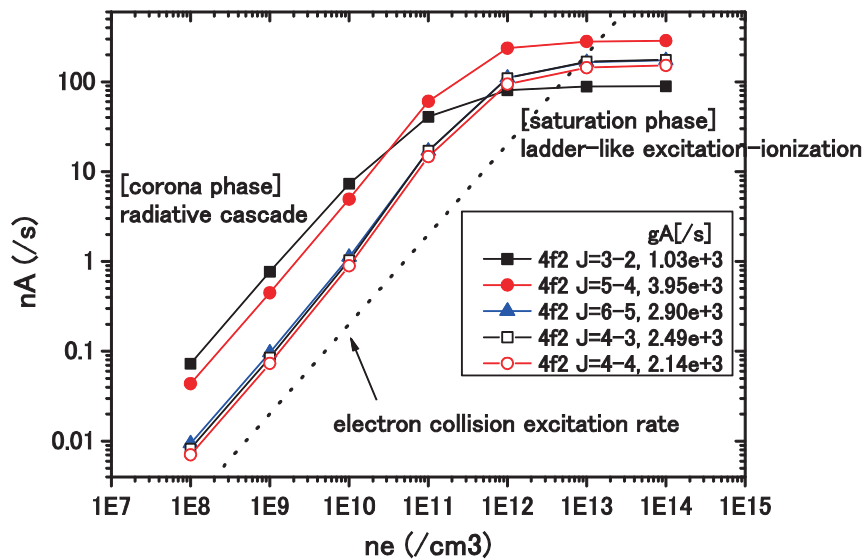


Fig. 2 Electron density dependence of W^{26+} M1 line intensity calculated by the present CR-model.

region between 10^{16} and 10^{18} m^{-3} ; the ratios serve as a probe for density diagnostics of plasmas.

3. LHD experiments

Discharges for present measurements were started with electron cyclotron heating followed by hydrogen NBI heating. Then, a solid pellet containing tungsten was injected into background hydrogen plasmas. We used the impurity pellet [9] which has a cylindrical carbon shell (diameter of 1.2 mm ϕ) with tin coating. Solid tungsten is contained inside a hole at the center of the carbon shell. Size of the solid tungsten in the pellet is 0.15 mm in diameter and 0.6 mm in length. Using the density of the solid tungsten, i.e. 19.25 g/cm³, number of tungsten atoms in the single pellet is estimated to be 6.9×10^{22} . The impurity pellet is injected at speeds of 30 ~ 300 m/s by using a pneumatic pellet injector with helium gas.

Time-resolved (sampling times for 38 ms at every 100 ms) measurements of emission lines were performed using a Czerny-Turner UV-visible spectrometer equipped with a CCD detector (10-O port). The pellet is injected at the same port with the observation port. Fig. 3 shows the viewing angle and the pellet injection angle at 10-O port. An optical fiber array of 40 lines of sight was used to measure vertical profiles of photon emission in a horizontally elongated poloidal cross section. It is noted that the poloidal cross section is asymmetric with respect to the horizontal axis, because the cross section is tilted 6 degrees from the normal direction. This asymmetry manifests itself in the vertical profiles of line-integrated intensities (along each line of sight) of emission lines in peripheral regions of the poloidal cross section.

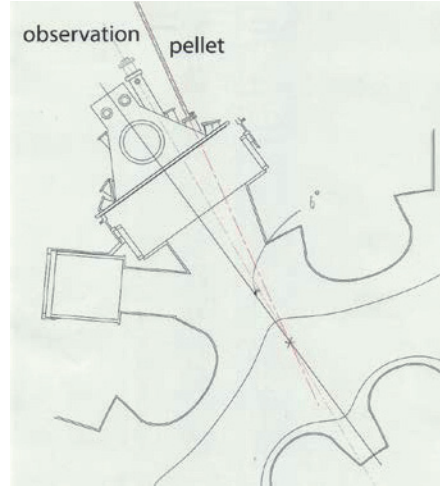


Fig.3 Viewing angle (thin dashed line) and pellet injection angle (bold dashed line) at 10-O port.

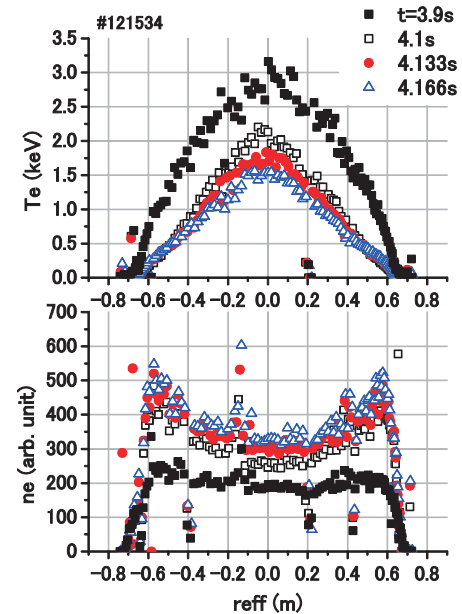


Fig. 4 Electron temperature and density profiles as a function of effective minor radius measured at the LHD (#121534) by Thomson scattering. A tungsten pellet is injected at $t=4.0$ s.

4. Experimental results and discussion

In a steady state before the pellet injection, a peak electron temperature at the plasma center is sustained at about 3 keV by NBI heating. Fig. 4 depicts electron temperature and density profiles changing after the pellet injection at 4.0 s. The peak temperatures are decreased after the tungsten injection, while the electron densities are increased: line-averaged densities are increased from $2 \times 10^{19} \text{ m}^{-3}$ to $4 \times 10^{19} \text{ m}^{-3}$. The radial distribution of the temperature before the pellet injection shows a steep gradient at the edge. After the pellet injection, the density increase is pronounced in the edge region. Since tungsten is mainly deposited in the plasma edge region, the change in the electron temperature and density profiles can be ascribed to ablation of the tungsten pellet, ionization of the ablated tungsten particles and cross-field transport of the tungsten ions.

A long-term behavior of the discharge and NBI heating is summarized in Fig. 5. Three NBIs (NBI 1-3) are used until $t=5.8$ s, then two of them (NBI 2-3) are turned off. The central electron temperature declines by the pellet injection, but it is gradually recovering until 5.8 s. Strong enhancement of radiation powers is seen in a short time just after the pellet injection, which is probably due to the pellet ablation cloud. The radiation power stays at an elevated level, which can be ascribed to line emissions of tungsten ions. After NBI 2 and 3 are tuned off, the radiation power gradually decreases until the end of discharge at 8.6 s.

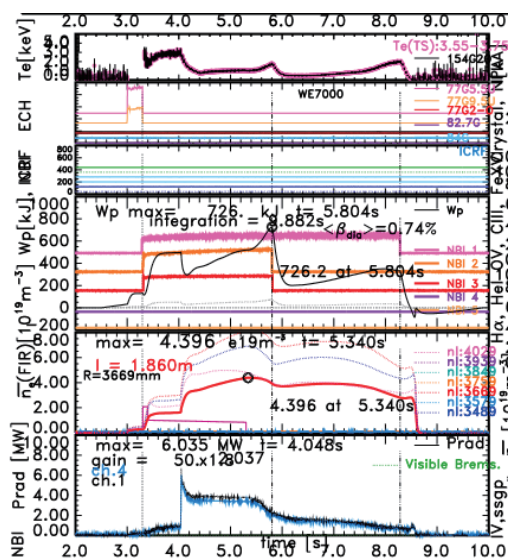


Fig. 5 A shot summary for the discharge #121534. From the top panel to the bottom, time variations of central electron temperatures, electron cyclotron heating (ECH), ion cyclotron resonance heating (ICRH), plasma stored energies (Wp) and NBI heating, line-averaged electron densities, and radiation power (Prad).

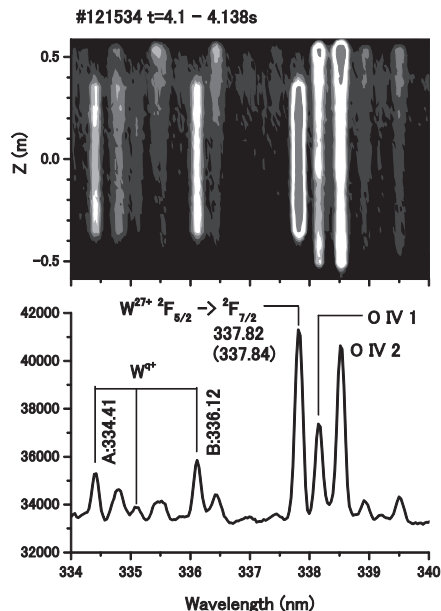


Fig. 6 Line emission measured after a tungsten pellet injection ($t=4.1-4.138$ s). Upper: A CCD image for vertical profile (Z) of an emission line spectrum. Lower: the emission line spectrum.

Fig. 6 shows an emission line spectrum measured during $t=4.1 - 4.138$ s in the discharge #121534. Wavelength calibration is done with the hydrogen Balmer series of lines emitted in the last phase of the same discharge. The wavelength uncertainty is about 0.04 nm. The line at 337.82 nm is due to the ground-term M1 transition, $4d^{10}4f^2F_{5/2} - 2F_{7/2}$, of W^{27+} ions. This M1 line has been discovered by using an EBIT at Fudan University [6]; its wavelength was determined to be 337.84 nm. Vertical profile of the M1 line emission indicates a line intensity distribution localized in the core plasma where electron temperatures are high enough to produce the W^{27+} ions (the ionization energy of W^{26+} is about 830 eV). Two lines adjacent to the M1 line at 337.82 nm are identified as lines emitted by O^{3+} ions in the peripheral region, which show a border distribution in the vertical direction. In the spectrum, another three lines are also assigned to emission lines of W^{q+} ions, because its vertical profiles are similar to that of W^{27+} .

Fig. 7(a) shows a vertical profile of the line-integrated intensity of the M1 line at 337.82 nm and a simulation of the vertical profile which is an integral transformation of the given radial distribution depicted in Fig. 7(b) on a horizontally elongated poloidal cross section. The radial distribution has the maximum at around 0.3 m in the effective minor radius where a local electron temperature is measured to be about 1 keV. We investigate the present results in terms of predicted ion distributions of W^{27+} assuming the ionization equilibrium. We assume the ionization equilibrium, because a time-scale for ionization and recombination processes is believed to be much shorter than that of cross-field ion transport inside the core plasma.

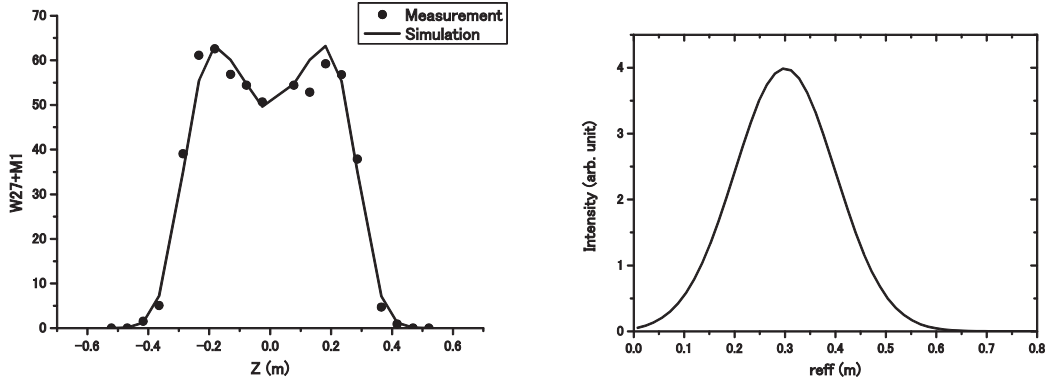


Fig. 7(a) left) Vertical-profile (Z) of line-integrated intensity of the W^{27+} M1 line at 337.82 nm. (b) right) Radial distribution of the line intensity on a horizontally elongated poloidal cross section.

A rate equation of local ion density n_q is written using ionization rate coefficients α and recombination rate coefficients β at a given local electron temperature,

$$\frac{\partial n_q}{\partial t} = -(\alpha_q + \beta_q)n_e n_q + \beta_{q+1}n_e n_{q+1} + \alpha_{q-1}n_e n_{q-1},$$

where q stands for charge states of ions and n_e is electron density. The coupled rate equations are integrated numerically using the implicit differencing method with the initial condition,

$$n_q(t=0) = \begin{cases} 1 & q=0 \\ 0 & \text{otherwise} \end{cases}.$$

Fig. 8 shows a comparison of the radial distribution of the W^{27+} M1 line intensity and two ion distributions $n_{q=27}(t=\infty)$ calculated with different sets of data for the ionization and recombination rate coefficients. One set is obtained by using a fitting formula of ADPAK data [10], the other uses data calculated by Sasaki [11]. ADPAK data appears to give the ion distribution consistent with the measured distribution of the M1 line intensity, while Sasaki's data gives the distribution whose maximum is located at a lower local electron temperature. This is puzzling, because Sasaki's data are believed to be improved by including detailed indirect processes, e.g. excitation auto-ionization, dielectronic recombination, using HULLAC code (ADPAK data is calculated assuming a simple screened hydrogenic model for the atomic states). This inconsistency is hardly ascribed to the cross-field ion transport, because in the core plasma it is believed to take place much slower than the ionization and recombination processes.

4. Summary

UV-visible M1 lines of tungsten highly charged ions are investigated by means of a CR model. The present calculations show that five ground-term ($4f^2$) M1 lines of W^{26+} ions have large emissivities in a UV-visible range. Three of them are assigned to the M1 lines already identified by the previous EBIT measurements. The present calculations predict that line intensity ratios of the five lines show significant electron density dependences in a range from 10^{16} and 10^{18} m^{-3} . Experimental validation of this prediction may be possible by combining measurements with EBITs in a low density ($\sim 10^{16} \text{ m}^{-3}$) region and LHD at a high density limit ($10^{19-20} \text{ m}^{-3}$).

Tungsten impurity pellet injection into high-temperature magnetically confined plasmas was

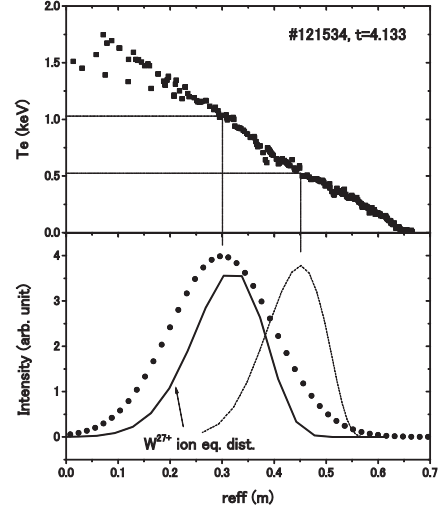


Fig. 8 An intensity distribution of the M1 line at 337.82 nm along the effective minor radius. Upper: Electron temperature distribution. Lower: Radial distributions of the M1 line intensity (dot) and W^{27+} ions calculated assuming the ionization equilibrium with ionization/recombination rate coefficients, ADPAK (solid) [10] and Sasaki (dashed) [11].

successfully performed at the LHD. An M1 line emission of W^{27+} ions due to the ground-term fine-structure transition has been identified in the present experiment, besides the previously identified M1 line of W^{26+} [8]. Vertical profile of the line-integrated intensity of the M1 line on a poloidal cross section serves for investigation of ionization and recombination rate coefficients of tungsten ions which are largely uncertain. The present result poses a puzzle that the measurements cannot be reconciled with rate coefficients by a recent theoretical work [11]. Further investigation is necessary.

Acknowledgement

The authors acknowledge all members of the LHD experiment group for their technical supports. This work is performed with the support and under the auspices of the NIFS Collaboration Research program (NIFS13KLPPF032) and JSPS-NRF-NSFC A3 Foresight Program in the field of Plasma Physics (NSFC: No.11261140328, NRF: 2012K2A2A6000443).

References

- [1] A. Kallenbach et al., *Plasma Phys. Control. Fusion B* 47 (2005) 207.
- [2] A. Komatsu et al., *Phys. Scr.* T144 (2011) 014012.
- [3] A. Komatsu et al., *Plasma and Fusion Res.: Rapid Communications*, 7 (2012) 1201158.
- [4] H. Watanabe et al., *Canadian J. Phys.* 90 (2012) 497.
- [5] X.-B. Ding et al., *J. Phys. B: At. Mol. Opt. Phys.* 44 (2011) 145004.
- [6] Z. Fei et al., *Phys. Rev. A* 86 (2012) 062501.
- [7] A. Bar-Shalom, M. Klapisch and J. Oreg, *J. Quant. Spectrosc. Radiat. Transfer* 71 (2001) 169.
- [8] D. Kato et al., *Phys. Scr.* T156 (2013) 014081.
- [9] H. Nihei et al., *Rev. Sci. Instrum.* 71 (2000) 3747.
- [10] K. Asmussen et al., *Nucl. Fusion* 38 (1998) 967.
- [11] A. Sasaki and I. Murakami, *J. Phys. B: At. Mol. Opt. Phys.* 46 (2013) 175701.

The First Announcement

The 5th China-Japan-Korea Joint Seminar on Atomic and Molecular Processes in Plasma (AMPP2014)

Jul. 28 – Aug. 1, 2014, Lanzhou, China

The seminar is scheduled as one of the academic activities of the project which entitled “Study on critical physics issues specific to steady state sustainment of high-performance plasmas” under the China-Japan-Korea A3 Foresight Program. The seminar will be organized for discussions on the atomic and molecular processes related to the plasma physics and also on the plasma analysis in close relation to the atomic and molecular physics. This seminar is an extension of the last four seminars which were also held by Northwest Normal University at Lanzhou in March 2004, Dunhuang in October 2007, Xian in October 2009, and Lanzhou in July 2012.

➤ **Scope of the Seminar**

In the laboratory and astrophysical plasmas, a variety of atomic processes exists such as photo-excitation and ionization, electron-impact excitation and ionization, heavy particle impact excitation, ionization and charge transfer, etc. The knowledge of these atomic processes is essential for the simulations and diagnostics on plasma properties. This joint seminar provides a chance for the researchers, who are working in the fields of atomic and molecular physics and plasma physics, to exchange their recent progress and discuss the future collaborations.

The seminar will include the following subjects for discussion:

1. Spectroscopic properties of atoms and molecules in plasma
2. Atomic collision dynamics in plasma
3. Plasma simulation and diagnostics
4. Atomic and molecular process in boundary plasmas and erosion dynamics in plasma wall interaction
5. Atomic and molecular data assessment and database construction

➤ **Scientific Sessions and Publication of the Proceedings**

1. All the participants who give a contribution are kindly requested to give an oral presentation for about 35 minutes; 25-30 minutes will be for talk, and 5-10 minutes for discussion.
2. We will supply the high-definition projector connected with laptop. A Windows-based laptop with Acrobat Reader and Microsoft PowerPoint 2007 is available. The participant is requested to supply their presentation material by CD-ROM or flash disk.
3. The contributions to this seminar will be published as one of the issues in the NIFS Research Report series. The details of the instruction for the submission will be announced at the seminar.

➤ **Registration and Fee**

It is recommended that you should contact with the Seminar Secretary or the Chairman of the seminar. We will make reservation of the hotel for all participants. The local committee will arrange some local colleagues and a small bus to meet the participants in the airport in Jul. 28, 2014 .

The fee for full registration attendee is CNY 2,500. It includes: full access to all the Scientific Program, book of abstracts, tea/coffee breaks, conference receptions and shuttle bus to the airport. The fee for lunch, dinner and banquet are also included. The fee for student attendee is CNY 1,700. The fee for accompanying person is CNY 1,200. The payment can ONLY be made by CASH. It is also convenient to take cash from the ATM by Visa/Master Card.

➤ Important Date

Jun. 10, 2014: If you are interested in this seminar, please contact the Seminar Secretary (dingxb@nwnu.edu.cn) before this date. If you would like to attend the seminar, it's better to tell us the tentative title of your talk or abstract even the manuscript.

Jul. 5, 2014: The deadline for submission of abstract. The abstract template will be available soon.

➤ Contact Information

Prof. Dr. Chenzhong Dong
Email: dongcz@nwnu.edu.cn
Tel: +86-931-797-1935
Fax: +86-931-776-8159
Mail: Northwest Normal University,
Anning East Road 967, Anning, Lanzhou
730070 China

Prof. Dr. Daiji Kato
Email: kato.daiji@nifs.ac.jp
Tel: +81-572-58-2260
Fax: +81-572-58-2628
Mail: National Institute for Fusion Science,
Oroshi-cho 322-6, Toki
509-5292, Gifu, Japan

➤ Seminar Secretary

Dr. Xiaobin Ding
Email: dingxb@nwnu.edu.cn
Alternative Email: ding.xiaobin2004@gmail.com
Phone: +86-139-0944-1978

➤ Sponsored by



National Science Foundation of China (NSFC)



Key Laboratory of Atomic and Molecular Physics & Functional Materials of
Gansu Province

Northwest Normal University (NWNU), China

Physical Society of Gansu, China

*This announcement also available at <http://ampfm.nwnu.edu.cn/templates/article.php?id=44>

The 5th China-Japan Joint Seminar on Atomic and Molecular Processes in Plasma

Scientific Program

July 28-August 1, 2014, Lanzhou, China

Tuesday, 29th July, 2014

Time	Title	
08:30-09:10	Opening Ceremony Chair: C. Z. Dong	
	Opening, Welcome address, Group Photo	
09:10-10:20	Session 1 Chair: H. Tanuma	
09:10-09:45	S. Morita	Intensity ratio among Ne-like Fe XVII n=3-2 transitions
09:45-10:20	X. Gao	A scenario for providing the atomic data with spectroscopic in a unified way
10:20-10:40	Coffee Break	
10:40-11:50	Session 2 Chair: J. M. Li	
10:40-11:15	H. Nishimura	Quantitative Ka line spectroscopy for energy transport in hot dense plasma generated with ultra-intense laser
11:15-11:50	T. Nishikawa	Atomic process modeling based on the nearest neighbor approximation
12:00-14:30	Lunch	
14:30-16:15	Session 3 Chair: S. Morita	
14:30-15:05	Z. Y. Cui	Edge impurity transport study based on VUV spectroscopy in the HL-2A tokamak
15:05-15:40	T. Oishi	Line spectrum and ion temperature of Tungsten ions at low ionization stage in Large Helical Device measured using VUV spectroscopy in wavelength range of 500-2200 Å
15:40-16:15	C. F. Dong	Spatial profile measurement and analysis of EUV impurity spectra in HL-1A tokamak
16:15-16:35	Coffee Break	
16:35-17:45	Session 4 Chair: Z. Y. Cui	

16:35-17:10	F. Koike	Electron correlation effects appeared in the lifetimes of subvalence shell vacancy states in atomic ions
17:10-17:45	Y. Wu	Theoretical investigation of ion-atom/molecule collisions in the low and intermediate energy range

Wednesday, 30th, 2014

08:30-10:15	Session 5 Chair: F. Koike	
08:30-09:05	A. M. Imai	Electron capture cross section scalings for low-q heavy ions
09:05-09:40	C. Z. Dong	Theoretical study on electron impact excitation and related polarization properties of subsequent photoemission
09:40-10:15	M. Takahashi	Development of time-resolved (e,2e) electron momentum spectroscopy: towards real-time imaging of frontier electron during chemical reaction
10:15-10:35	Coffee Break	
10:35-11:45	Session 6 Chair: L. F. Zhu	
10:35-11:10	H. Tanuma	How do we observe the forbidden lines from He-like ions in charge exchange collisions of H-like ions with neutral gases ?
10:10-11:45	L. F. Zhu	High resolution X-ray scattering and its applications in atomic and molecular physics
12:00-14:30	Lunch	
14:30-18:00	Local Committee	
	City Excursion	

Thursday, 31st July, 2014

08:30-10:15	Session 7 Chair: N. Nakamura	
08:30-09:05	B. W. Li	Recent progress in plasma spectroscopy and sources development for beyond EUB lithography and other applications
09:05-09:40	T. Higashiguchi	Laser-produced multi-charged heavy ions as efficient soft x-ray sources
09:40-10:15	J. Jiang	Tune-out wavelengths for potassium
10:15-10:35	Coffee Break	

10:35-11:45	Session 8 Chair: M. Imai	
10:35-11:10	N. Nakamura	Lost resonance lines in promethiumlike heavy ions
11:10-11:45	H. A. Sakaue	EUV spectrum of highly charged tungsten ions in LHD with help of CoBIT
12:00-14:30	Lunch	
14:30-16:15	Session 9 Chair: H. Nishimura	
14:30-15:05	K. Wang	Systematic calculations of energy levels and radiative rates of C-like ions with $Z=13-36$ using a combined configuration interaction and many-body perturbation theory approach
15:05-15:40	D. Kato	UV-visible M1 line emission from highly charged tungsten ions in LHD plasmas
15:40-16:15	D. H. Zhang	Theoretical investigation on electron impact ionization processes of W^{3+} and W^{17+} ions
16:15-16:35	Coffee Break	
16:35-17:45	Session 10 Chair: X. W. Ma	
16:35-17:10	Q. H. Yuan	Carbonaceous Thin-film Deposited with Radio-frequency Ar/ C_2H_5OH Atmospheric Pressure Plasma Jet
17:10-17:45	X. L. Zhu	Investigation of state-resolved charge exchange in low and intermediate energy ion-atom collisions
17:50-18:10	Closing Ceremony Chair: Daiji Kato	

Collection of Abstracts in AMPP2014

Intensity ratio among Ne-like FeXVII n=3-2 transitions

Shigeru MORITA^{*,†,1}, Xianli HUANG^{†,2}, Tetsutarou OISHI^{*,†,3}, Izumi MURAKAMI^{*,†,4}, Hongming ZHANG^{†,5} and Motoshi GOTO^{*,†,6}

^{*} National Institute for Fusion Science, Toki, Gifu 509-5292, Japan

[†] Department of Fusion Science, SOKENDAI (The Graduate University for Advanced Studies) Toki, Gifu 509-5292, Japan

Radial profiles of FeXVII $3s-2p$ and $3d-2p$ transitions emitted in wavelength range of 15-18Å have been observed in Large Helical Device (LHD) [1], as shown in Fig.1. Emissivity ratios among the FeXVII $n=3-2$ transitions are calculated from the radial emissivity profile, which are calculated from the chord-integrated radial profile by means of Abel inversion [2]. The emissivity ratios obtained among these lines are compared with calculation based on a collisional-radiative (CR) model developed for iron ions. The result reasonably confirms the effect of the electron temperature and the electron density on the emissivity ratios. However, the emissivity of 3C ($2p^53d\ ^1P_1\rightarrow 2p^6$) transition is obviously lower than the prediction from the CR model. This discrepancy is consistent with measurements in the solar corona and other laboratory plasmas.

References

- [1] X.L.Huang, S.Morita, T.Oishi, et.al., to be published in J. Korean Phys. Soc.
 [2] X.L.Huang, S.Morita, T.Oishi, et.al., Rev. Sci. Instrum. **85** (2014) 043511.

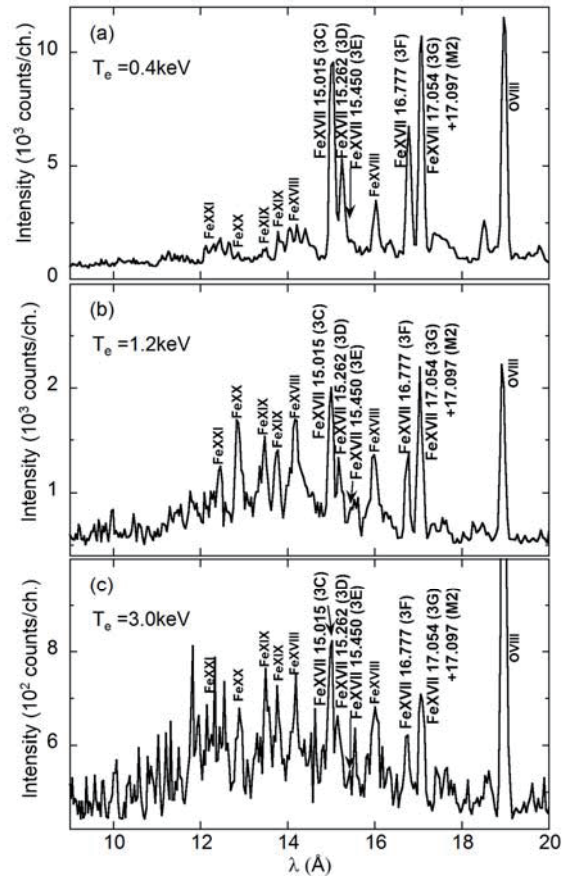


Fig.1 EUV spectra of Ne-like FeXVII n=3-2 transitions in discharges with different electron temperatures of (a) 0.4 keV, (b) 1.2 keV and (c) 3.0 keV.

¹ E-mail: morita@nifs.ac.jp

² E-mail: huang.xianli@nifs.ac.jp

³ E-mail: oishi@nifs.ac.jp

⁴ E-mail: mizumi@nifs.ac.jp

⁵ E-mail: zhang.hongming@nifs.ac.jp

⁶ E-mail: goto@nifs.ac.jp

A scenario for providing the atomic data with spectroscopic precision in a unified way

Xiang Gao^{*,1}, Jia-Ming Li^{†,2}

^{*} Beijing Computational Science Research Center, Beijing, 100084, China

[†] Key Laboratory for Laser Plasmas (Ministry of Education) and Department of Physics, Shanghai Jiao Tong University, Shanghai, China, 200240; Department of Physics and Center for Atomic and Molecular Nanosciences, Tsinghua University, Beijing, 100084, China; Collaborative Innovation Center of Quantum Matter, Beijing, 100084, China

The electron and photon scattering data of an atom are crucial for many scientific fields, including plasma physics, astrophysics, and so on. Because the above-mentioned scientific research fields advance into precision physics stage, the necessary atomic data are not only enormous but also accurate enough for their requirements. Therefore, the mission to compile such atomic data cannot be finished only by experimental measurements. Theoretical computations should play indispensable role to satisfy needs. Numerous efforts as well as progress have been made in this field during the recent 60 years. However the physical precisions of the electron-ion scattering cross sections are difficult to be determined due to the state-of-the-art experiment precisions about 20% of absolute measurements. On the other hand, based on analytic continuation of the scattering matrices, there exist intimate relations between atomic energy levels and the related electron-ion collision processes. According to this property, we propose a scenario to provide such atomic data with enough physical precisions which can be comparable with spectroscopic accuracies readily.

More specifically, we have developed the eigenchannel R-matrix method referred as R-eigen [1,2] to directly calculate scattering matrices as well as eigenchannel wavefunctions in the whole energy regions of interest, i.e., either discrete energy region or continuum energy region, on equal footing. Using our modified R-matrix code R-Eigen, the scattering matrices in the discrete energy region can be calculated with enough accuracy which can be determined readily by comparisons with precise spectroscopic measurements based on Multi-

channel Quantum Defect Theory (MQDT). Through analytical continuation properties, the accuracy of short-range scattering matrices can be ascertained. From the calculated short-range scattering matrices, we can obtain all energy levels and the related scattering cross sections with accuracies comparable with spectroscopic precision. With the corresponding high-quality eigenchannel wavefunctions, various transition matrix elements can be readily calculated, such as the optical oscillator strength densities (OOSD) and the generalized oscillator strength densities (GOSD). The GOSD is directly related with the high-energy electron impact excitation cross sections. In eigenchannel representation, the GOSD curves of the excited states in an eigenchannel form a surface, which is a smooth function of the momentum transfers and the excitation energies. From such smooth GOSDs, we can obtain the generalized oscillator strength of any specific excited state through MQDT, e.g. infinite Rydberg (including strongly perturbed one), autoionization and continuum states. As an example, we will present our recent calculation results of Kr and Ar, which are in good agreement with available benchmark experiments.

References

- [1] X. Gao, J. M. Li, 2012 *Chin. Phys. Lett.* **29** 033101.
- [2] X. Gao, J. M. Li, 2014 *Phys. Rev. A* **89** 022710.

¹ E-mail: xgao@csrc.ac.cn

² E-mail: lijm@sjtu.edu.cn

Quantitative $K\alpha$ line spectroscopy for energy transport in hot dense plasma generated with ultra-intense laser

H. Nishimura¹, Z. Zhang¹, T. Ikenouchi¹, S. Fujioka¹, Y. Arikawa¹, M. Nakai¹, H. Chen², J. Park², G. J. Williams², T. Ozaki³, H. Shiraga¹, S. Kojima¹, H. Hosoda¹, N. Miyanaga¹, J. Kawanaka¹, Y. Nakata¹, T. Jitsuno¹ and H. Azechi¹

1) Institute of Laser Engineering, Osaka University, 2-6 Yamada-oka, Suita, Osaka 565-0871, Japan

2) Lawrence Livermore National Laboratory, Livermore, California 94550, USA

3) National Institute for Fusion Science, LHD, High Temperature Plasma G. 322-6 Oroshi Toki, Gifu 509-5292, Japan

$K\alpha$ emission, caused by hot electrons propagation in a hot dense matter, can provide abundant information about the laser plasma interaction. Quantitative $K\alpha$ line spectroscopy is a potential method to derive energy transfer efficiency from laser to hot electrons. A Laue spectrometer, composed of a cylindrically curved crystal and a detector, has been developed and calibrated absolutely for high energy x-rays ranging from 17 to 77 keV. Either a visible CCD detector coupled to a CsI phosphor screen or a sheet of imaging plate can be chosen as detector. The absolute sensitivity of the spectrometer system was calibrated using pre-characterized laser-produced x-ray sources^[1] and radioisotopes, for the detectors and crystal respectively. The integrated reflectivity for the crystal is in good agreement with predictions by an open code for x-ray diffraction.

The energy transfer efficiency from incident laser beams to hot electrons, as the energy transfer agency is derived as a consequence of this work. The absolute yield

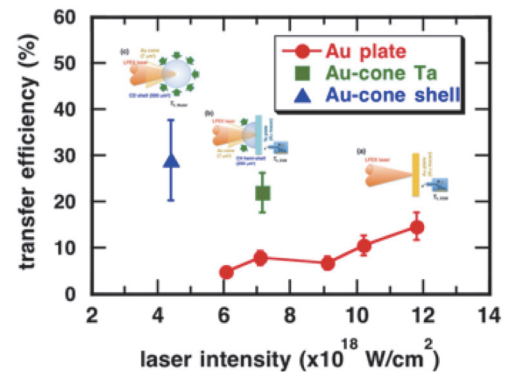


Figure 1: The transfer efficiency as a function of the laser intensity for three targets.

of Au and Ta $K\alpha$ lines were measured in the fast ignition experimental campaign performed at ILE Osaka U.. By applying the electron energy distribution from ESM data and scaling laws, energy transfer efficiency of incident LFEX, a kJ-class PW laser, to hot electrons was derived, as shown in Fig. 1.

References

[1]. Z. Zhang, et. al., Opt. Exp. **19**, 4560 (2011)

¹E-mail: nishimu@ile.osaka-u.ac.jp

Atomic process modeling based on nearest neighbor approximation

Takeshi NISHIKAWA¹

Graduate School of Natural Science and Technology, Okayama University,
3-1-1 Tsushima-naka, Okayama 700-8530, Japan

The atomic models based on the microfield in a plasma are conventionally used to solve the atomic processes in the plasma. Basically, the microfield-based atomic models do not treated the effect of the plasma on the free-electron state density. I propose a new atomic model in a plasma based on the nearest-neighbor approximation. Using this new model, one can evaluate the free-state density without making any ad-hoc assumptions.

In the atomic model based on the nearest-neighbor approximation, the electron-state densities are evaluated using the potential distribution formed by the superposition of the Coulomb potentials of two nearby ions. In order to evaluate the potential distribution, we need a distribution function of the nearest-neighbor ions. In the following, I discuss the simplest case of hydrogenic plasmas without Coulomb correlations. If the ions are evenly distributed in space, the probability of finding an ion in a small volume δV is given by $N_i \delta V$, where N_i is the ion number density. If there are no ions inside the ion sphere of radius R , and only one ion is found on the surface, the probability of finding the nearest-neighbor ion at R is given by [1]:

$$\begin{aligned} P(R) dR &= (1 - N_i \delta V)^{4\pi R^3/3\delta V} 4\pi R^2 N_i dR \\ &= 4\pi R^2 N_i \exp\left(-\frac{4}{3}\pi R^3 N_i\right) dR. \end{aligned}$$

If once the distribution function of the nearest-neighbor ions is obtained, we can compute the state densities for the free and bound electron from the potential profile formed by the two nearby ions. Typical results are shown in Figs. 1 and 2.

I will also show the results for higher densities case in which we cannot neglect the Coulomb correlation between a pair of ions.

References

- [1] Lochte-Holtgreven W 1968 *Plasma Diagnostics* (North-Holland) p. 81

¹E-mail: nishikawa.takeshi@okayama-u.ac.jp

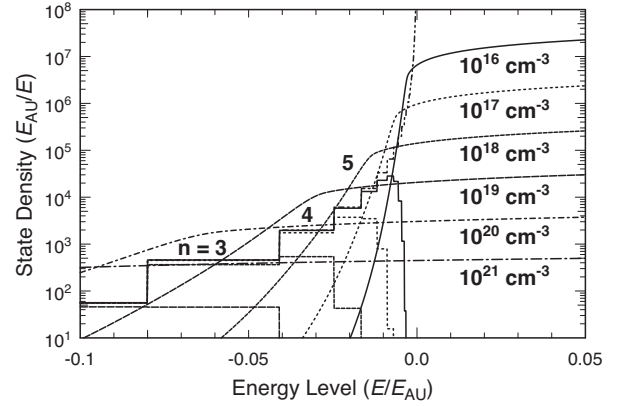


Fig. 1. State densities of bound and free electrons for various ion number densities in a fully ionized hydrogenic plasma, as obtained by an atomic model based on the nearest-neighbor approximation. The evaluated free-state density is significantly greater than the densities of the bound electron states that disappear at the corresponding energy.

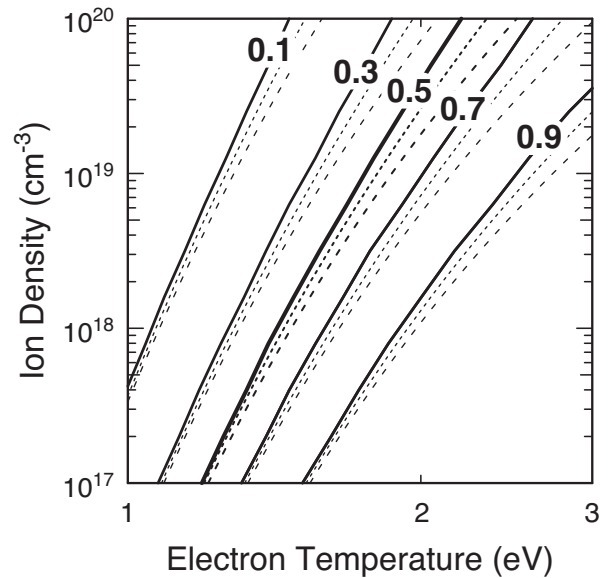


Fig. 2. Ionization degree of a hydrogenic plasma for various state-density models for bound and free electrons. The solid curves were obtained using the nearest-neighbor approximation. The dotted curves were the results using the plasma-microfield model. The dashed curves were the results obtained using the free-state density of free space.

Edge impurity transport study based on VUV spectroscopy in the HL-2A tokamak

Z. Y. Cui¹, S. Morita², C. F. Dong¹, H. Y. Zhou¹, X. T. Ding¹, P. Sun¹, M. Kobayashi², X. W. Cui¹, Y. Xu¹, X. L. Huang¹, Z. B. Shi¹, J. Cheng¹, Y. G. Li¹, B. B. Feng¹, S. D. Song¹, L. W. Yan¹, Q. W. Yang¹ and X. R. Duan¹

¹Southwestern Institute of Physics, P. O. Box 432, Chengdu 610041, China

²National Institute for Fusion Science, Toki, Gifu 509-5292, Japan

Impurity study is one of important issues in the fusion research since light and heavy impurities can cause fuel dilution and radiation loss in the plasma core, respectively. Spectroscopy is commonly used to monitor the impurity content and to study the impurity transport in fusion devices. In addition, basic plasma parameters necessary for the plasma confinement study such as electron temperature, T_e , ion temperature, T_i , plasma rotation velocity, V_p , and effective ion charge, Z_{eff} , can be also obtained through the spectroscopy measurements.

In the HL-2A tokamak, a 1 meter normal-incidence Rowland circle vacuum ultraviolet (VUV) spectrometer [1] has been utilized for measuring the impurity line emissions in the wavelength ranges of 300-3200 Å. The spectrometer has been equipped with a back illuminated charge-coupled device (CCD) with size of 6.6×26.6 mm² (255×1024 pixels). The radial profile of impurity line emissions has been measured by using the VUV spectrometer which has an excellent spatial resolution of 2 mm. The absolute calibration of the VUV spectrometer has been done *in situ* using the bremsstrahlung continuum radiation from the HL-2A plasma.

Based on the radial profile of carbon emissions of CV (2271 Å: 1s2s ³S-1s2p ³P) and CIV (1548 Å: 1s²2s ²S-1s²2p ²P) measurements as well as their analysis with a 1-D impurity

transport code [2], the edge impurity transport has been studied with electron cyclotron resonance heating (ECRH) in the HL-2A tokamak [3]. The diffusion coefficient and convective velocity of carbon ions are determined with the absolutely measuring the intensity of the two carbon line emissions. The ratio of CV to CIV can be also used as an index to characterize the edge impurity transport. The ratio measured from Ohmic discharges shows a gradual decrease with electron density. However, the ratio suddenly decreases by a factor of 3 when the ECRH focused in the plasma center is switched on, suggesting a strong enhancement of the impurity transport. The analysis with the transport code indicates a change in the convective term. The convective velocity of C⁴⁺ ions is changed to outward redirection during the ECRH phase, while the inward velocity is usually appeared in the Ohmic phase. The result is in good agreement with the observation in the experiment using the impurity injection [4].

References

- [1] Z.Y. Cui, S. Morita, B. Z. Fu, et al., 2010 *Rev. Sci. Instrum.* **81** 043503.
- [2] R. Dux 2006 *Technical Report* No 10/30 IPP Garching Germany
- [3] Z.Y. Cui, S. Morita, H.Y. Zhou, et al., 2013 *Nucl. Fusion* **53** 093017.
- [4] X.W. Cui, Z.Y. Cui, B.B. Feng, et al., 2013 *Chin. Phys. B* **22** 125201.

¹E-mail: cuizy@swip.ac.cn

Line Spectrum and Ion Temperature of Tungsten Ions at Low Ionization Stages in Large Helical Device Measured Using VUV Spectroscopy in Wavelength Range of 500-2200 Å

T.Oishi^{*,†,1}, S. Morita^{*,†,2}, X. L. Huang^{†,3}, H. M. Zhang^{†,4}, M. Goto^{*,†,5} and LHD Experiment Group*

* National Institute for Fusion Science, 322-6, Oroshi-cho, Toki, 509-5292, Japan

† Department of Fusion Science, Graduate University for Advanced Studies, 322-6, Oroshi-cho, Toki, 509-5292, Japan

Diagnostics of tungsten impurity ions in magnetically-confined high-temperature plasmas has attracted attention because tungsten is regarded as a leading candidate material for the plasma facing component in ITER and future fusion reactors. In the present study, vacuum ultraviolet (VUV) spectra of emissions released from tungsten ions were measured in the Large Helical Device (LHD). Identification of lines which are useful for diagnostics of tungsten ions at low ionization stages was attempted for the study of transport phenomena of tungsten ions in the edge plasmas. For this purpose, a VUV spectroscopy using a 3 m normal incidence spectrometer was utilized to measure tungsten lines. The working wavelength range of the spectrometer is 300 to 3200 Å. A back-illuminated CCD detector was placed at the position of the exit slit of the spectrometer. A time resolution of 50 ms was applied to measure the temporal evolution of the spectra. The high wavelength dispersion of 0.037 Å/pixel enabled measurements of the Doppler broadening of the impurity lines to obtain the ion temperature. Tungsten ions were distributed in the LHD plasma by injecting a polyethylene pellet containing a small piece of tungsten metal.

Figure 1 shows VUV spectra measured in the time frame just after the tungsten pellet injection in hydrogen discharge in LHD. The plasma was initiated by the electron cyclotron heating, and three neutral hydrogen beams based on negative ion sources with total port-through power of 8 MW were injected. Central electron density and temperature just before the pellet injection was $2 \times 10^{13} \text{ cm}^{-3}$ and 3 keV, respectively. Well-known intrinsic impurity lines used for absolute wavelength calibration are indicated by solid arrows. Except for those

intrinsic impurity lines, several bright lines have been successfully observed, such as 605.93 Å in Fig. 2(a), 639.66 Å in Fig. 2(b), 677.72 Å in Fig. 2(c), and 1168.15 Å in Fig. 2(d). These lines have wavelengths almost identical to WVI lines with the wavelengths of 605.926 Å, 639.683 Å, 677.722 Å (5d-6p), and 1168.151 Å (6s-6p).

This work was partially conducted under the LHD project financial support (NIFS13ULPP010). This work was also supported by Grant-in-Aid for Young Scientists (B) 26800282 and partially supported by the JSPS-NRF-NSFC A3 Foresight Program in the Field of Plasma Physics (NSFC: No.11261140328).

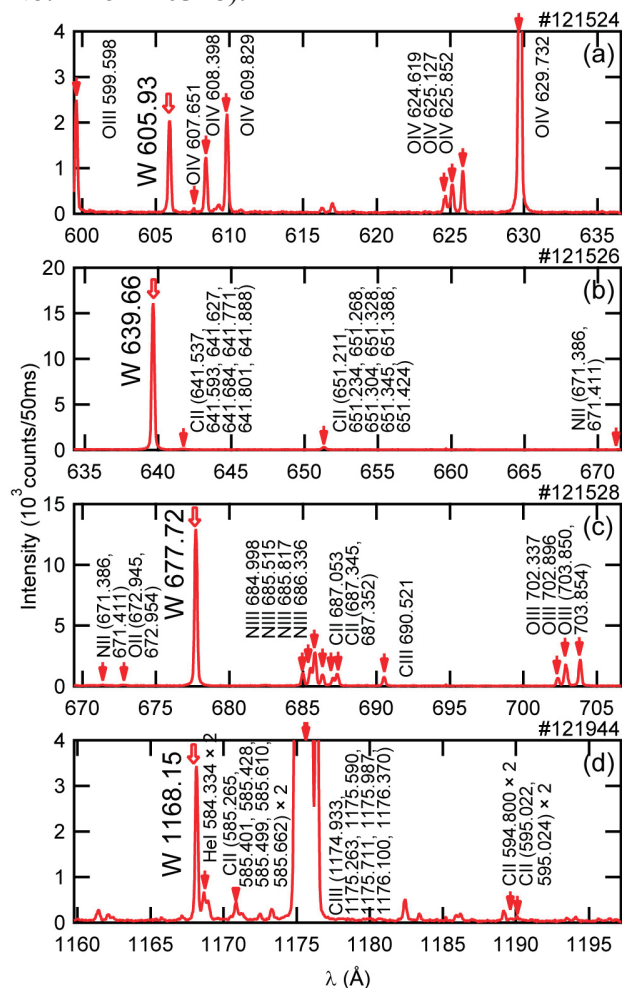


Fig. 1. VUV spectra including tungsten candidate lines measured just after the tungsten pellet injection in LHD.

¹ E-mail: oishi@LHD.nifs.ac.jp

² E-mail: morita@nifs.ac.jp

³ E-mail: huang.xianli@LHD.nifs.ac.jp

⁴ E-mail: zhang.hongming@LHD.nifs.ac.jp

⁵ E-mail: goto@nifs.ac.jp

Spatial profile measurement and analysis of EUV impurity spectra in HL-2A tokamak

Chunfeng Dong¹, Zhengying Cui¹, Hangyu Zhou¹, Shigeru Morita², Ping Sun¹, Bingzhong Fu¹, Ping Lu¹, Yan Zhou¹, Yuan Huang¹, Qingwei Yang¹ and Xuru Duan¹

¹Southwestern Institute of Physics, P. O. Box 432, Chengdu 610041, China

²National Institute for Fusion Science, Toki 509-5292, Japan

Spectroscopy plays an important role in both the impurity diagnostics and the impurity transport study in experiments using magnetically confined fusion devices. With the improvement of confinement properties and the development of heating systems in the past few decades, the plasma temperature has been drastically increased. As a result, most of line emissions from fusion plasmas shift towards shorter wavelength range such as extreme ultraviolet (EUV) range ($10 \leq \lambda \leq 500 \text{ \AA}$), in particular, for highly ionized ions of heavy impurities with high atomic number, e.g., tungsten with $Z=74$. The study of tungsten is an urgently important current topic in fusion research because the tungsten has been designated as a material for ITER divertor plates. A space-resolved EUV spectrometer working in wavelength range of 20-500 Å has been developed for the impurity study in HL-2A tokamak. A gold-coated varied-line-spacing (VLS) holographic grating with curvature of 5600mm and a back-illuminated charge-coupled device (CCD) with size of $6.6 \times 26.6 \text{ mm}^2$

(1024×256 pixels) are equipped to the spectrometer. The widths of entrance slit and space-resolved slit are 30 μm and 0.5mm, respectively. The spectral resolution of 0.22 Å at 200 Å and the spatial resolution is 12mm are achieved. Since the spectrometer is placed at a distance of ~8000 mm away from the plasma center, a half size of HL-2A plasma ($a=400 \text{ mm}$) can be observed. Identification of EUV spectra indicates a small discrepancy between experimentally observed and theoretically calculated reciprocal linear dispersions. The EUV spectra are analyzed using a collisional-radiative model. The result shows a good agreement between the experiment and modeling. It is also observed that the siliconization applied for the wall conditioning of HL-2A vacuum vessel significantly reduces oxygen and nitrogen influx, while such an impurity influx quickly recovers to the original level after certain plasma discharges. It may strongly suggest the presence of air leakage in the vacuum vessel including diagnostic ports.

¹E-mail: dongcf@swip.ac.cn

Electron correlation effects appeared in the lifetimes of sub-valence shell vacancy states in atomic ions

F. Koike¹, N. Suzuki, Y. Azuma

Faculty of Science and Technology, Sophia University, 7-1 Kioicho, Chiyoda-ku, Tokyo 102-8554, Japan

Atomic ions with a vacancy in a sub-valence shell may sometimes decay exclusively through radiative transitions to the vacancy-filled ground states. Examples are the $2s$ -hole state of neon singly charged ions or the $3s$ -hole state of argon singly charged ions. These hole states are often correlated to the lowermost excited states, providing us with the opportunity to study the electron correlations without being bothered by non-radiative decay processes. They can be good prototype models for electron correlations that are found in many atomic processes in plasmas.

Recently, Azuma and his collaborators have carried out time-resolved fluorescence spectroscopy measurement of $\text{Ne}^+ 2s2p^6$ and $\text{Ar}^+ 3s3p^6$ radiative decay[1] using the synchrotron photoionization of rare gas atoms.

In the present report, we elaborate large scale calculations for atomic structures and electric dipole transitions of the Ne^+ and Ar^+ systems by means of a multi-configuration Dirac-Fock method[2][3], and discuss the characteristics of electron correlations by comparing the experimental and the theoretical lifetimes.

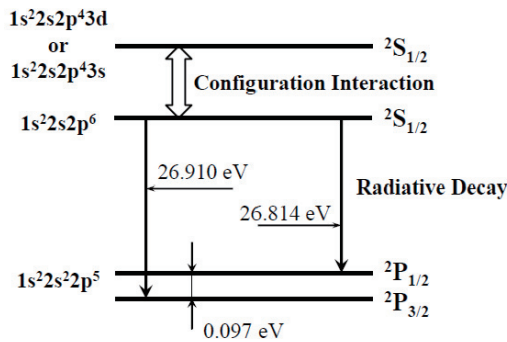


Fig. 1. The energy level diagram of Ne^+

As shown in Fig. 1, the $\text{Ne}^+ 2s2p^6$ sub-valence hole state decays by electric dipole transition into the doublet ground state $\text{Ne}^+ 2s^22p^5 2P_{1/2, 3/2}$. Because the $2s2p^6$ energy level lies close to the $2s2p^43s$ or $2s2p^43d$ energy levels, the hole state may be modified by them

due to the configuration interaction; the $2s$ hole may partially be filled by electron leading to the decay lifetime elongation.

We create a set of orbitals stepwise including higher lying orbitals using a program package GRASP92[2]. For step 1, we employ the minimal basis set that consists of $1s$, $2s$, $2p-$ and $2p$ and consider only the configurations $1s^22s^22p^5$ and $1s^22s2p^6$. For further steps, we consider the contribution from the configurations that contain $3s$, and $3d$ orbitals.

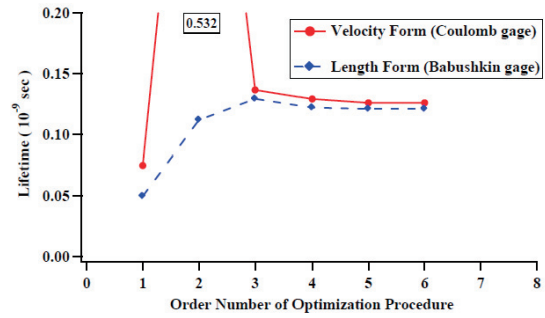


Fig. 2. The lifetime convergence of $\text{Ne}^+ 2s2p^6$

As illustrated in Fig. 2, we have obtained the lifetime $\tau = 0.121$ ns, which is in good agreement with experiment, whereas $\tau = 0.06$ ns in the minimal base calculation. We can see that the $2s2p^43s$ or $2s2p^43d$ configurations modify the transition rate substantially in spite of the small fraction, about 8%, of those configurations in the total atomic state wavefunction.

We have obtained a reasonable agreement with experiment also for $\text{Ar}^+ 3s3p^6$. The details will be presented in the seminar.

References

- [1] Y. Azuma, 2014 private communication.
- [2] Parpia F A, Fischer C F and Grant I P 1996 *Comput. Phys. Commun.* **94** 249.
- [3] Fritzsche S 2012 *Comput. Phys. Commun.* **183** 1525.

¹E-mail: koikef@sophia.ac.jp

Theoretical investigation of ion-atom/molecule collisions in the low and intermediate energy range

Yong Wu¹, Ling Liu, Chunlei Liu, LingLing Yan, Xuhai Hong and Jianguo Wang²

Institute of Applied Physics and Computational Mathematics, P. O. Box 8009, Beijing 100088, P. R. China

In this talk, I will report the recent progresses of our group on the ion-atom/molecule collisions. There are mainly five parts included in the talk:

I) The quantum molecular orbital close-coupling (MOCC) method has been developed to treat the low energy ion-atom collisions (10^{-11} eV - 10keV), especially focusing on the highly charged ions collisions with neutral atom and ultralow energy ion-atom collisions [1].

II) The atomic orbital close-coupling (AOCC) method has been developed to deal with the intermediate energy ion-atom / molecule collisions (from a few hundred eV/u to a few hundred keV/u). For the highly charged ions collisions with neutral atom/molecule, accurate total and state-resolved cross sections can be obtained. The charge exchange (CX) spectrum following the charge exchange process has been simulated and great agreements have been achieved in comparison with the related measurements. The polarization of the spectrum emitted has also been investigated [2].

III) The time-dependent Schrödinger equation (TDSE) method has been developed to handle the intermediate energy (from a few hundred eV/u to a few hundred keV/u) ion-atom collisions for the quasi-one-electron collision system. The method has been applied to H^+-H and $He^{2+}-H$ collisions and excellent agreements have been obtained compared with the available experimental measurements and theoretical calculations. In addition, the TDSE method has been developed to treat the ion-atom collision in the external laser and magnetic fields [3] respectively. Some interesting results have been obtained.

IV) The time-dependent DFT combined with molecular dynamic (TDDFT) method has been developed to treat the ion-atom/molecule collisions in the intermediate energy range (from a few hundred eV/u to a few hundred

keV/u) [4]. Compared with the above MOCC, AOCC and TDSE methods, TDDFT method can treat multi-electron processes in ion-atom /molecule collisions. The limitation of the current TDDFT method is that it can be only applied to obtain precise total cross sections, but the accurate treatment of the excited state and the state-resolved cross sections calculations can't be achieved.

V) The atomic and molecular database has been developed to meet with the atomic and molecular data requirement in the related fields, such as astrophysics and magnetic confined fusion studies. The ion-atom / molecular collisions data have been evaluated for some important systems and sets of recommendation cross sections have been proposed and added into the atomic and molecular database in our institute.

In summary, the MOCC, AOCC, TDDFT and TDSE methods have been developed to treat ion-atom/molecular collisions over a large energy range from about 10^{-11} eV/u to 10^3 keV/u. The excitation, charge transfer, ionization and dissociation processes in collisions can be treated effectively and total and state-resolved cross sections can be computed at a relatively high precision. Various physical effects in the collision processes have been investigated, including the electron-correlation effect, the coupling and interference effects between different channels, the isotopic effects and the polarization of the CX spectrum, *etc.*

References

- [1] L. L. Yan, L. Liu, Y. Wu, Y. Z. Qu, J. G. Wang, and R. J. Buenker, 2013 *Phys. Rev. A* **88**, 012709
- [2] L. Liu, J. G. Wang, and R. K. Janev, 2014 *Phys. Rev. A* **89**, 012710
- [3] C. L. Liu, J. G. Wang etc, 2014, in preparation
- [4] C. L. Zhang, X. H. Hong, F. Wang, Y. Wu, and J. G. Wang, 2013 *Phys. Rev. A* **87**, 032711

¹ E-mail: wu_yong@iapcm.ac.cn

² E-mail: wang_jianguo@iapcm.ac.cn

Electron capture cross section scalings for low- q heavy ions

Alex M Imai^{*,1}

^{*}Department of Nuclear Engineering, Kyoto University, Kyoto 615-8540, Japan

For high- q projectile ions in low collision energy range, the collision processes of which are exothermic, some scaling rules were introduced to predict electron capture cross sections using the initial charge state q of the projectile ion and the ionization potential (IP) of the target gas [1–3]. No such scaling behavior has been reported, however, for low- q projectile ions, for which the collision processes tend to expand into endothermic region. A new attempt has been made to scale electron capture cross sections for such low- q projectile ions in low collision energy range using ΔIP , *i.e.*, the first ionization potential of a target atom/molecule subtracted by that of the projectile ion after electron capture, which corresponds to the energy defect of the collision process in case all the involved projectile and target particles before and after the collision are in the ground states. Experimental cross sections used in the scalings were obtained in our laboratory for Be^{q+} , B^{q+} , C^{q+} , Fe^{q+} , Ni^{q+} , and W^{q+} ($q = 1, 2$) projectile ions on atomic and molecular gas targets of He, Ne, Ar, Kr, H_2 , CH_4 , C_2H_6 , C_3H_8 , CO , CH_2 , and N_2 at collision energy between 4 and 25 keV [4–7].

The measured single electron capture cross sections for singly and doubly charged projectile ions are plotted as a function of ΔIP . The cross sections decrease rather gradually up to ΔIP around -2 eV and turn to decrease steeply by three orders of magnitude between -1 and $+15$ eV as ΔIP increases. This picture suggests a possibility of scaling electron capture cross sections for not only exothermic but also endothermic collision processes for slow low- q projectile ions using ΔIP . Since the horizontal axis expands into the negative values, the IP power-law dependence used in the existing scaling rules for high- q ions [1–3] cannot be applied, and fits to exponential functions have been attempted to formulate the behavior respectively for exo- and endothermic regions as

$$\sigma_{\text{exo}} (\text{cm}^2) = 7.45 \times 10^{-16} \times 10^{-0.029 \Delta\text{IP} (\text{eV})},$$

$$\sigma_{\text{endo}} (\text{cm}^2) = 7.13 \times 10^{-16} \times 10^{-0.17 \Delta\text{IP} (\text{eV})},$$

which reproduced the measured cross sections within -0.57 to 0.62 order of magnitude for exothermic processes and within -1.36 to 0.64 order of magnitude for endothermic processes. Another fitting attempt has been made, individually and collectively, for singly and doubly charged projectile ions and for atomic and molecular targets, which reproduced the measured cross sections almost within an order of magnitude. The more specific the scaling was, *i.e.*, for limited initial charge state and target species, the smaller the deviation became [5].

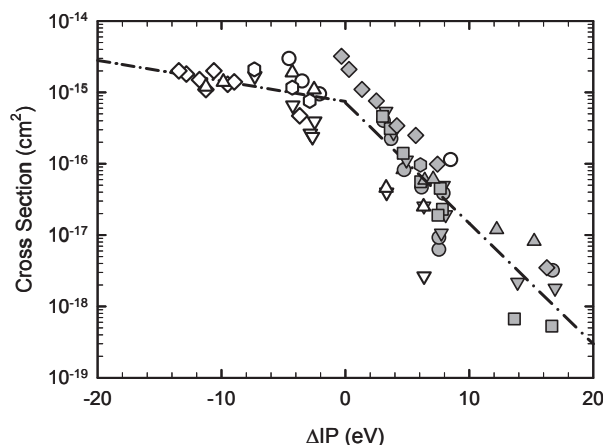


Fig. 1. Single-electron-capture cross sections as a function of ΔIP , the first ionization potential (IP) of the target minus that of the projectile ion after electron capture. The dotted-dashed line denotes exponential fit to the cross sections made separately in the exo- and endothermic regions

References

- [1] A Mueller and E Salzborn 1977 *Phys. Lett. A* **62** 391
- [2] T Kusakabe *et al* 1986 *J. Phys. B* **19** 2165
- [3] I Yamada *et al* 1999 *Abstracts of the 21st ICPEAC, Sendai, Japan* 553
- [4] A Itoh *et al* 1995 *J. Phys. Soc. Jpn.* **64** 3255
- [5] M Imai *et al* 2006 *J. Plasma Fusion Res. Ser.* **7** 323
- [6] M V Khoma *et al* 2008 *Chem. Phys.* **352** 142
- [7] I Yu Tolstikhina *et al* 2012 *J. Phys. B* **45** 145201

¹ E-mail: imai@nucleng.kyoto-u.ac.jp

Theoretical study on electron impact excitation and related polarization properties of subsequent photoemission

C. Z. Dong, Z. B. Chen, J. Jiang, Z. W. Wu, and L.Y. Xie

Key Laboratory of Atomic and Molecular Physics and Functional Material of Gansu Province,
College of Physics and Electronic Engineering, Northwest Normal University, Lanzhou 730070, China

Electron-impact excitation (EIE) is one of the most important atomic processes occurred frequently in various laboratory and astrophysical plasmas. From the polarization and angular distribution of decay products following the collision process, valuable information can be obtained for both the collision dynamics and the magnetic sublevel population of the impact excited states. These polarization data become indispensable for the detailed diagnosis of plasma state and the analysis of complex spectra formation mechanism. To satisfy application requirements, various activities have been attempted to compile data and develop databases. However, the accuracy of these available polarization data is often suspects, different calculations using similar methods/codes sometimes differ so much due to the presence of the higher order effects.

On the basis of the well-known GRASP92/2K and RATIP packages [1], a new fully relativistic distorted wave program, named REIE06 has been developed by our group in recent. In this presentation, some selected applications of the program are shown. A special attention has been paid on influences of the higher order effects to the polarization properties of the subsequent photonemission following EIE process. Such as, the effects of intermediate resonance states in an isolated resonance approximation [2], the effects of Breit interactions [3], the effects of $E1-M2$

interference [4], the effects of plasma screening [5] and so on [6]. We hope these efforts will be helpful for further understanding the contributions from the higher order effects and getting more accurate polarization data.

References

- [1] P Jonsson, X. He, C.F. Fischer and I. P. Grant, CPC 177, 597 (2007); S. Fritzsche, H. Aksela, and C. Z. Dong et al. Nucl. Instrum. Methods Phys. Res. B 205, 93 (2003)
- [2] J. Jiang, C. Z. Dong, L. Y. Xie, and J. G. Wang, Phys. Rev. A 78, 022709 (2008)
- [3] Z. W. Wu, J. Jiang, and C. Z. Dong, Phys. Rev. A 84, 032713 (2011)
- [4] Z. B. Chen, C. Z. Dong, L. Y. Xie, and J. Jiang, Phys. Rev. A 89, 022513 (2014)
- [5] B. W. Li, C. Z. Dong, J. Jiang, and J. G. Wang, Eur. Phys. J. D 59 201(2010)
- [6] Z. W. Wu, C. Z. Dong, and J. Jiang, Phys. Rev. A 86, 022712 (2012)

E-mail: dongcz@nwnu.edu.cn

Development of time-resolved (e,2e) electron momentum spectroscopy: towards real-time imaging of frontier electron during chemical reaction

Masahiko Takahashi

Institute of Multidisciplinary Research for Advanced Materials, Tohoku University, Sendai 980-8577, Japan

Electron momentum spectroscopy (EMS) is an (e,2e) experiment at large momentum transfer or a kinematically-complete electron-impact ionization experiment performed under the Compton scattering conditions. It is now well documented that EMS is a powerful means for studying spectral electron momentum densities in matter [1]. Since the early 1990s, we have been directing our efforts towards expanding frontiers of this promising research area [2]. For instance, measurements of 3-dimensional electron momentum densities of gaseous, isolated molecules have for the first time been made [3], as well as studies on such as the first observation of the giant resonance phenomenon in the 2nd-order electron-target interaction [4] and the first experimental determination of spatial orientation of the constituent atomic orbitals in molecular orbitals [5].

Based on the above-mentioned achievements in traditional EMS, we are now trying to move forward by leaps and bounds by developing a time-resolved EMS (TREMS) apparatus [6], which can be realized by the substitution of an ultra-short pulsed incident electron beam for the cw-type continuous electron beam. TREMS would inherently possess the ability to probe the change of electron motion in a transient species or to take snapshots of the changing molecular orbitals in momentum space, which is the driving force behind any chemical reaction. We have recently applied the TREMS apparatus to the 195 nm photo-induced three-body dissociation dynamics of the acetone molecule [7].

Despite the poor statistics and time-resolution of the data, however, the experimental results have represented the first time that the change of the frontier-electron motion during chemical reaction has been observed, thus exploring previously uncharted areas of photo-induced ultrafast dynamics. If the instrumental performance could be improved satisfactorily, it would also make it possible to study, for instance, electronic structures of laser-dressed states [8]. In this contribution, we report the present status and perspective of TREMS, together with its technical details.

References

- [1] E. Weigold and I. E. McCarthy, *Electron Momentum Spectroscopy*, Kluwer/Plenum, New York (1999).
- [2] M. Takahashi, 2009 *Bull. Chem. Soc. Jpn.* **82** 751.
- [3] M. Takahashi, N. Watanabe, Y. Khajuria, Y. Udagawa, and J.H.D. Eland, 2005 *Phys. Rev. Lett.* **94** 213202.
- [4] M. Takahashi, Y. Miyake, N. Watanabe, Y. Udagawa, Y. Sakai, and T. Mukoyama, 2007 *Phys. Rev. Lett.* **98** 013201.
- [5] N. Watanabe, X. J. Chen, and M. Takahashi, 2012 *Phys. Rev. Lett.* **108** 173201.
- [6] M. Yamazaki, Y. Kasai, K. Oishi, H. Nakazawa, and M. Takahashi, 2013 *Rev. Sci. Instrum.* **84** 063105.
- [7] M. Yamazaki, Y. Kasai, K. Oishi, H. Nakazawa, and M. Takahashi, 2013 *XXVIII ICPEAC Abstracts of Contributed Papers*.
- [8] K. A. Kouzakov, Yu. V. Popov, and M. Takahashi, 2010 *Phys. Rev. A.* **82** 023410.

How do we observe the forbidden lines from He-like ions in charge exchange collisions of H-like ions with neutral gases?

Hajime Tanuma^{*,1}, Hirofumi Shimaya^{*}, Takuya Ishida^{*}, Nobuyuki Nakamura[†], Naoki Numadate[‡], and Kunihiro Okada[‡]

^{*}Tokyo Metropolitan University, 1-1 Minami-Ohsawa, Hachioji, Tokyo 192-0397, Japan

[†]University of Electro-Communications, 1-5-1 Chofugaoka, Chofu, Tokyo 182-0021, Japan

[‡]Sophia University, 7-1 Kioicho, Chiyoda, Tokyo 102-8554, Japan

Generally speaking, in charge exchange collisions of multiply charged ions with neutral target gases, single electron captures are dominant reaction processes. Therefore, both singlet and triplet states of helium-like ions might be produced in the collisions of hydrogen-like ions. The transitions between $1s^2\ ^1S_0$ and $1s2s\ ^3S_1$ are optically forbidden with very long lifetimes, and the inter-combination lines between $1s^2\ ^1S_0$ and $1s2p\ ^3P_J$ ($J = 1, 2$) have also longer lifetimes than typical electric dipole allowed transitions. For example, these lifetimes of O^{6+} ions are about 1 ms, 2 ns, and 3 μ s, respectively. However, it is very difficult to measure the emission cross sections of the transitions with long lifetimes in the ordinary ion beam collision experiments.

On the other hand, the soft x-ray emissions by the solar wind charge exchange, which have been observed by the x-ray observatory satellites, might consist of the resonance lines, inter-combination lines, and forbidden lines, even though the separation of these lines has not been performed yet, because the energy resolution of the spectrometers in the satellites is not enough for this purpose [1, 2]. Therefore, the observation of the forbidden lines in the laboratory must be carried out to measure the emission cross sections for the quantitative analysis of the observed spectra by the satellites.

We had observed the soft x-ray emission spectra in collisions of multiply charged ions with He using a 14.25 GHz ECR (electron cyclotron resonance) ion source and window-less solid state detectors, namely, Si(Li) detector

(Oxford, model 6834) and silicon drift detector (PGT, SDD100145WL) [3, 4]. These spectra correspond to only the resonance lines, $1s^2\ ^1S_0 - 1snp\ ^1P_1^o$ ($n = 2 - 5$), with very short lifetimes of less than 1 ps, because the emission from the collision center had been observed in our experimental setup. Therefore, in order to observe the forbidden transitions of helium-like ions produced in collisions of hydrogen-like solar wind ions with neutral gases, we have developed a Kingdon ion trap.

This trap is an electrostatic ion trap which has a very simple structure with a cylinder electrode, central wire, and two end caps [5]. The performance of this trap had been tested with the injection of multiply charged ions in it [6]. The maximum of the storage time depends on the background pressure, because the charge exchange process dominates in the trap.

Now we have just started the experiment for the observation of the forbidden transition from O^{6+} ($1s2s\ ^3S_1$) produced in collisions of O^{7+} with H_2 and He.

References

- [1] C. M. Lisse *et al.*, 2001, *Science* **292**, 1343.
- [2] R. Fujimoto, K. Mitsuda, D. McCammon *et al.*, 2007, *Publ. Astron. Soc. Jpn.* **59**, S133.
- [3] T. Kanda *et al.*, 2011, *Phys. Scr.* **T144**, 014025.
- [4] H. Shimaya, T. Ishida, S. Ishikawa *et al.*, 2013, *Phys. Scr.* **T156**, 014002.
- [5] K. H. Kingdon, 1923, *Phys. Rev.* **21**, 408.
- [6] N. Numadate *et al.*, *to be submitted*.

¹E-mail: tanuma-hajime@tmu.ac.jp

High-resolution X-ray scattering and its applications in atomic and molecular physics

Lin-Fan Zhu^{*,1}

* Hefei National Laboratory for Physical Sciences at Microscale, Department of Modern Physics, University of Science and Technology of China, Hefei, Anhui, 230026, China

The dynamic parameters of atoms or molecules were traditionally determined by the electron scattering method, such as the low-energy or high-energy electron scattering methods. However, the electron scattering methods has its intrinsic merits and demerits. One of its merits is the large scattering cross sections, and one of its demerits is the strong interaction between the incident electron and target which leads to the invalidity of the first Born approximate (FBA), and that will strengthen the complexity of theoretical calculations. However, the X-ray scattering method has the advantages that the FBA is almost always satisfied, which provides a powerful tool to study the dynamic parameters and the structures of the ground and excited states of atoms and molecules. In this work, the current status of high-resolution X-ray scattering has been reviewed.

Generally speaking, the disadvantage of X-ray scattering technique is its very low cross sections, i.e., about 10^{-29}m^2 , and it is the reason that the X-ray scattering technique is extensively used in condensed matter physics rather than in atomic and molecular physics. Recently, with the dramatic progress of the third generation synchrotron radiation, it provides the possibility to measure the dynamic parameters and structures of atoms and molecules by using the high-resolution X-ray scattering technique.

X-ray scattering technique can be classified into resonant and nonresonant X-ray scattering according to the interaction between the X-ray and the target. If the incident photon energy matches the excitation energy of an atom or a molecule (commonly it is an inner shell excitation), the corresponding scattering is the resonant X-ray scattering (RXS), which can be treated as a two-step processes, i.e., a photoabsorption process followed by a photoemission process. The RXS has a large cross sections and it is out of this review. If the incident photon energy does not match the excitation energy of an atom or a molecule (generally the incident photon energy is much larger than the excitation energy), the corresponding scattering is the non-resonant X-ray scattering (NRXS), which is a one-step

processes. NRXS has very low cross sections and can be classified into elastic X-ray scattering (EXS), inelastic X-ray scattering (IXS) and Compton scattering (CS).

Very recently, the high-resolution EXS and IXS have been successfully applied to measure the benchmark data of the dynamic parameters of atoms and molecules [1-5]. And some investigations [3-4] show that the FBA is not sufficient to describe the high-energy electron collision process, even for several keV collision energies. Since the IXS is a weak probe and free from the high-order Born term, it is very appropriate to study the structures of the ground and excited states of atoms and molecules. It should be emphasized that the experimental technique of IXS is greatly different from the traditional high-energy electron energy loss spectroscopy (EELS), e.g., the target density in the work of IXS is about 10 atm while it is about 10^{-4} – 10^{-2} Pa in the traditional EELS. Therefore, the measured dynamic parameters by IXS and high-energy EELS provides an independent crosscheck. Furthermore, our investigation show that the pure electronic structure of a molecule in the ground state can be determined by EXS while it cannot be obtained by the high-energy EELS.

Using the Compton scattering technique, one can obtain the target's Compton profile which is the projection on z direction of the electron density in momentum space. The recent development is that the experimental accuracy has been improved greatly.

References

- [1] B. P. Xie, L. F. Zhu, K. Yang et al., 2010 *Phys. Rev. A* **82** 032501.
- [2] L. F. Zhu, L. S. Wang, B. P. Xie et al., 2011 *J. phys. B* **44** 025203.
- [3] L. F. Zhu, W. Q. Xu, K. Yang et al., 2012 *Phys.Rev. A* **85** 030501(R).
- [4] K. Xu, K. Yang, Y. W. Liu et al., 2012 *Phys. Rev. A* **86** 022509.
- [5] Y. W. Liu, X. X. Mei, X. Kang et al., 2014 *Phys. Rev. A* **89** 014502.

¹ E-mail: lfzhu@ustc.edu.cn

Theoretical study on the electron-impact single ionization of W^{17+}

Deng-hong Zhang^{*,†} and Duck-Hee Kwon^{*1}

^{*}Nuclear Data Center, Korea Atomic Energy Research Institute, Daejeon 305-353, Korea

[†]Key laboratory of Atomic and Molecular Physics & Functional Materials of Gansu Province, College of Physics and Electronic Engineering, Northwest Normal University, Lanzhou, 730070, China

Tungsten has now been seen as a promising candidate for plasma-faced material in the ITER diverter. Tungsten ions as impurities are unavoidable migrate to the core plasma. Due to its high nuclear charge and strong radiative power loss properties, only a small amount of tungsten would like to quench ignition of a deuterium-tritium plasma[1]. Thus, detailed knowledge including electron-impact ionization (EII) cross section of tungsten ions are most crucial and urgent in controlled fusion experiments. Recently, Rausch et al.[2] studied the electron-impact ionization of W^{17+} using the crossed-beam setup and obtained absolute cross section at collision energies from threshold up to 1000eV. However, no comprehensive theoretical predictions are available for comparison.

In this work, we have performed fully relativistic level-to-level distorted-wave (LLDW) calculations for both direct ionization (DI) and excitation autoionization (EA) of the W^{17+} ion, with the help of the Flexible Atomic Code (FAC)[3]. Particular attention has been paid to excitation-autoionization (EA) processes. The calculated EA cross section contributes to the total cross section as much as about 50%. Our calculated total cross sections have been compared with the recent experimental results [2]. The total cross section for the ground state is a little smaller than the experimental results, but that for the excited states with ionization threshold near the starting energy of the measured cross sections is very close to the experimental results. Maxwellian rate coefficients derived from our calculated cross sections for the ground state are also compared with the previous configuration-average distorted-wave rate coefficients in detail[4]. In figure 1(a), the calculated EA cross sections for the ground state W^{17+} of $[Kr]4d^{10}4f^{11}$ configuration are shown along with the calculated total DI cross section, where the theoretical ionization threshold has been shifted by +4.3 eV to match with the NIST value [5]. In figure 1(b), the calculated EISI cross section for the $[Kr]4d^{10}4f^{10}5s$ ground state of W^{17+} is shown. The theoretical ionization threshold has been shifted by +1.6 eV to match with the NIST recommended value.

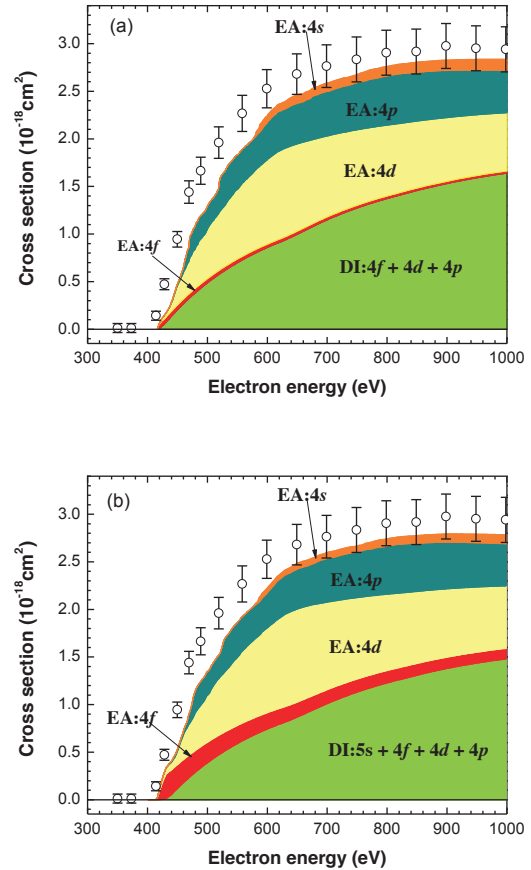


Figure 1. Our calculated EISI cross sections for W^{17+} : (a) the $[Kr]4d^{10}4f^{11}$ ground state and (b) the lowest level of the excited configuration $[Kr]4d^{10}4f^{10}5s$. The total DI cross section and various EA cross sections are shown by differently coloured areas. The experimental results of Rausch *et al* [2] are plotted using open circles.

References

- [1] Dux R et al 2011 *Nucl. Fusion* 51 053002
- [2] Rausch J et al 2011 *J. Phys. B* 44 165202
- [3] Gu M F 2008 *Can. J. Phys.* 86 675
- [4] www-cfadc.phy.ornl.gov
- [5] Kramida A and Shirai T 2009 *At. Data Nucl. Data Tables* **95** 305

[†] E-mail: hkwon@kaeri.re.kr

Recent progress in plasma spectroscopy and sources development for Beyond EUV Lithography and other applications

Bowen Li^{*1}, Elaine Long[‡], Chihiro Suzuki[‡], Takeshi Higashiguchi[†], Hayato Ohashi[†], Fergal O'Reilly[‡], Emma Sokell[‡], Padraig Dunne[‡] and Gerry O'Sullivan^{‡,2}

^{*} School of Nuclear Science and Technology, Lanzhou University, Lanzhou, 730070, China

[‡] School of Physics, University College Dublin, Belfield, Dublin 4, Ireland

[‡] National Institute for Fusion Science, Toki, Gifu 509-5292, Japan

[†] Department of Advanced Interdisciplinary Sciences and Center for Optical Research and Education (CORE), Utsunomiya University, Utsunomiya, Tochigi 321-8585, Japan

‡

Development of laser produced plasmas of potential sources in the extreme ultraviolet (EUV) and soft x-ray spectral regions matching available multilayer mirrors is currently of major interest and has been motivated by their application, such as lithography, x-ray absorption fine structure measurements and imaging of biological samples. For the former, the recent development of La/B₄C mirrors with a reflectivity of 53.6% in a 0.6% bandwidth centered near 6.7 nm has led to Gd and/or Tb based plasmas as potential sources for microchip fabrication for the next generation of EUV lithography beyond 13.5 nm [1]. For the latter [2-3], a major challenge is three-dimensional imaging and single-shot flash photography of microscopic biological structures, such as cells and macromolecules, *in vivo*. A number of theoretical and experimental studies have been carried out to find both the optimum temperature and

source conditions. In this work, we will present an overview of our recent progress in plasma spectra and source development.

Acknowledgment

One of the authors (B.L.) acknowledges support from the Fundamental Research Funds for the Central Universities while the UCD group was supported by Science Foundation Ireland International Co-operation Strategic Award 13/ISCA/2846.

References

- [1] B. Li *et al* 2012 *Appl. Phys. Lett.* [101 013112](#)
- [2] T. Higashiguchi *et al* 2012 *Appl. Phys. Lett.* [100 014103](#)
- [3] B. Li *et al* 2013 *Appl. Phys. Lett.* [102 041117](#)

¹ E-mail: libw@lzu.edu.cn

E-mail: gerry.osullivan@ucd.ie

Laser-produced multi-charged heavy ions as efficient soft x-ray sources

Takeshi Higashiguchi¹, Yuhei Suzuki¹, Masato Kawasaki¹, Hayato Ohashi², Nobuyuki Nakamura³, Chihiro Suzuki⁴, Hiroyuki A. Sakaue⁴, Daiji Kato⁴, Izumi Murakami⁴, Fumihiro Koike⁵, Shinsuke Fujioka⁶, Hiroaki Nishimura⁶, Atsushi Sunahara⁷, Bowen Li⁸, Pdraig Dunne⁹, and Gerry O'Sullivan⁹

¹DEEE & CORE, Utsunomiya University

²Graduate School of Science and Engineering for Research, University of Toyama

³Institute for Laser Science, The University of Electro-Communications

⁴National Institute for Fusion Science

⁵Faculty of Science and Technology, Sophia University

⁶Institute of Laser Engineering (ILE), Osaka University

⁷Institute of Laser Technology (ILT)

⁸School of Nuclear Science and Technology, Lanzhou University

⁹School of Physics, University College Dublin

Development of shorter wavelength sources in the extreme ultraviolet (EUV) and soft x-ray spectral regions has been motivated by their application in a number of high profile areas of science and technology. One such topic is the challenge of three-dimensional imaging and single-shot flash photography of microscopic biological structures, such as cells and macromolecules, *in vivo*. For x-ray microscopy, the x-ray source should emit a sufficient photon flux to expose the image of the biological sample on the detector. To date the most practical light source of high-power, high-brightness x-rays have been radiation from synchrotrons and more recently from free electron lasers (FEL). Table-top sources using ethanol sprays and liquid nitrogen droplets are being developed for use with zone plates for transmission microscopy. Recently $\lambda = 2.48$ nm narrowband emission from a liquid-nitrogen-jet laser-plasma was successfully combined with state-of-the-art normal-incidence multilayer condenser optics and 20-nm zone-plate imaging optics to demonstrate laboratory water-window x-ray microscopy with resolution less than 40 nm. The total collected energy, however, is low, when one combines the narrow line emission with the low reflectivity of the collector mirror. As a result long exposures are needed to record an image and there is not yet published evidence of single-shot exposures using a laboratory-scale source. To overcome the low efficiency imposed by line sources, we propose using high power water-window emission from laser-produced high- Z plasmas, analogous to the scheme used for efficient, high-volume manufacturing EUV sources.

We report the demonstration on the efficient “water window” soft x-ray source by strong UTA band emission in laser-produced high- Z plasmas. Our proposed procedure for producing the water window emission is expected to be efficient and scalable in output yield. Our calculations show that a bismuth plasma at an electron temperature in the range 570 to 600 eV radiates strongly near 3.9 nm. At electron temperatures above 800 eV, strong UTA emission around 3.2 nm would be expected [1].

Because it moves to shorter wavelength with increasing Z , the $n = 4 - n = 4$ UTA can be used for other applications, such as transmission x-ray microscopy for biological imaging in the water window (Fig. 1). We have made preliminary studies of the potential of Bi as the “water window” soft x-ray source [2].

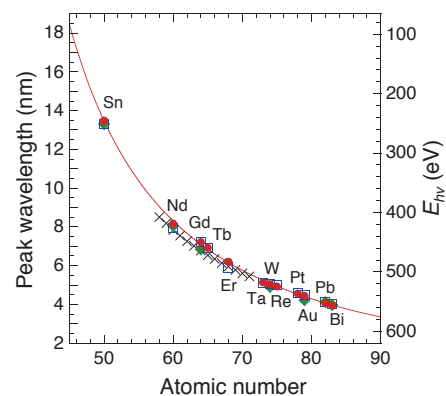


Fig. 1. Atomic number dependence of the peak wavelength of $n = 4 - n = 4$ UTA emissions.

References

- [1] T. Higashiguchi et.al., 2012 *Appl. Phys. Lett.* **100** 014103.
- [2] H. Ohashi et.al., 2014 *Appl. Phys. Lett.* **104** 234107.

¹E-mail: higashi@cc.utsunomiya-u.ac.jp

Tune-out wavelengths for potassium

Jun Jiang^{*†,1}, and Jim Mitroy^{*2}

^{*}School of Engineering, Charles Darwin University, Darwin NT 0909, Australia

[†]Key laboratory of Atomic and Molecular Physics & Functional Materials of Gansu Province, College of Physics and Electronic Engineering, Northwest Normal University, Lanzhou, 730070, China

The dynamic polarizability of an atom gives a measure of the energy shift of the atom when it is exposed to an electromagnetic field. For an atom in any given state, one can write

$$\Delta E \approx -\frac{1}{2} \alpha_d(\omega) F^2$$

where $\alpha_d(\omega)$ is the polarizability of the quantum state at frequency ω , and F is a measure of the strength of the AC electromagnetic field. The limiting value of the dynamic polarizability in the $\omega \rightarrow 0$ limit is the static dipole polarizability. The dynamic polarizability will go to zero for certain frequencies of the applied electromagnetic field. The wavelengths at which the polarizability goes to zero are called the tune-out wavelengths. Recently, tune-out wavelengths have been measured for the rubidium and the potassium atoms [1,2]

A relativistic description of the structure of heavy atoms using L-spinors and S-spinors has been developed. This approach is then used to calculate the dynamic polarizabilities of K. The five longest tune-out wavelengths for the potassium atom is presented. The lowest energy tune-out wavelength is primarily determined by the ratio of the line strengths for the $4s \rightarrow 4p_J$ transitions. The tune-out wavelengths near the $5p_J$ excited states are most sensitive to the ratio of the $4s \rightarrow 4p_J$ and $4s \rightarrow 5p_J$ matrix elements[3].

The influence of hyperfine interactions on the tune-out wavelengths of the $^{39,40,41}\text{K}$ isotopes of the potassium atom was investigated. The hyperfine interaction of the $4s_{1/2}$ state results in a shift and splitting of the primary tune-out wavelength near

769 nm. The $4s_{1/2}$ ground state hyperfine splittings of the primary tune-out were almost equal to the hyperfine splittings of the ground states. The hyperfine splitting of the np_J levels leads to the creation of additional tune-out wavelengths which could be difficult to detect due to very small differences from the transition wavelengths to the $4p_{J,F}$ states[4].

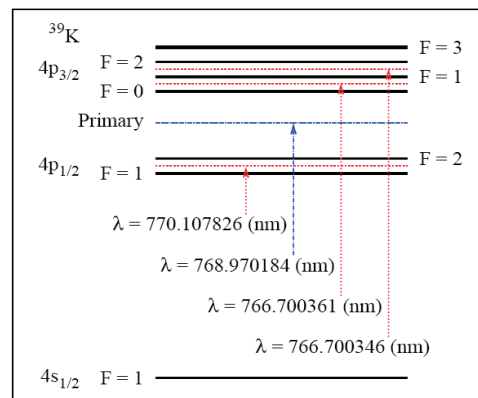


Fig. 1. The energy levels and tune-out wavelengths for the $4s_{1/2}$, $F=1$ state of ^{39}K . The diagram is not to scale. The position of the primary tune-out wavelength is indicated.

References

- [1] W. F. Holmgren, R. Trubko, I. Hromada, and A. D. Cronin, 2012 *Phys. Rev. Lett.* **109** 243004.
- [2] C. D. Herold, V. D. Vaidya, X. Li, S. L. Rolston, J. V. Porto, and M. S. Safronova, 2012 *Phys. Rev. Lett.* **109** 243003.
- [3] J. Jiang, L.Y. Tang and J. Mitroy 2013 *Phys. Rev. A* **87** 032518
- [4] J. Jiang and J. Mitroy 2013 *Phys. Rev. A* **88** 032505

¹E-mail: Jiangjun@nwnu.edu.cn

²E-mail: jim.mitroy@cdu.edu.au

Lost resonance lines in promethiumlike heavy ions

NAKAMURA Nobuyuki^{*,1}, KOBAYASHI Yusuke^{*}, KATO Daiji[†],
SAKAUE Hiroyuki A.[†], and MURAKAMI Izumi[†],

^{*}Institute for Laser Science, The University of Electro-Communications, Chofu, Tokyo 182-8585, Japan

[†]National Institute for Fusion Science, Toki, Gifu 509-5292, Japan

Identifying the $ns - np$ resonance lines in alkali-metal-like ions is an important issue in fusion plasma science in the view of spectroscopic diagnostics and radiation power loss. Whereas for $n = 2, 3$ and 4 these resonances are prominent and well studied, so far no one could clearly identify the resonance lines for $n = 5$ in the promethiumlike sequence [1].

We have now experimentally clarified the reason for the “lost resonance lines” [2]. In the present study, highly-charged bismuth ions have been studied using a compact electron beam ion trap (EBIT) [3] at the University of Electro-Communications in Tokyo. In the EBIT, a high-density electron beam compressed by a superconducting magnet ionizes bismuth trapped by the combination of an electrostatic well potential and the space charge potential of the compressed electron beam. Highly charged bismuth ions are thus produced through successive electron impact ionization. Emission from the bismuth ions in the extreme ultraviolet range is observed with a grazing-incidence flat-field spectrometer. The energy dependent spectra are compared with a collisional-radiative model calculation, and we show that the $5s - 5p$ resonance lines are very weak in plasma with a wide range of electron density, contrary to the theoretical prediction [4] made more than thirty years ago, due to the pres-

ence of a long-lived metastable state.

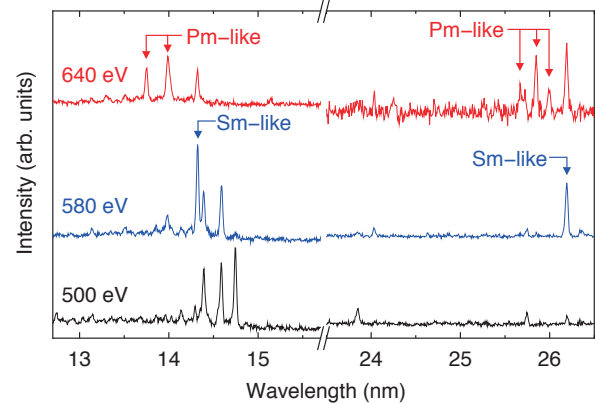


Fig. 1. Experimental spectra of highly charged bismuth ions at different electron energies. Promethiumlike and samariumlike spectral lines are identified.

References

- [1] S. Wu and R. Hutton, 2008 *Can. J. Phys.* **86** 125.
- [2] Y. Kobayashi, D. Kato, H. A. Sakaue, I. Murakami, and N. Nakamura, 2014 *Phys. Rev. A* **89** 010501(R).
- [3] N. Nakamura, H. Kikuchi, H. A. Sakaue, and T. Watanabe, 2008 *Rev. Sci. Instrum.* **79** 063104.
- [4] L. J. Curtis and D. G. Ellis, 1980 *Phys. Rev. Lett.* **45** 2099.

¹E-mail: n.nakamu@ils.uec.ac.jp

EUV spectrum of highly charged tungsten ions in LHD with help of CoBIT

H. A. Sakaue^{*1}, C. Suzuki^{*}, D. Kato^{*}, I. Murakami^{*} and N. Nakamura[†]

^{*} National Institute for Fusion Science, Toki, Gifu 509-5292, Japan

[†]Institute for Laser Science, The University of Electro-Communications,
Chofu, Tokyo 182-8585, Japan

Tungsten will be used as material for the divertor plates in ITER because of higher sputtering threshold energy for light ion bombardment, the highest melting point among all the elements, and less tritium retention compared with carbon based materials. However, since extremely high particle- and heat-fluxes of the intermittent edge plasma transport (e.g. edge-localized-mode) in ITER would cause serious damages to such components, tungsten is considered to be one of the most abundant impurities in the ITER plasma. Impurity tungsten enters the high-temperature plasma and is ionized to highly charged ions, and then highly charged ions emit very strong photons of EUV and/or X-ray. This emitted photon has very important information on plasma diagnostics; information on electron and ion temperature, electron density, impurity ion abundance and impurity transportation. Emission lines of highly charged tungsten ions thus play an important role in the spectroscopic diagnostics of the ITER plasma, and consequently the spectroscopic data of tungsten ions have been studied at several facilities.

On the other hand, an electron beam ion trap is a useful device for the systematic spectroscopic studies of highly charged tungsten ions. We have constructed a compact electron beam ion trap, called CoBIT[1-3], and

observed extreme ultraviolet (EUV) spectra of highly charged tungsten ions. Furthermore, we carried out the tungsten highly charged ions spectroscopic measurement in LHD plasma in parallel with the experiment of CoBIT.

For the first time, we succeeded in observation of unidentified emission lines which are expected from theoretical calculations from W^{26+} around 100Å at both experiments. We observed the emission lines of the 4f-5s transition by CoBIT and impurity pellet injection in LHD. Some emission lines of highly charged tungsten ions have been identified in this experiment. Furthermore it was confirmed as a single emission line in fusion plasma. These single emission lines of highly charged tungsten ions become very important lines in spectroscopic diagnostics of plasma. These details will be reported on this conference.

References

- [1] N. Nakamura, *et al.*. 2008 *Rev. Sci. Instrum.* **79** 063104.
- [2] H. A. Sakaue, *et al.*. 2009 *J. Phys.:Conf. Ser.* **163** 012020.
- [3] H. A. Sakaue, *et al.*. 2012 *AIP Conf. Proc.* 143891.

¹E-mail:sakaue@nifs.ac.jp

SYSTEMATIC CALCULATIONS OF ENERGY LEVELS AND RADIATIVE RATES OF C-LIKE IONS WITH $Z = 13 - 36$ USING AN COMBINED CONFIGURATION INTERACTION AND MANY-BODY PERTURBATION THEORY APPROACH

K. Wang¹, J. Yan, D.F. Li, H.T. Liu, X.Y. Han, B. Duan, C.Y. Li, J.G. Li

Institute of Applied Physics and Computational Mathematics, Beijing 100088, China

In the present work, we report the energy levels, and electric dipole, magnetic dipole, electric quadrupole and magnetic quadrupole transition properties for 46 levels of the $2s^22p^2$, $2s2p^3$, $2p^4$, $2s^22p3s$, $2s^22p3p$, and $2s^22p3d$ configurations in the C-like ions with $13 \leq Z \leq 36$, in an effort to provide a complete, self-consistent and accurate dataset. We employ a combined relativistic configuration interaction (RCI) and many-body perturbation theory (MBPT) approach implemented in the FAC code [1], in which both nondynamic and dynamic correlations can be well accounted for. Extensive comparisons with available observations and other systematic calculations show the present MBPT results are highly accurate: for level energies, uncertainties are less than 0.2% for most levels and within 0.5% for all levels; for transition rates, accuracies are better than 10% for a majority of transitions. As an example, Figure 1 shows the differences of present calculated energies relative to the observed values from the NIST database [2] for the lowest four excited states of $2s^22p^2$ configuration along the isoelectronic sequence. The present dataset can be used reliably for many purposes, such as the line identification of observed spectra, the modeling and diagnostics of astrophysical and fusion

plasmas.

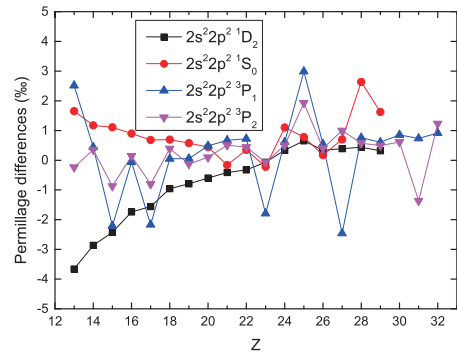


Fig. 1. Permillage differences of present calculated energies relative to the observed values from the NIST database [2] for the $2s^22p^2$ levels.

References

- [1] M. F. Gu , 2005 *The Astrophysical Journal Supplement* **156** 105.
- [2] A. Kramida, Yu. Ralchenko , J. Reader, and NIST ASD Team, NIST Atomic Spectra Database (ver. 5.1), [Online]. Available: <http://physics.nist.gov/asd> [2013, December 24].

¹E-mail: wang_kai10@fudan.edu.cn

UV-visible M1 line emission from highly charged tungsten ions in LHD plasmas

D. Kato^{*1}, H.A. Sakaue^{*}, I. Murakami^{*}, M. Goto^{*}, T. Oishi^{*}, C. Suzuki^{*}, S. Morita^{*},
N. Nakamura[†], A. Sasaki¹, F. Koike², X.-B. Ding³, C.-D. Dong³

^{*} National Institute for Fusion Science, Toki, Gifu 509-5292, Japan

[†] Institute for Laser Science, The University of Electro-Communications, Tokyo 182-8585, Japan

¹ Japan Atomic Energy Agency, Kyoto 619-0215, Japan

² Faculty of Science and Technology, Sophia University, Tokyo 102-8554, Japan

³ College of Physics and Electronic Engineering, Northwest Normal University, Lanzhou, 730070, China

One of important issues concerning steady state sustainment of magnetically confined plasmas (MCPs) is distribution of impurity ions in the MCPs and radiation powers by the ions. Since tungsten divertors will be used in ITER (International Thermonuclear Experimental Reactor) [1], the primary element of heavy impurity ions would be tungsten. Tungsten cannot be fully ionized even in core plasmas of ITER. Line radiations by bound electrons of the tungsten ions following electron impact excitations decrease temperatures of the core plasmas. A theoretical simulation predicts that tungsten concentrations in the core plasma should be limited below $N_W/N_e=5\times 10^{-5}$ [2].

In peripheral plasmas (scrape-off layers and divertor regions) of ITER, where electron temperatures are lower, charge states of the tungsten ions would be 30+ or lower (open 4f and 5l sub-shells). Recently, a theoretical investigation [3] has shown that strongly enhanced radiation powers at the lower temperatures are obtained with improved data of ionization and recombination rate coefficients for the charge states. However, experimental validation for the rate coefficients is necessary.

Electron temperatures in the core plasma of the Large Helical Device (LHD) is a few keV or lower using neutral beam injection (NBI) heating. We can, therefore, investigate tungsten line emissions of the lower charge states with the LHD, which are anticipated in the peripheral region of ITER. A novel idea of this work is to use forbidden lines in UV-visible ranges to measure the tungsten ion distributions in the core plasma of the LHD. Inherently narrow and isolated forbidden lines have features suitable for identifying a specific charge state of ions in emission spectra as well as plasma diagnostics.

We have observed a visible magnetic-dipole (M1) line emission from W^{26+} ions in the previous LHD experiments [4]. Recently, an M1 line of W^{27+} ions has also been identified, and its intensity distribution on a poloidal cross section was measured precisely. The measured intensity distribution was compared with W^{27+} ion distributions calculated using available data of the ionization and recombination rate coefficients at local electron temperatures measured by Thomson scattering. It is found that the measured intensity distribution is not explained by the equilibrium ion distribution of the improved rate coefficients.

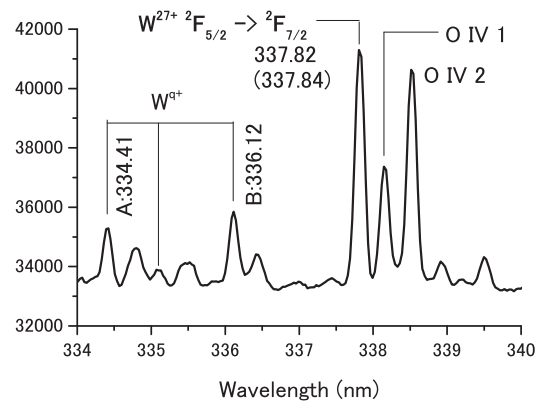


Fig. 1. Line emission spectrum of W^{q+} measured by tungsten pellet injection in the discharge #121534 of the LHD.

References

- [1] www.iter.org
- [2] A. Kallenbach et al., 2005 *Plasma Phys. Control. Fusion B* **47** 207.
- [3] A. Sasaki and I. Murakami, 2013 *J. Phys. B: At. Mol. Opt. Phys.* **46** 175701.
- [4] D. Kato et al., 2013 *Phys. Scr.* **T156** 014081.

¹ E-mail: kato.daiji@nifs.ac.jp

Multiconfiguration Dirac-Fock calculations of energy levels, oscillator strengths and hyperfine structures for low-lying states of Sm

Fuyang Zhou^{*}, Jiguang Li[†], Yizhi Qu^{*,1}, and Jianguo Wang[†]

^{*}University of the Chinese Academy of Sciences, Beijing 100049, China and

[†]Institute of Applied Physics and Computational Mathematics, Beijing 100088, China

The unique physical properties of lanthanide atoms are of great interest to various applications. The rich and broad spectra of rare earth elements are useful to astronomy studies and lighting community. However the spectra calculations of the rare earth atoms are very difficult due to the complicated and strong electron correlation effects originate from the electrons in the $4f$ shell. Among the lanthanide atoms, samarium exhibits the most complex spectra. The calculations of excitation energy and transitions of Sm carried out so far agree poorly with experimental data.

In the present work we calculated the excitation energies and transition probabilities of low-lying states for Sm within the framework of the multi-configuration Dirac-Fock (MCDF) theory [1], which take into account the electron correlation and relativistic effects in the same footing. In order to systematically and adequately include the electron correlations, the active space approach was adopted to generate the configuration space (CS). However, the CS is generally too large to be dealt with, especially for atoms with open- f shells. As a result, one can only consider the important configuration state functions (CSFs) in the CS. By enlarging the active set systematically, one can monitor the convergence of the physical quantities.

TABLE I Transition energy and oscillator strength(f) for $f^6 6s 6p \ ^9G^o_1 - 4f^6 6s^2 \ ^7F_0$ transitions

	$E(^9G^o_1)$	f_L	f_V	f_L/f_V
SC	6899	1.66	0.07	42
<i>1spdf</i>	13087	16.35	61.32	0.27
<i>2spdf</i>	14265	11.05	22.69	0.49
Porsev[2]	11533	6.9		
Dilip[3]	11726			
Expt [4]	13999.5	12.5		

The oscillator strengths(f) in Babushkin (length f_L) and Coulomb (velocity f_V) gauges for

$4f^6 6s 6p \ ^9G^o_1 - 4f^6 6s^2 \ ^7F_0$ transitions are shown in table I. The f_L are in good agreement with experimental value. However, the gauge difference is very large. The gauge consistency was improved, along with the expansion of the CSFs, which indicates the effects of selected valence and core-valence correlations are significant for the oscillator strengths in these transitions, the gauge difference may be caused by the incomplete treatment of the correlations.

TABLE II Hyperfine structure constants (A,B) for the excitation state $4f^6 6s 6p \ ^9F^o_1$ and $^7G^o_1$ of ^{147}Sm

Model	$^9F^o_1$		$^7G^o_1$	
	A(MHz)	B(MHz)	A(MHz)	B(MHz)
SC.	-241.05	19.24	-171.83	10.79
<i>1spdf</i>	-539.05	17.27	-89.22	-14.11
<i>2spdf</i>	-326.12	15.86	-169.75	-12.49
Expt. [5]	-423.34	13.21	-212.62	-9.63

The HFS constant A and B of the $4f^6 6s 6p \ ^9F^o_1$ and $^7G^o_1$ of ^{147}Sm were calculated with one-body correlations included, as shown in table II. The single-configuration (SC) calculations do not agree with the experimental results[5] well, e.g. even the sign of the HFS constant B of $^7G^o_1$ state is different. The calculated constant B can be improved a lot with the enlarging of one-particle correlation effects.

References

- [1] P. Jönsson, G. Gaigalas, J. Bieroń *et al*, 2013 *Comput. Phys. Comm.* 184, 2197
- [2] S. Porsev, 1997 *Phys. Rev. A* 56, 3535 .
- [3] A. Dilip, I. Endo, A. Fukumi, M. Iinuma *et al*, 2001 *Eur. Phys. J. D* 277, 271
- [4] K. B. Blagoev, V. A. Komarovskii, and N. P. Penkin, 1977 *Opt. Spektrosk* 42, 424
- [5] H. Park, M. Lee, and Y. Rhee, 2003 *J. Korean. Phys. Soc.* 43, 336

E-mail: yzqu@ucas.ac.cn

Carbonaceous Thin-film Deposited with Radio-frequency Ar/C₂H₅OH Atmospheric Pressure Plasma Jet

Q. H. Yuan[†], Y. J. Zhou, X. M. Wang, X. W. Chang, G. Q. Yin, and C. Z. Dong

Key laboratory of Atomic and Molecular Physics & Functional Materials of Gansu Province, College of Physics and Electronic Engineering, Northwest Normal University, Lanzhou, 730070, China

Atmospheric pressure plasma jets (APPJs) have attracted a great interest in different fields of technological applications, such as deposition of thin films, nanotechnology, and surface treatment. Nonthermal APPJ has a great advantage for the treatment of heat sensitive substrates and it also could be served as a depositing tool [1]. Carbon nanomaterials are being considered for nano-electronics, sensors, and nano-probes because of their prominent electronic and mechanical properties [2]. In the present work, we present a possible method of carbonaceous thin-film deposition by using an Ar/C₂H₅OH atmospheric pressure plasma jet.

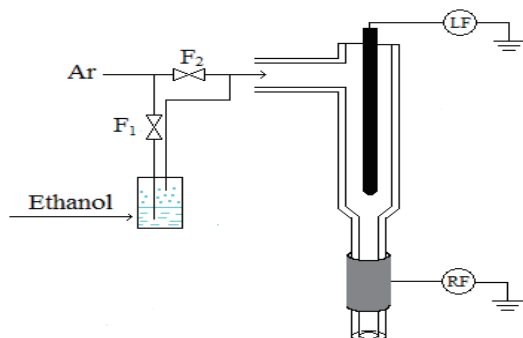


Fig.1. Schematic of experimental setup.

A spectrometer was used to obtain the plasma emission spectra. The introduction of ethanol (C₂H₅OH, 99.7%) leads to the generation of four excited carbonaceous species in plasma, namely C, CN, CH and C₂. With the increasing of ethanol content, the dependence of emission intensities of C,

CN, CH and C₂ on ethanol content have been investigated.

Scanning electron microscopy (SEM) and X-ray photoelectron spectroscopy (XPS) were used to characterize the deposited film. The carbonaceous films have been deposited on silicon wafer at room temperature. Figure 2 showed the surface profile of carbonaceous thin-film (deposited with 30 min) at different magnification.

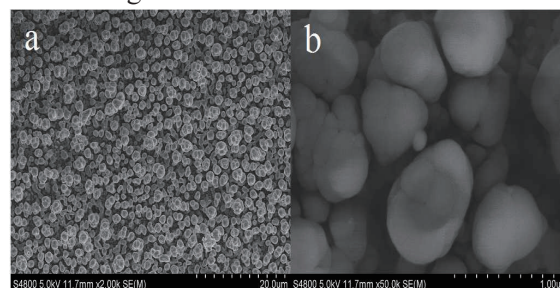


Fig.2. SEM images of the film at different magnification (deposited with 30min).

This work was supported by the National Natural Science Foundation of China under Grant No. 11165012, China Postdoctoral Science Foundation funded project (2011M501494, 2012T50831).

References

- [1] R. d'Agostino, P. Favia, Y. Kawai, H. Ikegami, N. Sato, and F. Arefi-Khonsari, *Advanced Plasma Technology* WILEY-VCH (2008).
- [2] T. Kato, G. -H. Jeong, T. Hirata, R. Hatakeyama, K. Tohji, K. Motomiya, *Chem. Phys. Lett.* **381**, 422 (2003).

[†]E-mail: yqh0669@126.com

State-selective electron capture in slow collisions of C^{5+} ion with H_2

X. L. Zhu^{*,1}, X. Ma^{†,2}, W. T. Feng^{*}, S. F. Zhang^{*}, D. L. Guo^{*}, S. Yan^{*}, S. Xu^{*}, D. B. Qian^{*}, W. Wen^{*}, Y. Gao^{*,†}, D. M. Zhao^{*}

^{*}Institute of Modern Physics, Chinese Academy of Sciences, Lanzhou 730000, China

[†]Graduate University of Chinese Academy of Sciences, Beijing 100049, China

Charge transfer in collisions of highly charge state ion with He and molecular hydrogen play an important roles in astrophysics and fusion plasmas physics. Electron capture cross section are need for use in modeling and interpreting observed astrophysical x-ray spectra [1]. For C^{5+} - H_2 collision system, M G Surdud et al. measured the absolute x-ray and VUV emission cross sections between 0.18 a.u. and 0.55 a.u. velocity range [2]. In the collision energy range, single electron capture into state $C^{4+}(1s3l)$ and $C^{4+}(1s4l)$ is dominant process. When the projectile velocity large 0.5a.u., the cross sections of single electron capture into $n=4$ large than $n=3$. D M Kearns et al. studied the state-selective one-electron capture within the range 250-833 eVamu⁻¹ by translational energy spectroscopy [3]. As the impact energy decreases, the dominant population retained $C^{4+}(1s3l)$ states. However, these measurement did not obtain the angular differential cross sections. The sensitivity of angular differential cross sections to the shapes of active potential curves, and the probabilities for transitions between them.

In this work, the energy-gain spectra and angular differential cross sections have been measured for nondissociative single electron capture processes in collisions of C^{5+} with H_2 at impact energies from 200 keV to 500 keV based on a cold target recoil ion momentum spectroscopy in Lanzhou, which has been described previously [4].

At impact energy of 200 keV, the dominant reaction channel is single electron capture into one of two n shells, $n=3$ or 4. The contribution of latter was more important than the former. Capture into $C^{4+}(1s5l)$ states is also identified as shown in Fig. 1. As impact energy increases, the importance of single electron capture into

$C^{4+}(1s4l)$ states increases, while the relative contributions of single electron capture into the $C^{4+}(1s5l)$ states strongly increases. The experimental results could be qualitatively understood from the Molecular Coulombic Barrier Model (MCBM) [5].

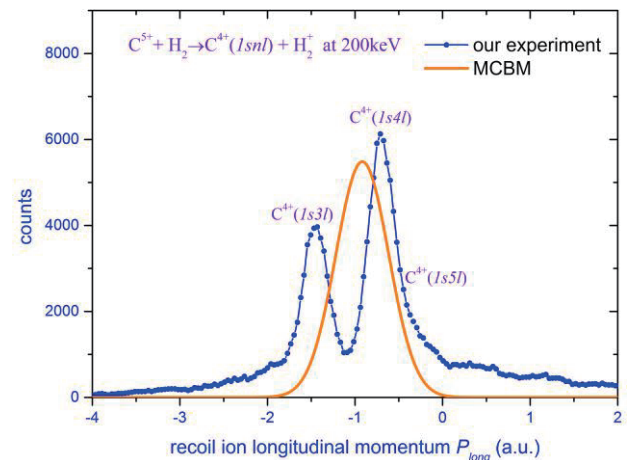


Fig. 1. The longitudinal momentum spectra of recoil H_2^+ ions for nondissociative single electron capture in collisions of C^{5+} ions on molecular hydrogen at projectile energy of 200 keV.

This work was supported by the NSFC of China under Grant Nos 11274317 and 10979007.

References

- [1] T. R. Kallman and P. Palmeri, 2007 *Rev. Mod. Phys.* **79** 79
- [2] M G Surdud, R Hoekstra, F J de Heer et al., 1991 *J. Phys. B: At. Mol. Opt. Phys.* **24** 2543
- [3] D M Kearns, R W McCullough, R Trassl et al., 2003 *J. Phys. B: At. Mol. Opt. Phys.* **36** 3653
- [4] X. Ma, R T Zhang, S F Zhang et al., 2011 *Phys. Rev. A* **83** 052707
- [5] A. Niehause, 1986 *J. Phys. B: At. Mol. Phys.* **19** 2925

¹E-mail: zhuxiaolong@impcas.ac.cn

²E-mail: x.ma@impcas.ac.cn

Visible M1 transition of the ground state of W^{26+} - W^{28+} ions

Ding Xiaobin^{*,1}, Fumihiko Koike^{†2}, Daiji Kato^{§3}, Hiroyuki A. Sakaue[§], Izumi Murakami[§], Dong Chenzhong^{*4}, Nobuyuki Nakamura[‡]

^{*}College of Physics and Electronic Engineering, Northwest Normal University, Key Laboratory of Atomic and Molecular Physics and Functional Materials of Gansu Province, Lanzhou, 730070, China

[†]Faculty of Science and Technology, Sophia University, 7-1 Kioicho, Chiyoda-ku, Tokyo, 102-8554, Japan

[§]National Institute for Fusion Science, 322-6 Oroshi-cho, Toki 509-5292, Japan

[‡]Institute for Laser Science, The University of Electro-Communications, Chofu, Tokyo 182-8585, Japan

Tungsten (W) is one of the major candidates for divertor or wall material in the next generation magnetic confinement fusion reactors due to its favorable properties. Tungsten atoms will be introduced into plasmas and they will act as impurity ions. Although the heavy ion impurities may cause a serious radiation power loss, their visible line emissions may still be helpful for diagnostics of the core and edge plasmas owing to their low opacities[1]. Accurate atomic data of energy levels and transition properties relevant for such line emission are indispensable for the precise measurement of plasma properties. In the present report, we carry out an elaborate non-empirical theoretical calculation for the electronic structures and the M1 transition properties of W^{26+} to W^{28+} ions.

Multi-configuration Dirac-Fock (MCDF) method is a widely used ab-initio method to carry out a relativistic calculation for many electron atoms or ions. The effect of electron correlations can properly be evaluated by choosing a suitable set of basis which consists of the orbitals and excitations among those orbitals. We employ a set of code family after the name of GRASP (General purpose Relativistic Atomic Structure Program) for our present calculation[2,3]. We have carried out an MCDF calculation for the ground state multiplets of W^{26+} and W^{27+} ion-

s[4,5] and the first excited state of W^{28+} ions. The Breit interaction was estimated in low frequency limits and the vacuum polarization effect was evaluated by perturbation. In the framework of a restricted active space (RAS) on the MCDF procedure, the visible M1 transitions of W^{26+} to W^{28+} have been calculated. We have obtained a good agreement with experiment in Tokyo-EBIT[4,6] and Shanghai permanent magnet EBIT[5]. The disagreement of the theory with the experiment is only about 0.03eV, which is about 1% of the experimental transition energy.

References

- [1] R. Doron and U. Feldman, 2001, *Phys. Scr.*, **64** 319.
- [2] F. A. Parpia, C.F. Fischer and I. P. Grant, 1996, *Comput. Phys. Commun.*, **94** 249.
- [3] P. Jönsson, X. He, C.F. Fischer and I. P. Grant, 2007, *Comput. Phys. Commun.*, **177** 597.
- [4] X.B. Ding, F. Koike, I. Murakami et. al., 2011 *J. Phys. B: At. Mol. Opt. Phys* **44** 145004.
- [5] X.B. Ding, F. Koike, I. Murakami et. al., 2012 *J. Phys. B: At. Mol. Opt. Phys* **45** 035003.
- [6] M. Minoshima, J. Sakoda, A. Komatsu et. al., 2013 *Phys. Scri.* **T156** 014010.

¹E-mail: dingxb@nwnu.edu.cn

²E-mail: koikef@sophia.ac.jp

³E-mail: kato.daiji@nifs.ac.jp

⁴E-mail: dingcz@nwnu.edu.cn

Alignment of the excited states and angular distribution of subsequent decay following the radiative electron capture into lithium-like ions*

Y. L. Shi^{†,1}, X. B. Liu[†], D. H. Zhang[‡], L. Y. Xie[‡], and C. Z. Dong^{‡,2}

[†] College of Physics and Information Science, Tianshui Normal University, Tianshui 74100, China

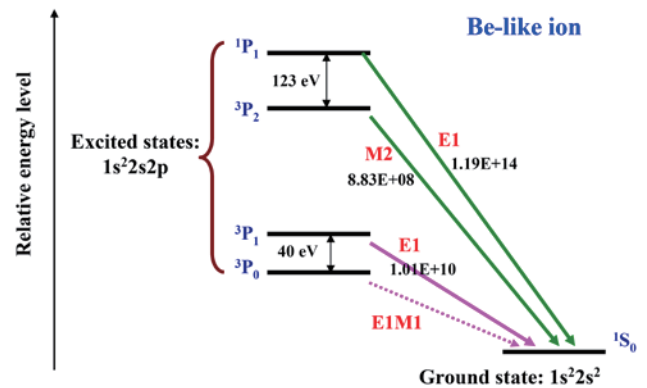
[‡] Key Laboratory of Atomic and Molecular Physics & Functional Materials of Gansu Province, College of Physics and Electronic Engineering, Northwest Normal University, Lanzhou 730070, China

During the last two decades, collisions of highly charged, heavy ions with atoms and free electrons have been studied intensively both at ion storage rings and at electron beam ion traps. In these collision studies, special interest has been devoted to the production of excited ionic states and on the measurement of their subsequent radiative decay. Indeed, the analysis of the bound-state transitions in high-Z ions plays a key role in our understanding of electron-electron and electron-photon interactions in the presence of strong fields, including important information about the relativistic and quantum electrodynamics effects in few-electron systems [1]. In addition to accurate studies of transition energies and probabilities for highly charged ions, measurements of the angular distributions of characteristic x-ray photons provide an important route to learn more about the structure and dynamics of high-Z ions.

At high energies, the radiative electron capture (REC) is known as one of the dominant processes for medium- and high-Z ions at storage rings. In this charge transfer process, a (quasi) free electron from either the (electron) cooler or some rest gas is captured into a bound state of the ion under the simultaneous emission of a photon. A great advantage of angle-resolved x-ray studies is that they are often much more sensitive to the magnetic and retardation effects than the analysis of the total (i.e., integrated over the angles) rates. Within the last several years, a new generation of experiments has been performed at the GSI storage ring to explore the angular distributions of the characteristic photon emission from REC process, especially for the capture into bare ion and form an excited state of the ion [2].

Less attention, in contrast, has been paid so far to the capture into few- and many-electron

ions where the radiative recombination is influenced also by interactions of the incoming electron with the bound-state electron density. In this contribution, the REC into highly charged lithium-like U^{89+} ions is studied in the framework of the density matrix, based on Dirac's equation. Detailed computations have first been carried out for the total and angle-differential cross sections (i.e. the angular distribution of the REC photon) of L-REC into the ground state $1s^2 2s^2 J=0$ and the low-lying excited state $1s^2 2s 2p J=1,2$ of final beryllium-like ion. Emphasis is placed on the population of $1s^2 2s 2p_{3/2} J=1,2$ excited states, as well as the angular distribution and polarization of subsequent characteristic photon emissions ($E1$ and $M2$ transition) [3].



References

- [1] S. Fritzsche, P Indelicato, Th. Stöhlker, 2005 *J. Phys. B: At. Mol. Opt. Phys* **38** S707.
- [2] J. Eichler and Th. Stöhlker, 2007 *Phys. Rep.* **439**, 1.
- [3] Y. L. Shi, C. Z. Dong et. al., 2014 *in preparation*.

* This work has been supported by the NNSF of China (No. 11274254, 11264033) and the Scientific Research Foundation of the Higher Education Institutions of Gansu Province, China (Grant No. 2014A-104).

¹ E-mail: shiy1@tsnc.edu.cn

² E-mail: dongcz@nwnu.edu.cn

A theoretical investigation of inner-shell photoionization of higher charged ions

K. Ma, C. Z. Dong[†] and L. Y. Xie

Key laboratory of Atomic and Molecular Physics & Functional Materials of Gansu Province, College of Physics and Electronic Engineering, Northwest Normal University, Lanzhou, 730070, China

The information about the polarization transfer in the inner-shell photoionization (PI) is important for the diagnostics of many laboratory and astrophysical plasmas and for understand the ongoing measurements on laboratory plasmas which exposed to polarized x-ray emission from Z-pinchs. Moreover, many astrophysical x-ray sources such as magnetized neutron stars or black-hole accretion disks are expected to emit strongly polarized light. But due to lack of appropriate radioactive sources as an excitation beam and efficient polarization detectors, to the best of our knowledge, most of the experimental and theoretical studies of the x-ray properties of anisotropy and polarization have dealt with electron-ion collisions, but less attention has been previously paid to the linear polarization and angular distribution of x-ray lines following the inner-shell PI process of highly charged ions [1], especially for the polarized incoming photon.

In this paper, the inner-shell $2p_{3/2}$ ionization of Mg-like Fe^{14+} , Cd^{36+} , W^{62+} and U^{80+} ions by linear polarized light and the subsequent decay x-ray radiation are studied theoretically within the multiconfiguration Dirac-Fock (MCD-F) method [2] and the density matrix theory [3]. Special attention is paid to explore how the polarization properties of the incident photons and the non-dipole relativistic effects to influence the decay x-ray radiation. Results show that the degree of linear polarization of the characteristic x-ray radiation have a linear relationship with ones of the incident light, this can be used for diagnosis the polarization of light source. In addition, with the photon-energies increasing the non-dipole contribution to alignment of the excited ionic states, the degree of linear polarization (DLP) and angular distribution of the characteristic x-ray radiation following the inner-shell photoionization will be increase.

Fig. 1 shows the P^{out} as a function of P^{in} at 4 times energy threshold units. As seen from this figure, the simple linear relationship arise between P^{in} and P^{out} , moreover, this phe-

nomenon has nothing to do with non-dipole effects in the PI process. When P^{in} increase from 0 to 1, P^{out} will be enhanced by a factor of 2, this result is consist with Sharma and coworkers [4]. Additionally, we can see that the non-dipole terms have depolarization effects, for example, $P^{out} = -12.6$ and -21.15 when calculations performed with and without non-dipole contribution, respectively, at 4 times energy threshold units for U^{80+} ions.

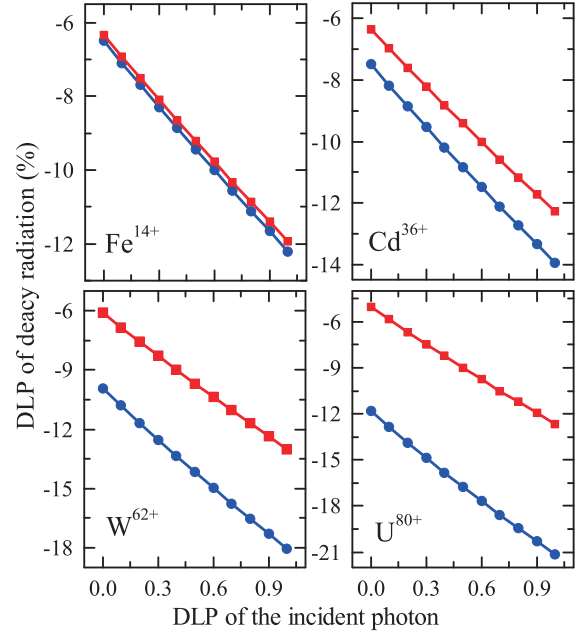


Fig. 1. DLP of subsequent $L\ell$ x-ray following the PI as a function of the DLP of the incident photon. Calculations have been performed with (square) and without (circle) non-dipole contribution.

References

- [1] K. Ma, C. Z. Dong, L. Y. Xie et. al., 2014 *Chin. Phys. Lett.* **31** 05321.
- [2] I.P. Grant, 2007 *Relativistic Quantum Theory of Atoms and Molecules* (Berlin: Springer)
- [3] Blum K, 1981 *Density Matrix Theory and Applications* (New York: Plenum Press)
- [4] L. Sharma, A. Surzhykov, M. K. Inal et al 2010 *Phys.Rev.A* **81** 023419

E-mail:dongcz@nwnu.edu.cn

Multiconfiguration Dirac-Fock calculation for the inner-shell photoionization of ground-state sodium atom

X.B. Liu^{*1}, Y.L. Shi^{*}, X.B. Ding^{†2}, C.Z. Dong^{†3}

^{*} School of Physics and Information Science, Tianshui Normal University, Tianshui 741001, China

[†] Key laboratory of Atomic and Molecular Physics & Functional Materials of Gansu Province, College of Physics and Electronic Engineering, Northwest Normal University, Lanzhou, 730070, China

The photoionization of atom is one of the most important physical processes because it allows a versatile diagnostics of the atomic structure. In this process an electron in a bound state at an atom is moved into a free state. The atomic photoionization have been studied for decades because of the importance of these parameters in many fields of science such as astrophysics, plasma physics, atmospheric science and so on. Despite a long history of measurements and calculations, the calculations of atomic photoionization are still in progress.

The main photoionization processes are due to single electron processes, in which the other electrons leaving inert. This picture has obtained a great success to identify the major photolines. However, there are the cases that the independent particle approximation breaks down for the photoionization process when an electron which resides in sub-valence or inner sub-shells is photoionized. We should have the rearrangement and modification of the electron structures in the residual ions. In the present paper, we try to give an alternative explanation to the shake-up processes within the sudden approximation in which the removal of photoelectron causes a sudden change in the potential for other electrons [1, 2]. The satellites, which generally are much weaker but often display a very rich structure, are known to provide insight into the role of electron correlations. The details of the satellite structure can provide us with a useful and sensitive test to the relevant theoretical methods.

In the present paper, we calculate the sub-valence 2p shake-up as well as diagram the photoelectron spectra of the ground-state sodium atoms. The photoionization from the $2p^63s$ ground states are studied using the multiconfiguration Dirac-Fock (MCDF) method by applying the GRASP code [3] and a comparison is presented with previously reported data. Our aim is to gain a better understanding of the photoionization processes and also to test the

theoretical predictions, so the main emphasis is placed on the investigation of electron correlations to obtain accurate results.

This work was supported by the National Natural Science Foundation of China (Grant Nos. 11264033, 10774122), the Scientific Research Foundation of the Higher Education Institutions of Gansu Province (Grant No. 2014A-104) and the Science Research Foundation of Tianshui Normal University (Grant No. TSA1108).

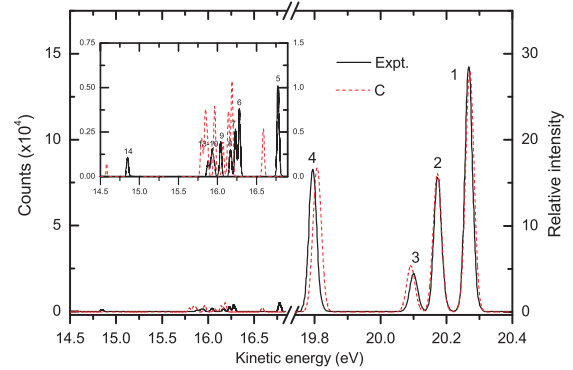


Fig. 1. The $2p^53s$ photoelectron spectra (1, 2, 3 and 4 peaks) of sodium atoms together with $2p^53p$ conjugate shake-up satellite structure (5-14 peaks) at the photon energy $h\nu = 58.3$ eV. Solid lines denote the experimental photoelectron counts [4] and dash lines are theoretical relative intensities with wavefunctions from CSF set C.

References

- [1] T. Åberg, 1967 *Phys. Rev.* **156** 35
- [2] L. Ungier and T.D. Thomas, 1984 *Phys. Rev. Lett.* **53** 435
- [3] K.G. Dyall, I.P. Grant, C.T. Johnson *et. al.*, 1989 *Comput. Phys. Commun.* **55** 425
- [4] D. Cubaynes, H.L Zhou, N. Berrah *et. al.*, 2007 *J. Phys. B: At. Mol. Opt. Phys.* **40** F121

¹E-mail: Liuxb_tstc@sohu.com

²E-mail: Dingxb@nwnu.edu.cn

³E-mail: Dongcz@nwnu.edu.cn

Collision strengths calculations for O-like Ni by Dirac R-matrix theory

Quanping Fan^{*,†,1}, Gang Jiang^{*,2}

^{*} Institute of Atomic and Molecular Physics, Sichuan University, Chengdu, Sichuan 610065, China

[†] Research Center of Laser Fusion, China Academy of Engineering Physics, Mianyang, Sichuan 621900, China

Spectral lines of O-like Ni ions have been observed in solar flares and laboratory plasmas. Accurate atomic parameters such as energy levels, collision strengths and rate coefficients for O-like Ni are required for identification of various spectral lines and to infer properties of solar and laboratory plasmas. However, experimental data for most of the above named parameters are not available, so theoretical data are desirable.

In this work, we use Dirac R-matrix theory to calculate the collision strengths for electron impact excitation of O-like Ni by the Dirac atomic R-matrix code (DARC) [1], which includes contributions of resonances, channel coupling, and relativity. In our DARC calculations, we have considered all transitions among 86 levels of $(1s^2) 2s^2 2p^4$, $2s^2 2p^5$, $2p^6$ and $2s^2 2p^3 3l$ ($l=0, 1, 2$) configurations of O-like Ni. The GRASP code [2] has been adopted for the description of target. A comparison is made with the results of Bhatia et al [3] for the collision strengths of five incident energies, 85, 170, 255, 340, and 425 Ryd, which use distorted wave calculations that do not include channel coupling. Effective collision strengths are calculated by averaging collision strengths over a Maxwellian velocity distribution.

The typical characteristics of convergence of collision strengths are shown in Fig. 1. It's easy to converge at low incident energies, but becomes more and more difficult with the increasing of incident energy.

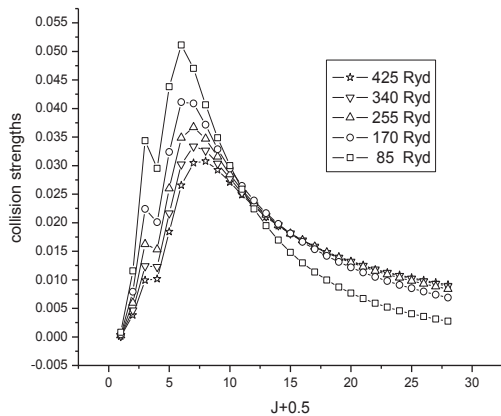


Fig. 1. Partial collision strengths for transition $2s^2 2p^4(^3P_2) - 2s 2p^5(^3P_2)$

Comparisons are made with the results of Bhatia et al and an example is shown in Fig. 2. Obvious resonances exist in threshold region, which implies that resonance effects have a great influence on accurate calculations of rate coefficients.

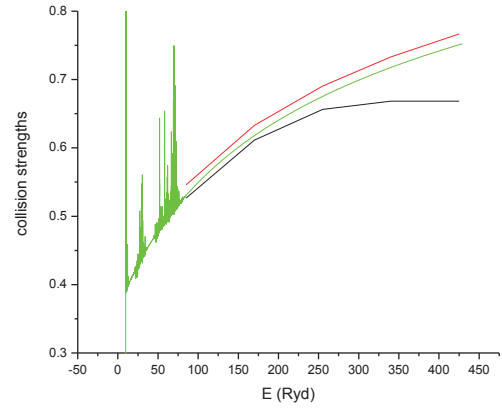


Fig. 2. Comparison of ours (green and black) and Bhatia's (red) results for $2s^2 2p^4(^3P_2) - 2s 2p^5(^3P_2)$

By averaging collision strengths over a Maxwellian velocity distribution, effective collision strengths are calculated with the equation as follows:

$$\gamma(T_e) = \int_0^\infty \Omega(E) \exp\left(-\frac{E_j}{kT_e}\right) d(E_j / kT_e)$$

Then, the corresponding results for excitation $q(i, j)$ and de-excitation $q(j, i)$ rates can be easily determined by the following equations:

$$q(i, j) = \frac{8.63 \times 10^{-6}}{\omega_j T_e^{1/2}} \gamma(T_e) \exp\left(\frac{E_{ij}}{kT_e}\right) \text{ cm}^3 \text{ s}^{-1}$$

$$\text{And } q(j, i) = \frac{8.63 \times 10^{-6}}{\omega_j T_e^{1/2}} \gamma(T_e) \text{ cm}^3 \text{ s}^{-1}$$

References

- [1] P.H. Norrington et al., 1987 *J. Phys. B: At. Mol. Opt. Phys.* **20** 4869.
- [2] K.G. Dyall, I.P. Grant et al, 1989 *Comput. Phys. Commun.* **55** 425.
- [3] A.K. Bhatia et al. 2003 *Atomic Data and Nuclear Data Tables* **83** 71

¹ E-mail: fanquanping@sina.cn

² E-mail: gjiang@scu.edu.cn

State mixing by spin-orbit coupling in the anionic chloroiodine dissociations

Shan X. Tian^{*,1}, Xu-Dong Wang^{*}, Kai-Chung Lau^{†,2}, Yi Pan[†], Chuan-Jin Xuan^{*}, Lei Xia^{*}, Xian-Jin Zeng^{*}, and Hong-Kai Li^{*}

^{*}Hefei National Laboratory for Physical Sciences at the Microscale and Department of Chemical Physics, University of Science and Technology of China, 96 Jinzhai Road, Hefei, Anhui 230026, China

[†]Department of Biology and Chemistry, City University of Hong Kong, 83 Tat Chee Avenue, Kowloon, Hong Kong

Spin-orbit (SO) coupling is known to cause many novel phenomena, while its fundamental knowledge stemmed from the electron behaviors in atoms and molecules. Within the Born-Oppenheimer approximation, the SO coupling can lead to the adiabatically mixed electronic states that however are frequently found as the result of nonadiabatic state-to-state transformation.

In this work, using our home-made anion velocity time-sliced image mapping apparatus, we find that three SO splitting states, $1^2\Pi_{1/2}$, $2^2\Pi_{3/2}$, and $2^2\Pi_{1/2}$, of chloroiodine anion (ICI^-) formed by low electron attachment in the Franck-Condon region are associated with the dissociative limits of Γ (1S_0) and Cl ($^2P_{3/2}$) or Cl^* ($^2P_{1/2}$) fragments. Within the adiabatic scheme, the presumptive Π -symmetry of the fragment angular distributions is dramatically changed to be Π - Σ mixing symmetry, due to the significant SO interaction effect on the electronic state couplings of ICI^- .

The present experimental approach also enables us to separate the contributions of different electronic states from the mixed states, providing a crucial method for quantitatively evaluating the configuration interaction wavefunctions.

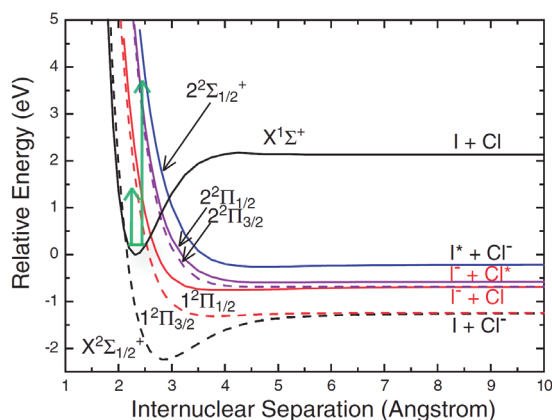


Fig. 1. Potential energy curves of the neutral and anionic chloroiodine.

¹E-mail: sxtian@ustc.edu.cn

^{*}E-mail: kaichung@cityu.edu.hk

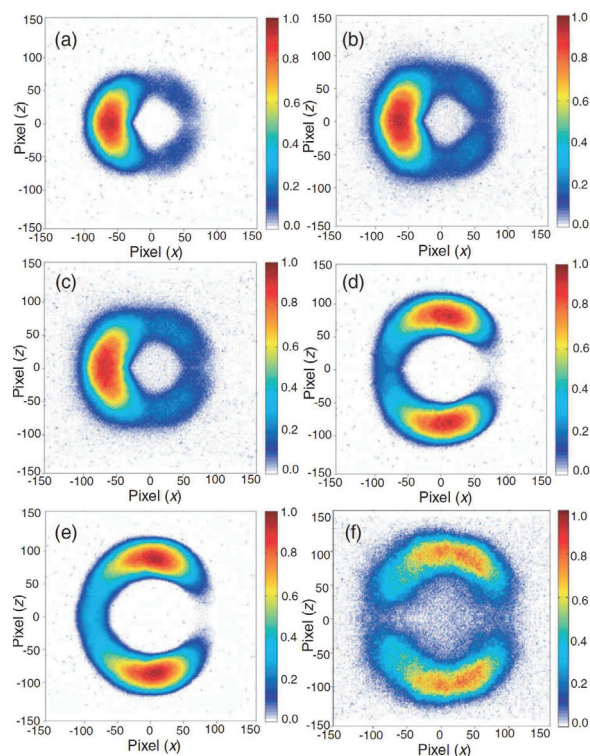


Fig. 2. Sliced images of I^- recorded at the electron energies of 1.2 (a), 1.5 (b), 1.8 (c), 3.0 (d), 3.7 (e), and 4.5 eV (f). The electron incident direction is from left to right and through the image center.

References

- [1] B. Wu, L. Xia, H.-K. Li, X.-J. Zeng, and S. X. Tian, 2012 *Rev. Sci. Instrum.* **83**, 013108.
- [2] L. Xia, *et al.*, 2014 *J. Chem. Phys.* (communication) **140**, 041106.

A plasma shielding and plasma diagnostic study of laser induced air plasmas generated in a collinear double pulse arrangement

Sun Duixiong^{*1}, Su Maogen^{*}, and Dong Chenzhong^{*2}

^{*}Key laboratory of Atomic and Molecular Physics & Functional Materials of Gansu Province, College of Physics and Electronic Engineering, Northwest Normal University, Lanzhou, 730070, China

Laser-induced breakdown spectroscopy (LIBS) has been developed as a very popular and useful elemental analysis technique in recent years. The technique has numerous advantages stemming from its many advantages in physical and chemical analysis, such as multi-elemental analysis, real time analysis, stand-off analysis, apparatus or experimental simplicity, inexpensiveness and quickness. However, compared with other conventional spectrometric methods such as ICP-OES or ICP-MS, a single-pulse (SP) LIBS is less sensitive. Recently, the double-pulse (DP) technique consisting in the application of two delayed laser pulses is used to improve the performance of LIBS measurement. The detailed mechanisms responsible for the improvement of the emission signal are still not clear and many contradicting explanations can be found in the literature.

In this work, an physical phenomenon of the plasma shielding in collinear double-pulse LIBS has been studied experimentally. It's found that the absorbed laser energy of the second laser pulse by the plasma ignited with the first laser pulse depends strongly on the mutually delay time. Most of the second laser pulse energy is absorbed while mutually delay time is less than about 1000 ns, and for mutually delay time larger than 1000 ns, absorption becomes weak gradually. And we found that the correlation between the emission signal enhancement and

excitation energy implies two kinds of emission signal enhancement mechanisms, i.e. reheating and more effective ablation.

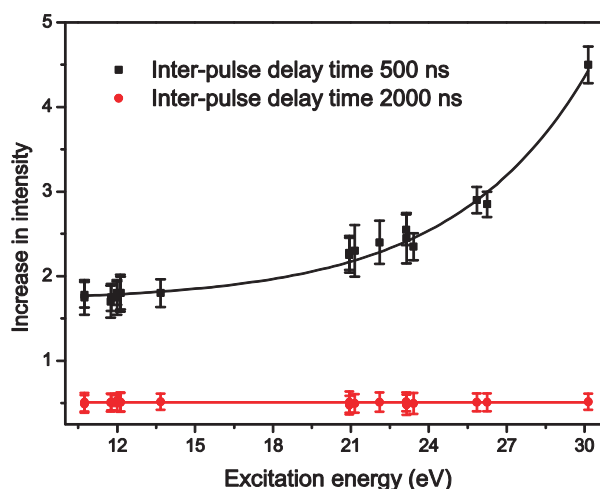


Fig. 1. Correlations between the increase in intensity of line emissions and their excitation energy levels.

References

1. Duixiong Sun, Maogen Su, Chenzhong Dong, 2014, *Plasma Sci. Technol.* **16**, 374,

¹ E-mail: sundx@nwnu.edu.cn

² E-mail: dongcz@nwnu.edu.cn

Investigation of Laser-induced breakdown spectroscopy of uranium element

D.C. Zhang¹, X. Ma², X. L. Zhu and D.M. Zhao

Institute of Modern Physics, Chinese Academy of Sciences, Lanzhou, 730000, Gansu, China

With the rapid development of nuclear power and nuclear industry, it is urgently needed to develop a novel measurement technology for nuclear materials, nuclear fuel and nuclear waste inspection. As a purely optical method, Laser-induced breakdown spectroscopy (LIBS) was pursued by IAEA and many countries for nuclear safeguards inspection. However, the spectra of atomic and singly-ionized actinide elements are extremely complex, need to be investigated exhaustively [1].

The spectra of uranium metal were measured by LIBS in our laboratory. The third harmonic of Nd:YAG laser was used for laser ablation. The typical pulse energy of laser beam was 5mJ. The spectra recorded by a CCD detector after a delay of 1500ns to the laser pulse showed that uranium spectrum was very complex and thousands of emission lines from U I and U II were observed. It can be found that the complex spectrum also resulted in the strong continuum spectrum. In order to choose the optimum parameters for uranium elements analysis by LIBS, the character of time evolution of U lines intensity in air and ambient gas of argon, neon, were studied. The results show that U lines can be enhanced in ambient gas of argon. The same result was seen in lead LIBS spectrum for argon bath gas [2]. The weakest intensity of uranium spectrum was obtained in neon. This may be caused by the low electron density were created in neon gas for its less electrons and the probability of collision excited was decreased.

The results from different gas flow rate of argon were compared. The experimental results show that the intensity of ion lines will be

increased rapidly when the gas flow rate increased from 1L/min to 2.5L/min and then the intensity will not increase with the gas flow rate. The intensity of atomic lines increased more slowly with the gas flow rate. The results show that the low gas flow rate is enough for LIBS signal enhancement.

In the future, the isotope spectra of the elements will be analyzed in our laboratory with a high revolution spectrometer. It will be helpful to apply the LIBS in nuclear safety, the geologic survey and so on.

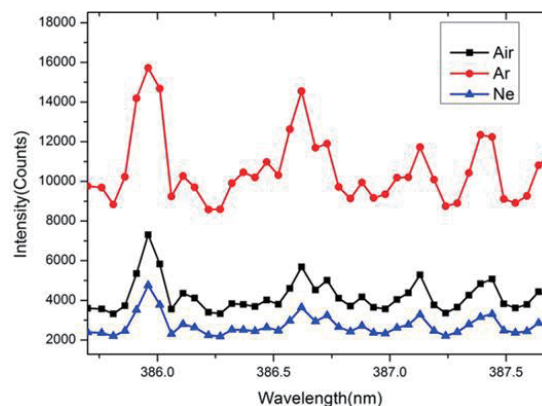


Fig. 1. The intensity of the uranium spectra in three kinds ambient gas.

The work is supported by the projects of instrument function development of Chinese Academy of Sciences (Grant No. YG2012080).

References

- [1] X.K. Shen and Y.F. Lu. 2008 *Appl. Opt.* **47** 1810
- [2] V.I. Babushok et al. 2005 *Spectrochi. Acta Part B* **60** 926

¹ E-mail: dch-zhang@impcas.ac.cn

² E-mail: x.ma@impcas.ac.cn

Dynamics of transfer ionization process in p -He collisions at intermediate energy

D. L. Guo^{*,†,1}, X. Ma^{*,2}, S. F. Zhang^{*}, X. L. Zhu^{*}, W. T. Feng^{*}, R. T. Zhang^{*}, Gao Yong^{*,†}

^{*} Institute of Modern Physics, Chinese Academy of Sciences, Lanzhou 730000, China

[†] University of Chinese Academy of Sciences, Beijing 100049, China

Studies of the dynamics of transfer ionization for collisions of charged particles, in particular proton with helium have been the subject of many experimental and theoretical works for a long time [1]. This kind of research is of great interest not only because of its fundamental nature to understand the few-particle dynamics but also because of its various applications, such as laboratory and astrophysical plasmas. Using the reaction microscope in Lanzhou, we performed a kinematically complete experiment to study the transfer ionization in p -He collisions [2].

The electron momentum distribution projected onto the scattering plane displays some features characterized by binary encounter electron emission (Fig. 1 (a)). The deviation of the distribution from the binary encounter ridge expected from classical two-body kinematics is attributed to the binding energy effect and a higher-order effect involving the interaction between the electron and the residual recoil ion. A comparison with the binary encounter model involving the binding energy effect reveals that the transfer ionization is more likely to happen in a sequential order of transfer first and ionization second.

Another interesting observation of the electron emission is the absence of the cusp-shaped electrons centered at a speed equal to that of the incident projectile in the forward direction (Fig. 1 (b)). This is contrary to the previous results [3]. A preliminary analysis indicates that for neutralized outgoing projectile with the captured electrons in the ground state the cusp does not exist and the contamination due to the double collisions could cause the cusp-shaped electrons reported in the literature. The present results also pose severe challenges to the existing mechanisms responsible to the cusp-shaped electron for the neutral outgoing

projectile. Further investigations are desirable to clarify the problem.

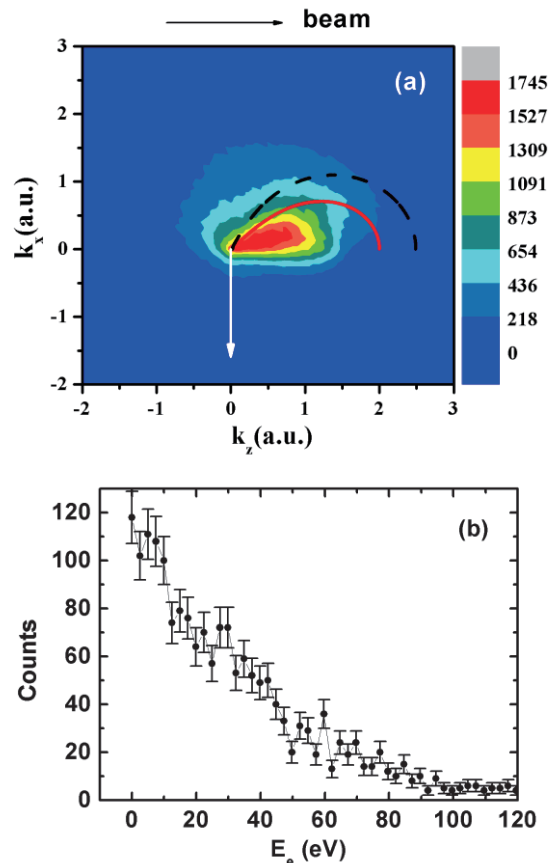


Fig. 1. (a) The electron momentum projected onto the scattering plane for 50 keV impact energy; (b) The electron energy distribution for electron emission angles of $0 - 5^\circ$ for 75 keV impact energy.

References

- [1] J. Ullrich, R. Moshhammer, A. Dorn et al., 2003 *Rep. Prog. Phys.* **66** 1463.
- [2] D. L. Guo, X. Ma, S. F. Zhang et al., 2012, *Rhys. Rev. A* **86** 052707
- [3] G. Bernardi, P. Focke, A. D. González et al., 1999 *J. Phys. B: At. Mol. Opt. Phys* **32** L451.

¹ E-mail: guodalong@impcas.ac.cn

² E-mail: x.ma@impcas.ac.cn

Dielectronic resonant measurements of oxygen-like $^{8}\text{Kr}^{28}$ at the HIRF main cooler Storage Ring CSRm of IM

Z K Huang^{*,†}, X Ma^{*,2}, Shen^{*}, Huang^{*,†}, Xu^ξ, X Zhu^{*}, X Xu^ξ, F Zhu^ξ,
Shi, Zong, M Zhao^{*}, Guan^{*}, Xiang^{*}, Li^{*}, X M Ma^{*}, Mao^{*}, Tian^{*},
Zhang^{*}, Xia^{*}, H S Xu^{*}, and G Xiao^{*}

* Institute of Modern Physics, Chinese Academy of Sciences, Lanzhou 730000, Gansu, China.

† University of Chinese Academy of Sciences, 100049, Beijing, China.

ξ University of Science and Technology of China, Hefei 230026, Anhui, China

College of Physics and Electronic Engineering, Northwest Normal University, Lanzhou, 730070, China.

Total recombination rate coefficients of $^{78}\text{Kr}^{28+}$ ions have been measured by employing the electron-ion merged-beams technique [1] at the main cooler storage ring (CSRm) at the Institute of Modern Physics, Lanzhou. The relative energies from 0 to 13.5 eV between the electron beam and the ion beam at c.m. frame is precisely tuned by a fast electron beam energy detuning system. The recombined ions are separated by a dipole magnet and detected by a scintillation detector [2].

Table 1: the main experimental parameters

HVPS	- 2.2890 keV
Uc/Ua	~0.14
Electron beam current	123.9 mA
Electron beam radius	2.95 cm
Beam energy	4.014 MeV/u
Highest beam current	45 μA
Lowest beam current	5 μA
Beam momentum spread	3.7×10^{-4}

Where the HVPS is the high voltage power supply for the electron gun which denotes electron kinetic energy. Uc/Ua is dominate the electron beam profile and transverse distribution. The radiative recombination (RR) rate coefficients has been removed from the spectrum by subtracting an empirical function fitting to the experimental points which only contain the RR contribution (see Fig.1). A theoretical calculation using the flexible atomic code (FAC) has been carried out to calculate the recombination cross section. The theoretical calculations will be analyzed and compared with the experimental results by

$$\alpha(E) = \int \sigma(v) v (v, \nu) d^3 v$$

Where σ is characterized by the electron velocity distribution. The further data analysis is in progress.

In order to calibrate the detuning system at the CSRm, a DR experiment with Lithium-like Ar^{15+} ion beam is in preparation. We will also extend the DR experiments with highly charged ions (He-like and Li-like) into the experimental cooler storage ring (CSRe). The details of DR experiments at the CSRm and CSRe including experimental results and preparation works will be presented on the conference.

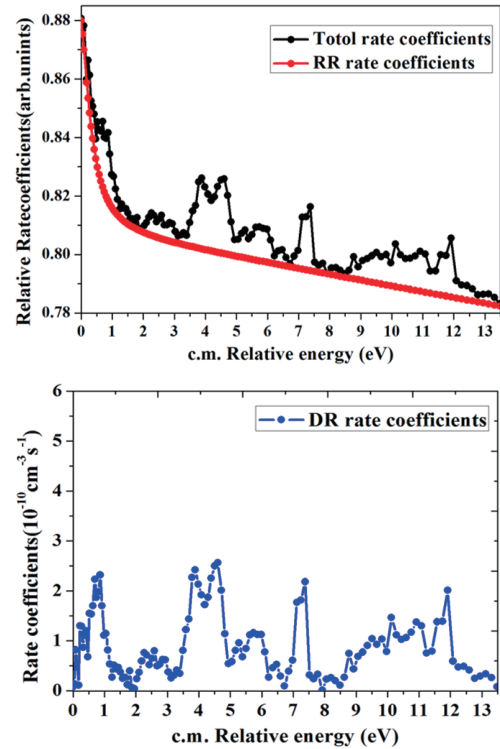


Fig. 1. The rate coefficients of total (up) and subtracted RR contribution (down) as a function of c.m. relative energy of Kr^{28+} at c.m.

References

- [1] A. Müller, Adv. At. 2008 Mol. Phys., **55**, 293.
- [2] W. Q. Wen, X. Ma, W.Q.Xu et al. 2013. Nucl. Instr. Meth. B **3** 731-733.

¹ Email: huangzhongkui@impcas.ac.cn

² Email: x.ma@impcas.ac.cn

Electron capture in collisions of Be^{q+} and B^{q+} with H at low energies

C. H. Liu ^{*,1}, J. G. Wang [†], and R. K. Janev [‡]

^{*}Institute of Modern Physics, Chinese Academy of Sciences, Lanzhou, 730000, China

[†]Institute of Applied Physics and Computational Mathematics, P.O. Box 8009, Beijing 100088, China

[‡]Macedonian Academy of Sciences and Arts, PO Box 428, 1000 Skopje, Macedonia

The electron capture processes of multiply charged impurity ions with neutral hydrogen are important in the studies of impurity transport in the edge and divertor of Tokamak plasmas. Beryllium and boron are important impurity species in the edge plasmas of thermonuclear fusion devices. Boron is released in the plasma from boronized graphites used as plasma facing materials in many tokamaks because of the plasma-wall interaction processes, while beryllium is envisaged as a first wall material in the International Thermonuclear Experimental Reactor [1]. The charge-exchange processes of these impurities in all charge states with the hydrogen plasma constituents are required for modeling of their transport in the plasma and their contribution to the plasma energy and particle losses. In the edge and divertor plasma regions the character temperatures are below 100-200eV. With respect to the fusion energy research, electron-capture cross sections at low energies are needed for the modeling and diagnostics of plasmas.

In this work, we studied the electron capture processes in the Be^{q+} ($q=1-3$) and B^{q+} ($q=3-4$) collisions with atomic hydrogen in the low energy region using the quantum-mechanical molecular orbital close coupling (MOCC) method [2]. The *ab initio* molecular structure is calculated by the multireference single- and double-excitation configuration interaction (MRDCI) method [3]. The electron translation effect was considered according to the treatment of Ref. [4].

The present MOCC results of the total cross sections agree well with the available experimental and theoretical results at energies

below 5keV/u. According to the present calculations and other available results, the recommend cross section data are given. The recommend total electron capture cross sections for $\text{Be}^{q+}+\text{H}$ ($q=1-4$) collision systems are shown in Fig.1. The electronic structure of the collision system plays important role in the electron-capture dynamics at $E < 10$ keV/u. At higher energies, the charge transfer cross sections mainly depend on the charge of the projectile.

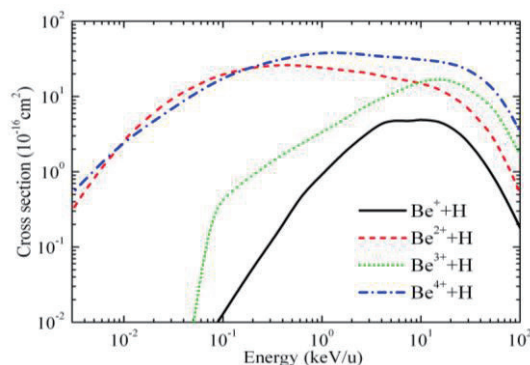


Fig. 1. The recommend electron capture cross sections for the Be^{q+} -H collisions.

This work was supported by the National Natural Science Foundation of China (Grants Nos. 10979007 and 11004014).

References

- [1] A. Loarte *et al.*, 2007 *Nucl. Fusion* **47** S203.
- [2] B. Zygelman, D. L. Cooper and M.J. Ford *et al.*, 1992 *Phys. Rev. A* **46** 3846.
- [3] R.J. Buenker and R.A. Phillips, 1985 *J. Mol. Struct.: THEOCHEM* **123**, 291.
- [4] M.C. Bacchus-Montabonel and P. Ceyzeriat 1998 *Phys. Rev. A* **58** 1162.

¹ E-mail: liuch@impcas.ac.cn

Kinematically complete experiment for ionization-excitation of helium

S. Xu,¹ X. Ma,² S. Yan, P. Zhang, X. L. Zhu, J. Yang, W. T. Feng, D. M. Zhao, and S. F. Zhang

Institute of Modern Physics, Chinese Academy of Sciences, Lanzhou 730000, China

Electron induced ionization-excitation of helium is a basic four-body Coulomb problem in which all the four charged particles are actively involved. It is much more challenging to both experiment and theory compared to direct ionization with the residual He⁺ ion in the ground state. Only very recently, Zatsarinny and Bartschat claimed that ionization-excitation to the n=2 state of He⁺ is solved in theory with the B-spline R-matrix with pseudostates (BSRMPS) method [1, 2]. Their BSRMPS calculations were tested with the measured triple-differential cross section (TDCS) ratios for ionization leaving the residual ion in either the 1s state or the n = 2 (2s + 2p) excited states [3] or with the absolute cross sections to the 2p state.

The 2s and 2p separated TDCS data, especially at low and intermediate incident energy range where the high order effects are expected to play a significant role, would offer the most stringent test to theoretical models. However, only one experiment at high incident energy achieved the TDCSs for 2p state till now due to the small cross section and the low detection efficiency for multi-coincidence events [4].

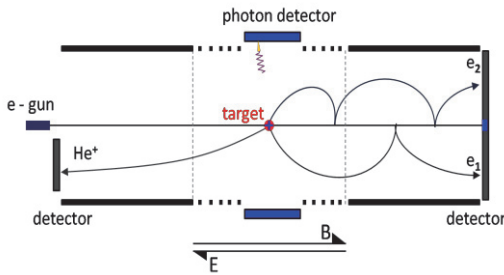


Figure 1. Schematic view of the setup.

Here we present the measurement of electron impact ionization-excitation of helium aiming to obtain the 2s and 2p separated TDCSs. Experimentally this is accessible by using a (e, 2e) reaction microscope equipped with two multi-channel plate photon detectors (Figure 1). The two electrons, the recoil ion and the photon

in the radiative decay from np to 1s state in the final state are recorded either in the (2e+ion) or in the (γ +e+ion) triple coincidence mode. In the (2e+ion) case, the summed energy of the two electrons in the final state separates the ns+np state of the He⁺ ion from the ground 1s state. While in the (γ +e+ion) case the photon signal from radiative decay of np state make it possible to measure the np contribution individually. Figure 2 is the triple coincidence timing spectrum at 150eV projectile energy for the (γ +e+ion) measurement. As shown in the figure, the ionization-excitation events to np states are well separated. The momentum vectors of the recorded ion and electron are reconstructed and the momentum of the second electron is calculated using momentum conservation, and thus the TDCSs could be deduced.

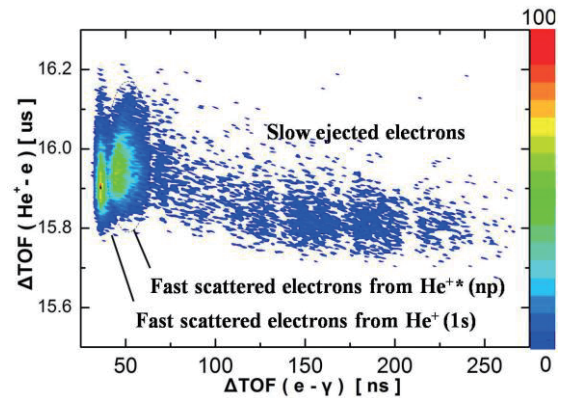


Fig. 2. 2D plots for γ +e+ion triple coincidence events as function of the time of flight differences $\Delta\text{TOF}(e-\gamma)$ and $\Delta\text{TOF}(\text{He}^+-e)$.

References

- [1] O. Zatsarinny et al 2011 Phys. Rev. Lett. 107, 023203
- [2] O. Zatsarinny et al 2014 J. Phys. B, 47, 061001
- [3] S. Bellm et al 2006 Phys. Rev. Lett. 96, 223201
- [4] G. Sakhelashvili et al 2005 Phys. Rev. Lett. 95, 33201

¹E-mail: s.xu@impcas.ac.cn

²E-mail: x.ma@impcas.ac.cn

A new MOTRIMS apparatus perspective at IMP

Jie Yang^{*,1}, Xiaowei Cheng^{*†}, Xiaolong Zhu^{*}, Xinwen Ma^{*} and Dongmei Zhao^{*}

^{*} Institute of Modern Physics, Chinese Academy of Sciences, 730000 Lanzhou, China

[†] Graduate University of Chinese Academy of Sciences, 100049 Beijing, China

There are two powerful experimental techniques have been developed in the past decades atomic and molecular physics, cold target recoil ion momentum spectroscopy (COLTRIMS) and magneto-optical traps (MOTs). Very recently, both MOTs and COLTRIMS were merged [1-5] by using trapped atoms as a cold target for the COLTRIMS methodology. This new development, called MOTRIMS, has several advantages to the standard COLTRIMS in which the cold target usually provided by a supersonic gas jet. Firstly, cold alkali or alkaline-earth atoms experiment can be performed, which could not be cooled in a supersonic expansion without forming molecules or clusters. The initial states of these atomic species, including aligned or oriented states, can be easily controlled by exciting the atoms with a laser. Secondly, the temperature of the atoms in MOTs is of the order of 100 μ K, and no longer a limit for the resolution of recoil momentum.

Fig. 1 shows a simplified schematic of the experimental setup, which comprises three parts: (i) MOTs of ^{87}Rb atoms, (ii) a project ion beam line with a charge-state analyzer, (iii) the recoil ion spectrometer. Now the whole system is under installation at Institute of Modern Physics Chinese Academy of Sciences.

^{87}Rb atoms are cooled in MOTs with Three pairs of counterpropagating laser beams and anti-Helmholtz magnetic coils, where two laser frequencies are required: one tuned 110 MHz below the cooling transition $5^2S_{1/2}(F=2)-5^2P_{3/2}(F'=3)$, and the other laser tuned on the repumping transition $5^2S_{1/2}(F=1)-5^2P_{3/2}(F'=2)$. A fast triggered charge coupled device (CCD) camera is also designed to imaging the atomic cloud. The temperature and density of atomic cloud will be deduced from the speed of the cloud expansion. As the simulation, when the cooling laser has a total energy of 100 mW and a diameter of 13 mm, and then the cold ^{87}Rb

atomic cloud will has a temperature of ~ 1 mK, a density of 1×10^{11} atoms/cm³ and a diameter of 0.5 mm.

The recoil ion spectrometer consists of time of flight (TOF) and a 2-dimensional position sensitive detector (2D-PSD). Using SIMON software, a special electric field is designed to extract the recoil ions from collision region and 3-dimension focuses them in the detection plane. Both the TOF and the detector are optimized to ensure the maximum detection efficiency and the highest resolution of the recoil ion momentum.

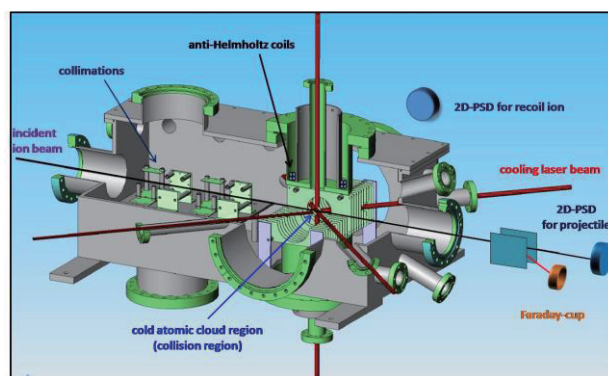


Fig. 1. Schematic of the MOTRIMS setup

Based on the new MOTRIMS apparatus, our research interest in ion-atom collisions will focus on the electron capture process, including inner-shell and outer-shell electron captures, MOT population dynamics, and photoassociation in cloud atoms.

References

- [1] J. Blicek, X. Flechard, A. Cassimi et al., 2008 Rev. Sci. Instrum. **79** 103102
- [2] M. van der Poel, C. V. Nielsen, M.-A. Gearba et al., 2001 Phy. Rev. Lett. **87** 123201
- [3] J. W. Turkstra, R. Hoekstra, S. Knoop et al., 2001 Phy. Rev. Lett. **87** 123202
- [4] X. Flechard, H. Nguyen, E. Wells et al., 2001 Phy. Rev. Lett. **87** 123203
- [5] D. Fischer, D. Globig, J. Goullon et al., 2012 Phy. Rev. Lett. **109** 113202

¹ E-mail: jie.yang@impcas.ac.cn

A new mechanism induced by the third atom in ionized Ar trimer by high energy electrons impact

S. Yan^{*1}, X. Ma^{*2}, P. Zhang^{*}, S. Xu^{*}, S. X. Tian[†], B. Li^{*}, X. L. Zhu^{*}, W. T. Feng^{*} and D. M. Zhao^{*}

^{*}Institute of Modern Physics, Chinese Academy of Sciences, Lanzhou 730000, China

[†]Hefei National Laboratory for Physical Sciences at the Microscale and Department of Chemical Physics, University of Science and Technology of China, Hefei, Anhui 230026, China

If a constituent in the cluster is excited or ionized, the energy and charge transfer may occur, and some environmental enhancement effects may be involved [1-3]: such as Interatomic Coulombic Decay (ICD), Radiative Charge Transfer (RCT) and Electron Transfer Mediated Decay (ETMD).

In this experiment, we measured the kinetic energy distributions (KER) of the fragment ions of ionized argon dimers and trimers using 3000 eV electron impact. It can be seen from the left panel of figure 1 that, for the dissociation of parent ion $(Ar_2)^{2+}$, two peaks appear in the KER spectrum. One locates at 3.7 eV (peak A), consistent with the equilibrium internuclear distance of Ar dimer. It is demonstrated that peak A corresponds to ICD and Sequential Ionization (SI). In contrast, peak B corresponds to a much shorter internuclear distance. This peak indicates that the slow decay process: RCT, should be involved [4].

For the decay of $(Ar_3)^{2+}$, as shown in the right panel of figure 1, only one pronounced peak locates at 3.5 eV is observed. In contrast, the peak corresponds to the RCT process, which should locate in the larger energy area, does not appear at all. This result indicates that a new dynamics has been induced by the additional atom in Ar trimer [5].

Similar to RCT process in the $(Ar_2)^{2+}$ ion, the Ar-Ar²⁺-Ar initial state can also be formed by double ionization of Ar trimer. And the charge transfer can happen in the equilibrium internuclear distance of Ar²⁺-Ar ion, in which process an $(Ar_2)^{+}+Ar^{+}$ intermediate state can be formed. However, because the equilibrium internuclear distance of Ar²⁺-Ar is much shorter than that of Ar⁺-Ar (see Figure 2), the produced Ar⁺-Ar ion populate in a predissociation state, resulting in the loss of the neutral Ar atom.

Consequently, the predissociation three body fragmentation ($Ar^{+}+Ar^{+}+Ar$) occurs instead of two body fragmentation ($Ar^{+}+Ar_2^{+}$).

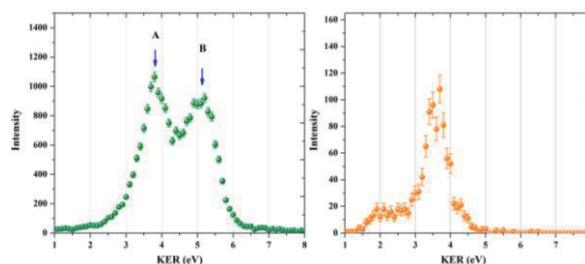


Fig. 1. Left panel: KER distribution of the $Ar^{+}+Ar^{+}$ pair from the fragmentation of $(Ar_2)^{2+}$; and right panel: KER distribution of the $Ar_2^{+}+Ar^{+}$ pair from the fragmentation of $(Ar_3)^{2+}$.

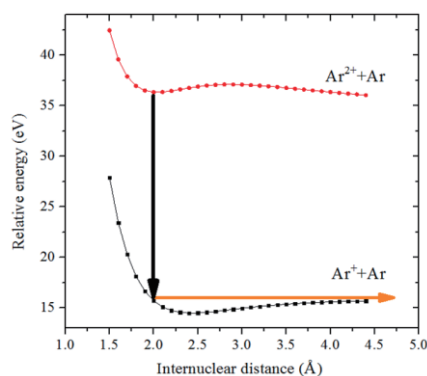


Fig. 2. Potential energy curves from the CCSD calculation; upper curve: the ground state of the $Ar^{2+}-Ar$ ion, lower curve: the $Ar^{+}-Ar$ ion.

This work is supported by the 973 Program of China through Grant No. 2010CB832902, the West Light Doctoral Foundation of CAS, the NSFC through Grants No. 10979007 and No. 11304325, and the Knowledge Innovation Program of CAS through Grant No. KJCX1-YW-N30.

References

- [1] L. S. Cederbaum et al., 1997 *Phys. Rev. Lett.* **79**, 4778.
- [2] N. Saito et al., 2007 *Chem. Phys. Lett.* **441**, 16.
- [3] J. Matsumoto et al., 2010 *Phys. Rev. Lett.* **105**, 263202.
- [4] S. Yan et al., 2013 *Phys. Rev. A* **88**, 042712.
- [5] S. Yan et al., 2014 *Phys. Rev. A* **89**, 062707.

¹E-mail: yanshuncheng@impcas.ac.cn

²E-mail: x.ma@impcas.ac.cn

The influence of Breit interaction and quantum interference on polarization of radiative transitions following electron-impact excitation of Li-like ions

Y. L. Ma*, L. Y. Xie ^{*.1}, C. Ma*, and C. Z. Dong*

*Key laboratory of Atomic and Molecular Physics & Functional Materials of Gansu Province, College of Physics and Electronic Engineering, Northwest Normal University, Lanzhou, 730070, China

The magnetic sublevels of an excited state produced by electron-impact excitation (EIE) process may not be populated statistically in plasmas. The radiation emitted during the decay of these unequally populated sublevels to a lower level is polarized. The degrees of polarization of x-ray, which depend on the degree of anisotropy of the velocity distribution, provide important diagnostic tool for studying the high-temperature plasmas as the Sun and laser-produced plasmas [1].

X-rays emitted by highly charged ions arise not only optically allowed electric dipole (E1) transitions but also from forbidden magnetic quadrupole (M2) and higher-order electric transitions. In one important mixture of E1 and M2 transition, which are simultaneously allowed by the angular momentum selection rules. However, almost of previous works on the polarization have been dealt with purely electric or purely magnetic transitions of definite multipole order due to the transition probabilities associated with the two allowed multipoles usually differ from each other by several orders of magnitude. To our knowledge, there exists a few works [2-4] on the polarization of mixed multipole lines so far.

In this work, the polarizations of mixed E1 - M2 radiative transition lines, i.e. $1s2p^2 \ ^4P_{3/2} - 1s^22p \ ^2P_{1/2}$ (labeled by *g*), $1s2s2p(^3P) \ ^2P_{3/2} - 1s^22s \ ^2S_{1/2}$ (labeled by *q*), $1s2s2p(^2P) \ ^2P_{3/2} - 1s^22s \ ^2S_{1/2}$ (labeled by *s*), and $1s2s2p(^3P) \ ^4P_{3/2} - 1s^22s \ ^2S_{1/2}$ (labeled by *u*) in highly charged Li-like Pr^{56+} , W^{71+} , Hg^{77+} , and U^{89+} ions following electron-impact excitation are calculated. We also explored the influence of Breit interaction on the total and magnetic sublevel cross sections, and the polarization of emitted x-ray lines. In Fig. 1 and 2, taking the *g*-line of W^{71+} ion as an example, the EIE cross sections from the $1s^22p \ ^2P_{1/2}$ to $1s2p^2 \ ^4P_{3/2}$ state and the polarization of corresponding radiative emission are presented, respectively. It is found that the Breit interaction and E1-M2 interference is very important for obtaining accurate cross sections

and x-ray polarization of highly charged Li-like ions.

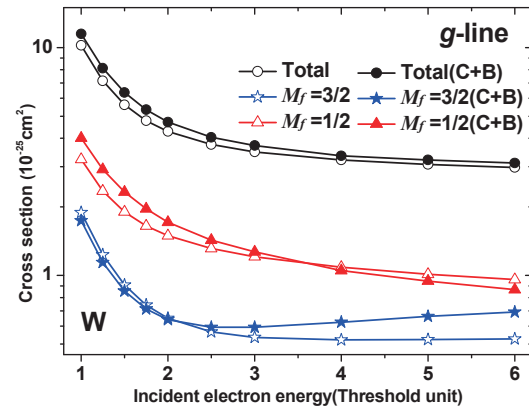


Fig. 2. EIE cross sections (10^{-25}cm^2) for the total and specific magnetic sublevel of upper excited states of *g*-line in W^{71+} ion. C+B: the results with Breit+Coulomb interaction; C: the results Coulomb interaction only

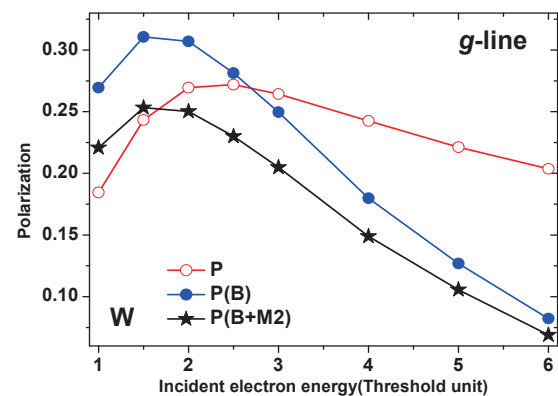


Fig. 2. Polarization of *g*-line in W^{71+} ion. The open red circle (P): the results without Breit and M2 ; Solid blue circle (P(B)): present the results including Breit; Solid black star (P(B+M2)): the results Breit and M2 included.

References

- [1] R. Beier, C. Bachmann, et al., 1981 *J. Phys. D* **14** 643.
- [2] J. R. Henderson et al., 1990 *Phys. Rev. Lett.* **65** 705.
- [3] J. Dubau, Y. Garbuzov, and A. Urnov, 1994 *Phys. Scr.* **49** 39.
- [4] B. Bensaid, M. K. Inal, and J. Dubau, 2006 *J. Phys. B* **39** 4131.

¹ E-mail: xiely@nwnu.edu.cn

Japanese Participants

	First Name	Last Name	Name in JP	Affiliation
1	Fumihiro	Koike	小池文博	Sophia University
2	Takeshi	Higashiguchi	東口武史	Utsunomiya University
3	Takeshi	NISHIKAWA	西川 亘	Okayama University
4	Shigeru	Morita	森田 繁	National Institute for Fusion Science
5	Hiroyuki	A. Sakaue	坂上裕之	National Institute for Fusion Science
6	Daiji	Kato	加藤太治	National Institute for Fusion Science
7	Tetsutarou	Oishi	大石鉄太郎	National Institute for Fusion Science
8	Makoto	IMAI	今井 誠	Kyoto University
9	Hajime	TANUMA	田沼 肇	Tokyo Metropolitan University
10	Hiroaki	Nishimura	西村博明	Osaka University
11	NAKAMURA	Nobuyuki	中村信行	The University of Electro-Communications
12	Masahiko	Takahashi	高橋正彦	Tohoku University

Chinese Participants

	First Name	Last Name	Name in CN	Affiliation
1	Jiaming	Li	李家明	Shanghai Jiaotong University Tsinghua University
2	Xiang	Gao	高翔	Beijing Computational Science Research Center
3	Zhengying	Cui	崔正英	Southwestern Institute of Physics
4	ChunFeng	Dong	董春风	Southwestern Institute of Physics
5	Linfan	Zhu	朱林繁	University of Science and Technology of China
6	Yong	Wu	吴勇	Institute of Applied Physics and Computational Mathematics
7	Kai	Wang	王凯	Institute of Applied Physics and Computational Mathematics
8	Xiaolong	Zhu	朱小龙	Institute of Modern Physics, CAS
9	Yueying	Qi	祁月盈	Jiaxin University
10	Bowen	Li	李博文	Lanzhou University
11	Xiaobin	Liu	刘晓斌	Tianshui Normal University
12	Yinglong	Shi	师应龙	Tianshui Normal University
13	Quanping	Fan	范全平	Sichuan Univrsity
14	Jun	Jiang	蒋军	Charles Darwin University, Australia
15	Chenzhong	Dong	董晨钟	Northwest Normal University
16	Xiaobin	Ding	丁晓彬	Northwest Normal University
17	Luyou	Xie	颀录有	Northwest Normal University
18	Denghong	Zhang	张登红	Northwest Normal University
19	Yanbiao	Fu	符彦飙	Northwest Normal University
20	Maogen	Su	苏茂根	Northwest Normal University
21	Qianghua	Yuan	袁强华	Northwest Normal University
22	Kun	Ma	马堃	Northwest Normal University
23	Qi	Min	敏琦	Northwest Normal University
24	Yaopeng	Yin	殷耀鹏	Northwest Normal University
25	Yulong	Ma	马玉龙	Northwest Normal University
26	Chi	Ma	马驰	Northwest Normal University
27	Jinming	Liu	刘进明	Northwest Normal University
28	Feng	Yang	杨峰	Northwest Normal University
29	Junshun	Ding	丁军顺	Northwest Normal University
30	Xi	Chen	陈曦	Northwest Normal University
31	Shiquan	Gao	曹世权	Northwest Normal University
32	Fei	Jiao	焦飞	Northwest Normal University
33	Haiyue	Cui	崔海月	Northwest Normal University

Chinese Participants

	First Name	Last Name	Name in CN	Affiliation
34	Jiaxin	Liu	刘佳欣	Northwest Normal University
35	Jianqiang	Jing	景建强	Northwest Normal University
36	Teng	Liang	梁腾	Northwest Normal University
37	Xundong	Wang	王旭东	Northwest Normal University
38	Xiaowei	Chang	常小伟	Northwest Normal University